



THE UNIVERSITY OF QUEENSLAND  
AUSTRALIA

**Multiple, Object-Oriented Segmentation Methods of  
Mammalian Cell Tomograms**

Nur Intan Raihana Ruhaiyem  
BMM (Hons), Msc. (Comp. Sc.)

*A thesis submitted for the degree of Doctor of Philosophy at  
The University of Queensland in 2014  
Institute for Molecular Bioscience*

## **Abstract**

Electron tomography (ET) is a powerful tool for the 3D mapping of the complex 3D sub-cellular structures of cells. It can provide detailed structural data for the extraction, segmentation and annotation (e.g. organelle type, spatial location, volume, surface area, shape and cellular interactions). The ability to map and model sub-cellular volumes is dependent on the quality of the electron tomography data and the ability to segment the resolved features accurately. In particular low signal to noise ratios can result in the loss of structural data as well as the incorrect identification of false positives. Manual segmentation is currently considered the gold standard but is subjective and the process is slow. This is highlighted by the finding that the careful segmentation of ~1% of an insulin-secreting HIT-T15 cell required approximately 3600 person-hours (Marsh et al., 2001a). Consequently as the volume and quality of cellular electron tomography data increases so will the need for automated segmentation approaches. Such automated processes will likely require the integration of image filtration methods, boundary-based and region-based segmentation algorithms and edge detector algorithms. To be of real utility these automated methods must be fast as well as accurate ideally across multiple scales ranging from tissues to molecules. Semi-automated approaches will also be of value if they are able to yield significant gains in data quality and speed.

The process of segmentation is principally made difficult by limitations caused by low signal-to-noise ratio (SNR) of volumetric image data typical of that generated by electron tomography. Indeed compared with MRI and CT data-sets electron microscopy has a low SNR and so is good test system for the development of segmentation algorithm. To date the low SNR of electron tomography data has resulted in limited examples of successful automatic segmentation. Improved image pre-processing techniques, such as increasing the SNR through improved sample preparation and imaging, as well as the careful application of denoising algorithms in conjunction with carefully managed segmentation processes have proven most beneficial, but there is still substantial scope for improvement.

The aim of this project has been to analyse the pancreatic beta cell tomograms and to conduct a detailed investigation into the structural diversity of their insulin granules, mitochondria and the Golgi apparatus to provide a framework for their classification. The image and structural data obtained by this process was used to guide the development of an image processing pipeline for the

semi-automated segmentation of specific classes of these organelles on the path to developing more advanced automated processes.

Chapter 1 provides an overview of biology of pancreatic beta cells and the process of insulin secretion as well as electron tomography and the motivation for the development of automated segmentation processes.

Chapter 2 describes the methods used to prepare and analyse these data sets. A number of cellular tomograms of insulin-secreting pancreatic beta cells recorded at high (i.e. 4-5 nm) resolution were used as primary ‘proof-of-concept’ datasets for this project. To control the number of datasets (i.e. organelle sub-volumes) for the project, three key organelles of insulin secretion were selected; the Golgi apparatus (GA), mitochondria (MC) and insulin granules (IG).

Chapter 3 introduces and describes the proposed segmentation pipeline which is referred to as the ‘*cellular tomography segmentation*’ (CTS) workflow. It also introduces a scoring system that is based on mesh surface area (MSA) of an organelle’s 3D model and provides a useful, quantitative comparison for assessing the quality of various segmentation approaches, compared with the results obtained by manual tracing. Overall this chapter covers significant computational considerations for the development of segmentation algorithms for electron tomography.

Chapter 4 introduces the concept of the categorisation of sub-cellular organelles according to their image properties both to provide a basis for morphological classification of organellar subtypes and to enable improved image segmentation of each of these subclasses. The performances of tracing tools are quantitatively compared and conclusions on best performance drawn in this chapter.

Concurrent with the research described here, a new filter for automated edge detection-based processing of 3D volumetric image data was developed in the Hankamer Lab at the University of Queensland. The 3D Bilateral Edge detector (3D BLE) (Ali et al., 2012) yielded their first successful results in automatically segmenting organelles in high resolution electron tomograms. In Chapter 5 the 3D BLE filter was used to segment the selected data sets for comparison with semi-automated processes based on the ‘*cellular tomography segmentation*’ (CTS) workflow. The segmentation results obtained using the best detected settings identified for each organelle sub-volume were compared to those obtained using the semi-automated CTS workflow, as outlined in Chapters 3 and 4. This comparison suggested that for the datasets and conditions analysed, the CTS

workflow was superior in performance, both in terms of quantitative and qualitative comparison. In terms of quality it proved comparable to manual tracing but also better than the best detected 3D BLE settings.

Overall, this newly developed semi-automated CTS workflow and the image categorisation technique enable improved rates of segmentation of sub-cellular compartments. It also enables rapid, quantitative comparison of the morphology and function of three key organelles of insulin secretion of non-stimulated pancreatic beta cells. It also offered sets of scoring objectives for different organelle sub-groups to expedite the process of optimising method settings not currently afforded by any other technique.

## **Declaration by author**

This thesis is composed of my original work, and contains no material previously published or written by another person except where due reference has been made in the text. I have clearly stated the contribution by others to jointly-authored works that I have included in my thesis.

I have clearly stated the contribution of others to my thesis as a whole, including statistical assistance, survey design, data analysis, significant technical procedures, professional editorial advice, and any other original research work used or reported in my thesis. The content of my thesis is the result of work I have carried out since the commencement of my research higher degree candidature and does not include a substantial part of work that has been submitted to qualify for the award of any *other* degree or diploma in any university or other tertiary institution. I have clearly stated which parts of my thesis, if any, have been submitted to qualify for another award.

I acknowledge that an electronic copy of my thesis must be lodged with the University Library and, subject to the General Award Rules of The University of Queensland, immediately made available for research and study in accordance with the *Copyright Act 1968*.

I acknowledge that copyright of all material contained in my thesis resides with the copyright holder(s) of that material. Where appropriate I have obtained copyright permission from the copyright holder to reproduce material in this thesis.

### **Publications during candidature**

**Nur Intan Raihana Ruhaiyem**, Semi-automated cellular tomogram segmentation workflow (CTSW): towards an automatic target-scoring system. Proceedings of the International Conference on Computer Graphics, Multimedia and Image Processing, Kuala Lumpur, Malaysia, 17-19 November 2014, 38-48.

**Nur Intan Raihana Ruhaiyem**, Boundary-based versus region-based approaches for cellular tomography segmentation. Proceedings of the 1<sup>st</sup> International Engineering Conference, Iraq, 24-26 November 2014.

*(Pending publication at the time of this PhD thesis is submitted)*

### **Publications included in this thesis**

**Nur Intan Raihana Ruhaiyem**, Semi-automated cellular tomogram segmentation workflow (CTSW): towards an automatic target-scoring system. Proceedings of the International Conference on Computer Graphics, Multimedia and Image Processing, Kuala Lumpur, Malaysia, 17-19 November 2014, 38-48.

*(Partly incorporated into Chapter 3)*

**Nur Intan Raihana Ruhaiyem**, Boundary-based versus region-based approaches for cellular tomography segmentation. Proceedings of the 1<sup>st</sup> International Engineering Conference, Iraq, 24-26 November 2014.

*(Partly incorporated into Chapter 3)*

### **Contributions by others to the thesis**

Electron tomograms were prepared by the Marsh Group from the Institute for Molecular Bioscience. 3D Bilateral edge detector algorithm was developed by Rubbiya Ali from the Hankamer Group from Institute for Molecular Bioscience. All other work was undertaken by the candidate including manual tracing of tomograms (with assistance from experts in the Marsh Group), development and application of the new semi-automated segmentation workflow, and analysis of the results gained for each experimental chapter.

### **Statement of parts of the thesis submitted to qualify for the award of another degree**

None.

## **Acknowledgements**

Bismillahirrahmaanirraheem...Alhamdulillah Rabbilalameen.

All praises due to Allah, the Almighty.

I would like to express my appreciation to my committee members who were so patient with me. Dr. Brad Marsh, who, provided support and instilled mental stimulation in regards to my research. Without his guidance this study would not have been possible. He inspired me to take pride in my research; his enthusiasm for research efforts will have a significant effects on my future projects. I would like to express the deepest appreciation to my committee chair Professor Ben Hankamer, who embodied the figure of a kind professor, who has the attitude and the substance of a genius: he continually and convincingly conveyed a spirit of adventure in regard to research and scholarship. Special thanks to Dr. Michael Landsberg gave direction when it was most needed. His advices throughout this process kept me focused on this topic. Without these two important people guidance and persistent help this thesis would not have been possible.

In addition, a thank you to Mr. Peter van der Heide and Dr. Andrew Noske, who introduced me to IMOD software, and whose enthusiasm for the “underlying structures” had lasting effect. Also, I am grateful to my friends Neelime, Garry Morgan, Rubbiya Ali, and all Marsh Group members who helped me tremendously. I would also like to thank to Ministry of Education of Malaysia and Universiti Sains Malaysia for their financial support granted through doctorate fellowship. Thank you to Amanda Carrozi, who listened to my complaints and made my school life easier. I wish to thank my beloved husband, Mohd. Syukuri Jaafar and my sweet sisters, Siti Farhanis, Farah Amalina and Fatin Zafirah, and friends in Australia and Malaysia who continuously keep supporting me whenever I feel down.

Last but not least, I express my deepest appreciation to my mom and my dad, Fridah Saod and Ruhaiyem Yahaya who love and pray for me every day and without them I wouldn't be where I am today. Without their persistence, I would have lost my motivation. I love both of you, Ibu Abah.



## **Keywords**

electron microscope tomography, automatic segmentation, beta cell, insulin secretory pathway, image processing, semi-automated segmentation, image filtration, whole cell tomography

## **Australian and New Zealand Standard Research Classifications (ANZSRC)**

ANZSRC code: 060112, Structural Biology (incl. Macromolecular Modelling), 40%

ANZSRC code: 060114, Systems Biology, 20%

ANZSRC code: 080106, Image Processing, 20%

ANZSRC code: 080301, Bioinformatics Software, 20%

## **Fields of Research (FoR) Classification**

FoR code: 0601, Biochemistry and Cell Biology, 60%

FoR code: 0801, Artificial Intelligence and Image Processing, 20%

FoR code: 0803, Computer Software, 20%

# TABLE OF CONTENTS

---

Abstract .....	ii
Declaration by author.....	v
Publications during candidature.....	vi
Publications included in this thesis .....	vi
Contributions by others to the thesis.....	vii
Statement of parts of the thesis submitted to qualify for the award of another degree.....	vii
Acknowledgements.....	viii
Keywords .....	ix
Australian and New Zealand Standard Research Classifications (ANZSRC).....	ix
Fields of Research (FoR) Classification .....	ix
Table of Contents.....	x
List of Figures .....	xv
List of Tables .....	xix
Abbreviations.....	xx
<b>Chapter 1    General Introduction.....</b>	<b>1</b>
1.1    Background: Biological motivation for this study.....	3
1.1.1    Basic biology of the endocrine pancreas.....	3
1.1.1.1    Islets of Langerhans: home of the beta cell .....	3
1.1.1.2    Pancreatic beta cells and relation to diabetes mellitus.....	4
1.1.2    Insulin secretory pathway .....	6
1.1.2.1    The endoplasmic reticulum (ER).....	7
1.1.2.2    Intracellular insulin storage: mature granules.....	8
1.1.2.3    Transport mechanisms: the Golgi apparatus .....	8
1.1.2.4    Cellular power plants: Mitochondria.....	9
1.1.3    Limitations of conventional electron microscopy (EM) studies .....	10
1.2    Electron Tomography (ET) .....	11
1.2.1    Introduction to ET and data collection techniques.....	11
1.2.2    Resolution gap in 3D imaging of ET .....	12
1.2.3    Data collection: From specimen to tilt-series and tomograms.....	13
1.2.4    Cryo-EM of frozen-hydrated cells versus EM of fast-frozen/freeze-substituted cells embedded in plastic sections and the limitations in the EM .....	15
1.2.5    Image resolution and tilt-series alignment .....	17

1.2.6	Segmentation: manual, semi-automated and automated .....	17
1.3	Background Study: Computational methods of Image Processing for ET .....	19
1.3.1	Introduction.....	19
1.3.2	Image filter: Noise reduction algorithms .....	20
1.3.2.1	Classical noise reduction filters.....	21
1.3.2.2	Complex filters.....	22
1.3.2.3	Rank filters .....	22
1.3.2.4	Diffusion-based methods.....	25
1.3.2.5	Bilateral filtering .....	26
1.3.3	Segmentation .....	27
1.3.3.1	Watershed Transform.....	27
1.3.3.2	Energy-based techniques ('snakes' or 'active contours') .....	28
1.3.3.3	Hybrid techniques.....	30
1.3.4	Segmentation of organelles of interest: Studies for sub-cellular compartments categorisation .....	32
1.3.4.1	The Golgi Apparatus .....	33
1.3.4.2	Mitochondria .....	34
1.3.4.3	Secretory (Insulin) Granules.....	36
(a)	Mature Granules .....	36
(b)	Immature Granules .....	36
1.4	Thesis Hypothesis.....	37
1.5	Thesis objectives .....	38
1.6	Thesis structure.....	39
<b>Chapter 2</b>	<b>Materials and Methods.....</b>	<b>41</b>
2.1	Pancreatic islet/cell preparation.....	43
2.1.1	Mouse islet isolation culture .....	43
2.1.2	High-pressure freezing and freeze substitution.....	43
2.2	Cell section tomography.....	44
2.2.1	Microtomy and preparation for ET .....	44
2.2.2	Surveying the section to find candidate cells: whole islet montages at 4700× .....	44
2.2.3	Tilt series acquisition .....	45
2.2.4	Reconstruction and joining of sections into a whole cell tomogram.....	45
2.3	Sub-volume extraction and classification.....	45
2.4	Towards automated segmentation of cellular tomography.....	50
2.5	Quantitative 3D analysis and statistical analysis .....	52
<b>Chapter 3</b>	<b>Parameter Optimisation for Cellular Tomography Segmentation: A systematic and Reliable Procedure towards an Automatic Target-Scoring System.....</b>	<b>54</b>

3.1	Introduction .....	56
3.2	Materials and Methods .....	58
3.2.1	Subject Data and Cell Tomography Reconstruction .....	58
3.2.2	Organelle of Interest: Selection, Extraction and Manual Tracing.....	58
3.2.3	Development of the CTS pipeline for accurate segmentation.....	59
3.3	Designing a workflow for cellular tomography segmentation .....	61
3.3.1	Dataset preparation .....	61
3.3.1.1	Sub-volume extraction of three key organelles of insulin secretion; the Golgi apparatus (GA), mitochondria (MC) and insulin granules (IG) .....	61
3.3.1.2	Manual segmentation .....	61
3.3.2	Segmentation approaches.....	62
3.3.2.1	Processed image for accurate contour tracing .....	62
3.3.2.2	Boundary-based versus region-based segmentations .....	75
3.3.2.3	Contour line refinement: Mathematical morphologies algorithm .....	82
3.3.2.4	Meshing: Contour volume value and mesh surface area scoring .....	82
3.3.2.5	Proposed method flow for automated and accurate cellular compartment segmentation.....	85
3.3.3	Refining parameter settings of segmentation method flows .....	90
3.3.3.1	Quantitative and qualitative analyses .....	93
3.4	Conclusion.....	97

**Chapter 4 3-Dimensional Characteristics and Image Features to Dictate Parameter of Choice towards Automated Cellular Tomography Segmentation ..... 99**

4.1	Introduction .....	101
4.2	Results .....	102
4.2.1	Classification of organelles of interest sub-types.....	102
4.2.1.1	Insulin granules .....	103
4.2.1.2	Mitochondria .....	106
4.2.1.3	The Golgi apparatus .....	108
4.2.2	Parameter optimisation on each sub-class.....	111
4.2.2.1	Insulin granules .....	112
4.2.2.2	Mitochondria .....	117
4.2.2.3	The Golgi apparatus .....	122
4.2.3	Segmenting the rest of the sub-volumes of each organelle sub-class with respective optimised method settings 125	
4.2.3.1	Insulin granules .....	126
4.2.3.2	Mitochondria .....	126
4.2.3.3	The Golgi apparatus .....	126
4.2.4	Discussion.....	127
4.2.5	Future plan .....	128

4.2.5.1	Improving the Golgi apparatus scoring for improved segmentation results .....	128
<b>Chapter 5</b>	<b>Application of Edge-Detection Filter in Segmenting Complex Cellular Organelles at High Resolution</b>	<b>130</b>
5.1	Introduction .....	132
5.2	Results .....	135
5.2.1	Automated segmentation of organelles within a whole sub-cellular tomogram .....	135
5.2.2	Automated segmentation of organelles extracted as small sub-volumes using 3DBLE .....	139
5.2.2.1	The Golgi apparatus (GA) .....	142
5.2.2.2	Mitochondria .....	143
5.2.2.3	Insulin granules .....	144
5.2.3	Optimising settings of 3D BLE for segmentation of different cellular compartments.....	145
5.2.3.1	Insulin granules .....	146
5.2.3.2	Mitochondria .....	148
5.2.3.3	The Golgi apparatus .....	150
5.3	Discussion .....	153
<b>Chapter 6</b>	<b>General Discussion.....</b>	<b>156</b>
6.1	Overview .....	158
6.2	Segmentation challenges .....	159
6.2.1	Relationship between sub-cellular structures and the event of insulin secretion .....	159
6.2.2	The role of image classification in insulin release .....	160
6.3	More accurate modelling of cells .....	160
6.3.1	Faster and more accurate segmentation using a semi-automated method workflow .....	160
6.3.2	The importance of identifying and sub-classifying cellular compartments according to image properties	162
6.3.3	Improving model accuracy of 3D BLE by optimising the settings of sigma 2 and threshold values.....	162
6.4	Future directions.....	163
6.4.1	Towards automated annotation of cellular compartments using machine learning approaches.....	163
6.5	Conclusion.....	166
References.....		168

# LIST OF FIGURES

---

## Chapter 1-6:

Figure 1.1 Location and function of human beta cell in the islets of Langerhans .....	4
Figure 1.2 Process of insulin secretion. Rising blood glucose levels trigger insulin release by beta cells. ....	6
Figure 1.3 The insulin secretory pathway involves both regulated and constitutive release. ....	7
Figure 1.4 Mitochondrial compartments and subcompartments with descriptions of specific processes and proteins. ...	10
Figure 1.5 Generation of a 3D volume from a tilt-series. ....	11
Figure 1.6 Three popular data collection techniques used in 3D image reconstruction.....	12
Figure 1.7 Schematic diagram comparing the resolution of various imaging technologies and the objects that they can resolve. ....	13
Figure 1.8 Quality of back-projection as a function of tilt increment and range. ....	14
Figure 1.9 Dual-axis tomography improves reconstruction quality.....	15
Figure 1.10 Manual segmentation of 2D slice of tomograms and rendered models for 3D surface visualisation. ....	18
Figure 1.11 Comparison of different noise reduction algorithms applied to tomographic data.....	24
Figure 1.12 Schematic diagram illustrating the watershed transform. ....	28
Figure 1.13 Semi-automated image segmentation by the ‘Snakes’ or ‘active contours’ techniques. ....	29
Figure 1.14 Application of Watershed (A) versus Watersnake (B) segmentation to 2D image data. ....	30
Figure 1.15 Comparison of Watershed and Watersnake segmentation techniques applied to 2D medical imaging datasets. ....	31
Figure 1.16 Illustrative schematic images to highlight different levels of shape complexity for the Golgi apparatus with respect to segmentation. ....	34
Figure 1.17 Illustrated images to represent different levels of complexity of mitochondrial ultrastructure. ....	35
Figure 1.18 Cartoon images to represent different levels of complexity of granule ultrastructure. ....	37
Figure 2.1 The schematic diagram and the example of real images of the Golgi apparatus. ....	47
Figure 2.2 The schematic diagram and the example of real images of mitochondria. ....	48
Figure 2.3 The schematic diagram and the example of real images of insulin granules. ....	49
Figure 2.4 Flowchart showing the whole process of the research. ....	51
Figure 3.1 An example of selection and extraction process for multiple GA from the same tomogram. ....	60
Figure 3.2 Manual tracing of the Golgi apparatus from real electron tomogram.....	64
Figure 3.3 (Continue from Figure 3.2) 3D surface-rendered models of optimised pre-processed image volume for the Golgi apparatus. ....	65
Figure 3.4 (Continue from Figure 3.3) 3D surface-rendered models of optimised pre-processed image volume for the Golgi apparatus for Minimum, Maximum, 2D Median and 3D Median filter. ....	66
Figure 3.5 (Continue from Figure 3.4) 3D surface-rendered models of optimised pre-processed image volume for the Golgi apparatus. ....	67
Figure 3.6 Manual tracing of mitochondrion from real electron tomogram. ....	68
Figure 3.7 (Continue from Figure 3.6) 3D surface-rendered models of optimised pre-processed image volume for mitochondrion. ....	69

Figure 3.8 (Continue from Figure 3.7) 3D surface-rendered models of optimised pre-processed image volume for mitochondrion. ....	70
Figure 3.9 Manual tracing of insulin granule from real electron tomogram. ....	71
Figure 3.10 (Continue from Figure 3.9) 3D surface-rendered models of optimised pre-processed image volume for insulin granule. ....	72
Figure 3.11 (Continue from Figure 3.10) 3D surface-rendered models of optimised pre-processed image volume for the insulin granule. ....	73
Figure 3.12 The applications of <i>snakes</i> on the optimised filtered images (insulin granule). ....	77
Figure 3.13 The applications of <i>watershed</i> on the optimised filtered images (insulin granule). ....	78
Figure 3.14 Visual comparison between manual tracing (green contours) and automated segmentation (red contours) for the Golgi apparatus. ....	79
Figure 3.15 Difference image properties influenced segmented contour result. ....	81
Figure 3.16 Application of <i>opening</i> and <i>closing</i> (mathematical morphologies operations) in membrane disconnection. ....	83
Figure 3.17 Removing unwanted contours computationally from optimised segmentation result. ....	84
Figure 3.18 Pseudocode for the proposed pipeline of cellular compartments segmentation. ....	87
Figure 3.19 Workflow diagram of the proposed systematic approach for accurate segmentation. ....	88
Figure 3.20 Target scoring system. ‘100%’ is referred as a ‘target point’ of ground truth datasets. ....	89
Figure 3.21 Differences between segmentation results (i.e. ‘best’ settings of different method flows) for mitochondria. ....	90
Figure 3.22 Comparison of segmentation results between method 1 – method 9 with manual tracing. ....	92
Figure 3.23 Comparison between result retrieved from recommended settings and optimised settings of method 2 (M2). ....	93
Figure 3.24 Five ranges of mean density of filtered images identified. ....	94
Figure 3.25 Nine segmentation results representing nine different method flows (M1 – M9). ....	95
Figure 3.26 The best five results have a score of 5. ....	96
Figure 4.1 Schematic diagram showing the transition of insulin granule appearance (upper row) and respective examples of raw data (bottom row). ....	103
Figure 4.2 Image classes for insulin granules. ....	104
Figure 4.3 Identification of insulin granule locations within a subcellular environment. ....	105
Figure 4.4 Image classes for mitochondria. ....	107
Figure 4.5 Image classes for the Golgi apparatus. ....	109
Figure 4.6 Examples of three image classes of the GA. ....	110
Figure 4.7 Best methods with optimised settings for insulin granules. ....	114
Figure 4.8 (a) Comparison between manual tracing (red contours) and ‘best’ automated methods (cyan contours) on raw dataset (i.e. unfiltered). ....	115
Figure 4.9 (b) Comparison between manual tracing (red contours) and ‘best’ automated methods (cyan contours) on raw dataset (i.e. unfiltered). ....	116
Figure 4.10 Best methods with optimised settings for mitochondria. ....	118
Figure 4.11 (a) Optimised settings for different mitochondria classes. ....	119
Figure 4.12 (b) Optimised settings for different mitochondria classes. ....	120
Figure 4.13 (c) Optimised settings for different mitochondria classes. ....	121

Figure 4.14 Best methods identified for all 3 sub-classes of the Golgi apparatus. ....	123
Figure 4.15 (a) Optimised setting for different classes of the Golgi apparatus. ....	124
Figure 4.16 (b) Optimised setting for different classes of the Golgi apparatus. ....	125
Figure 5.1 Segmentation and extraction of molecular contours from electron tomography. ....	133
Figure 5.2 Segmentation of cellular tomographic reconstruction ( <i>previous page</i> ). ....	134
Figure 5.3 Cellular tomogram used for this study, showing an area of complex cellular environment. ....	136
Figure 5.4 Result of applying the 3DBLE (default settings) to the sub-tomogram extracted from Figure 5.3. ....	137
Figure 5.5 A representation of contours after <i>imodauto</i> function presenting white contours in Figure 5.4. ....	138
Figure 5.6 Surface-rendered 3D model of sub-region demarcated in red box in Figure 5.5. ....	139
Figure 5.7 3D BLE segmentation on the Golgi apparatus. ....	142
Figure 5.8 3D BLE segmentation on mitochondria. ....	143
Figure 5.9 3D BLE segmentation on insulin granule. ....	144
Figure 5.10 Optimised settings of 3D BLE for insulin granules. ....	147
Figure 5.11 Comparison between meshed model of 3D BLE (green) and manual tracing (red). ....	149
Figure 5.12 (a) Optimised settings of 3D BLE for the Golgi apparatus and visual comparison of image section and the GA 3D models between two methods; Method 8 (left) and 3D BLE (right). ....	150
Figure 5.13 (b) Optimised settings of 3D BLE for the Golgi apparatus and visual comparison of image section and the GA 3D models between two methods; Method 8 (left) and 3D BLE (right). ....	151
Figure 6.1 Concept of contour space (A) and three examples of different contours (B). ....	165
Figure 6.2 Three contour selection spaces to generate MAXMAJOR and MINMINOR from the (black) contour shown in all three panels. ....	165



# LIST OF TABLES

---

## Chapter 1-6:

Table 3.1 Summary of sub-volume datasets comprised of the Golgi apparatus, mitochondria and insulin granules. ....	61
Table 3.2 Summary of processing time for conventional tracing of each of key organelle. ....	62
Table 3.3 Nine pre-filtering approaches and their respective initial settings (i.e. proposed by the software/method developer).....	63
Table 3.4 Comparison of processing time between manual tracing and processed images (followed by automated surface rendering) and comparison of surface area value between manual tracing and proposed approaches for each organelle sub-volume.....	74
Table 3.5 Processing time of two combination approaches between optimised image filtration methods followed by <i>snakes</i> (S) and image filtration methods followed by <i>watershed</i> (W).....	76
Table 4.1 Three sub-classes were assigned to each of key organelle; insulin granules, mitochondria and the Golgi apparatus. ....	111
Table 4.2 Analysis for the top 3 methods for insulin granule segmentation. ....	113
Table 4.3 Percentage of acceptable results (i.e. score 5) using the best method flow; i.e. Method 8 (M8) of each key organelle sub-class. ....	126
Table 5.1 Scores for individual filtering of boxed out organelles of interest GA (Golgi apparatus), MC (mitochondria) and IG (insulin granules).....	141
Table 5.2 Processing time of three different segmentation methods; manual, CTS and 3D BLE. ....	153

# ABBREVIATIONS

---

<b>Abb</b>	<b>Description</b>
2D	two-dimensions / two-dimensional
3D	three-dimensions / three-dimensional
Å	Ångström ( $10^{-10}$ m)
ATP	adenosine triphosphate
°C	degrees Celsius
CAT	computed axial tomography
CCD	charge-coupled device
CT	computed tomography
DNA	deoxyribonucleic acid
EM	electron microscope / microscopy
ER	endoplasmic reticulum
ET	electron tomography
FBS	fetal bovine serum
GB	gigabyte ( $1024^3$ bytes)
GPU	graphics processing unit
GUI	graphical user interface
h	hour / hours
keV	kilo electron Volt
LM	light microscope / microscopy
MB	megabytes
min	minute / minutes
MRI	magnetic resonance imaging
mRNA	messenger ribonucleic acid
MSA	meshed surface area
nm	nanometre(s)
PET	positron emission tomography
ROI	region of interest
S	second / seconds
SA	surface area
SNR	signal-to-noise ratio
TEM	transmission electron microscope / microscopy

---

---

TGN	<i>trans</i> -Golgi network
μg	microgram
μm	micrometre ( $1 \times 10^{-6}$ m)
XY	2D plane containing the X and Y axis
XZ	2D plane containing the X and Z axis

---



# **Chapter 1    GENERAL INTRODUCTION**

---



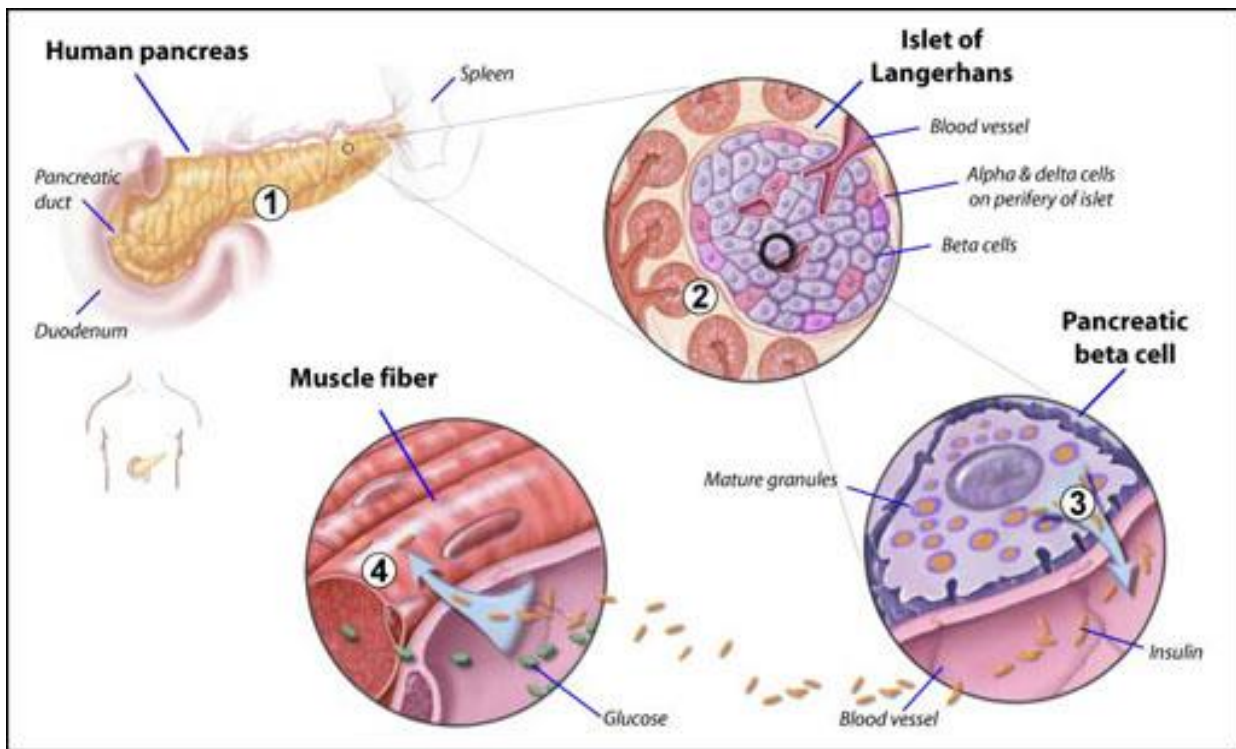
## **1.1 Background: Biological motivation for this study**

### **1.1.1 Basic biology of the endocrine pancreas**

#### ***1.1.1.1 Islets of Langerhans: home of the beta cell***

The islets of Langerhans are regions of specialised tissue within the pancreas – an organ located in the abdomen behind the stomach – that is important in converting the food we eat into fuel for the body's cells. Whereas the bulk of the pancreas is comprised of exocrine cells which are responsible for the production and release of digestive enzymes into the gut, these pancreatic islets consist of a mixture of several different types of endocrine cells (**Figure 1.1**) which play important roles in regulating the body's metabolism through the production of several key hormones for release directly into the bloodstream. The islets of Langerhans consist mostly (~80%) of insulin-secreting beta cells which form the core of the tissue. They are surrounded by a mantle comprised of the other major islet endocrine cell types such as the glucagon-releasing alpha cells, somatostatin-producing delta cells, and pancreatic polypeptide-secreting PP cells (Orci and Unger, 1975, Gepts and Lecompte, 1981). A new population of specialised islet (epsilon) cells that produce the peptide ghrelin was recently identified (Prado et al., 2004). The islets therefore form a complex paracrine feedback system for maintaining systemic blood glucose homeostasis.

The islets of Langerhans were originally discovered in 1869 by German pathological anatomist Paul Langerhans. Collectively, they account for 1-2% of the mass of the pancreas. The proportion of different cell types in each islet depends on the species, stage of development and also the location of each islet within the organ (Baetens et al., 1979, Elayat et al., 1995). A healthy adult human pancreas contains about one million islets, with the average islet containing approximately 2,500 cells, although this can vary anywhere between 10 and 10,000 cells (Weir & Bonner-Weir 1990). An average mammalian islet is 0.1-0.2 mm in diameter with the mean diameter of individual component cells measuring ~10-12  $\mu\text{m}$  (Jo et al. 2007).



**Figure 1.1 Location and function of human beta cell in the islets of Langerhans**

(1) The pancreas is located below the stomach and in humans is connected to the duodenum via a small pancreatic duct which releases digestive enzymes. (2) Islets are comprised predominantly of beta cells with a small number of alpha and delta cells making up the outer layer. (3) Insulin secretion into the blood stream by beta cells is stimulated in response to elevated blood glucose. (4) Insulin released into the circulation triggers glucose uptake by muscle and fat cells. (Winslow, 2001) Figure 7.1.

### 1.1.1.2 Pancreatic beta cells and relation to diabetes mellitus

The beta cells produce, store and secrete insulin, a physiological hypoglycaemic hormone that regulates the blood glucose levels, as well as C-peptide, which is a by-product of insulin processing within the beta cell that helps prevent neuropathy and other symptoms of diabetes related to vascular deterioration (Rorsman et al., 2000). Insulin release from beta cells *in vivo* is normally a biphasic process, as illustrated in (Figure 1.2). The initial quantity of insulin secreted upon glucose stimulation depends on the amount of stored insulin available for immediate release. Once the stores of readily releasable insulin are depleted, a second phase of insulin release is initiated (Rorsman and Renstrom, 2003). This second release process is prolonged since insulin that has already been synthesised, processed and packaged into secretory granules stored deeper within the cytoplasm, must be transported to the cell surface. The vesicles undergo subsequent fusion and as a result secrete insulin into the blood stream, under conditions of high blood glucose levels. Furthermore, beta cells also have to regenerate the stores of insulin depleted during both phases of release. Although insulin release into the bloodstream occurs primarily in response to high levels of extracellular glucose, there are several important paracrine and autocrine interactions among islet endocrine cells which also act to regulate insulin secretion (Aspinwall, 1999). Whereas insulin acts

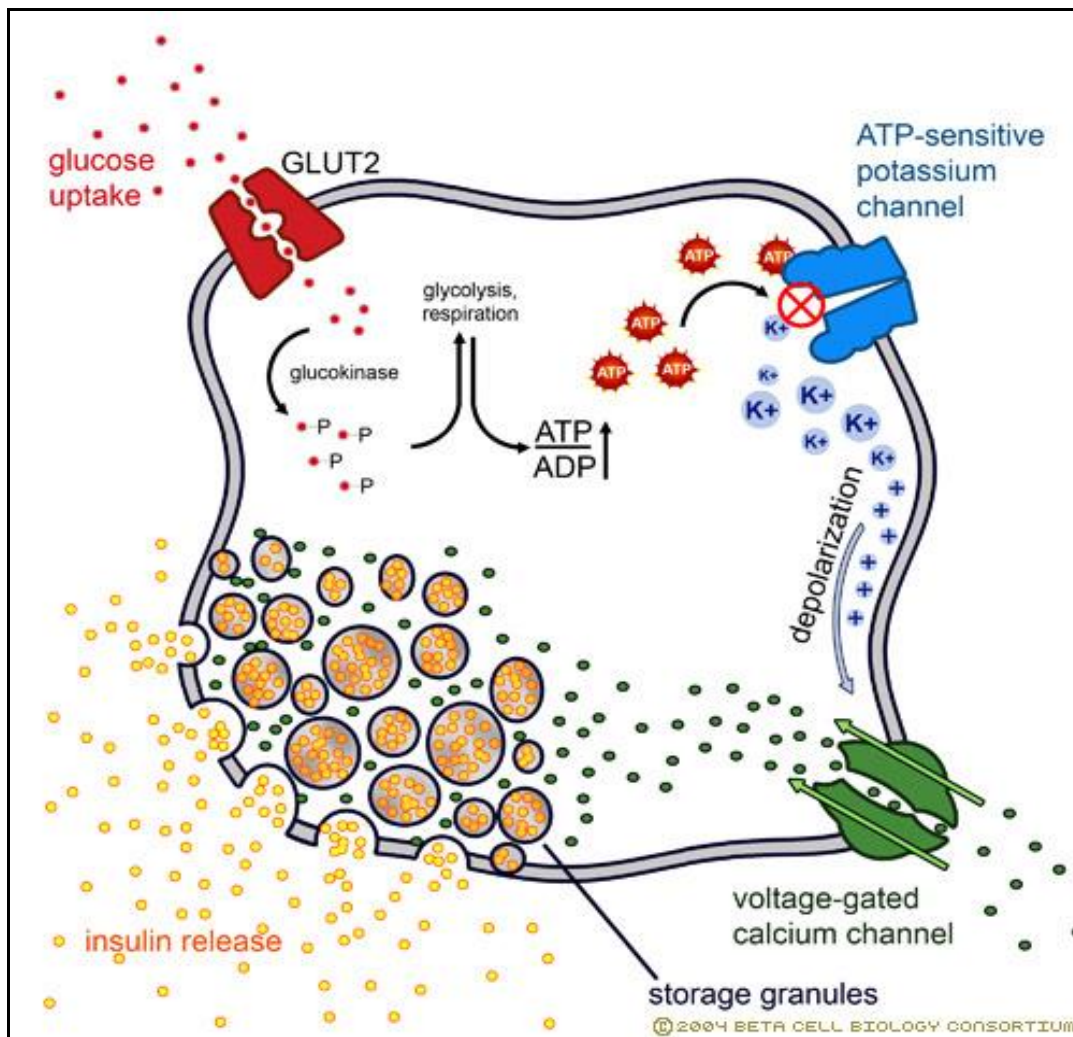


## CHAPTER 1-GENERAL INTRODUCTION

to lower blood sugar, another hormone (glucagon) produced by alpha cells within pancreatic islets, acts to raise blood sugar. By working in concert in this way, islet cells are able to maintain proper blood sugar levels, which are crucial to maintain normal function and health of key organs including the brain, liver, and kidneys. Consequently, dysfunction or death of beta cells affects insulin production and release, eventually manifesting as the chronic disease diabetes mellitus, commonly known as diabetes.

Diabetes mellitus comprises a number of disease states that ultimately lead to a reduction in the production and/or secretion of the hormone, insulin. Broadly, diabetes is a metabolic disease that is characterised by abnormally high levels of glucose in the blood. Normally the pancreas releases insulin to help the body store and use sugar and fat from food. Diabetes can occur when one or more of the following three situations occurs: (1) the pancreas does not produce any insulin, (2) the pancreas produces very little insulin, or (3) the body does not respond appropriately to insulin, a condition called 'insulin resistance'(Alberti and Zimmet, 1998).

Diabetes is typically classified as one of two main forms of the disease: type 1 or type 2. Type 1 diabetes, also called juvenile diabetes or insulin-dependent diabetes mellitus (IDDM), is a chronic autoimmune disease that destroys beta cells and is lethal unless treated with exogenous insulin. Type 2 diabetes, formerly known as adult-onset diabetes or non-insulin dependent diabetes (NIDDM) is marked by high-levels of blood sugar due to beta cell dysfunction (insulin resistance) (Alberti and Zimmet, 1998).

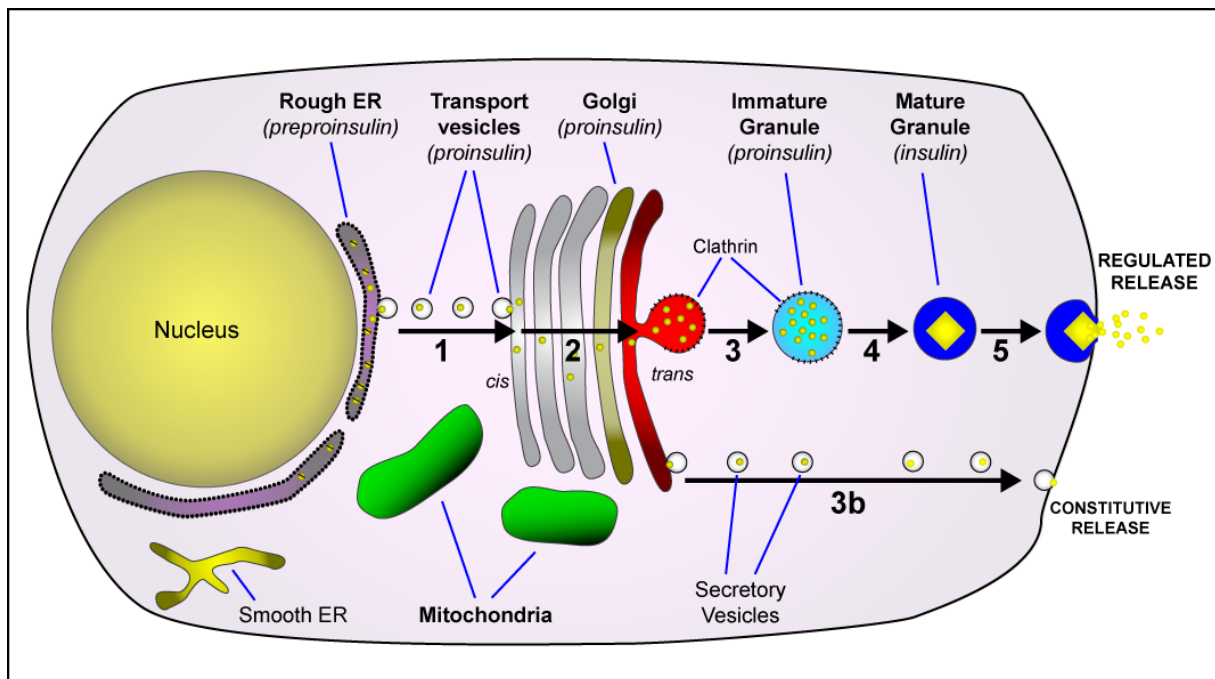


**Figure 1.2 Process of insulin secretion. Rising blood glucose levels trigger insulin release by beta cells.**

Specifically, glucose uptake by the GLUT2 glucose transporter protein raises the intracellular glucose concentration, glycolysis and respiration and thereby increases the intracellular ATP:ADP ratio. The rise in intracellular ATP in turn inactivates the ATP-sensitive potassium channel which results in depolarization of the plasma membrane. This depolarization in turn activates the calcium channel which allows calcium ions to flow into the cell. This rise in intracellular calcium triggers the exocytotic release of insulin from the storage granule pools within the beta cell's cytoplasm. (Cartailler, 2004) Figure 2.

### 1.1.2 Insulin secretory pathway

The insulin secretory pathway comprises a series of steps that involves a number of functionally distinct membrane-bound organelles which include the Golgi apparatus, mitochondria, insulin granules, lysosomes, the endoplasmic reticulum (ER) and vesicles. In general, there are two different patterns of secretion. One pattern is referred to as regulated secretion (**Figure 1.3 arrow 1-5**), as proteins are continuously secreted from the cell regardless of environmental factors. No external signals are required to initiate this process. The second pattern is referred to as constitutive secretion (**Figure 1.3 arrow 3b**) for which an external signal is required before secretion occurs.



**Figure 1.3** The insulin secretory pathway involves both regulated and constitutive release.

Cartoon image showing the organelles involved in insulin production and secretion: the rough endoplasmic reticulum (ER), transport vesicles, Golgi apparatus, immature granules, mature granules and mitochondria. (Noske, 2010) Figure 1.3.

### 1.1.2.1 The endoplasmic reticulum (ER)

All insulin secretion begins in the rough ER, where it is converted from its initial precursor form (pre-proinsulin) and packaged into small transport vesicles. These are transported from the ER to the cis-most Golgi cisternae, from where proinsulin gradually progresses to the trans-most cisternae of the Golgi stack. During packaging into vesicles, the precursor peptide is cleaved off to generate proinsulin. Within the trans-most Golgi cisternae, regions of membrane enclosing proinsulin bud off to form immature granules. Eventually, as the proinsulin undergoes further processing within the acidified granule interior to yield the mature form of insulin and C-peptide, the concentrated insulin typically begins to crystallize, at which point the granule is called a mature granule. In the final stage of release, the mature granules fuse with the plasma membrane and release the insulin from the cell following stimulation by glucose or other ‘secretagogues’ (i.e. substance like hormone that causes or stimulates another substance to be secreted) in the blood stream. A small amount (<1%) of proinsulin is constitutively released to the cell surface via small secretory vesicles which also bud directly from the Golgi apparatus but take an alternative route to the plasma membrane (**Figure 1.3 arrow 3b**).

**1.1.2.2 Intracellular insulin storage: mature granules**

Mature granules represent the beta cells' which act as storage sites for the vast reserves of insulin produced. A typical unstimulated mouse beta cell contains approximately 10,000 mature granules (Olofsson et al., 2004); each measures approximately 200-300 nm in diameter (Hutton, 1989) and contains 150,000-280,000 insulin molecules (Howell, 1974). Mature granules represent different pools; a non-releasable 'reserve pool', a 'readily releasable pool' (RRP) and an 'immediately releasable pool'.

**1.1.2.3 Transport mechanisms: the Golgi apparatus**

The Golgi apparatus - first described over a century ago (Golgi, 1898) - is a key organelle found in all eukaryotic cells. Its primary function is to further modify macromolecules (e.g. lipids, proteins) by special enzymes possessed by the Golgi stacks after their export from the ER. This process is particularly important in the maturation of many proteins, for example prior to secretion. In normal mammalian cells, the Golgi structure consists of a number of discrete stacks of fenestrated, flattened membranous compartments called cisternae, which are laterally inter-connected to form a ribbon-like structure (Marsh et al., 2001a, Marsh and Howell, 2002, Noske et al., 2008). The Golgi typically consists of five to seven individual cisternae, including the trans-most cisternae (Griffiths et al., 1989), and are somewhat analogous to a stack of pancakes; this morphology contributes to a high surface-to-volume ratio.

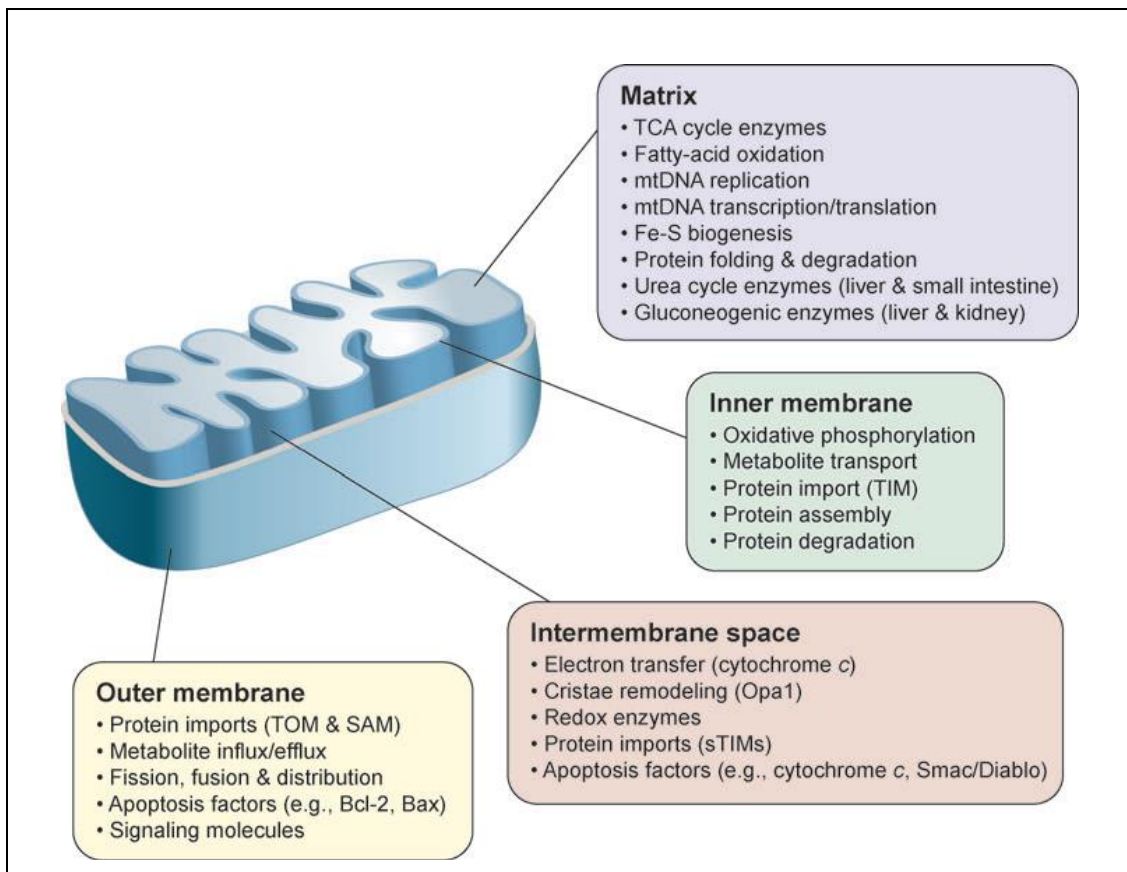
The Golgi apparatus plays a principal role in sorting, modifying, packaging and trafficking various proteins. It can be divided into three different spatial and functional regions, termed the cis-, medial-, and trans-cisternae, each distinguished by different marker enzymes. These regions selectively modify the different types of proteins as they progress along the cis-trans axis. From the ER, membrane transport vesicles and tubules carrying newly synthesized proteins fuse with cis-Golgi cisternae. Their protein cargo then progressively transits across the stack to the trans-Golgi cisternae, where proteins are then sorted and packaged for shipment to the required destination either within the cell (e.g. lysosome) or for release to the extracellular space. In some cases, tubular connections between non-adjacent (and more rarely, adjacent) cisternae have been observed and this in conjunction with functional stratification of the different regions of the stack. For membrane transport and luminal cargo, there are three main theories: 1) 'cisternal progression', 2) 'vesicular transport' and 3) 'tubule-mediated trafficking' (Farquhar and Palade, 1998, Marsh et al., 2004, Pelham, 1998). Tomographic studies have successfully provided evidence for all three mechanisms

and have also demonstrated that all of them can act in concert in the same region of the Golgi (Marsh, 2005). To fuel this activity, the Golgi requires energy that comes in the form of adenosine triphosphate (ATP) produced by mitochondria.

### **1.1.2.4 Cellular power plants: Mitochondria**

Mitochondria are membrane-enclosed organelles found in most eukaryotic cells. Collectively they mediate cellular ATP production, resulting in their description as ‘cellular power plants’. Several fundamental changes to the way scientists think about mitochondrial structure and function have been reported in the past decade (Kargul and Laurent, 2009, Ryan and Hoogenraad, 2007). Mitochondria comprise multiple subregions that carry out specialised functions. They are bounded by an outer membrane layer, which is separated by a small inter-membrane space from the inner membrane layer that is organised into cristae and the matrix (the space within the cristae) (**Figure 1.4**). As the generators of the cell that supply the chemical energy (ATP) necessary to carry out basic cellular activities, mitochondria tend to have a heavy/dark density when viewed by electron microscopy (EM). Morphologically, mitochondria can be quite complex, as they often branch and form irregular shapes presumably due to fission or fusion events determined by the energy state/needs (Hales, 2010) of the cell prior to fixation ahead of ultrastructural analysis.

Fusion and fission events appear to regulate mitochondrial shape and morphology to a remarkable degree. Non-branched mitochondria display a relatively consistent shape when viewed by EM from one section to the next (usually tubular or pancake-like) and exist as ‘singular’ spatially discrete objects in the cytoplasm (meaning that their outer membrane does not contact any other mitochondrion or other organelles/compartments). The mitochondria can also be branched in some regions. It should be noted that it remains a subject of debate as to whether these branched mitochondria should be considered one mitochondrion, two mitochondria in the process of fusion (or fission), or three separate mitochondria (Chen and Chan, 2005, Frazier et al., 2006, Karbowski and Youle, 2003, Okamoto and Shaw, 2005, Perkins and Frey, 2000).



**Figure 1.4 Mitochondrial compartments and subcompartments with descriptions of specific processes and proteins.**

Abbreviations: Bcl-2-associated X protein; Bcl-2, B-cell lymphoma protein 2; Opa1, Optic atrophy 1; SAM, sorting and assembly machinery; sTIMs, small TIM proteins; TIM, translocase of the mitochondrial inner membrane; TOM, translocase of the mitochondrial outer membrane. Adapted from (Ryan and Hoogenraad, 2007).

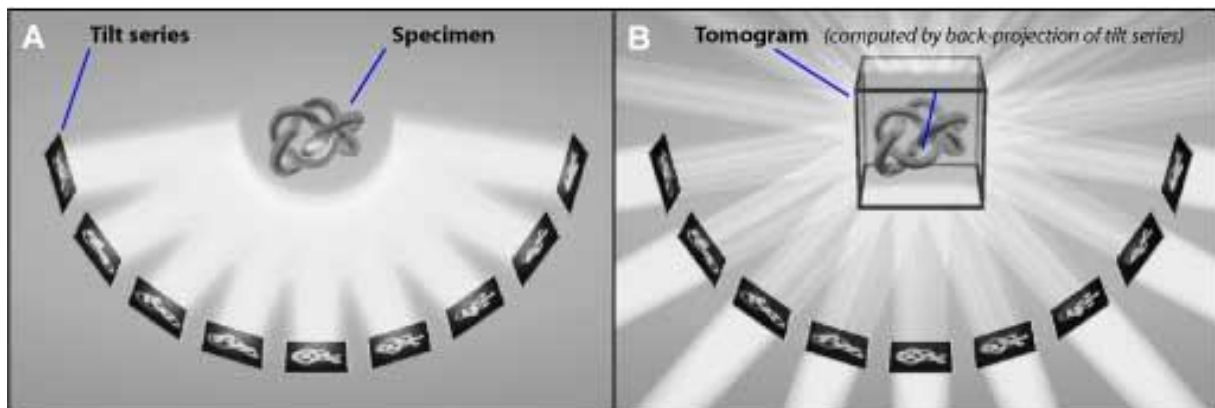
### 1.1.3 Limitations of conventional electron microscopy (EM) studies

In conventional EM, thin (40-100 nm) sections are cut and imaged in two dimensions (2D) (Ladinsky et al., 2002, Marsh, 2005). The benefit of this technique is improved when combined with EM stereological techniques (Russ and DeHoff, 2000). This combination of techniques (spatial sampling based on small numbers of 2D images) has underpinned numerous morphometric studies to quantify changes in Golgi structure (Derganc et al., 2006, Griffiths et al., 1989). However, neither of these methods offers reliable insights into the three dimensional (3D) detail or connectivity between Golgi cisternae (Marsh et al., 2001a). Thin sections from multiple cells and/or multiple regions from a single cell are unable to reveal the complete 3D organisation of the Golgi and other structures involved in the secretory pathway (Ladinsky et al., 1999). Thus, this PhD project centred on developing improved methods for analysing and characterising variations in organelle morphology based upon the semi-automated image processing and segmentation of subregions extracted from high resolution 3D image volumes previously generated by the Marsh laboratory using the technique of electron tomography (ET).

## 1.2 Electron Tomography (ET)

### 1.2.1 Introduction to ET and data collection techniques

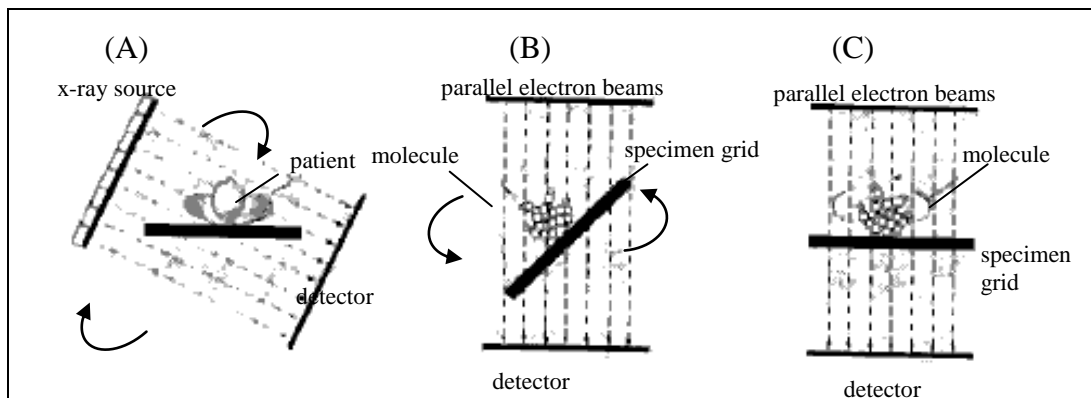
Computed axial tomography (CAT) – also referred to as computed tomography (CT) - is a widely used technique for visualising the internal structure of an object in 3D. It is based on the reconstruction of an image volume from a series of 2D projections taken over a range of angles. CAT/CT 'scans' in medical/clinical imaging are perhaps the best known examples of tomography. In these techniques an x-ray beam and detector are rotated 360° around the patient to collect a series of projection images taken at incremental angles. These are then automatically computed to yield a 3D image volume (**Figure 1.5**) displaying the patient's internal organs at different densities (often assisted by an image contrast enhancing agent).



**Figure 1.5** Generation of a 3D volume from a tilt-series.

(A) A specimen or detector is rotated incrementally around one axis to produce a series of 2D density maps to yield a tilt-series. (B) The final 3D density map (the tomogram) is created by back-projecting (*in silico*) the 2D images. This figure was modified from Fig 1 (Baumeister et al., 1999).

The tomographic reconstruction process involves acquiring and then aligning a tilt-series. Specifically, a set of 2D images are collected over a large angular range at regular, small angular increments around a single axis of rotation relative to the object. After alignment, these 2D images are then back-projected in Fourier space using Radon transform (Radon, 1917) to compute a 3D density distribution, called a tomogram. **Figure 1.6** shows that CAT/CT, TEM for ET (B) and single particle analysis (SPA) (C) use similar arrangement of the source detector to compute 3D reconstructions. The specimen of SPA is not normally tilted where different views are obtained from the random orientation of 'identical' particles dispersed on a specimen grid.



**Figure 1.6 Three popular data collection techniques used in 3D image reconstruction.**

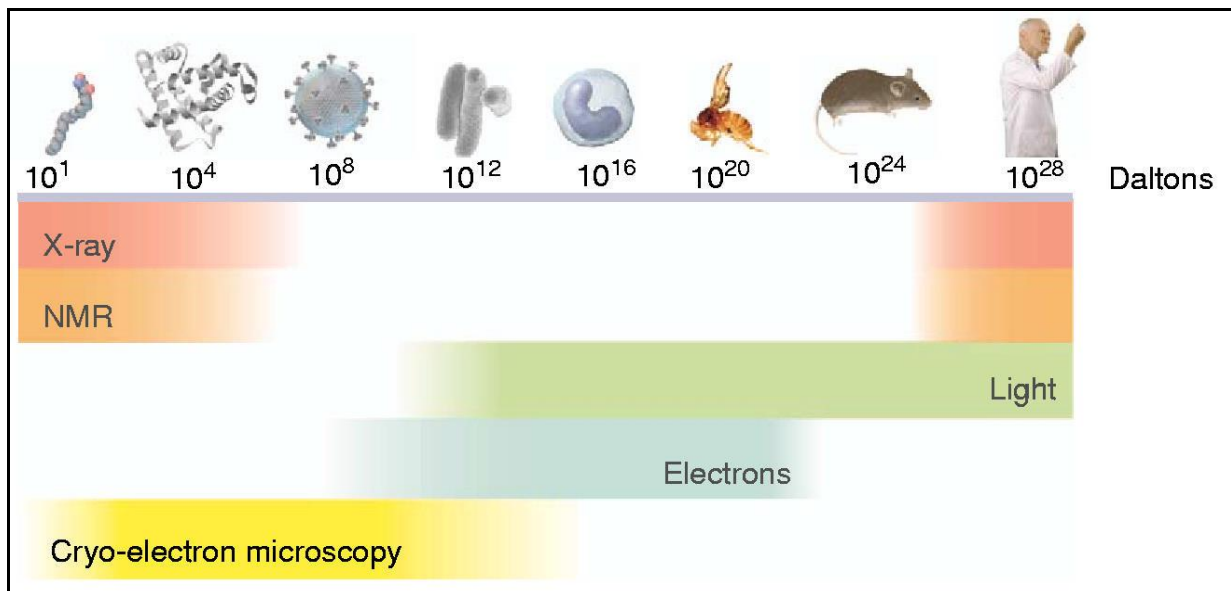
(A) CAT scans rely on the patient being stationary and a rigid source-detector being tilted by equal increments around the patient; (B) equivalent single-axis tilt geometry in the TEM for ET, where the source-detector arrangement remains stationary while the specimen is tilted by angular increments; (C) as in (B), but instead of tilting the random orientation of large numbers of identical particles (i.e. macromolecules) derived from each 2D projection image provides the information used to compute the 3D structure of the original specimen. Adapted from (Frank, 1992).

### 1.2.2 Resolution gap in 3D imaging of ET

Electron microscopy (EM) tomography is a general method for tomographic 3D reconstruction of a microscopic object imaged with a specialised transmission electron microscope (TEM). The term ‘cellular tomography’ is used when this method is applied to cells. ET has become a powerful tool not only for the 3D visualisation of internal cell structure, organelles and macromolecular complexes but also fills a critical gap in the 3D imaging spectrum between light microscopy (LM) and SPA techniques (**Figure 1.7**). SPA is a technique used to image and model the 3D structure of macromolecules. Generally, SPA is well suited to studying the structure of macromolecules which are too large to permit structural analysis by nuclear magnetic resonance (NMR) or for which no crystals are available for electron or X-ray crystallography. However, aside from some overlap in image processing techniques, the methods used for SPA are not relevant to this project and will not be discussed further.

ET has proven capable of providing valuable structure-function information. Although a high relative cost is needed for maintaining ET instrumentation, advances in data acquisition, software for reconstruction and analysis, have helped ET to become the prime method for understanding relationships between organelles in the case of mammalian cells (Perkins et al., 1997) as well as whole cells in the case of simple eukaryotes and prokaryotes (Baumeister, 2005).





**Figure 1.7** Schematic diagram comparing the resolution of various imaging technologies and the objects that they can resolve.

Top row, left to right: lipids, proteins, whole virus, organelles, whole cells and various size organisms. This image was reproduced from Fig 1 in (Subramaniam, 2005).

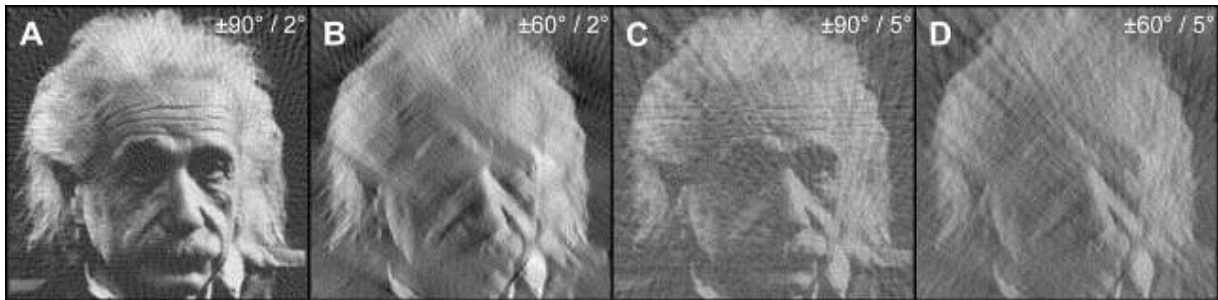
In practice, the main limitation of ET is the specimen size – limited by the field of view of the microscope as well as the specimen thickness that the electron beam is able to penetrate (typically up to 300 nm, beyond which point there is a rapid falloff in signal-to-noise ratio). The resolution achieved by ET is limited by thickness, as well as radiation damage and signal-to-noise dependency, however, it is generally agreed that ~4 nm resolution is routinely achievable from the majority of specimens (Grünewald et al., 2003, McEwen and Marko, 2001, O'Toole et al., 1999, Baumeister et al., 1999, Baumeister, 2002). A monograph on ET is also available (Frank, 1992).

### 1.2.3 Data collection: From specimen to tilt-series and tomograms

Data collection for ET involves a few basic steps including 1) placing a small biological specimen on a thin (~80 nm) layer of transparent plastic support film in a small (~3mm diameter) disc-like 'grid', 2) loading the grids into an electron microscope and tilt-rotating a specimen holder, which allows maximum tilt range of  $\pm 60-70^\circ$ , 3) completing data collection, 4) rotating the specimen around the Z axis to facilitate data acquisition around a second axis orthogonal to the first (dual-axis tomography).

The tilt/angular range and the tilt increment are reported to be important factors affecting the final quality of the tomographic reconstruction. Because the biological specimen is tilted in the column of the microscope while the electron beam remains stationary (due to practical hardware

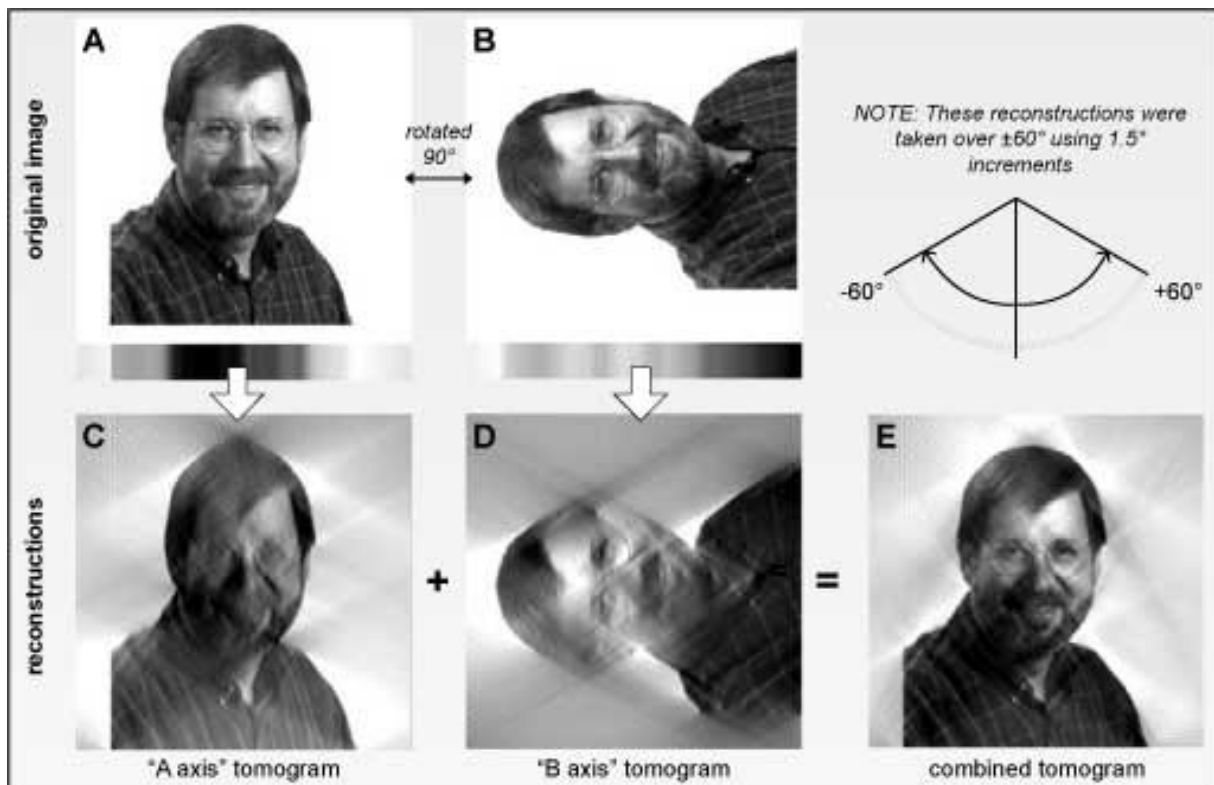
considerations), tomograms in ET suffer from a restricted angular range of  $\pm 60\text{-}70^\circ$  which results in an effect known as the ‘missing wedge’, whereby anisotropic distortion exists in the tomogram in the direction of the beam, as illustrated in **Figure 1.8**.



**Figure 1.8 Quality of back-projection as a function of tilt increment and range.**

Four 2D images demonstrate the effect of a tilt range and increment size on tomogram quality. These images were reprojected from the same image using a series of 1D slice. (A)  $\pm 90^\circ$  range with  $2^\circ$  increments, (B)  $\pm 60^\circ$  range with  $2^\circ$  increments, (C)  $\pm 90^\circ$  range with  $5^\circ$  increments and (D)  $\pm 60^\circ$  range with  $5^\circ$  increments. Reproduced from Fig 1 in (Baumeister et al., 1999).

Because the total angular range is limited due to the hardware configuration of standard TEMs (e.g. to  $\pm 70^\circ$  from horizontal), the data set is corrupted by anisotropic distortion. Typically, this is minimised by collecting a second series of projections after the EM grid supporting the specimen has been rotated  $90^\circ$  around the Z-axis (Mastronarde, 1997) and this is commonly called dual-axis tomography (**Figure 1.9**). This technique substantially improves image quality and reduces the missing wedge to a ‘missing pyramid’, and the result is improved symmetry and isotropy in all three dimensions (Mastronarde, 1997).



**Figure 1.9 Dual-axis tomography improves reconstruction quality.**

(A) From a 2D specimen, a series of simulated 1D projections are calculated to form a reconstruction (C). (B) The same specimen is rotated  $90^\circ$  to produce a second series of reconstructions (D). (E) A combined tomogram with fewer artefacts is formed by averaging (C) and (D) effectively. The tilt range for both axes in this simulation was  $\pm 60^\circ$  using  $1.5^\circ$  increments. Modified from Fig 1 (Marsh, 2005).

#### 1.2.4 Cryo-EM of frozen-hydrated cells versus EM of fast-frozen/freeze-substituted cells embedded in plastic sections and the limitations in the EM

EM imaging of frozen hydrated specimen sample slices, directly cut from vitrified cells/tissues, just prior to imaging, uses a low electron dose to minimise the damage to the specimen. The definition here pertains to cryo-EM of cellular sections for the purpose of cellular ET. The combination of cryo-preservation and low dose imaging improves the resolved cellular ultrastructure in a near-native-state. However this technique is used routinely for smaller specimens, e.g. viruses and these specimens are small enough to be captured in their entirety. Therefore sectioning is not required. Low signal-to-noise ratio (SNR) images, as a result from low dose rates are required to prevent excessive radiation damage, making it difficult to see cell substructures. As a consequence, this results in significant technical challenges both at the level of sample handling and image processing (Al-Amoudi et al., 2004).

To improve SNR and sample robustness as well as allowing images to be captured in normal condition, rapidly-frozen cells or tissue can be further processed. Such processing steps include:

- 1) The fixation of frozen specimens with chemical cross-linking agents.

- 2) Fixation with heavy metals and the substitution of water molecules with, for example, uranyl acetate at low temperatures (typically  $-90^{\circ}\text{C}$ ) by the process of 'freeze-substitution'. Not only does this fast-frozen substituted cell deliver samples with high membrane and filament contrast similar to that obtained by conventional EM preparative methods, but also provides the rapid cryo-immobilisation of all processes in the cell. Freeze substitution therefore improves the SNR and offers an acceptable trade off between improved contrast and ultrastructural preservation (McDonald and Morphew, 1993) and is therefore used in the work described in this thesis.

After freeze substitution, cells or islets are embedded in monomeric liquid resin, such as Epon (Craig et al., 1962) to produce a polymeric solid. As a result, about 400 nm thick cell sections can be successfully cut and imaged by using modern intermediate voltage EMs operating at around 300 kV. The consequence of electron absorption by the section results in thicker sections having a vastly decreased transparency to the electron beam. The effect is exacerbated at high tilt, as the electron path through the section doubles when the section is tilted  $\pm 60^{\circ}$  and triples  $\pm 70^{\circ}$  (McEwen and Marko, 2001).

'Specimen collapse' and 'specimen thinning' are two significant limitations resulting in two problems, a compression of specimen thickness by 25% in the Z axis (Kremer et al., 1990, Luther, 2005) and additional loss of specimen thickness by up to 4% respectively. In the case of 'specimen collapse', this occurs within the first few seconds of exposure while 'specimen thinning' occurs over the time course of collecting a tilt-series.

Specimen collapse has been estimated at 40% in the Z axis for Epon-embedded samples imaged at 300-1000keV. Computationally, this can be dealt with by stretching the image (the computed tomogram/3D volume) by 1.7x (Luther, 1992, Luther et al., 1988, McIntosh et al., 2005). Various strategies have been used to deal with 'specimen thinning' during data collection, where 1) the specimen is 'pre-irradiated' at low magnification and dose so that the changes across the entire specimen for tomography are more uniform, 2) the specimen exposure is minimised (as much as possible). Ultimately it is most important that the distance between objects and surfaces in Z reflect their correct spatial relationship. To compensate for collapse of the specimen, the final 3D tomogram is rescaled in Z after imaging in the electron microscope, and thus to obtain accurate spatial information from cellular tomograms, additional techniques for measuring and accounting for section distortion are needed, (Marsh and Howell, 2002).

### 1.2.5 Image resolution and tilt-series alignment

Currently, the best image resolution that can be achieved using EM of resin-embedded sections is approximately 5 nm, using the latest charge-coupled device (CCD) camera technology at 23,000× magnification (with a pixel of ~ 1.4 nm). This is thus referred to as ‘high resolution’ tomography (Marsh and Howell, 2002).

A key step in ET is the alignment of the tilt-series. Two methods can be used to define the alignment: marker or fiducial alignment and cross-correlation function or marker-free alignment (Brandt et al., 2001; Liu et al., 1995; Owen and Landis, 1996; Taylor et al., 1997). The vast majority of tomographic data alignment is performed using marker alignment (Penczek et al., 1995). Colloidal gold particles of a nominal diameter (e.g. 10 nm) are typically used. A basic alignment procedure consists of three main steps, 1) gold particles are non-specifically deposited on both surfaces of each section, 2) within the tilt-series images, manually select a subset of these gold ‘fiducials’ using *in silico* methods 3) semi-automatic methods are then used to track the path of the fiducials over each image through the tilt-series. Tracking is particularly beneficial to help with computing non-uniform deformation, as it allows more accurate alignment of tilt-series.

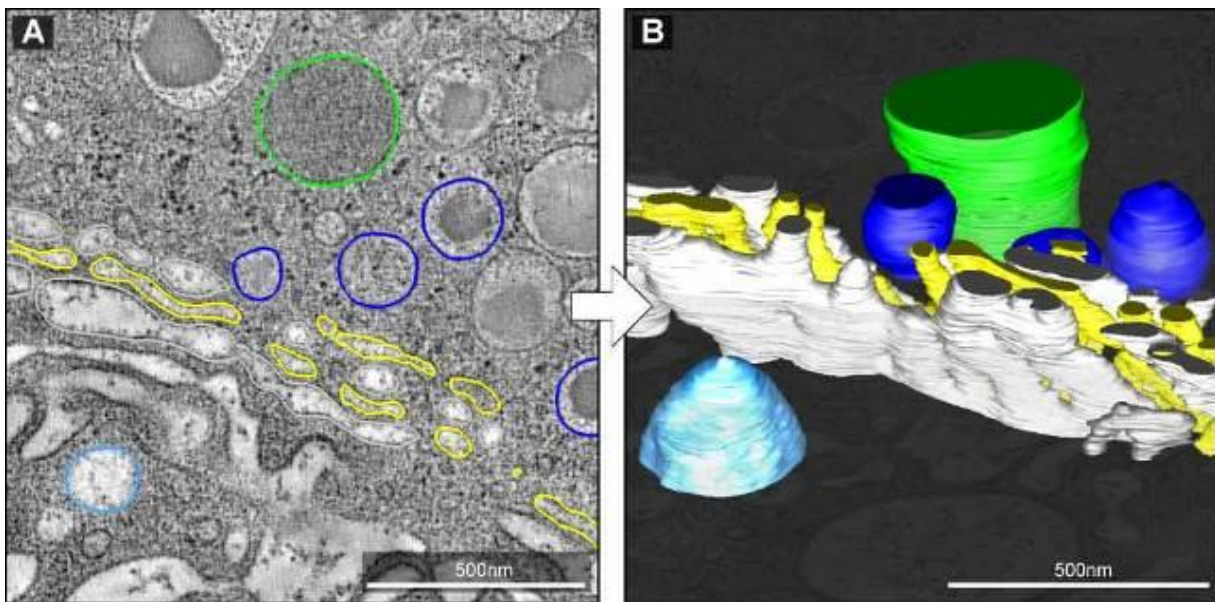
A modification of this procedure is known as ‘local alignment’. This procedure can be further employed on larger cellular areas in order to correct the heterogeneous distortion without significant loss of resolution (Marsh et al., 2004). Generally, a better tomogram quality is achieved by fiducial alignment compared to cross-correlation (marker-free) alignment methods. The number, spread and accuracy of the fiducials tracked are the main factors in determining the final tomogram quality. It is reported that tracking approximately 100 fiducials on each surface (top and bottom of the section) ensures the best possible quality (Marsh et al., 2001a).

### 1.2.6 Segmentation: manual, semi-automated and automated

Tomograms are usually stored and viewed as a series of computer generated, pixel-thick 2D ‘slices’ along the Z axis. Due to the inherently noisy nature of cellular tomograms, direct interpretation and/or visualisation of the tomograms is generally uninformative. Instead image processing steps help to visualise important cellular features, allowing for further interpretation and analysis such as volumetric analysis following segmentation (either manually, or semi-automatically).

Others have reported that high-fidelity segmentation can be performed by manual tracing. To accomplish this, biologists need to manually trace lines or ‘contours’ of compartments and membranes on every single slice of the Z stack. Manual segmentation is very time consuming, but yield contours that closely resemble the actual image.

To date, automated segmentation of whole tomograms has produced largely unsatisfactory results (Marsh et al., 2004) although the processing time for segmentation is significantly reduced. A few automated computational segmentation methods have demonstrated acceptable contouring of ET, albeit with some limitations (Narasimha et al., 2008). A survey was conducted – forming the initial part of this research work – to assess the performance of existing semi-automated segmentation algorithms, and to determine the parameters controlling accurate segmentation of different organelles of interest. To accomplish the objective of identifying the best algorithms and parameter, results were compared to manually segmented reference sets. Contours were then automatically connected to generate a final 3D surface-rendered model of the sub-cellular entities (**Figure 1.10**).



**Figure 1.10 Manual segmentation of 2D slice of tomograms and rendered models for 3D surface visualisation.**

(A) An XY single slice of tomogram is segmented by manually tracing (drawing) the lines on organelle’s membrane contour. The process is done on every slice of tomogram. (B) A 3D triangular mesh model is produced by connecting the contour lines from (A). Adapted from (Noske, 2010).

### **1.3 Background Study: Computational methods of Image Processing for ET**

#### **1.3.1 Introduction**

Creating 3D geometrical representations of compartments of interest from cellular tomograms is vital for both quantitative analysis and detailed visualisation. Due to the background noise present in ET and the nature of the data, the majority of segmentation has historically been performed manually (Frey et al., 2006). Contours are manually traced through successive Z slices by the expert, and are then meshed computationally to form a geometric surface. Organelles of interest may occupy up to thousands of image slices in Z.

The detailed 3D segmentation of ~1% of an insulin-secreting HIT-T15 cell (Marsh et al., 2001a) required an estimated 3600 person-hours of image analysis. Clearly a more efficient solution is required. Apart from the time required, the impacts of human error can be significant. Furthermore, most artefacts introduced by human error only become apparent after the surface has been meshed. As each Z slice is traced individually, even small errors manifest as ridges and shifts in the final surface that can alter an object's surface area dramatically.

Consequently, semi-automated interactive segmentation tools have been developed (Noske et al., 2008). Rather than attempting to interpret the volume data directly, these tools expedite the manual contouring process by further harnessing the expert knowledge of the operator. At the contour level, the '*DrawingTools*' plug-in of the *IMOD* software package (Kremer et al., 1996) has extended the manual tracing capabilities beyond simple point editing, through incorporation of tools that allows contours to be manipulated quickly as curves. This allows direct warping and sculpting of the contours using tools similar to those used routinely in commercial illustration software packages such as Adobe's Creative Suite.

Noske's '*Interpolator*' plug-in for *IMOD* simplifies the segmentation procedure for a variety of shaped objects. For example, in video compression where key frames mark points of dramatic change, likewise *Interpolator* allows an object to be marked-up based on the user defining key contours at points where an object's shape changes. These serve to guide and refine subsequent iterative rounds of automated interpolation between these key contours until an object has been

accurately segmented. While this has less utility for application to highly convoluted organelles, most compartments of interest possess some semi-regular structural features that benefit substantially from this hybrid approach. Secretory granules and other vesicles commonly present like distorted spheres and hence can be segmented using a handful of user-drawn key contours to guide the generation of interpolated contours, rather than requiring upwards of 50-100 individually traced contours. An example of a simple structure is a lysosome, which can be marked up rapidly with simple smooth interpolation. This semi-automated interpolation technique not only exponentially reduces tracing time (Noske et al., 2008), but also minimises user-drawn error such as the ridging effect described above. Nevertheless, interpolation is actually an expedited version of manual tracing.

To complement and extend such interactive approaches for improved segmentation, the main objective of this project is to focus and enhance semi and/or fully automated segmentation approaches. Automated segmentation algorithms have already proven their efficiency in segmentation of natural scenes, medical tomography images, biometrics and synthetic data. This project aims to assess the most appropriate techniques for application to 3D cellular reconstructions generated by ET.

### **1.3.2 Image filter: Noise reduction algorithms**

Image noise typically refers to the ‘interference’ in an image. It varies qualitatively and quantitatively and its severity depends on specimen preparation and incidental imaging conditions. Heavy metal staining during resin infiltration is the most unpredictable step. This may be caused by the use of same reagents on virtually identical specimens which can result in different degrees of stain density (McIntosh et al., 2005). Additionally irrespective of human error, both quantum noise in the electron beam and noise accrued during imaging are combined. This is particularly the case for the majority of current cameras which use phosphor scintillators to ‘convert’ electrons into photons for capture by regular charge-coupled device (CCD) cameras. Unlike other related 3D EM techniques, cells, do not contain repeating, identical substructures that can be averaged to improve signal-to-noise ratio (SNR) and so ET images cannot be processed using crystallographic or single particle averaging methods, with few exceptions; examples include infecting viruses of certain types (ones with icosahedral geometry), as well as clathrin and a few other cellular machines e.g. bacterial secretion systems.



Since this project is focused on semi-automated segmentation, it is necessary to first enhance the signal to noise ratios of images of 2D slices of the final 3D tomogram. To do this, it is necessary to employ noise reduction algorithms. Studies analysing the suitability of existing image filters for 2D and 3D ET image datasets are performed. The understanding of these comparable filters could be achieved by grouping them according to their primary criteria. Existing noise reduction filters can in this way be divided into two primary groups; classical and complex filters. Complex filters can be further arranged into three subgroups, based on the specific developmental principle. The principle, application, performance level, data output, advantages and disadvantages of application on the ET will be discussed below.

### **1.3.2.1 Classical noise reduction filters**

The most basic filtering operation is known as ‘low-pass’ filtering which is also called a ‘blurring or ‘smoothing’ filter. The main purpose of these filters is to remove high-frequency (impulse) noise by averaging out rapid changes in intensity. Along with high-pass (removes low frequency information), band-pass (removes high and low frequency information, retaining a "band" of frequency space information in the middle) and other related filters, it remains a cornerstone of signal processing. Unfortunately, the low-pass filter does not discriminate between noise and valid high-frequency information, thus resulting in more of a ‘blurring’ effect rather than true noise dampening.

Kernel filters improve results over low-pass filters by using a matrix to weight the averaging of pixels/voxels based on proximity. Gaussian filter (Canny and John, 1986, Aurich and Weule, 1995) is one of the most popular and effective method particularly for enhancing the edge detection using a discretised Gaussian function to calculate the weighting across a kernel of a suitable size. The application of basic Gaussian filter is conceived to be promising for ET images based on its established performance – where the method has demonstrated its efficiency improving the detection of (targeted) edges prior to contour segmentation; e.g. an important component in bilateral filter (Pantelic et al., 2007). Gaussian filter plugin from *ImageJ* software was used for this experiment.

### 1.3.2.2 *Complex filters*

Complex filters maintain the main function of classical image filters (smoothing and blurring) but are designed to additionally enhance the edge/membrane of the cellular compartments in ET. Implemented with 'special role/s' in algorithms, ideally noise reduction filters designed for electron tomography should operate as an 'edge and corner preserving smoother' (ECPS) (Papari et al., 2007). Such filters have important and specific roles in a large number of image processing applications, ranging from enhancing photographic images to the rapid and more accurate analysis of microarray data. As they execute distinctive roles, the algorithms involved are more refined and complex compared to classical filters.

ECPS filters such as the median (Pratt, 1978), bilateral (Tomasi and Manduchi, 1998) and diffusion-based filters (Perona and Malik, 1990) have demonstrated effectiveness in ET. While other filtering methods, including the use of connected morphological operators (Heijmans, 1999, Meijster and Wilkinson, 2002), mean shift (Comaniciu and Meer, 1999) and nonlinear total variation (Rudin et al., 1992), unfortunately have limited usefulness in denoising ET images for a variety of reasons, but particularly due to the heavy noise contamination of ET images. ECPS filters can be further sub-classified into three main groups 1) rank filters, 2) diffusion-based methods and, 3) bilateral filtering below.

### 1.3.2.3 *Rank filters*

Similar to kernel filters (as discussed in 1.3.1.1) in terms of processing, rank filters use an odd-sized window in 2D or 3D centred on the region of interest (ROI) that progressively passes through the 2D image or 3D volume in XY or XYZ, respectively. However, in terms of its specific weighting calculation, unlike kernel filters, rank filters sort the values in the neighbourhood based on intensity and weight (calculate) based on these intensity values.

#### *Minimum, maximum and median filters*

The simplest examples of rank filtering are minimum and maximum filtering. The intensity values of neighbourhood around each image pixel are sorted and weighted (calculated). In these examples, the smallest intensity (minimum) and greatest intensity (maximum) values from neighbourhood pixels were used and stored as the corresponding resulting value. Finally, each pixel in the image is replaced by the resulting value generated for its associated neighbourhood. These transforms have a crude darkening and lightening effect on the image respectively, so despite being not appropriate

for denoising large image volumes, they are potentially useful for localised areas. The minimum and maximum filter plugins from *ImageJ* software were used for this experiment.

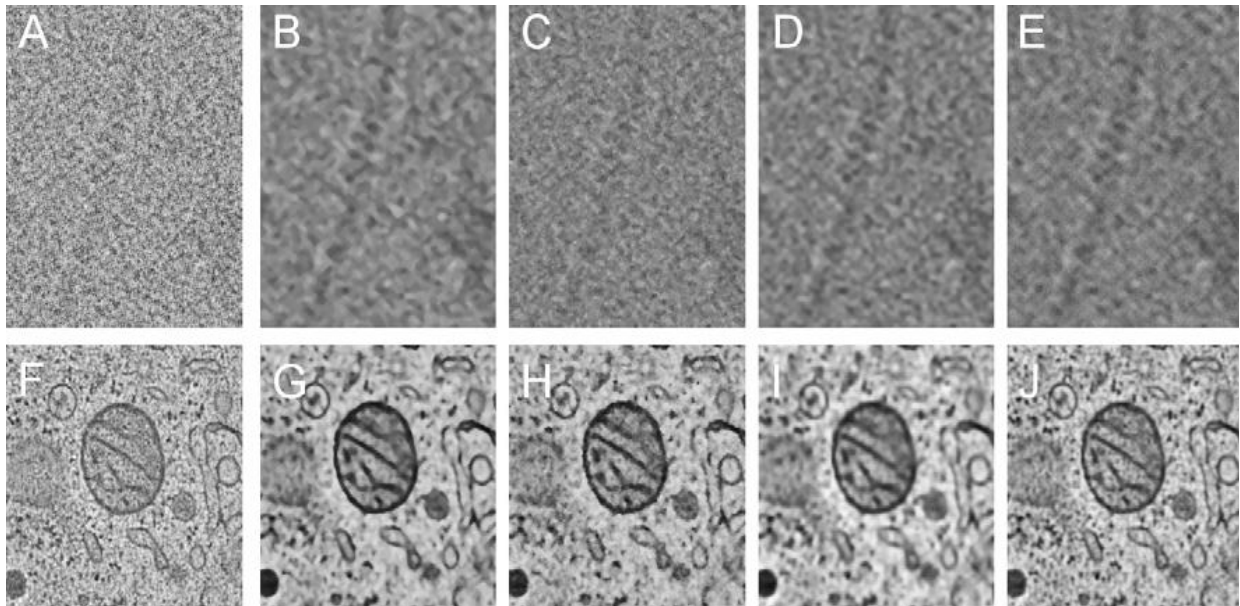
Unlike minimum and maximum that directly take and store the smallest or greatest intensity value from pixel's neighbourhood, median filter and mean filter need some calculation. Median filter is the most commonly applied rank filter used in ET (van der Heide et al., 2007, Arias-Castro and Donoho, 2009). Here, the focal voxel is replaced by median value taken from the ranked list of values adjacent to (and within the) neighbourhood of the focal voxel. It effectively eliminates impulse noise by ignoring outlying values. In addition, if a smaller window is used, voxels take on a density similar to their most prominent immediate neighbours, which improve edge gradients that define e.g. membranes, as well as the coherence of densely stained compartments. As the median is chosen from the ranked list, the resulting value will be identical to at least one neighbour, avoiding arbitrary values potentially introduced by impulse noise.

Median filtering was originally suggested in its one-dimensional form and improved to two-dimensional image processing (Russ, 2002). In three-dimensions, median filtering is performed by letting a three-dimensional (3D) window move over voxels in a volume. The value at the window centre is replaced by the median (value). Improved results of processed images obtained from the application of 3D median filter on tomographic reconstruction – demonstrated with iterative 3D median filtering in (van der Heide et al., 2007). The 2D Median filter plugin from *ImageJ* software and the 3D Median filter from *CoAn* software were used for this experiment.

Compared to other ECPS or complex filters, rank filtering is computationally efficient, with modest memory requirements. However, as the window size is increased, the number of values to be sorted increases exponentially, introducing a bottleneck even with the most efficient quicksort-based algorithms (theoretically  $O(n \log n)$  before parallelisation) (van der Heide et al., 2007, Volkmann et al., 2000). Additional problems are introduced with increased window size, most notably structures smaller than half the neighbourhood are likely to be eliminated completely.

Due to its speed, reliability and the fact no significant parameters require adjustment other than the window size, the median filter has historically been preferred by our lab for noise reduction of cellular tomograms throughout work undertaken as part of a long-standing collaboration with A/Prof. Niels Volkmann at the Sanford-Burnham Medical Research Institute in the USA. When applied iteratively, the median filter has been shown to achieve comparable results to those

typically attained using much more sophisticated filters (**Figure 1.11**) which generally require substantial parameter optimisation, sometimes even out-performing them yet using only a fraction of the computational resources (van der Heide et al., 2007). For example, the 3D median filter requires computer memory to be allocated equivalent to approximately twice as many Z slices as the size of the window. In comparison, the nonlinear anisotropic diffusion (NAD) filter (described below) requires around 36 times the total number of voxels in the volume and adjustment of at least two parameters, both of which are difficult to predict a priori (van der Heide et al., 2007).



**Figure 1.11 Comparison of different noise reduction algorithms applied to tomographic data.**

(A and F) Detail from original slice through tomographic reconstruction of ice-embedded actin filaments and original slice through tomographic reconstruction of pancreatic beta cell showing a mitochondrion and surroundings, respectively. (B and G) Result of med3 filtering (van der Heide et al., 2007). Note the clear appearance and delineation of the actin monomers close to the center of the figure (B) and noise is significantly removed while the edges are largely intact (G). (C–E and H–J) Results of (C and H) progressive switch median filtering (Zhou and Zhang, 1999), (D and I) non-linear anisotropic diffusion (Heymann and Belnap, 2006), and (E and J) bilateral filtering (Tang et al., 2007) for comparison. Note that no attempt at parameter optimisation for any of the algorithms was made. Only the settings recommended in the respective papers were used. (van der Heide et al., 2007) Figure 6.

### ***Extended mean filter (Meanshift filter and Kuwahara filter)***

Meanshift filter is the latest application of mean filter and the Kuwahara filter (Kuwahara et al., 1976) have shown its efficiency on ET images (Bilbao-Castro et al., 2010). Kuwahara filter behaves as an extension of the mean filter, where a larger window is initially used and then divided along its midlines into a number of smaller areas. Each of these smaller windows is individually averaged and then the variance of intensity values is calculated. The resulting value (output pixel) is the mean of the sub-window with the smallest variance. This technique strongly improves low-frequency information such as edges and coherence, but like the mean filter, tends to introduce an overall blurring effect as a result of filtering across borders, since it makes no distinction between high-frequency data and impulse noise. However, an improved variant of the generalised Kuwahara filter

developed by (Bakker et al., 1999) combines orientation adaptive filtering and edge preserving filtering to avoid this problem. This approach has been reported to preserve edges and improve the SNR. Generalised Kuwahara filter that combines orientation adaptive filtering and edge filtering was implemented to avoid problems such as overall blurring effect (Bakker et al., 1999). Both Meanshift and Kuwahara filters plugins from *ImageJ* software were used for this experiment.

#### **1.3.2.4 Diffusion-based methods**

The term ‘diffusion’ in image processing is analogous to physical diffusion events, such as molecular diffusion through Brownian motion and heat conduction. In image processing, diffusion moves the grey value of an image from higher grey concentration to areas with lower grey value, with the aim of preserving object edges while smoothing the regions in between, as the edges are the information-carrying features.

Since blurring is the typical property of linear diffusion, (Perona and Malik, 1990) suggested a modification of the diffusion flux by minimising or blocking diffusion across edges in order to detect and preserve edges. Unfortunately, however, this fails to address one of the key goals of image pre-processing for this project, i.e. the thinning and linking of the broken edges of an object, as the property of conventional scale space is highly preserved. Therefore, this method is not applicable for ET images that exhibit a high level of noise, where the noise degrades the edge signal.

Broken edges and/or a degraded edge signal remain a common problem in image processing generally and particularly for ET data. In order to avoid this undesirable property, (Weickert, 1998) has appropriately created a new nonlinear and anisotropic diffusion approach, where the partial differential equation for anisotropic diffusion has been modified. As such, two different diffusion variables are proposed, depending on the structural features in the images (Weickert, 1994, Weickert, 1998, Weickert, 1999). The first method is called edge-enhancing diffusion (EED) and the second one is coherence-enhancing diffusion (CED). EED is basically a modified method where the Perona-Malik diffusion model (Perona and Malik, 1990) is correctly discretised to improve low SNR and enhance edges, while CED is a method with the capacity to connect lines interrupted by noise (i.e. broken edges), when the gradient's directionality and 'flow-like' properties can be averaged from structural information in the larger volume and its mean orientation calculated to close any gaps.

Although the performance of these diffusion methods was originally shown to produce successful results for 2D applications (Perona and Malik, 1990, Weickert, 1998) and more recently for use with 3D images from MRI (Burgeth et al., 2009), so far these have not proven suitable for denoising highly corrupted volume data that is typical for EM. Therefore, Frangakis and Hegerl (Frangakis and Hegerl, 1999) proposed to take advantage of the combination of methods suggested by (Weickert, 1998) by combining both EED and CED to accommodate a larger variety of structural features in 3D images with a higher noise level, leading to development of a new method called hybrid NAD.

To prove the suitability of this hybrid NAD filter for ET reconstructions, Frangakis and Hegerl presented in detail the parameter settings and discretisation stencils from two example test volumes (Frangakis and Hegerl, 2001). By combining the advantages of EED and CED, which respectively demonstrate good performance at low SNR and a capability to connect lines interrupted by noise, this hybrid approach even further improves the capacity for 3D visualisation by iso-surface representations or volume rendering to aid in drawing useful biological interpretations from the test data. At the time, the results presented in (Frangakis and Hegerl, 1999, Frangakis and Hegerl, 2001) demonstrated that NAD was superior to more conventional methods of noise reduction, such as low-pass or median filtering.

The effectiveness of hybrid NAD for ET reconstructions of cellular data was further documented in a paper by (Fernández and Li, 2003) describing the development of software based on hybrid EED/CED, which demonstrated that in addition to reducing local noise, using a hybrid NAD filter enhanced the edges of both curvilinear and planar objects resulting in improved delineation of object shapes. Hybrid NAD – i.e. where two diffusion tensors are combined; edge-enhancing diffusion (EED – used to improve low signal-to-noise ration and enhance edges) and coherence-enhancing diffusion (CED – used to connect lines interrupted by noise, i.e. broken edges) – was implemented in 3D for ET reconstruction segmentation (Fernández and Li, 2003). The NAD filter provided in *IMOD* software was used for this experiment.

### **1.3.2.5 Bilateral filtering**

Bilateral filtering was first developed by (Tomasi and Manduchi, 1998) as a novel ECPS filter designed to be effective both with RGB photographs and grey-scale images, but was later demonstrated by (Jiang et al., 2003) to be useful in a wide range of EM applications, including ET

and SPA. It was originally designed to be photometrically weighted, to account for the human optical colour space, but this aspect is obviously unused in greyscale electron tomograms.

The bilateral filter is essentially a regular low-pass filter, with weighting determined by the Gaussian value corresponding to distance from the centre, combined with a modified low-pass filter which instead weights based on the variance, or distance in colour/grey space. The values of pixels with a similar density to the pixel of interest are weighted more heavily, which results in improved preservation of both edges and coherence, especially when used with a large window. Jiang and colleagues at the Baylor College of Medicine subsequently incorporated the bilateral filter as a standard feature of the *EMAN* software package. In addition to *EMAN*, there is also 'Bernard's Software Package' (*Bsoft*) that provides a bilateral filter (Heymann, 2001, Heymann and Belnap, 2006). Under extremely low SNR conditions, such as in cryo-specimens or SPA micrographs with small particles of interest, the bilateral filter also faces the same limitations of other complex filters; the difficulty in distinguishing between high-frequency data and impulse noise. To allow for even greater control in such situations, (Pantelic et al., 2006) developed the discriminative bilateral filter (DBL), which adds a second photometric function to distinguish between edges and impulse noise. As well as each pixel being weighted based on its difference in density to the pixel of interest, each pixel is weighted independently relative to its own neighbours and attributed a weight of 0 if density differs by more than the given threshold for impulse noise. Bernard's Software Package (*Bsoft*) provides this type of bilateral filter (Heymann, 2001, Heymann and Belnap, 2006) and was used for this experiment.

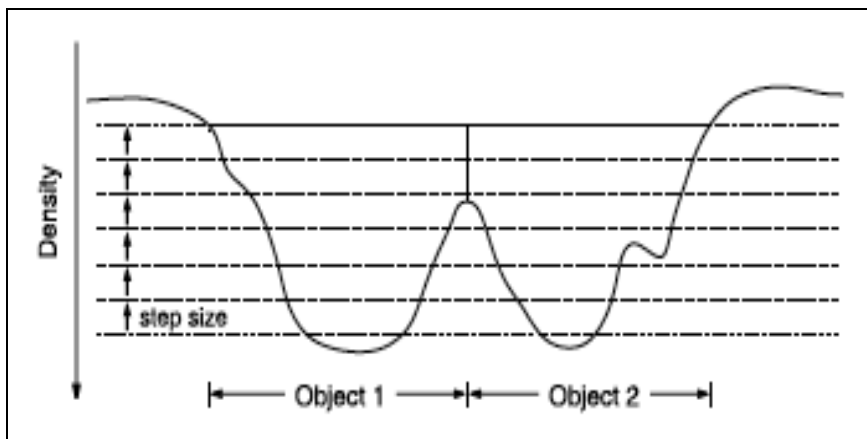
### 1.3.3 Segmentation

#### 1.3.3.1 Watershed Transform

The watershed transform is a mathematical morphology-based segmentation algorithm analogous to topographic reliefs (Beucher and Meyer, 1993, Hagyard et al., 1996, Vincent and Soille, 1991). In the simple 2D greyscale case, elevation is equated with density and the terrain is progressively 'flooded' from each of the minima. As the catchment basins expand, watershed lines are placed where they finally touch to segment the image (Volkman, 2002). The resulting catchment basins correspond to homogenous grey areas in the original image. The accuracy of region finding and computational efficiency of the transform has been demonstrated by (Hagyard et al., 1996).

Over-segmentation, where one object is broken up into multiple pieces, is a common problem in processing ET data, not just via watershed transform but with many different segmentation

algorithms, due to e.g. the high noise levels and inconsistent staining. To overcome this problem when using the watershed transform, neighbouring basins with similar qualities are merged once the flooding is complete. Even after extensive pre-processing to enhance edges and remove noise, it is still difficult to strike a balance between over- and under-segmentation. To minimise the need for basin merging, an additional ‘step’ parameter in a novel 3D variant of the watershed transform was introduced by Niels Volkman in 2002 (Volkman, 2002), specifically targeted for use in segmenting electron density maps (**Figure 1.12**). This parameter allows the rate of immersion to be specified, allowing finer grain controls over the assignment of watershed lines.



**Figure 1.12** Schematic diagram illustrating the watershed transform.

Low elevation shows the objects while background is on high elevation. The image is initially thresholded at a low elevation. Then the elevation is raised gradually one step at a time. The boundaries of the objects will expand as the threshold increases. When they touch, however, they are not allowed to merge. Thus, the points of first contact become the final boundaries between adjacent objects. Step size must be appropriately chosen. Adapted from (Volkman, 2002).

In practice, determining the ‘step size’ in application of the modified watershed transform to noisy ET images of ET is a tedious process. To overcome this problem and increase the power of this technique, a preceding denoising step is beneficial.

### 1.3.3.2 Energy-based techniques (‘snakes’ or ‘active contours’)

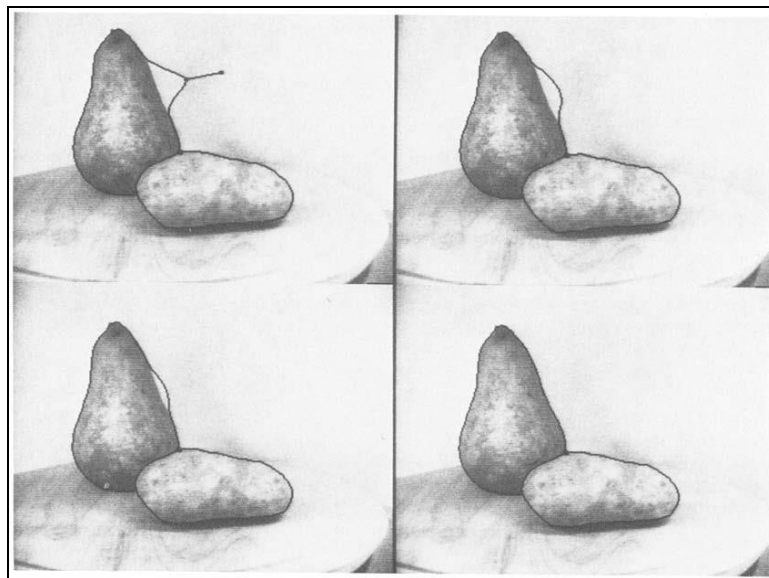
An energy-minimising deformable spline, commonly known as a ‘snake’ or ‘active contour’, is a deformable shape that is influenced and guided by image forces and external constraints that pull it towards object contours (edges) by using the gradient information as input data. It was originally introduced by (Kass et al., 1988) and often used in applications and visual problems such as object tracking, motion tracking and segmentation which utilises edge detection and shape recognition. An ‘active contour model’ is presented as a set of  $n$  points that exhibit dynamic behaviour, by locking onto the membrane of an object (manually segmented in one Z-slice only), from which the object is



then segmented across all Z-slices. The accuracy of segmentation is subsequently improved through iterative refinement, up to a point beyond which accuracy is diminished.

In the review of (Nguyen and Ji, 2008) there is an extensive discussion of active contour segmentation methods applied to various ET volumes, including reconstructions of: DNA filaments (Jacob et al., 2002); chromosomes, segmented by parametric active contours (Babu et al., 2004); and subcellular features of HIV-infected macrophages, by geodesic active contours (Bartesaghi et al., 2005). Segmentation of cell image data by globally optimal geodesic active contours (Appleton and Talbot, 2005) and using the level set method (Sethian, 1999, Bajaj et al., 2003) is also compared.

As with the manual process, a rough initial contour (indicating an initialisation curve/contour) is drawn and then lets the snake evolve under pre-set parameters, such as the gradient threshold and number of iterations. The snakes may also be used with fully automated segmentation, in which seed points are calculated at the snake's initialisation slice and will evolve from there (Bajaj et al., 2003). A simple example of how the snake functions can be viewed in **Figure 1.13**; the snake's spline energy term attracts the erroneous contour back to the object's boundary after several iterations.



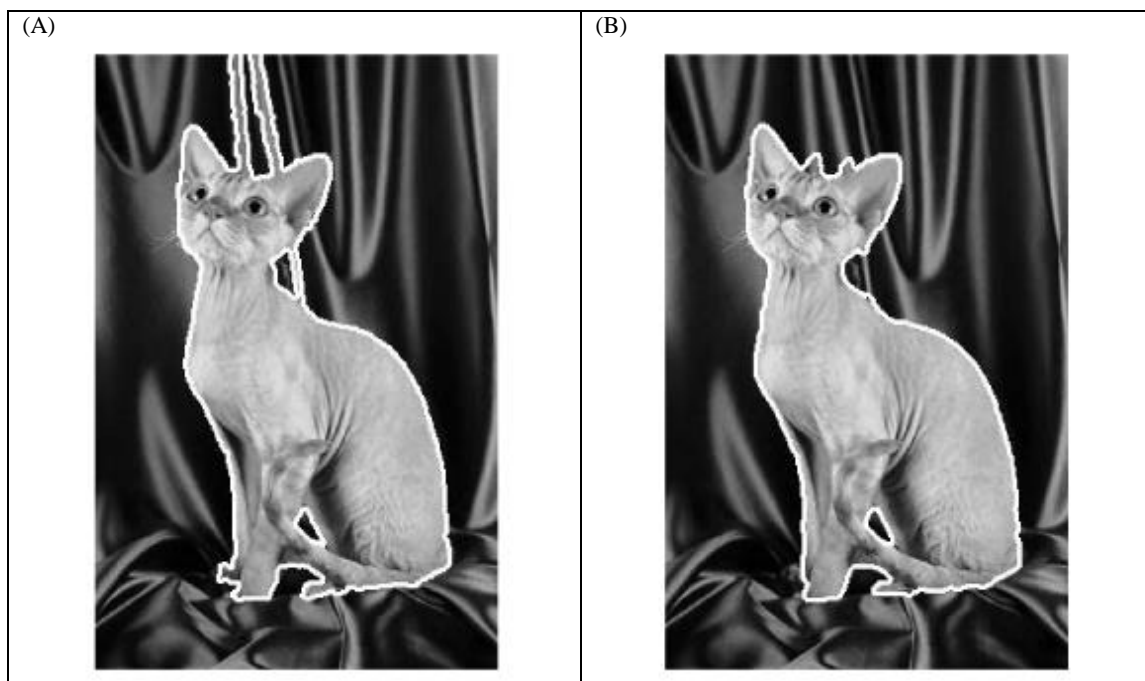
**Figure 1.13** Semi-automated image segmentation by the 'Snakes' or 'active contours' techniques.

Two edge snakes on a pear and potato. Upper-left: The user has pulled one of the snakes away from the edge of the pear. Others: After the user lets go, the snake snaps back to the edge of the pear (Kass et al., 1988).

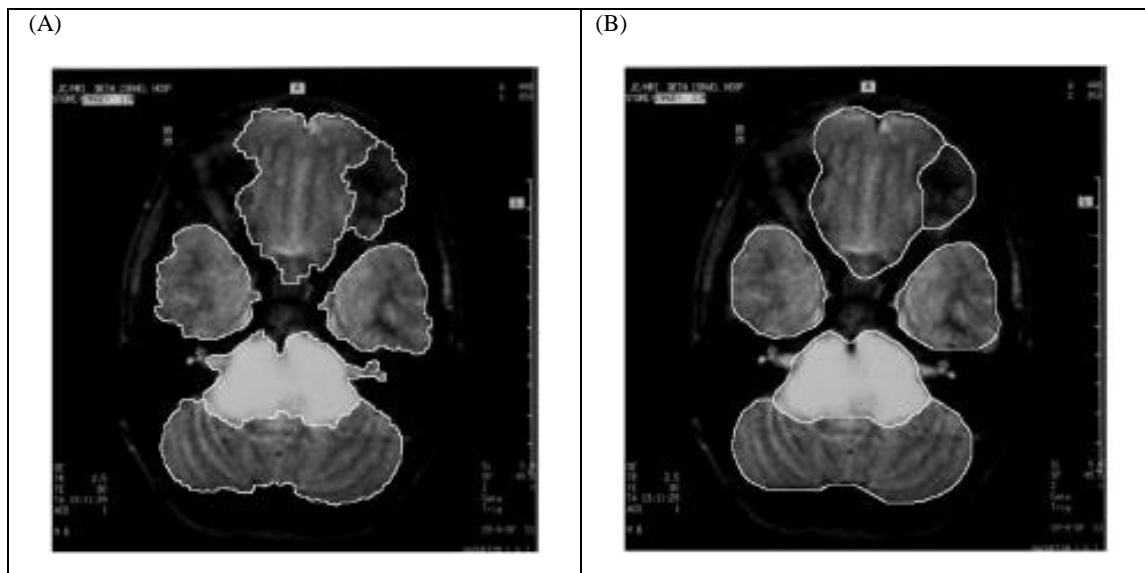
### 1.3.3.3 Hybrid techniques

Although the watershed transform (Volkman, 2002) has been extensively shown to be a powerful tool for mathematical morphological segmentation, its use can result in over-segmentation of noisy electron tomograms. The snake method, reported to be efficient for segmenting subcellular structure (Bajaj et al., 2003), also has a major drawback: the erroneous convergence of edges that may occur when true edges are broken, or blurred by noise. To overcome these significant problems, the integration between watershed and energy-based segmentation techniques, called ‘watersnake’, was developed and tested (Nguyen et al., 2003). It was designed to overcome the problems encountered with energy minimisation by using the ‘distance-based definition’ - a concept of topographical distance - of the watershed line.

Two significant advantages of watersnake have been identified: improved smoothing results and the reduction of unwanted convergence of edges. A comparison between watershed and watersnake applied on 2D image and medical datasets is shown in **Figure 1.14** and **Figure 1.15** respectively.



**Figure 1.14** Application of Watershed (A) versus Watersnake (B) segmentation to 2D image data. The results are shown for the object of interest only (adapted from (Nguyen et al., 2003)).



**Figure 1.15 Comparison of Watershed and Watersnake segmentation techniques applied to 2D medical imaging datasets.** (A) The result of original watershed segmentation. (B) The result of the watersnake algorithm. The result shows that (B) is smoother than (A), while still accurately identifying the main objects (adapted from (Nguyen et al., 2003)).

In 2003, Nguyen *et al* concluded that the efficiency of *watersnakes* has not yet been proven on the ET volumes of biological samples, which often contain relatively complex organelle shapes with inconsistent edges and significant noise (Nguyen et al., 2003). However, in a subsequent study (Nguyen and Ji, 2008), the authors improved on their original model by incorporating prior knowledge of the shape/features of organelles of interest, as well as the mathematical framework necessary to adopt it to 3D volumes. Based on this additional information, a powerful method has been developed for automatic segmentation of sub-cellular structures with different complexity levels.

Another hybrid technique uses a model-based approach to segment reconstructions. Applied to the segmentation of kinetochore microtubules (MTs) in PtK cells (McEwen et al., 2005), the automated algorithm consists of five steps, including three types of filtration: a median filter, used to remove speckle noise so that the subvolume is enhanced; an anisotropic invariant wavelet filter, applied to enhance elongated structures; and an eigenvector-based filter for 3D surface-enhancement to detect circular contours. The filtration steps are followed by conversion of the model to a binary image, with the MT plus-ends then traced in a probabilistic manner.

Jiang et al. further investigated the segmentation of MTs in 3D cellular reconstructions to develop an automated extraction process for MT plus-ends (Jiang et al., 2006b, Jiang et al., 2006a). This method contains three main steps: 1) volume pre-processing using an anisotropic invariant wavelet transform; 2) a 3D tube-enhancing filter and surface-enhancing filter for MT body segmentation

employing a modified active contour shape model; 3) MT plus-end tracing, where an improved probabilistic tracing method has been applied. Although these techniques were demonstrated to accurately segment kinetochore MTs, they have not yet been successfully applied to segment MTs in the context of other ET datasets on a broader scale. The approach has been found to be practical for microtubules and such morphology (tubelike shape) (Jiang et al., 2006b, Jiang et al., 2006a), and has not been selected for this study.

### **1.3.4 Segmentation of organelles of interest: Studies for sub-cellular compartments categorisation**

Accurately tracing (e.g. manual segmentation) through the centre of the membrane bilayer of a cellular organelle is not an easy task, especially when the organelle's exact morphology is unknown beforehand and the staining of the membrane may vary in texture and intensity. Factors such as the crowded cytoplasm (Grünwald et al., 2003), image noise and distortion may also hinder accurate manual segmentation. Much of the previous research in automated ET segmentation has been in the development and application of tools for quantitative analysis and interpretations are mainly based on ET volumes with low SNR (Frangakis and Forster, 2004, Narasimha et al., 2008, Winkler, 2007). Sandberg (Sandberg, 2007) has also shown that using orientation information can assist in the automatic segmentation of microtubules or other fiber-like structures and that image information alone (such as intensity and texture, which are non-uniform along the microtubule) is not sufficient.

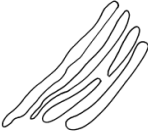
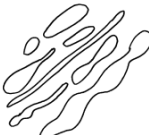
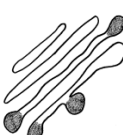
Consequently, the shape and complexity of the organelle is perhaps the most significant information in obtaining the best segmentation result. In this study, I will show that by categorising the complexity (and therefore segmentation difficulty) of each compartment based on its shape (and eventually extending to other features such as texture), we will improve the precision of the process of segmenting ET volumes. To achieve this aim, I have undertaken a background study that summarises the primary morphology and degree of complexity of three significant compartments/organelles found in the ET volumes of pancreatic beta cells that I intend to segment in the course of our group's biological investigations of beta cell biology: the Golgi apparatus, mitochondria and insulin granules.

### 1.3.4.1 *The Golgi Apparatus*

The Golgi apparatus is a key organelle found in all eukaryotic cells whose primary function is to further modify macromolecules (e.g. lipids, proteins) from the endoplasmic reticulum (ER). This processing is particularly important for proteins to achieve their final functionality for a number of fundamental cell processes, such as secretion. The Golgi apparatus consists of a number of discrete stacks of fenestrated, flattened membranous compartments called cisternae, which are laterally inter-connected to form a ribbon-like structure (Marsh et al., 2001a, Marsh and Howell, 2002, Noske et al., 2008). In prior ET studies of the beta cell, the Golgi typically consists of 5 to 7 individual cisternae and is somewhat analogous to a stack of pancakes; this morphology contributes to a high surface-to-volume ratio.

The Golgi can be divided into a series of different spatial and functional regions, termed the cis, medial-, and trans-cisternae, each distinguished by different enzymes which selectively modify the different types of molecules as they progress through these regions along the cis-trans axis. From the ER, membrane transport vesicles and tubules carrying newly synthesised proteins fuse with cis-Golgi cisternae. Their protein cargo then progressively transits across the stack to the trans-Golgi cisternae, where proteins are then sorted and packaged for shipment to the required destination either within the cell or for release to the extracellular space.

In some cases, tubular connections between non-adjacent (and more rarely, adjacent) cisternae have been observed; this, in conjunction with functional stratification of the different regions of the stack, mean that the organisation of Golgi cisternae shape can be divided into three levels of morphological complexity for the purposes of this study (presented as Case 1, Case 2 and Case 3 in **Figure 1.16**). Each has been simplified as a cartoon image to illustrate more clearly the basic morphological/shape complexity variations that exist, as determined by evaluating existing ET datasets produced by our group to date.

Level of complexity <span style="float: right;">→</span>		
Case 1 	Case 2 	Case 3 
Each cisterna is an individual 'pancake' layer, relatively uniform in length, with only slight variations in shape and size.	The cisternae appear to have differences in shape, length and width, but are still clearly separated. Some examples of variations in shape include a long tubular profile, wide/roundish or 'distended' cisternae and elliptical membranes.	Trans- or cis-Golgi often have vesicles budding off, but still attached and are typically segmented as the same surface as the attached cisternae. These shape anomalies, as well as variations in staining density usually associated with these buds, can cause difficulties using a smooth segmentation algorithm.

**Figure 1.16** Illustrative schematic images to highlight different levels of shape complexity for the Golgi apparatus with respect to segmentation.

### 1.3.4.2 Mitochondria

Mitochondria comprising multiple subregions that carry out specialised functions are ultimately bound by an outer membrane layer, together with a small inter-membrane space followed by an inner membrane layer that is organised into cristae and the matrix (the space within the cristae). Mitochondria work as power generators in the cell that supply chemical energy in the form of adenosine triphosphate (ATP), necessary to carry out basic cellular activities. They tend to have a heavy/dark staining density. Morphologically, this organelle can be quite complex, as they often branched and forming irregular shapes presumably due to fission or fusion events determined by the energy state/needs of the cell prior to freeze-fixation of the cells.

In this study, I will only consider the gross surface morphology of mitochondria as delineated by the outer membrane. For this purpose I have assigned four levels of complexity to the overall morphology of mitochondria in beta cells (**Figure 1.17**). Case 1 is the most simple, with only non-branched mitochondria, which display a relatively consistent shape from one Z-slice to the next (usually tubular or pancake-like) and exist as 'singular' spatially discrete objects in the cytoplasm (meaning that their outer membrane does not contact any other mitochondrion or other organelles/compartments). We have also observed, in accordance with other studies, that mitochondria can be branched in some regions. Branched mitochondria that remain spatially discrete within the cytoplasm constitute the second level of complexity (Case 2). It should be noted that it is a subject of debate whether these branched mitochondria should be considered one mitochondrion, two mitochondria in the process of fusion (or fission), or three separate mitochondria (Chen and Chan, 2005, Frazier et al., 2006, Karbowski and Youle, 2003, Okamoto

and Shaw, 2005, Perkins and Frey, 2000). Case 3, is similar to Case 2, but rather than being branched, each mitochondrion appears to have two distinct shapes. Case 4, the most difficult to segment, exhibits the proximity of other organelles/compartments to our mitochondria of interest. In this case, it is hard for computational tools to assign a membrane/edge to the correct organelle, as they are similar in density and grey value.


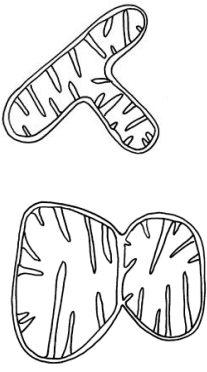


Level of complexity			
			→
Case 1	Case 2	Case 3	Case 4
			
<p>Singular and free in cytoplasm: e.g. the outer membrane is clearly separated from that of other organelles/compartments and significantly denser than the surrounding cytoplasm.</p>	<p>Singular/free in the cytoplasm. Branched or proximal to a branch. An artifact (or limitation) of ET is seen as the membrane surface curves away from being in perfect cross-section, it becomes less distinct (e.g. blurry or cloudy) and therefore harder to segment.</p>	<p>Singular/free in the cytoplasm. Not necessarily branched, but mitochondria appear to have two distinct shapes (slender shape)</p>	<p>Proximal to, or in (apparent) contact with other organelles or compartments.</p>

Figure 1.17 Illustrated images to represent different levels of complexity of mitochondrial ultrastructure.

### 1.3.4.3 Secretory (*Insulin*) Granules

Insulin granules are typically spherical and computationally easy to segment if the membrane is intact. In beta cells, there are predominantly two types of insulin granules: mature and immature. In this study, we have ignored this distinction, limiting our focus to the granule's general shape, as the insulin core is not to be segmented. That being said, the position of the insulin core or crystal (relative to the granule membrane) plays a crucial role in determining the level of complexity, illustrated in **Figure 1.18**.

#### *(a) Mature Granules*

Mature granules in beta cells isolated from normal mice have an average diameter of approximately 300 nm and are roughly spherical in shape. Granules often appear to have an empty lumen with a more densely stained insulin core. This staining pattern in combination with an insulin crystal that does not come into contact with the granule membrane is the simplest condition for segmentation (Case 1). We have also regularly observed a densely stained lumen with a less stained crystalline core, which is slightly more difficult to segment (Case 2, when the crystal does not contact the membrane). When the insulin crystal contacts (or comes very close to) the membrane, segmentation is considerably more difficult, giving us Case 3. In this category, existing segmentation algorithms often combine the crystal and membrane into one surface, or even fail to segment the membrane altogether and erroneously segment the insulin crystal itself.

#### *(b) Immature Granules*

Immature granules can be either considerably larger or similar in size to mature granules but lack the well-defined insulin crystal core; instead, their uncleaved proinsulin cargo can be visualised as small punctate stain density of relatively uniform size and distribution within the granule lumen. Due to the fact that they appear less dense since the protein has not yet condensed in the granule core, immature granules are often called 'pale granules' (Rorsman and Renstrom, 2003, Noske et al., 2008) in morphological studies due to this difference in stain density and can also exhibit more irregular shapes.




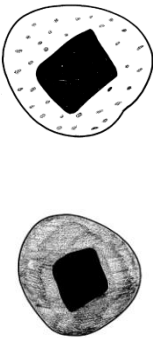
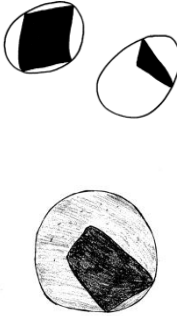

Level of complexity <span style="float: right;">→</span>			
Case 1 	Case 2 	Case 3 	Case 4 
Singular/free in the cytoplasm. Throughout the reconstruction, empty lumen space separates the insulin core from the granule membrane, allowing for easy segmentation.	Singular/free in the cytoplasm. Morphologically the same as Case 1, with one distinction: the granule lumen has varying degrees of staining density.	Singular/free in the cytoplasm. The insulin crystal contacting (or appearing to contact) the granule membrane. Because these often have a similar density, segmentation algorithms tend to fail, irrespectively of the density (or lack of density) of the remaining lumen.	Proximal to, or in (apparent) contact with other organelles/compartments

Figure 1.18 Cartoon images to represent different levels of complexity of granule ultrastructure.

### 1.4 Thesis Hypothesis

Dr Brad Marsh and colleagues at the Institute for Molecular Bioscience have extensively studied beta cells by ET and have observed significant variation amongst the morphology and shape of cell compartments in beta cells. Qualitative observations also show that there are morphological differences among membrane bound organelles within beta cells, which proves that each membrane bound organelle can undergo significant reorganization of their shape and size in response to specific biochemical stimuli, including but not limited to, a decrease in the number of mature secretory granules, remodelling of Golgi cisternae and an expansion of the Golgi ribbon, an increase in mitochondrial mass, rearrangement of the mitochondrial network to be closer to the Golgi in order to provide energy for insulin upregulation, and presumably a decrease in the number of autophagic bodies (Noske, 2010). From a purely geometric viewpoint, these events can be concluded as being deterministic of subcellular structures that present a range of complexity levels in image processing terms.

Until recently, the application of automatic and semi-automatic segmentation algorithms to ET datasets has only satisfactorily segmented specific organelles (membrane bound and non-membrane bound organelles) when particular/special conditions are implemented, so it has not been possible to

automate such segmentation process in the context of a diverse organelle's shape complexity. These observations thus led to the formulation of the primary hypothesis of this PhD project: that a particular combination of method flows and parameter settings could be developed and identified, to expedite the semi-automated segmentation of different 'levels of complexity' (different image entities) membrane bound organelles within a beta cell. It was the goal of this PhD project to segment key organelles of importance in insulin secretion and ultimately to support the mapping of an entire beta cell in 3D using a number of automatic and semi-automatic algorithms in order to support or reject the above hypothesis.

### **1.5 Thesis objectives**

This project is divided into four inter-related aims:

1. To select and categorise key organelles/compartments of interest within large cellular tomograms already in hand (previously generated by the Marsh Group at the IMB) into subtypes according to 'complexity' in terms of computerised image segmentation (using numbers of significant image entities) with the aim to provide a range of representative sub-classified organelles of interest.
2. To provide schematic diagrams for highlighting the distinguishing features for each category. Based on these schematics, tomogram sub-volumes will then be extracted from the pre-existing tomograms of pancreatic beta cells to test and evaluate a variety of different mathematical approaches for image segmentation.
3. To survey the major image processing methods which have already demonstrated at least some level of success for accurately segmenting EM/ET images, as well as algorithms employed for segmenting other types of tomographic image volumes produced by CT/CAT and MRI. These algorithms are methodically applied to the extracted sub-volumes in various combinations and trialling a range of parameters, with the aim to identify the best suited methods for a reliable segmentation for ET images based on their performance in terms of accuracy and ability to deal with increasingly complex cases.
4. To examine and analyse the segmentation results comparatively and objectively based on the comparison with manual tracing. The results of the successful combination

methods and its settings will be recorded to enable the segmentation process with minimal user interaction.

## **1.6 Thesis structure**

The remainder of this thesis is organised as follows. **Chapter 2** outlines the general methods used to prepare and reconstruct the ET images of the beta cells and covers the whole segmentation process including noise dampening and automatic segmentation. **Chapter 3** evaluates the proposed methods to identify the optimal sets of parameters of combination segmentation methods by comparing the outcomes to those produced by manual segmentation. **Chapter 4** outlines a number of image classes according to organelles characteristics to assist in identifying the optimal parameters for each organelle type. **Chapter 5** evaluates and discusses a recently developed "parameter-free" segmentation method, 3-Dimensional Bilateral Edge detection (3D BLE) in the context of our datasets. It then discusses in more detail the script development and application of tools for multiple sub-volume extractions and their importance for expediting whole semi-automated cellular segmentation. **Chapter 6** discusses both technical and biological outcomes from this project in the context of future directions, and concludes the thesis with a summary of major findings and important future applications of these approaches for rapidly and accurately classifying and analysing sub-cellular compartments for high throughput ET of cells under different conditions.



## **Chapter 2 MATERIALS AND METHODS**

---



## **2.1 Pancreatic islet/cell preparation**

### **2.1.1 Mouse islet isolation culture**

Intact islets of Langerhans were obtained from the pancreata of freshly euthanized adult female BALB/c mice. Islets were isolated with collagenase (Sigma type V, lot tested; Sigma Chemical Co., St. Louis, MO, USA), and were purified with a Histopaque-1119 density gradient (Sigma) (Marsh et al., 2004, Gotoh et al., 1985, Nicolls et al., 2002). Islets were hand-picked and then cultured in RPMI medium 1640 containing 10% (vol/vol) heat inactivated calf serum (NCS) or foetal bovine serum (FBS) and 7 mM D-glucose equilibrated with 5% CO<sub>2</sub> at 37°C. The medium was supplemented with 100 U/ml penicillin/100 µg/ml streptomycin/L-glutamine/2-mercaptoethanol. The islets were cultured for 2-3 h for tissue recovery and to promote re-initiation of protein synthesis, and transferred to RPMI medium containing low glucose (3 mM) and cultured overnight (~12-18 h). The islets were removed for immediate high-pressure freezing (HPF). Islets were not cultured or used beyond 48 h.

### **2.1.2 High-pressure freezing and freeze substitution**

Islet cultures were maintained at 37°C in HEPES-buffered (10 mM) RPMI medium (Sigma), containing either NCS or FBS 10% (vol/vol) (Invitrogen Australia Pty Ltd), prior to freezing. Immediately prior to freezing, 10-30 islets (depending on size) were manually transferred by pipette under a dissecting microscope (Olympus Australia Pty Ltd) into brass, HPF interlocking hats (Swiss Precision Inc., CA, USA). Islets were rapidly frozen under high pressure (~2,100 atm/~2,000 bar) using a Balzers HPM 010 high-pressure freezer (Leica Microsystems) to ensure vitrification of water and therefore minimal tissue damage, and then stored in liquid nitrogen until freeze-substituted and resin-embedded as described previously in (Marsh et al., 2001a).

## **2.2 Cell section tomography**

### **2.2.1 Microtomy and preparation for ET**

Thin (40-60 nm) or thick (300-400 nm) sections were cut using a Diatom diamond knife on a Leica UltraCut (-UC6) ultramicrotome, and collected onto Formvar-coated copper (2×1 mm) slot grids (Gilder, <http://www/gildergrids.co.uk>). Sections were post-stained with 2% aqueous uranyl acetate and Reynold's lead citrate. Grids with thick sections (for ET) were then coated with 5, 10 or 15 nm colloidal gold particles on both surfaces, and typically an additional carbon-coating step was required to minimize sample charging/movement in the electron beam, particularly when tilted for tomography (Marsh, 2005, Marsh, 2007). Conventional 2D TEM surveys of thin sections were conducted on a Tecnai T12 (FEI Company) operating at 120 kV, or a JEOL 1011 TEM (JEOL), operating at 80 kV. Electron tomography data of thick sections was collected on an FEI Tecnai F30 FEG-TEM operating at 300 kV.

Slot grids or open aperture grids are ideal for ET because they afford the maximum possible unobstructed viewing area when the specimen is tilted beyond 60° in the electron microscope. Ribbons of serial sections are essentially laid down the length of the grid parallel to the long axis of the slot and tomographic 'tilt series' are collected around two orthogonal axes. The gold particles are for use as fiducial markers during subsequent image alignment (Marsh et al., 2001a). On a small subset of these sections, gold particles of 10 nm diameter were used for purposes of quality comparison and the goal of later re-imaging some of these sections at high magnification.

### **2.2.2 Surveying the section to find candidate cells: whole islet montages at 4700×**

The procedures used for surveying sections to find candidate cells have been described in detail in (Noske, 2010). Briefly, each section was 'pre-irradiated' at low magnification (140×) for 10 min at 300 kV, with the electron beam spread wide and using a high spot size, to uniformly collapse a large area of the section/sample. Islets were then imaged at 4700× magnification using the stage-shift montage function of SerialEM. Cells were then selected from the montage images for whole cell tomography.



### 2.2.3 Tilt series acquisition

To reduce non-anisotropic specimen thinning during tilt series acquisition, the cell section was pre-irradiated for 10 min at  $+60^\circ$  and 10 min at  $-60^\circ$ . The process was performed immediately prior to each tilt series acquisition using the same microscope settings used for pre-irradiation at  $0^\circ$ . The combined  $4700\times$  montage images were used as a reference image to help find, rotate and position the target cell in the centre of the TEM imaging area. As the sections were serially tilted using the microscope control program *SerialEM* (Mastronarde, 2003, Mastronarde, 2005), tilt series data were digitally recorded using semi-automated methods for CCD image montaging, data acquisition and image alignment. The cell was slightly too large to fit in cross-section at  $4700\times$ , but rather than reduce magnification, tilt series were beam shifted to create a  $1\times 2$  montage on the middle-most sections of the cell, where they would not otherwise fit in the image. The cell was imaged at  $4700\times$  magnification (pixel size = 5.058 nm) by tilting at  $1.5^\circ$  increments over a range of  $\pm 63^\circ$ . The process of collecting the tilt series took approximately 3 weeks.

### 2.2.4 Reconstruction and joining of sections into a whole cell tomogram

Tilt series images ( $2K\times 2K$ ) were first brought into register with one another by cross-correlation using the *IMOD* software package which incorporated two graphical user interfaces (GUI); *eTomo* and *3dmod* (Kremer et al., 1996). To improve the tomogram quality,  $\sim 120$  gold fiducial markers (most of which were 15 nm diameter) were tracked across the A axis tilt series and the same fiducials tracked across the B axis tilt series for each section. As described in (Ladinsky et al., 1999, Marsh et al., 2001a, Shoop et al., 2002, Sosinsky et al., 2005), the serial tomograms were joined along the Z axis using the interactive program *MIDAS* (which is distributed as part of the *IMOD* image analysis package). Following the reconstruction process, R-weighted back-projection was performed to generate a general linear transform that accounted for rotation, translation and stretch of one section relative to its nearest neighbour. After joining sections, the final 'whole cell tomogram' was cropped in XY as much as possible to reduce its file size.

## 2.3 Sub-volume extraction and classification

Three key cell compartments/organelles within the tomographic volumes (i.e. the Golgi apparatus, mitochondria and insulin granules) were extracted using the *IMOD* software package (Kremer et al., 1996). Each of the sub-volume extracts was saved together with information such as volume size, mean density, minimum density and maximum density. Due to the variety of cellular compartment

information as well as inherently high levels of background noise in the volumes, it was necessary to optimise automated and semi-automated methods to segment these key compartments. This was initially done based on their ‘sub-group’.

These sub-groups are based on organelle types and in particular the Golgi, mitochondria and insulin granules. Each has discrete shapes, and sizes and differences in complexity (see **Section 1.3.4**). As shown in Chapter 1, Figure 1.16 – Figure 1.18, each sub-group was named as ‘case’. To further relate the simplified case scenarios (as shown in Figure 1.16 – Figure 1.18) for compartment structural complexity to actual examples drawn from the numerous tomograms generated by our group. The actual dataset examples used are incorporated into Figure 2.1 (the Golgi apparatus), Figure 2.2 (mitochondria) and Figure 2.3 (insulin granules).

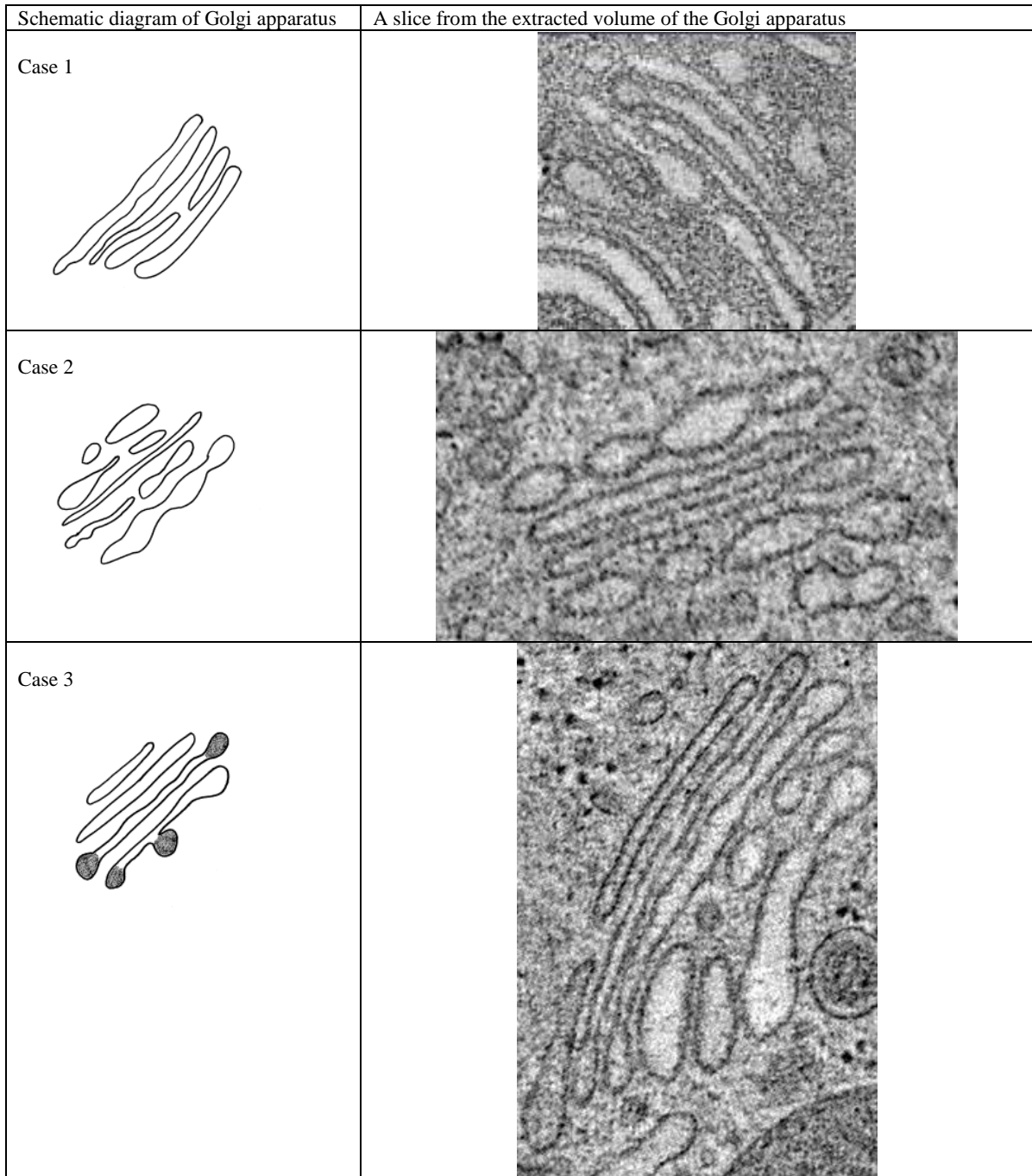


Figure 2.1 The schematic diagram and the example of real images of the Golgi apparatus.


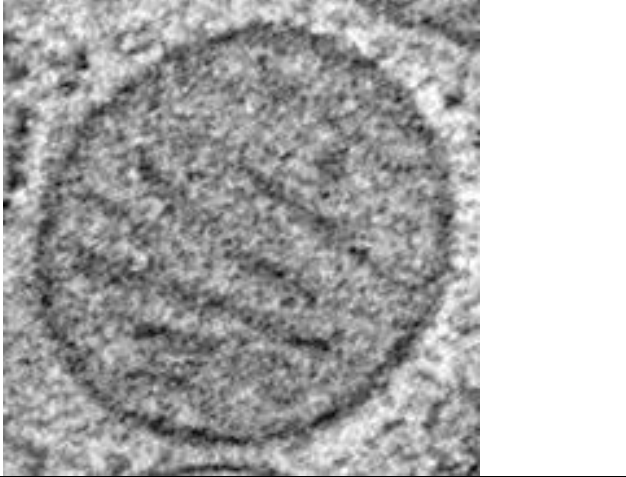

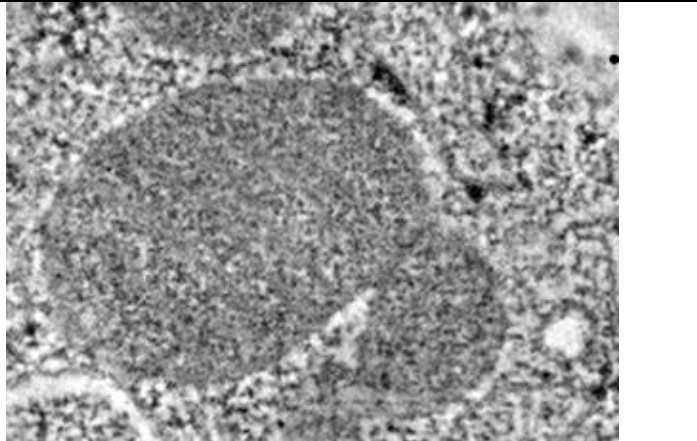



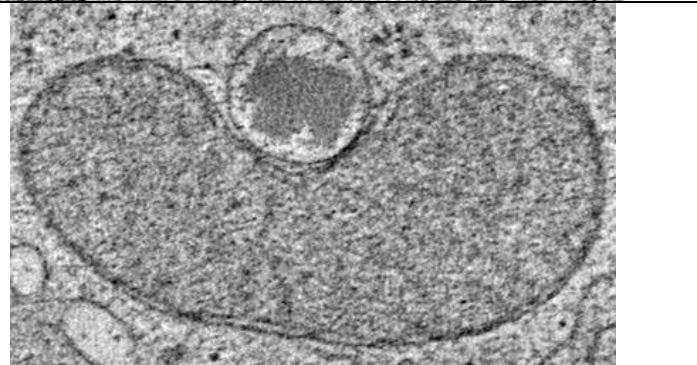
Schematic diagram of mitochondria	A slice from the extracted volume of mitochondria	
<p>Case 1</p> 		
<p>Case 2</p> 		
<p>Case 3</p> 		
<p>Case 4</p> 		

Figure 2.2 The schematic diagram and the example of real images of mitochondria.

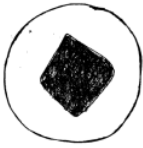
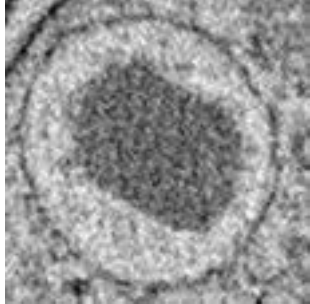
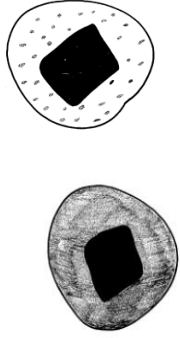
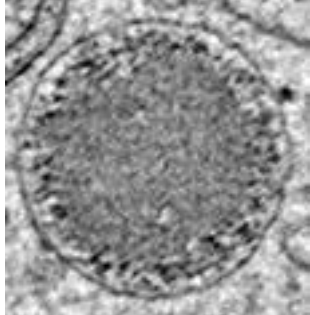
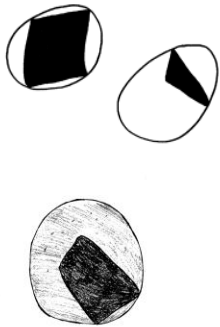
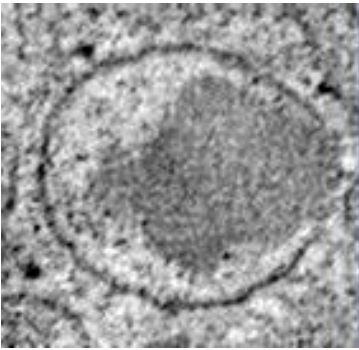

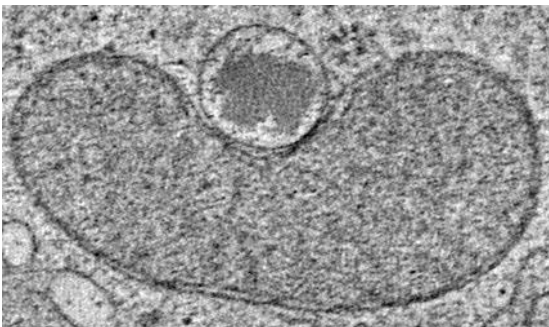
Schematic diagram of granules	A slice from the extracted volume of insulin granules	
<p>Case 1</p> 		
<p>Case 2</p> 		
<p>Case 3</p> 		
<p>Case 4</p> 		

Figure 2.3 The schematic diagram and the example of real images of insulin granules.

## **2.4 Towards automated segmentation of cellular tomography**

Compartments/organelles within the tomographic volumes were extracted, filtered, segmented, and viewed using the *IMOD* (Kremer et al., 1996), *CoAn* (Volkman et al., 2000), *ImageJ* (Rasband, 1997-2014) and *BSoft* (Heymann, 1999-2014) software packages, as well as other approaches proposed within this project. Due to the low signal-to-noise ratio of the cellular tomograms, it was necessary to adjust the segmentation methods and optimise their parameter settings to accurately segment different compartments. Sub-volumes of the three key organelles were extracted and each was manually segmented. All sub-volume extracts of key organelles were also segmented using combination of segmentation methods (see **Chapter 3, Section 3.3.2**) using the systematic approach shown in **Figure 2.4**. This approach is explained in detail in **Section 3.2**. The segmentation data was then used to generate 3D triangular meshes describing the subcellular surfaces of the segmented organelles.

Because sections cut from plastic resin are reported to collapse in the direction of the beam upon initial exposure to the electron beam (Luther et al., 1988), the 3D surface-rendered model data were re-expanded by a factor of 1.7 in Z to more accurately represent the original topology of sub-cellular structures under study (Marsh et al., 2001a). To optimise the parameter settings of each combination of method flows, the results, i.e. numbers of contours (NOC), contour volume (CV) and total mesh surface area (TMS) were compared to those obtained by manual segmentation.

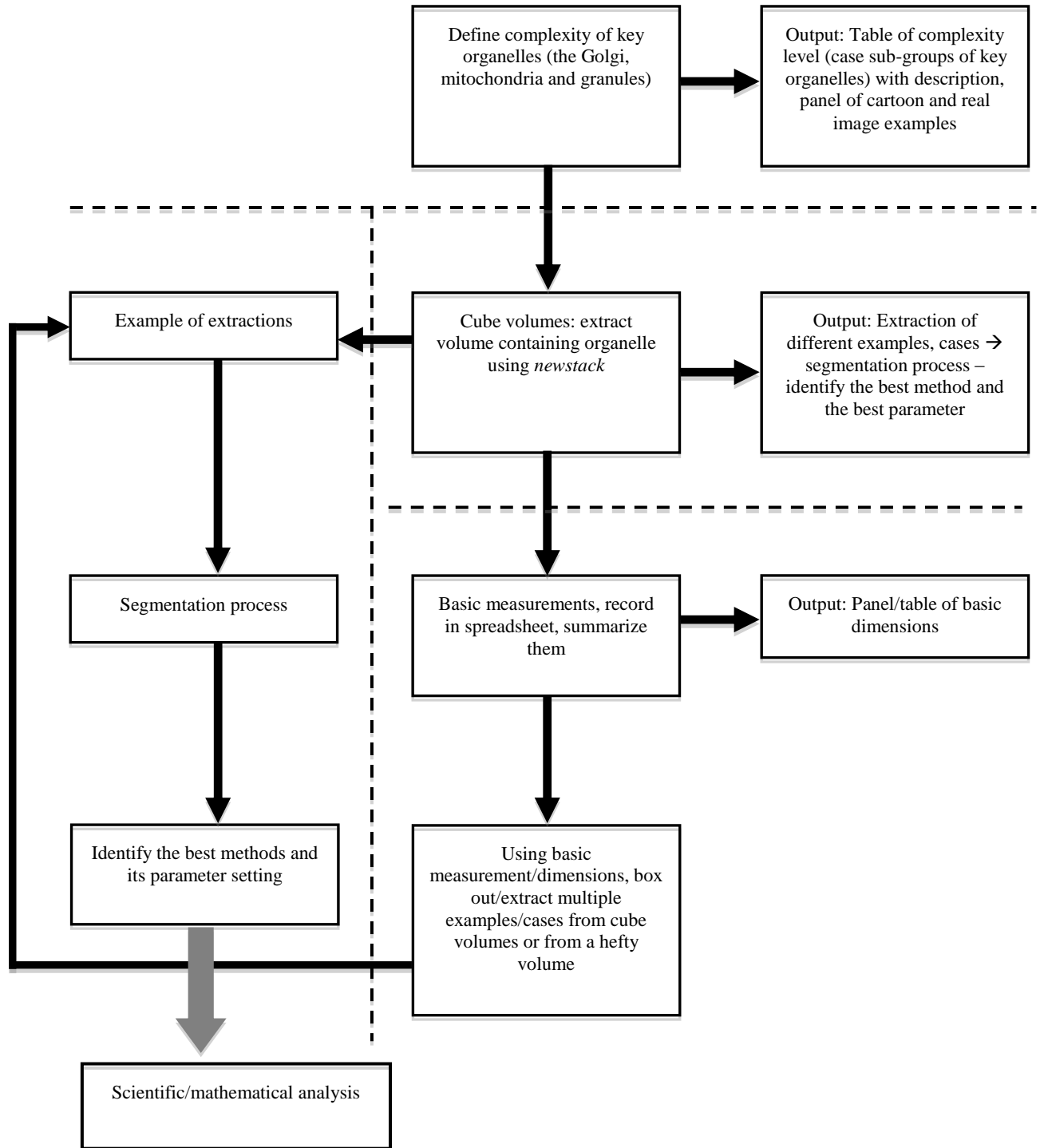


Figure 2.4 Flowchart showing the whole process of the research.

## **2.5 Quantitative 3D analysis and statistical analysis**

Membrane surface area and volumes were computed from the contours and triangular meshes using *IMOD* (Marsh et al., 2001a, Marsh et al., 2001b). The comparison between the results of automated segmentation and manual tracing was performed systematically using the approaches developed within this project. High-resolution figures were generated from the data many of which are included as supporting materials for **Chapter 3**, **Chapter 4** and **Chapter 5** of this thesis. Images of tomogram slices and 3D meshes of cellular data were all recorded using the *3dmod* and/or *ModelView* window of *IMOD*.





**Chapter 3    PARAMETER OPTIMISATION FOR CELLULAR  
TOMOGRAPHY SEGMENTATION: A SYSTEMATIC AND RELIABLE  
PROCEDURE TOWARDS AN AUTOMATIC TARGET-SCORING  
SYSTEM**

---



### **3.1 Introduction**

Image segmentation is defined as the mathematical process of separating or partitioning a digital image of an object (e.g. an organelle) from a larger, more complex image dataset into multiple ‘segments’ (i.e. sets of pixels) of non-overlapping, adjacent regions. These segments have some basic visual characteristic in common (i.e. intensity, colour, texture) (Pal and Pal, 1993, Volkmann, 2002) which when accurately defined, can provide a meaningful yet simplified representation of the information within the original image. Segmentation is thus a crucial step in defining basic structural features of cells and sub-cellular compartments, prior to quantitative analysis and annotation of complex cellular images.

Manual tracing is most widely used for segmenting complex structure resolved by electron tomography. Typically users experienced in the cellular and/or biological processes of interest must analyse each tomogram before the objects of interest (OOI) can be properly segmented. Dedicated software packages that provide manual contour drawing tools for biological image analysis include *IMOD* (Kremer et al., 1996) and *TomoJ* (Messaoudii et al., 2007). Familiarisation with the visual heuristics of the tomographic image data, aids the expert in recognising cell organelles, thereby enabling them to carefully draw the contour lines defining each organelle boundary. The drawing process is then repeated on each adjacent slice of objects in the tomograms across every slice spanned in Z. A set of contours for each object are created prior to generating a continuous 3D surface where the triangular/polygonal meshes between adjacent contours belonging to the same surface are matched. The meshing process is carried out on each organelle to produce a high fidelity 3D model to describe the spatial and structural organisation of compartments and other structures within a cellular region, and to compute precise quantitative data (Noske, 2010).

The drawback of manual segmentation of large cellular tomograms is that it is very labour intensive. As reported in (Marsh et al., 2001b) a tomogram estimated to represent just 1% of the total volume of a mammalian cell required approximately 3600 h (9-12 months) to completely segment manually at the organelle level. Furthermore differences in criteria applied by different experts/users can lead to differences in volume estimation of some cellular tomogram regions. The highest consistency and sensitivity of manual tracing is therefore achieved when a single individual traces the entire dataset. Achieving consistency in tracing such complex structures is also

painstaking for the expert and time consuming. For these reasons, computational procedures for segmenting and quantifying the organelles have attracted considerable interest.

Segmentation of high-throughput cellular datasets, using a ‘one size fits all’ fully automated segmentation algorithm is complicated by the inherent structural diversity within various cellular compartments. Furthermore to achieve accurate 3D models of organelles for visualisation and/or annotation purposes, particularly for complex organelle structures, the performance of fully automated segmentation algorithms (i.e. that use ‘one standard parameter setting’ or parameter free algorithm) may highly depends on post-processing. Post-processing at the final stage of organelle segmentation is always time consuming and less consistent in terms of accuracy (Fernandez, 2009, Lebbink et al., 2007, Winkler, 2002).

The problems of manual and fully automated segmentation processes can be addressed through the development of semi-automated segmentation processes based on the careful definition of structural features of cellular compartments such as organelles.

The process of segmentation is greatly enhanced by first applying an image filter that ‘reduces the noise of inherently low signal: noise electron tomography data while preserving object edges. Several methods have been developed for reducing image noise either using general approaches such as image filters (e.g. rank filters, classical filters) or by focusing on a particular type(s) of noise (Narasimha et al., 2008). Many image filters have been developed to suppress background noise, such as low pass, Wavelet transforms and median filters (Gonzalez, 2002). Image filters that have been successfully applied on ET include median filters (Pratt, 1978, van der Heide et al., 2007), bilateral filter (Tomasi and Manduchi, 1998, Jiang et al., 2003, Pantelic et al., 2007, Pantelic et al., 2006, Ali et al., 2012) and diffusion-based filters (Perona and Malik, 1990). Nonetheless, the capability to suppress noise without blurring the high resolution details (the signal) remains the main challenge in image filtration processes and typically there it is a requirement to balance noise reduction with signal preservation.

The aim of this chapter is to design and develop a semi-automated workflow for cellular tomogram segmentation (CTS). The purpose of this workflow is to highlight feasible procedures for obtaining optimised settings for accurate organelle segmentation. Essentially a dataset containing sub-volumes representing Golgi apparatuses, mitochondria and insulin granules are classified into their

types and a range of pre-filters and edge detection methods tested with the aim of developing a more automated process of image segmentation based on the concept that the properties of images in a given subset class (e.g. organelle complexity) will be relatively similar. Performance of the workflow is evaluated by comparison to the manually-segmented reference set.

## **3.2 Materials and Methods**

### **3.2.1 Subject Data and Cell Tomography Reconstruction**

The procedures and approaches used to prepare 3D reconstructions of dual-axis tomography mammalian cell images were detailed in Chapter 2 of the thesis. *IMOD* software package (Kremer et al., 1996), developed and maintained by the Boulder Laboratory for 3D Electron Microscopy of Cells, was used for all of these procedures.

### **3.2.2 Organelle of Interest: Selection, Extraction and Manual Tracing**

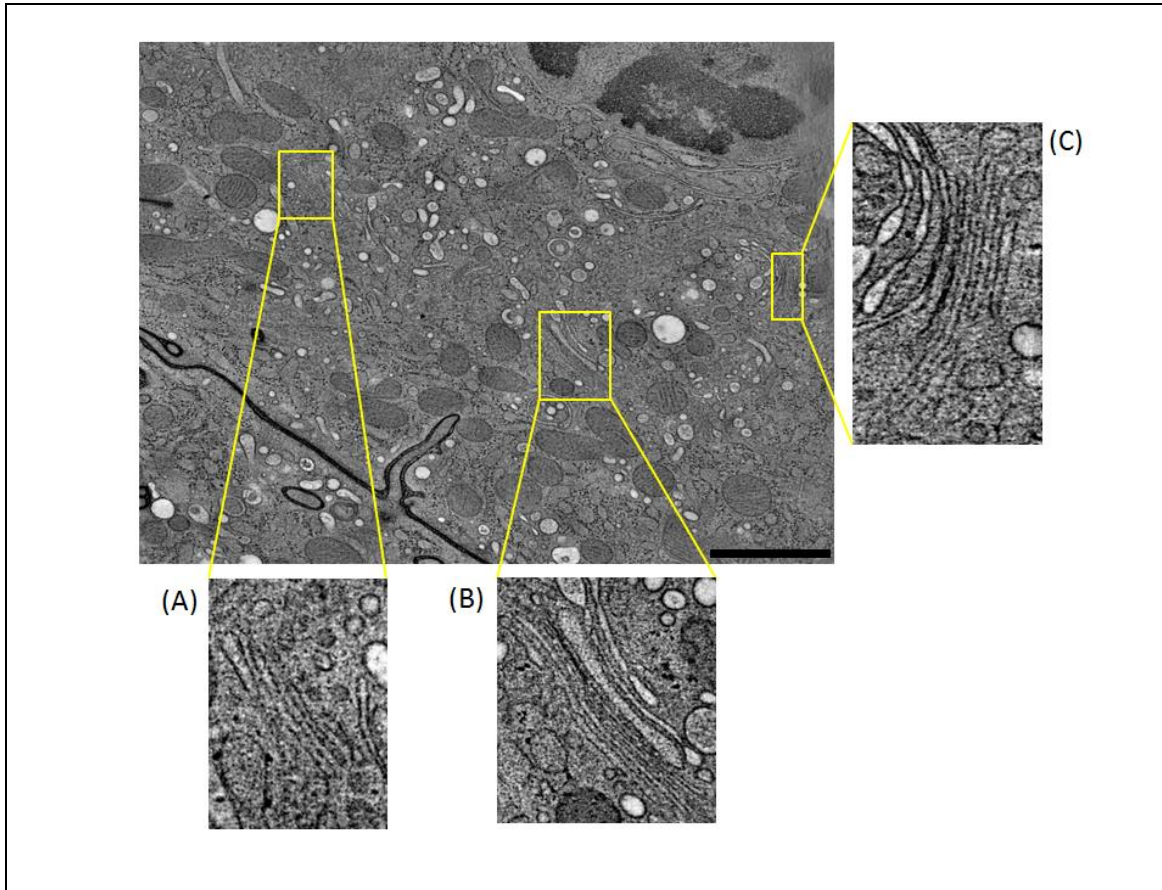
A normal human cell consists of a multitude of compartments with varying structure characteristics that depicted its individual function(s). Generally, these respective compartments can be divided into two main groups: 1) membrane-bound (e.g. the Golgi apparatus, mitochondria, insulin granules, vesicles) and 2) non-membrane-bound organelles (e.g. microtubules). Computational segmentation methodologies as discussed in **Section 3.1** are typically specified for membrane-bound organelles. Of these membrane-bound organelles, the Golgi apparatus (GA), mitochondria (MC) and insulin granules (IG) were selected due to their biological importance in the insulin secretion process (Olofsson et al., 2002, Srivastava and Goren, 2003, Wiederkehr and Wollheim, 2006, Maechler et al., 1997, D'Ambra et al., 1990, Jitrapakdee et al., 2010, Aspinwall, 1999). These key organelles have distinct, distinguishing image features and organelle structures (Noske et al., 2008, Emr et al., 2009, Marsh, 2005, Chen and Chan, 2009, Chan, 2006, Marsh et al., 2001a) which potentially make the segmentation technically challenging.

Cellular compartments were extracted using the ‘*newstack*’ function in *IMOD* and the organelle was boxed out as a set of 2D slices. The XYZ coordinates were then adjusted to the particular organelle. Multiple organelles of interest could also be extracted using the ‘*boxstartend*’ function in *IMOD*. In

the example (**Figure 3.1**), multiple Golgi stacks with a range of sizes were manually selected and marked (draw box for X and Y values using *toggle* function and determine the number of slices for Z value). These values (X, Y and Z) were copied into the *boxstartend* command in *IMOD* for multiple extractions. Each of these sub-volumes was saved into a separate file. These sub-volumes were then classified into their organelle type (i.e. the Golgi apparatus, mitochondria and insulin granules). The membranes of the organelles were manually traced in order to obtain a control contour dataset. Manual tracing of the cell organelles was performed using *IMOD* Package Tools (Kremer et al., 1996) in native space.

### 3.2.3 Development of the CTS pipeline for accurate segmentation

To design and develop the CTS pipeline, a series of studies were conducted on nine image pre-filtering methods (Gaussian filter, Minimum filter, Maximum filter, 2D Median filter, 3D Median filter, Meanshift filter, Kuwahara filter, Non-linear Anisotropic Diffusion (NAD) filter and Bilateral filter) and two segmentation algorithms (*Watershed* algorithm and *Snake* algorithm) to evaluate their benefits and limitations for the proposed study. Detailed information of each of these methods was discussed in **Chapter 1, Section 1.3**. Based on these results the CTS pipeline/workflow was developed and the performance of this validated against the manual tracing method.



**Figure 3.1 An example of selection and extraction process for multiple GA from the same tomogram.**

These three Golgi apparatus structures represent different volume sizes and varied morphologically and structurally. The value of XYZ dimensions of each of these Golgi apparatus structures was manually inserted in the '*newstack*' command in *IMOD* prior to extraction process. (A) XYZ: 155 nm x 283 nm x 410 nm. (B) XYZ: 255 nm x 290 nm x 421 nm. (C) XYZ: 149 nm x 310 nm x 690 nm. Scale bar: 400 nm.



### 3.3 Designing a workflow for cellular tomography segmentation

#### 3.3.1 Dataset preparation

##### 3.3.1.1 Sub-volume extraction of three key organelles of insulin secretion; the Golgi apparatus (GA), mitochondria (MC) and insulin granules (IG)

More than 400 sub-volumes were extracted from the large tomograms collected within the Marsh group at IMB. These represented the Golgi apparatus (75 extracts), mitochondria (191 extracts) and insulin granules (157 extracts). Image properties - namely sub-volume location within the raw tomogram, sub-volume dimension (i.e. XYZ), minimum density, maximum density, mean density and pixel spacing (angstrom unit) - were retrieved and saved simultaneously (**Table 3.1**). Measurements in 2D and 3D (volume) were as standard converted from pixels and voxels to nanometre (nm).

**Table 3.1 Summary of sub-volume datasets comprised of the Golgi apparatus, mitochondria and insulin granules.**

Key organelles	Number of extracts	Minimum	Maximum	Pixel spacing (nm)
GA	75	X: 170 nm Y: 188 nm Z: 185 nm	X: 1200 nm Y: 1200 nm Z: 1100 nm	2.144
MC	191	X: 120 nm Y: 195 nm Z: 185 nm	X: 1500 nm Y: 1500 nm Z: 1500 nm	2.144
IG	157	X: 120 nm Y: 142 nm Z: 110 nm	X: 588 nm Y: 600 nm Z: 570 nm	2.144

##### 3.3.1.2 Manual segmentation

Manual segmentation is usually considered the best and possibly the only practical approach for segmenting organelle contours of heavily noise contaminated cellular tomograms (Noske et al., 2008), and hence was used to establish a reference set (or control dataset) to validate the performance of computational workflow segmentation results. For this purpose, organelle membranes were manually traced to produce sets of contours using the *drawing tools* in *IMOD*. Sets of contours of every sub-volume were then modelled (using *imodauto* function in *IMOD*) and meshed (using *imodmesh* function in *IMOD*).

Tracing time varied between sub-volumes depending on the organelle type, ‘complexity’ of membrane shapes and number of membrane contours per image slice (**Table 3.2**). The Golgi apparatus (GA) frequently had about 5 to 7 cisternum per cisternae stack for the simpler, unbranched Golgi, or 5 to 13 cisternum contours on each slice given that some of the stack have ‘broken/branching’ cisternae. The cisternae membranes were also different in shape and size. Therefore, amongst these key organelles, the GA recorded the highest total number of contours (NOC). Commensurate with the substantial difference between the NOC for the GA and the other two organelles (i.e. MC and IG), segmenting of the Golgi cisternae accounted for almost 70% of the total time of manual contour drawing of more than 400 sub-volumes.

Table 3.2 Summary of processing time for conventional tracing of each of key organelle.

GA: Golgi apparatus; MC: Mitochondria; IG: Insulin granules; NOC: Number of contours.

	GA	MC	IG
Total extracts	75	191	157
Averaged number of image slice	~200	~150	~150
Total number of image slices (z)	15053	29657	24552
Total NOC	195789	35589	24552
Mean NOC of each slice	~13	~1.2	~1
Total tracing time per organelle type	~180 h / ~10800 min	~120 h / ~7200 min	~70 h / ~4200 min
Mean total tracing time per sub-volume	~144 min (69%)	~38 min (18%)	~27 min (13%)

### 3.3.2 Segmentation approaches

#### 3.3.2.1 Processed image for accurate contour tracing

Pre-filtering is an effective way to de-noise the images prior to segmentation – in particular 2D image filters such as median filter and non-linear anisotropic diffusion filter (Narasimha et al., 2008). Based on previous reports (**Chapter 1, Section 1.3.2**), nine noise reduction pre-filters were chosen. These were Gaussian filter (**Section 1.3.2.1**), Minimum filter, Maximum filter, 2D Median filter, 3D Median filter, Meanshift filter, Kuwahara filter (**Section 1.3.2.3**), Non-linear anisotropic diffusion (NAD) filter (**Section 3.1.2.4**) and Bilateral filter (**Section 1.3.2.5**). These nine selected image filters were classified into two primary groups; classical and complex noise reduction (**Table 3.3**).

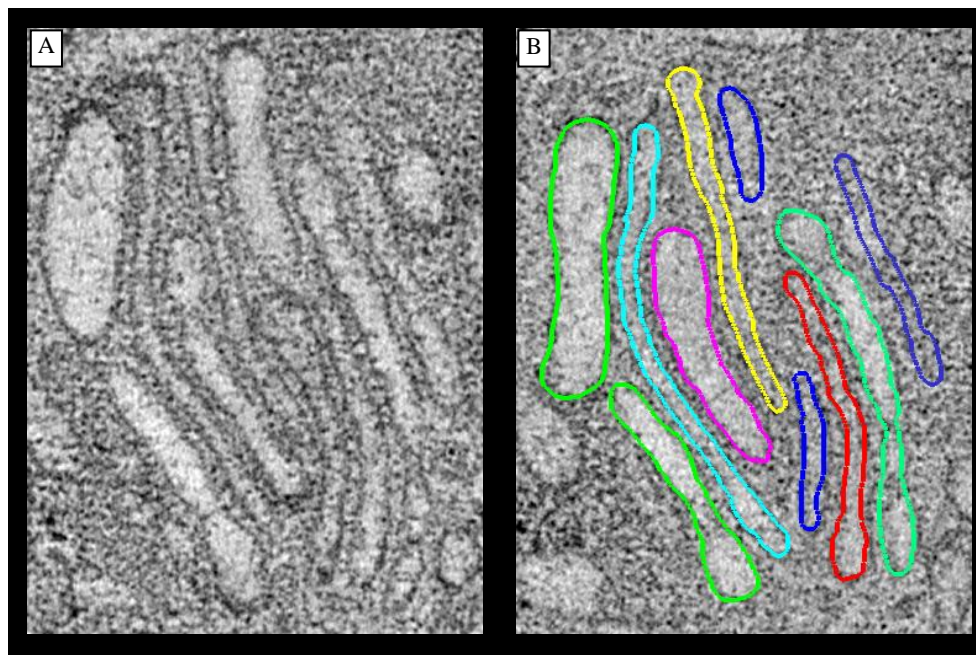
**Table 3.3 Nine pre-filtering approaches and their respective initial settings (i.e. proposed by the software/method developer).** These proposed settings are the settings used for initial experiment prior to pre-filtering optimisation.

	Image filter (name)	Filter group i.e. Classical, Complex (Rank, diffusion-based, or bilateral filter )	Software Package	Reported optimal parameter setting (initial settings)
F1	Gaussian filter	Example for classical filter	<i>ImageJ</i>	Sigma (radius): 2
F2	Minimum filter	Simplest example for <b>rank filter</b>	<i>ImageJ</i>	Radius: 2 pixels
F3	Maximum filter	Simplest example for <b>rank filter</b>	<i>ImageJ</i>	Radius: 2 pixels
F4	2D Median	<b>Rank filter</b> – Current findings show efficient result	<i>ImageJ</i>	Radius: 2 pixels
F5	3D Median	<b>Rank filter</b> – Current findings show efficient result	<i>CoAn</i>	Kernel size: 3x3x3 Iteration: 3
F6	Kuwahara filter	<b>(Rank filter)</b> Extension of mean filter (classical filter)	<i>ImageJ</i>	Kernel size: 5x5
F7	Meanshift filter	<b>(Rank filter)</b> Extension of mean filter (classical filter)	<i>ImageJ</i>	Spatial radius: 3 Color distance: 25.0
F8	NAD	Diffusion-based filter	<i>IMOD</i>	K value: 5.6 Iteration: 20
F9	Bilateral filter	Bilateral filtering	<i>BSoft</i>	SpaceSigma: 1.5 RangeSigma: 23.8

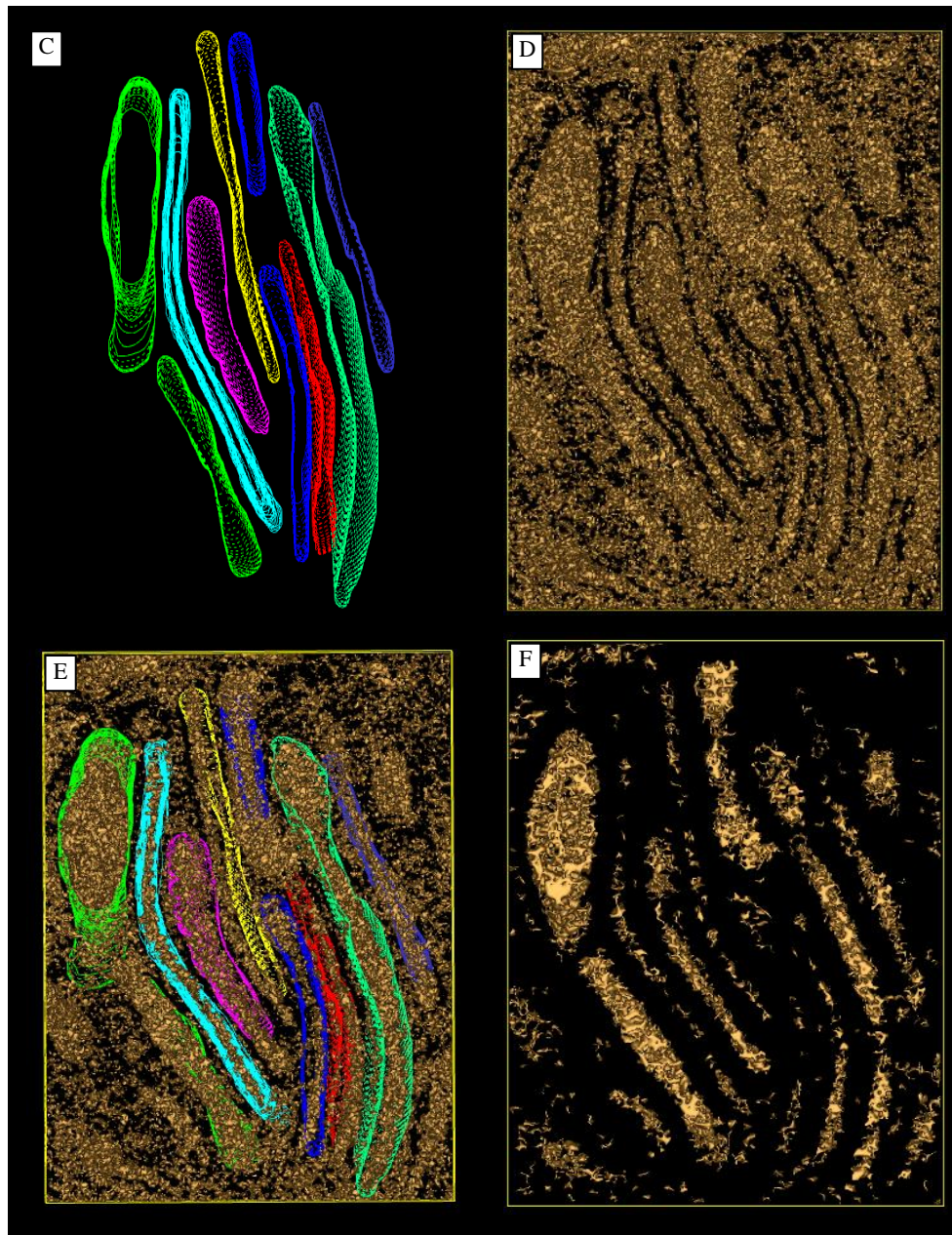
Based on the method descriptions, all of these image pre-filters could significantly improve the signal-to-noise ratios of these ET images prior to organelle segmentation, thereby improving the quality of the latter. The effectiveness of the denoising algorithms was expected to depend largely on the image characteristics. Consequently the pre-filter tests of all nine filters were individually run on all organelle types (i.e. the GA, MC and IG). In this experiment, the recommended parameter settings of respective image filters (see **Table 3.3**) were used. After the stacks of ET images were filtered, they were surface-rendered by automatically. Surface-rendered images were then compared to respective surface-renderings of the manually traced ground truth dataset. The comparison was made both visually (general rendering quality) and mathematically (i.e. deviation of the total surface area value from that of the manually traced control). Settings were adjusted until the surface area value was close to its respective ground truth dataset, without compromising its 3D representation (the targeted contour and structure of an organelle is comparable to manual tracing contour set). The results of this experiment are shown in **Figure 3.2 – Figure 3.5** (the Golgi apparatus), **Figure 3.6 – Figure 3.8** (mitochondrion) and **Figure 3.9 – Figure 3.11** (insulin granule).

### *The Golgi apparatus*

The ground truth dataset for the Golgi apparatus (GA) was the first to be evaluated. A stack comprising eight cisternae (**Figure 3.2 A**) was manually traced (**Figure 3.2 B**) using different colours to represent different cisternae (**Figure 3.3 C**). The manual process of tracing this dataset took about 30 min (1800 s). The total surface area value of the ground truth dataset for this example data is  $\sim 1.5 \times 10^5 \text{ nm}^2$ . The unprocessed GA was rendered (**Figure 3.3 D**). The visualisation of unprocessed data (**Figure 3.3 E**) took less than 20 s. However the process yielded a very high surface area value ( $\sim 10 \times 10^5 \text{ nm}^2$ ) of automated rendering (compared to manual set which was  $\sim 1.5 \times 10^5 \text{ nm}^2$ ) and the result was thus unacceptable. Next, the nine image filters were applied on the same (unprocessed/real) dataset (the GA volume) (**Figure 3.3 F**, **Figure 3.4 G-J** and **Figure 3.5 K-N**). Their settings were optimised manually in a systematic manner, i.e. by modifying one variable setting at a time. The optimisation process was halted when the surface area value reached the closest surface area value of the ground truth – while maintaining accurate 3D visualisation of the organelle structure, i.e. the eight cisternae.

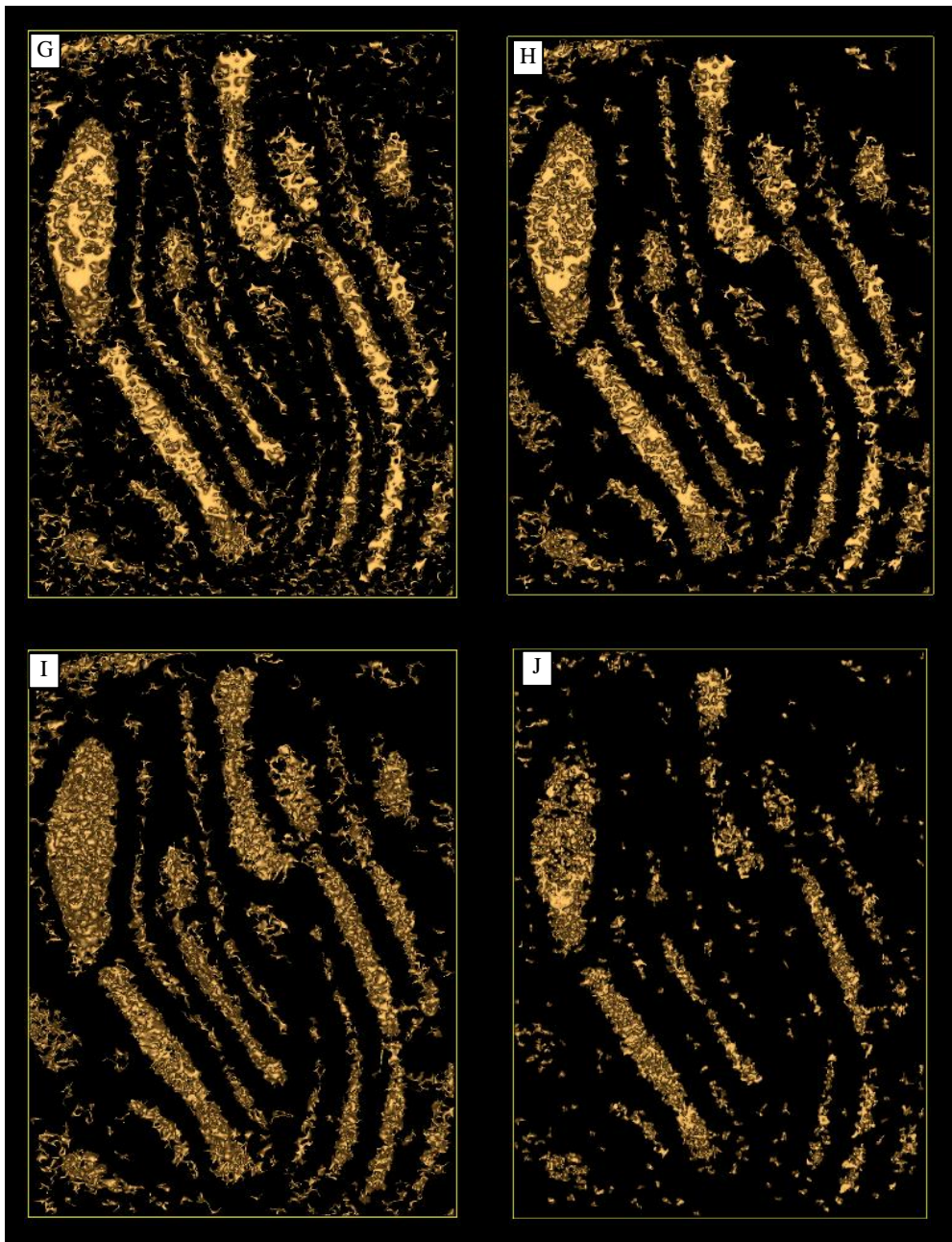


**Figure 3.2 Manual tracing of the Golgi apparatus from real electron tomogram.**  
 (A) A slice of real electron tomogram shows the Golgi apparatus. (B) Manual tracing of (A).



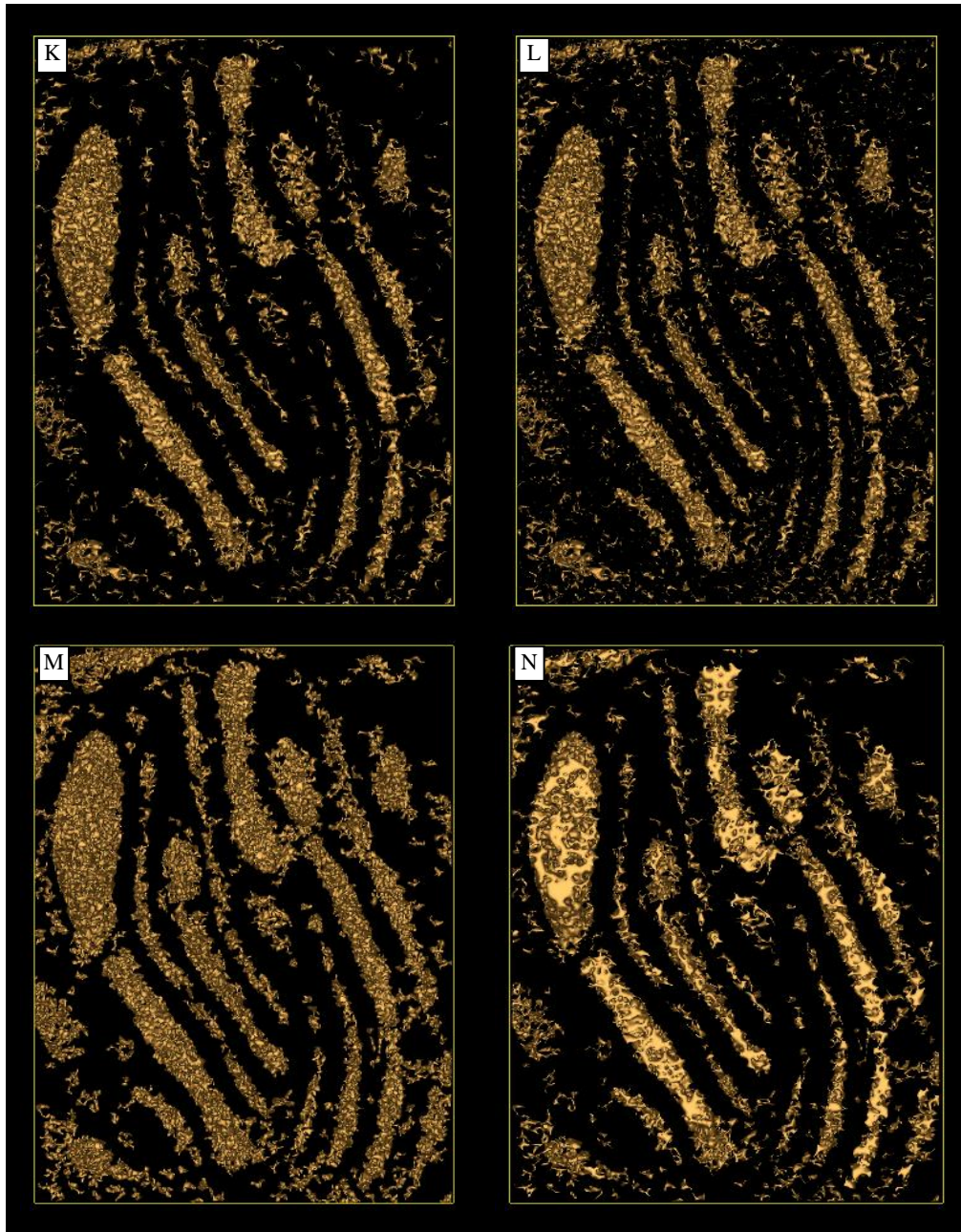
**Figure 3.3 (Continue from Figure 3.2) 3D surface-rendered models of optimised pre-processed image volume for the Golgi apparatus.**

(C) Set of contours of manual tracing, PT: 1800 s, SA:  $\sim 1.5 \times 10^5$  nm<sup>2</sup>. (D) Surface rendering of unprocessed image volume, PT: 15 s, SA:  $\sim 10 \times 10^5$  nm<sup>2</sup>. (E) Set of manually traced contours compared to surface-rendered models for unprocessed tomograms. Pre-filtered images using their respective initial settings, where (F) Gaussian filter, PT: 15 s, SA:  $\sim 6 \times 10^5$  nm<sup>2</sup>. **PT**: processing time; s: seconds; **SA**: surface area.



**Figure 3.4 (Continue from Figure 3.3) 3D surface-rendered models of optimised pre-processed image volume for the Golgi apparatus for Minimum, Maximum, 2D Median and 3D Median filter.**

(G)-(J) Pre-filtered images using their respective initial settings, where (G) Minimum filter, PT: 15 s, SA:  $\sim 6 \times 10^5$  nm<sup>2</sup>. (H) Maximum filter, PT: 15 s, SA:  $\sim 6 \times 10^5$  nm<sup>2</sup>. (I) 2D Median, PT: 15 s, SA:  $\sim 6 \times 10^5$  nm<sup>2</sup>. (J) 3D Median, PT: 15 s, SA:  $\sim 6 \times 10^5$  nm<sup>2</sup>. PT: processing time; s: seconds; SA: surface area.

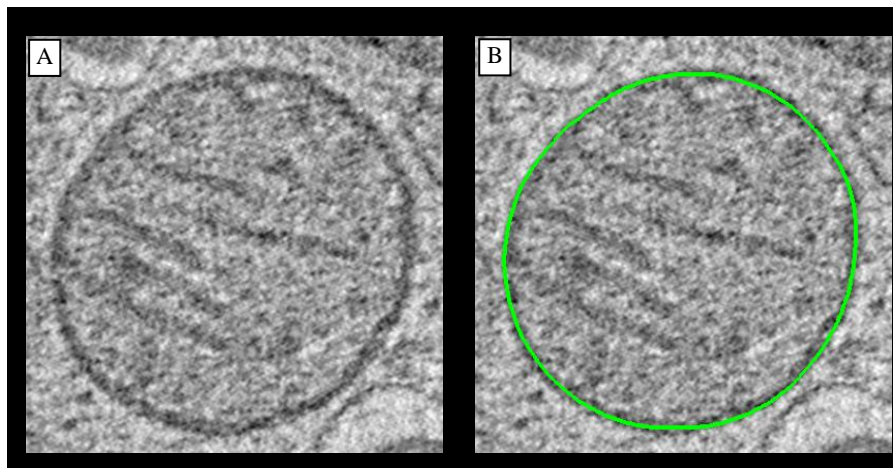


**Figure 3.5 (Continue from Figure 3.4) 3D surface-rendered models of optimised pre-processed image volume for the Golgi apparatus.**

(K)-(N) Pre-filtered images using their respective initial settings, where (K) Kuwahara filter, PT: 15 s, SA:  $\sim 6 \times 10^5$  nm<sup>2</sup>. (L) Meanshift filter, PT: 15 s, SA:  $\sim 6 \times 10^5$  nm<sup>2</sup>. (M) NAD, PT: 15 s, SA:  $\sim 6 \times 10^5$  nm<sup>2</sup>. (N) Bilateral filter. PT: 15 s, SA:  $\sim 6 \times 10^5$  nm<sup>2</sup>. **PT**: processing time; s: seconds; **SA**: surface area.

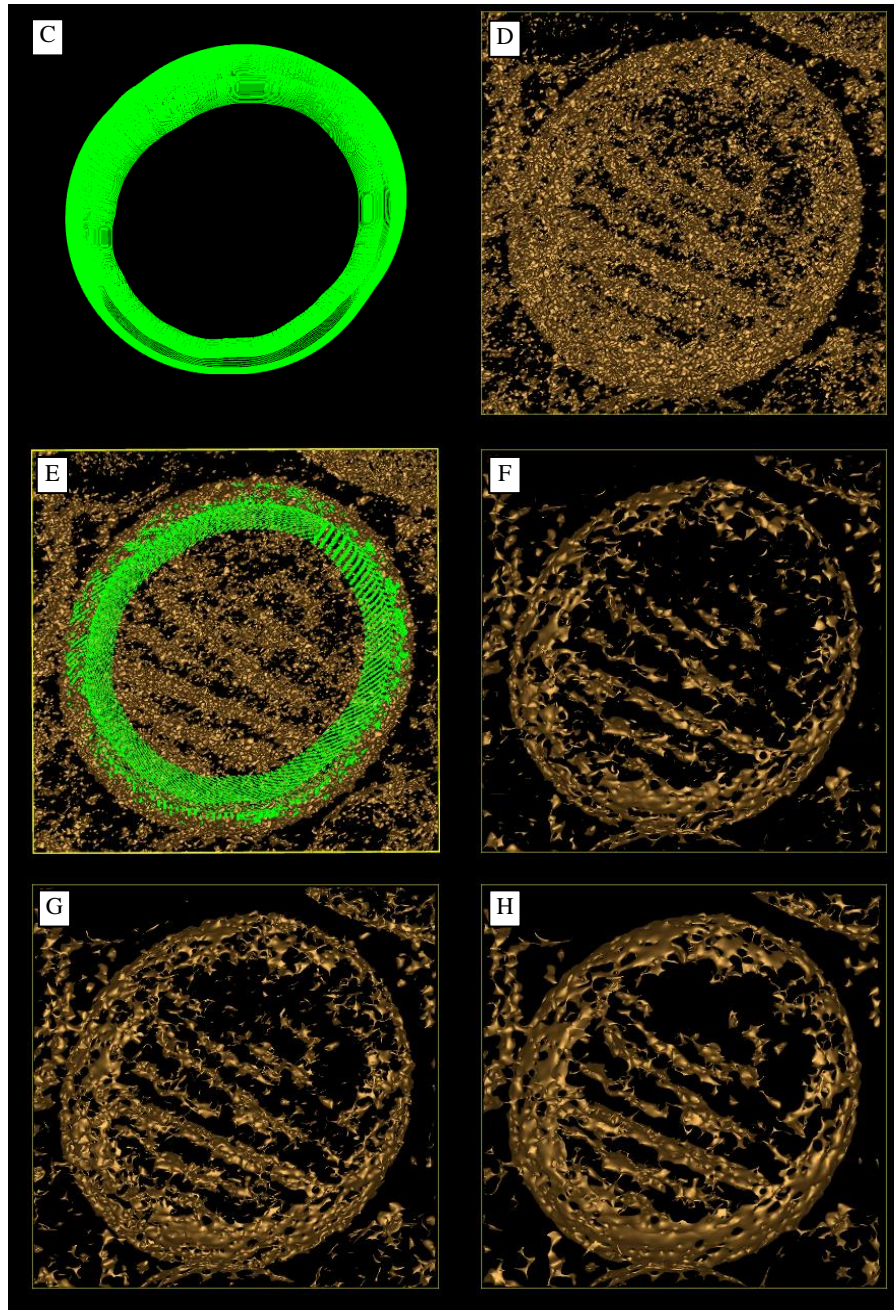
### *Mitochondria*

The outer membrane of a mitochondrion (**Figure 3.6 A**) was manually traced (**Figure 3.6 B**) to yield the contoured (**Figure 3.7 C**) and automatically rendered image (**Figure 3.7 D**). Details on the mitochondria specific of focused membrane are represented in Chapter 2 of the thesis. The manual tracing process for this dataset took about 10 min (600 s) and yielded the ground truth dataset of  $\sim 5 \times 10^4$  nm<sup>2</sup>. The background noise and the cristae matrix within the inner membrane of mitochondrion affected the surface-rendering of the unprocessed MC (**Figure 3.7 E**). The processing time of this automated rendering took about 8 s but again yielded a very high surface area value ( $\sim 6 \times 10^5$  nm<sup>2</sup>) compared to manual set. The nine image filters were applied on the same (unprocessed/real) dataset (the MC volume) (**Figure 3.7 F-H** and **Figure 3.8 I-N**). The post-processing, i.e. the extra separated contours were removed, was done to encounter the problem of unwanted contours from the mesh – particularly the cristae and inner membrane. Their settings were manually optimised in the same manner as used for the Golgi apparatus. Contours with +/- surface area value of manual tracing would stay.



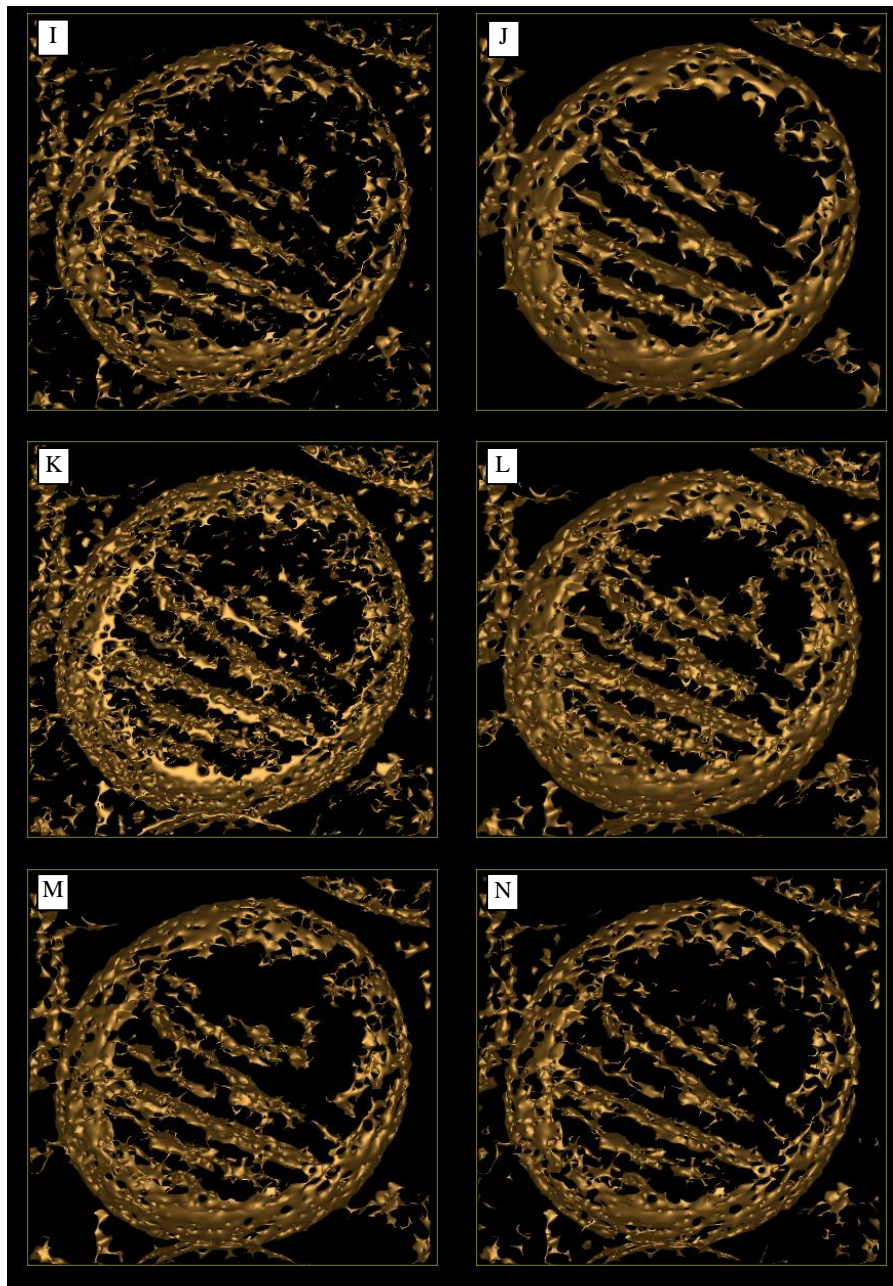
**Figure 3.6 Manual tracing of mitochondrion from real electron tomogram.**  
 (A) A slice of real electron tomogram shows mitochondrion. (B) Manual tracing of (A).





**Figure 3.7 (Continue from Figure 3.6) 3D surface-rendered models of optimised pre-processed image volume for mitochondrion.**

(C) Set of contours of manual tracing, PT: 600 s, SA:  $\sim 5 \times 10^4$  nm<sup>2</sup>. (D) Surface rendering of unprocessed image volume, PT: 8 s, SA:  $\sim 5 \times 10^5$  nm<sup>2</sup>. (E) Set of manually traced contours compared to surface-rendered models obtained for unprocessed tomograms. (F)-(H) Pre-filtered images using their respective initial settings, where (F) Gaussian filter, PT: 8 s, SA:  $\sim 2 \times 10^5$  nm<sup>2</sup>. (G) Minimum filter, PT: 8 s, SA:  $\sim 2 \times 10^5$  nm<sup>2</sup>. (H) Maximum filter, PT: 8 s, SA:  $\sim 2 \times 10^5$  nm<sup>2</sup>. **PT**: processing time. **SA**: surface area.

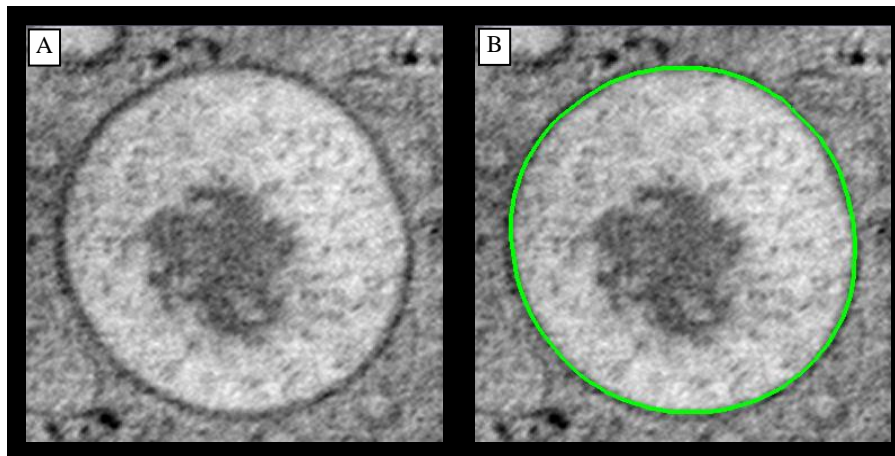


**Figure 3.8 (Continue from Figure 3.7) 3D surface-rendered models of optimised pre-processed image volume for mitochondrion.**

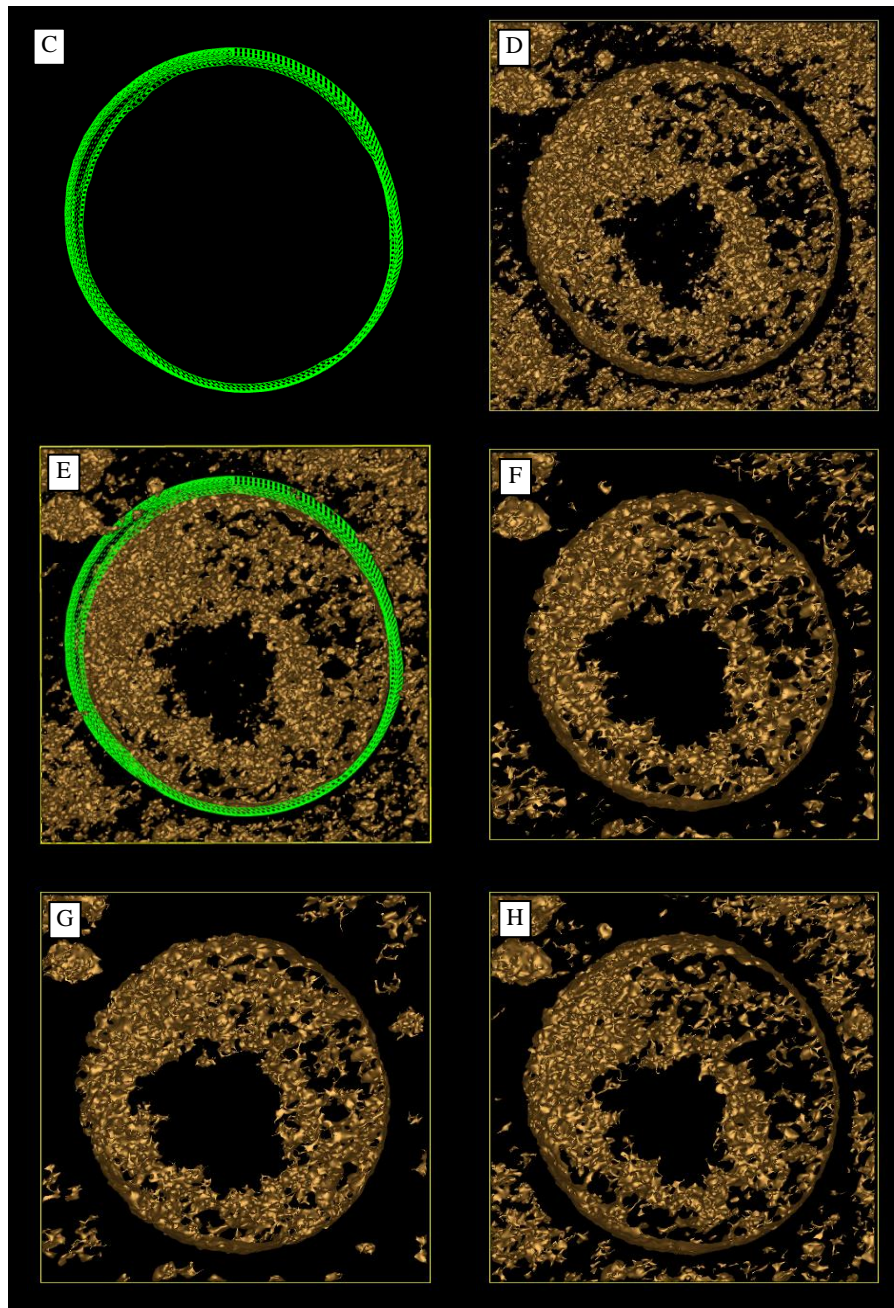
(I)-(N) Pre-filtered images using their respective initial settings, where (I) 2D Median, PT: 8 s, SA:  $\sim 2 \times 10^5$  nm<sup>2</sup>. (J) 3D Median, PT: 8 s, SA:  $\sim 2 \times 10^5$  nm<sup>2</sup>. (K) Kuwahara filter, PT: 8 s, SA:  $\sim 2 \times 10^5$  nm<sup>2</sup>. (L) Meanshift filter, PT: 8 s, SA:  $\sim 2 \times 10^5$  nm<sup>2</sup>. (M) NAD, PT: 8 s, SA:  $\sim 2 \times 10^5$  nm<sup>2</sup>. (N) Bilateral filter. PT: 8 s, SA:  $\sim 2 \times 10^5$  nm<sup>2</sup>. **PT**: processing time. **SA**: surface area.

***Insulin granules***

The membrane of an insulin granule (**Figure 3.9 A**) was manually traced (**Figure 3.9 B**) to yield the contoured (**Figure 3.10 C**) and automatically rendered image (**Figure 3.10 D**). The manual tracing process took about 10 min (600 s). The total surface area value of manual tracing for this example of insulin granule data was  $\sim 5 \times 10^4 \text{ nm}^2$ . The unprocessed IG was rendered (**Figure 3.10 E**). The processing time of automated surface rendering is only 8 s. The unprocessed surface-rendered data recorded  $\sim 5 \times 10^5 \text{ nm}^2$  of surface area – this made the result unacceptable. Accordingly, the nine image filters were applied on the same (unprocessed/real) dataset (the IG volume) (**Figure 3.10 F-H** and **Figure 3.11 I-N**). Their settings were manually optimised. As for the preceding test, the optimisation process was halted when it reached the closest value of surface area to the ground truth – while maintaining its 3D visualisation of the IG structure. The surface area values (pixels) of optimised-filtered image volumes were recorded, respectively.

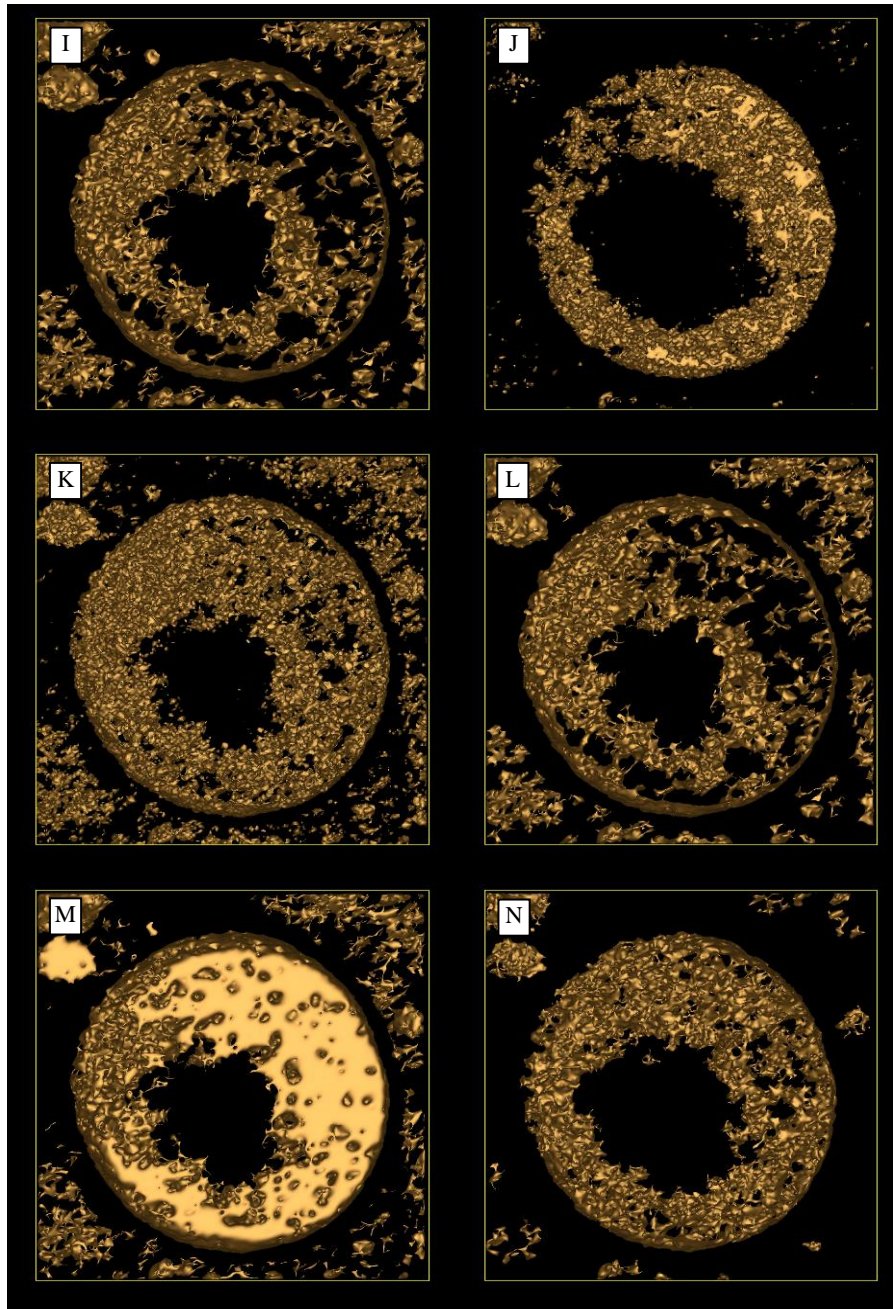


**Figure 3.9 Manual tracing of insulin granule from real electron tomogram.**  
 (A) A slice of real electron tomogram shows insulin granule. (B) Manual tracing of (A).



**Figure 3.10 (Continue from Figure 3.9) 3D surface-rendered models of optimised pre-processed image volume for insulin granule.**

(C) Set of contours of manual tracing, PT: 600 s, SA:  $\sim 5 \times 10^4 \text{ nm}^2$ . (D) Surface rendering of unprocessed image volume, PT: 8 s, SA:  $\sim 5 \times 10^5 \text{ nm}^2$ . (E) Set of manually traced contours compared to surface-rendered models obtained for unprocessed tomograms. (F)-(H) Pre-filtered images using their respective initial settings, where (F) Gaussian filter, PT: 8 s, SA:  $\sim 2 \times 10^5 \text{ nm}^2$ . (G) Minimum filter, PT: 8 s, SA:  $\sim 2 \times 10^5 \text{ nm}^2$ . (H) Maximum filter, PT: 8 s, SA:  $\sim 2 \times 10^5 \text{ nm}^2$ . **PT**: processing time. **SA**: surface area.



**Figure 3.11 (Continue from Figure 3.10) 3D surface-rendered models of optimised pre-processed image volume for the insulin granule.**

(I)-(N) Pre-filtered images using their respective initial settings, where (I) 2D Median, PT: 8 s, SA:  $\sim 2 \times 10^5$  nm<sup>2</sup>. (J) 3D Median, PT: 8 s, SA:  $\sim 2 \times 10^5$  nm<sup>2</sup>. (K) Kuwahara filter, PT: 8 s, SA:  $\sim 2 \times 10^5$  nm<sup>2</sup>. (L) Meanshift filter, PT: 8 s, SA:  $\sim 2 \times 10^5$  nm<sup>2</sup>. (M) NAD, PT: 8 s, SA:  $\sim 2 \times 10^5$  nm<sup>2</sup>. (N) Bilateral filter. PT: 8 s, SA:  $\sim 2 \times 10^5$  nm<sup>2</sup>. PT: processing time. SA: surface area.

**Processing time manual segmentation vs. automated surface rendered of filtered images**

Even though the 3D visualisation of the surface-renderings shown in **Figure 3.2** until **Figure 3.11** were not so accurate, mathematically and visually, as the results of manual tracing, the processing time of each of these computational approaches (shown in **Table 3.4**) achieved significant reduction. Each of the approaches (F1 – F9) for the Golgi apparatus achieved a 99% reduction in processing time, while mitochondria and insulin granules achieved ~ 98% reduction. Overall, each approach recorded only 93 s to process all nine sub-volumes.

**Table 3.4 Comparison of processing time between manual tracing and processed images (followed by automated surface rendering) and comparison of surface area value between manual tracing and proposed approaches for each organelle sub-volume.**

Processing time is calculated in seconds (s) and surface area is calculated in  $10^3 \text{ nm}^2$ . **Man** is referred to manual segmentation. There are three sub-volumes of each organelle type, the Golgi apparatus (GA), mitochondria (MC) and insulin granules (IG). **F1**: Gaussian filter and automated surface rendering. **F2**: Minimum filter followed by automated surface rendering. **F3**: Maximum filter followed by automated surface rendering. **F4**: 2D median filter followed by automated surface rendering. **F5**: 3D Median filter followed by automated surface rendering. **F6**: Kuwahara filter followed by automated surface rendering. **F7**: Meanshift filter followed by automated surface rendering. **F8**: NAD filter followed by automated surface rendering. **F9**: Bilateral filter followed by automated surface rendering.

	Man	F1	F2	F3	F4	F5	F6	F7	F8	F9
<b>GA1</b>										
s	1500	15	15	15	15	15	15	15	15	15
nm <sup>2</sup>	~1.5x10 <sup>5</sup>	~6x10 <sup>5</sup>	~6x10 <sup>5</sup>	~6x10 <sup>5</sup>	~6x10 <sup>5</sup>	~6x10 <sup>5</sup>	~6x10 <sup>5</sup>	~6x10 <sup>5</sup>	~6x10 <sup>5</sup>	~6x10 <sup>5</sup>
<b>GA2</b>										
s	1800	15	15	15	15	15	15	15	15	15
nm <sup>2</sup>	~1.6x10 <sup>5</sup>	~6x10 <sup>5</sup>	~6x10 <sup>5</sup>	~6x10 <sup>5</sup>	~6x10 <sup>5</sup>	~6x10 <sup>5</sup>	~6x10 <sup>5</sup>	~6x10 <sup>5</sup>	~6x10 <sup>5</sup>	~6x10 <sup>5</sup>
<b>GA3</b>										
s	1800	15	15	15	15	15	15	15	15	15
nm <sup>2</sup>	~1.6x10 <sup>5</sup>	~6x10 <sup>5</sup>	~6x10 <sup>5</sup>	~6x10 <sup>5</sup>	~6x10 <sup>5</sup>	~6x10 <sup>5</sup>	~6x10 <sup>5</sup>	~6x10 <sup>5</sup>	~6x10 <sup>5</sup>	~6x10 <sup>5</sup>
Total (s)	5100 s	45 s	45 s	45 s	45 s	45 s	45 s	45 s	45 s	45 s
<b>MC1</b>										
s	600	8	8	8	8	8	8	8	8	8
nm <sup>2</sup>	~5x10 <sup>4</sup>	~2x10 <sup>5</sup>	~2x10 <sup>5</sup>	~2x10 <sup>5</sup>	~2x10 <sup>5</sup>	~2x10 <sup>5</sup>	~2x10 <sup>5</sup>	~2x10 <sup>5</sup>	~2x10 <sup>5</sup>	~2x10 <sup>5</sup>
<b>MC2</b>										
s	750	8	8	8	8	8	8	8	8	8
nm <sup>2</sup>	~5x10 <sup>4</sup>	~2x10 <sup>5</sup>	~2x10 <sup>5</sup>	~2x10 <sup>5</sup>	~2x10 <sup>5</sup>	~2x10 <sup>5</sup>	~2x10 <sup>5</sup>	~2x10 <sup>5</sup>	~2x10 <sup>5</sup>	~2x10 <sup>5</sup>
<b>MC3</b>										
s	750	8	8	8	8	8	8	8	8	8
nm <sup>2</sup>	~5x10 <sup>4</sup>	~2x10 <sup>5</sup>	~2x10 <sup>5</sup>	~2x10 <sup>5</sup>	~2x10 <sup>5</sup>	~2x10 <sup>5</sup>	~2x10 <sup>5</sup>	~2x10 <sup>5</sup>	~2x10 <sup>5</sup>	~2x10 <sup>5</sup>
Total (s)	2100 s	24 s	24 s	24 s	24 s	24 s	24 s	24 s	24 s	24 s
<b>IG1</b>										
s	600	8	8	8	8	8	8	8	8	8
nm <sup>2</sup>	~5x10 <sup>4</sup>	~2x10 <sup>5</sup>	~2x10 <sup>5</sup>	~2x10 <sup>5</sup>	~2x10 <sup>5</sup>	~2x10 <sup>5</sup>	~2x10 <sup>5</sup>	~2x10 <sup>5</sup>	~2x10 <sup>5</sup>	~2x10 <sup>5</sup>
<b>IG2</b>										
s	750	8	8	8	8	8	8	8	8	8
nm <sup>2</sup>	~5x10 <sup>4</sup>	~2x10 <sup>5</sup>	~2x10 <sup>5</sup>	~2x10 <sup>5</sup>	~2x10 <sup>5</sup>	~2x10 <sup>5</sup>	~2x10 <sup>5</sup>	~2x10 <sup>5</sup>	~2x10 <sup>5</sup>	~2x10 <sup>5</sup>
<b>IG3</b>										
s	750	8	8	8	8	8	8	8	8	8
nm <sup>2</sup>	~5x10 <sup>4</sup>	~2x10 <sup>5</sup>	~2x10 <sup>5</sup>	~2x10 <sup>5</sup>	~2x10 <sup>5</sup>	~2x10 <sup>5</sup>	~2x10 <sup>5</sup>	~2x10 <sup>5</sup>	~2x10 <sup>5</sup>	~2x10 <sup>5</sup>
Total (s)	2100 s	24 s	24 s	24 s	24 s	24 s	24 s	24 s	24 s	24 s
Grand Total	9300 s	93 s	93 s	93 s	93 s	93 s	93 s	93 s	93 s	93 s

Using optimised settings for all nine image filtrations approaches a significant improvement in processing speed was achieved for the GA, MC and IG, as expected. While basic structures of targeted organelles were visually preserved, in many cases non-specific rendering was also seen and this influenced the accuracy of final 3D visualisation of targeted membrane organelle. Thus, technically to produce more accurately traced contours, accurate tracing algorithms are also important. Two segmentation algorithms were chosen; the *snake* algorithm (boundary-based approach) (Kass et al., 1988, Nguyen and Ji, 2008) and the *watershed transform* algorithm (region-based approach) (Volkman, 2002). Both were tested on all nine pre-filtered images to evaluate their performance.

### 3.3.2.2 *Boundary-based versus region-based segmentations*

The processing time of all combinations of pre-filtering and edge detection (18 in total; 9x2) were compared to their respective manual ground truth sets (**Table 3.5**). The sub-volumes were processed with optimised settings for each of the nine image filters before initiating the boundary-based (*snakes* segmentation) and region-based (*watershed* segmentation) algorithms.

#### *Snakes (S)*

Semi-automated active contours known as *snakes* (Andrey and Boudier, 2006) require an initial contour to be drawn on every image slice prior to contour segmentation. This initial contour evolves continuously according to the number of iterations (*snakes* parameter). Selecting the right number of iteration is crucial as it limits the rigidity of the *snakes* during evolution towards an image contour. However, besides the importance of iteration number, initial contour(s) should be carefully depicted as close as possible to the actual organelle membranes to facilitate the evolution of active contour. The *snakes* approach has shown its potential in extracting complex object contours including from biological specimens (Andrey and Boudier, 2006). Even though the *snakes* remain a continuous contour, and no ‘unwanted’ objects are segmented (because only the targeted object is selected to be traced), *snakes* can be prone to errors related to the initial contour, and/or inappropriate parameters (i.e. iteration number) that could lead to over- or under-segmentation. Furthermore like all edge detection algorithms, *snakes* are susceptible to noisy edges and/or broken edges (**Figure 3.12**).

#### *Watershed algorithm (W)*

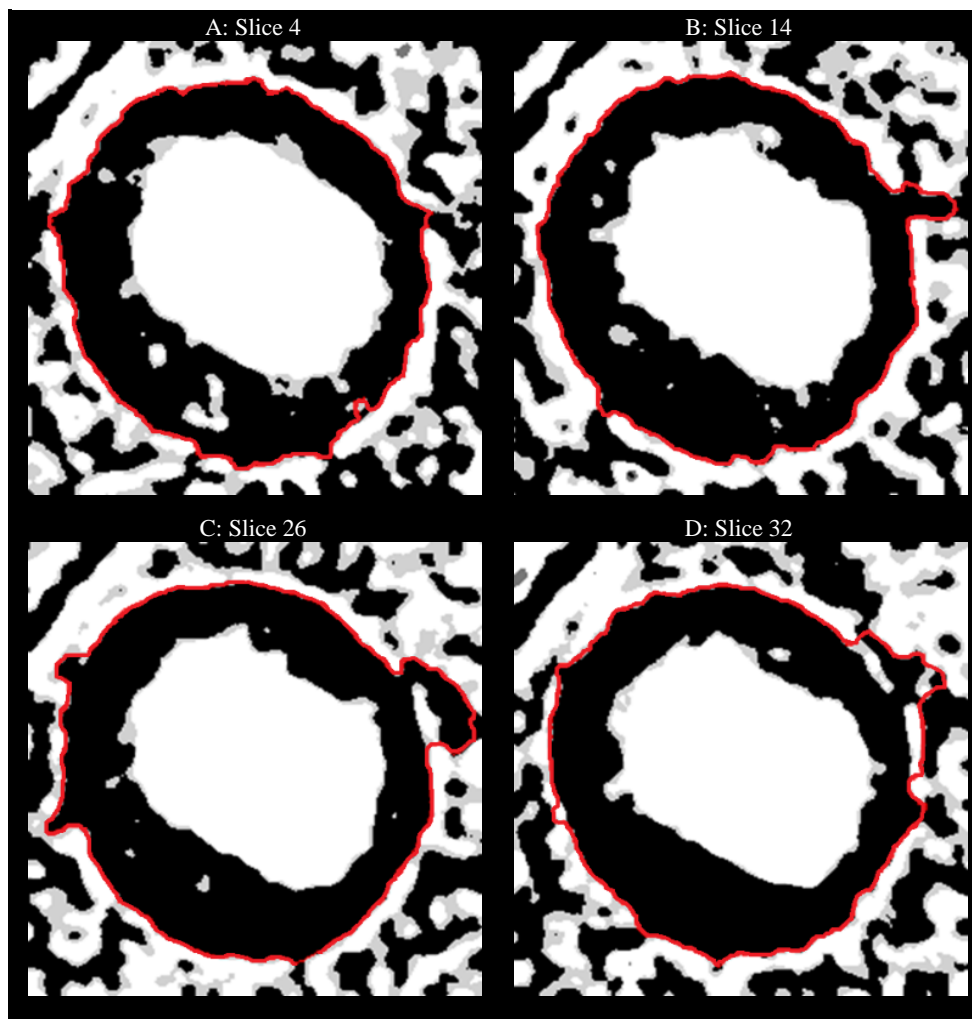
The *Watershed transform* (Volkman, 2002) (**Section 1.3.3.1**) was developed for accurate biological specimen segmentation, and thus was selected to be used in this experiment. This automated region-based segmentation has technically proven its ability in detecting object regions based on region's intensity. The method accurately extracted or detected the contour of interest (i.e. the organelle's membrane) including those 'unwanted neighbouring contours' (**Figure 3.13**). Using optimised settings of the *watershed*, the segmentation result of insulin granule yielded a clear separation between the contour of interest (granule's membrane) and the contour of 'neighbouring' objects. Similarly, the most complex of the three key organelles, the Golgi apparatus, yielded good tracing result for the majority of the combination approaches (**Figure 3.14**).

**Table 3.5 Processing time of two combination approaches between optimised image filtration methods followed by *snakes* (S) and image filtration methods followed by *watershed* (W).**

**S1:** Optimised Gaussian filter followed by *snakes*. **S2:** Optimised Minimum filter followed by *snakes*. **S3:** Optimised Maximum filter followed by *snakes*. **S4:** Optimised 2D Median filter followed by *snakes*. **S5:** Optimised 3D Median filter followed by *snakes*. **S6:** Optimised Kuwahara filter followed by *snakes*. **S7:** Optimised Meanshift filter followed by *snakes*. **S8:** Optimised NAD filter followed by *snakes*. **S9:** Optimised Bilateral filter followed by *snakes*. **W1:** Optimised Gaussian filter followed by *watershed*. **W2:** Optimised Minimum filter followed by *watershed*. **W3:** Optimised Maximum filter followed by *watershed*. **W4:** Optimised 2D Median filter followed by *watershed*. **W5:** Optimised 3D Median filter followed by *watershed*. **W6:** Optimised Kuwahara filter followed by *watershed*. **W7:** Optimised Meanshift filter followed by *watershed*. **W8:** Optimised NAD filter followed by *watershed*. **W9:** Optimised Bilateral filter followed by *watershed*. Calculation of processing times is in seconds (s).

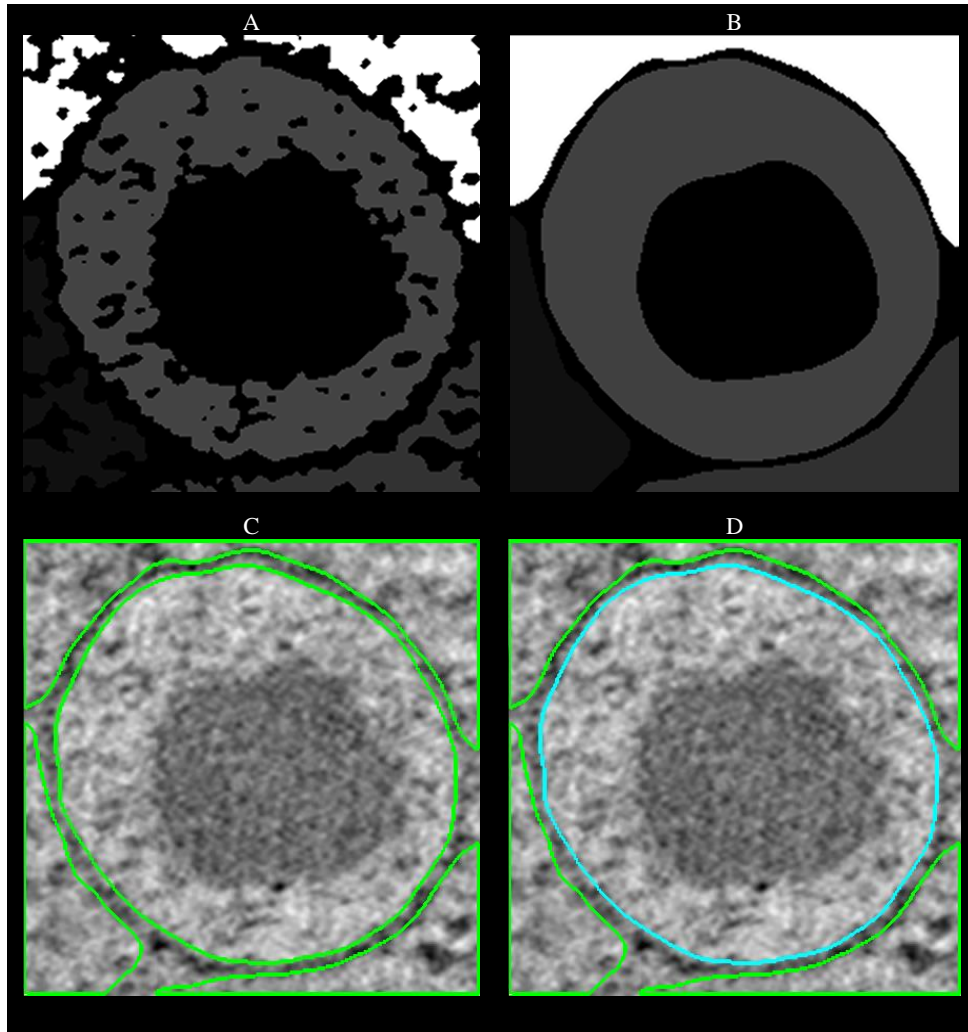
	Man	S1	S2	S3	S4	S5	S6	S7	S8	S9
GA1	1500	1500	1500	1500	1500	1500	1500	1500	1500	1500
GA2	1800	2000	2000	2000	2000	2000	2000	2000	2000	2000
GA3	1800	2000	2000	2000	2000	2000	2000	2000	2000	2000
<b>Total</b>	<b>5100</b>	<b>5500</b>	<b>5500</b>	<b>5500</b>	<b>5500</b>	<b>5500</b>	<b>5500</b>	<b>5500</b>	<b>5500</b>	<b>5500</b>
MC1	600	800	800	800	800	800	800	800	800	800
MC2	750	800	800	800	800	800	800	800	800	800
MC3	750	800	800	800	800	800	800	800	800	800
<b>Total</b>	<b>2100</b>	<b>2400</b>	<b>2400</b>	<b>2400</b>	<b>2400</b>	<b>2400</b>	<b>2400</b>	<b>2400</b>	<b>2400</b>	<b>2400</b>
IG1	600	800	800	800	800	800	800	800	800	800
IG2	750	800	800	800	800	800	800	800	800	800
IG3	750	800	800	800	800	800	800	800	800	800
<b>Total</b>	<b>2100</b>	<b>2400</b>	<b>2400</b>	<b>2400</b>	<b>2400</b>	<b>2400</b>	<b>2400</b>	<b>2400</b>	<b>2400</b>	<b>2400</b>
<b>Grand Total</b>	<b>9300</b>	<b>10300</b>	<b>10300</b>	<b>10300</b>	<b>10300</b>	<b>10300</b>	<b>10300</b>	<b>10300</b>	<b>10300</b>	<b>10300</b>
	Man	W1	W2	W3	W4	W5	W6	W7	W8	W9
GA1	1500	80	80	80	80	80	80	80	80	80
GA2	1800	80	80	80	80	80	80	80	80	80
GA3	1800	80	80	80	80	80	80	80	80	80
<b>Total</b>	<b>5100</b>	<b>240</b>	<b>240</b>	<b>240</b>	<b>240</b>	<b>240</b>	<b>240</b>	<b>240</b>	<b>240</b>	<b>240</b>
MC1	600	20	20	20	20	20	20	20	20	20
MC2	750	20	20	20	20	20	20	20	20	20
MC3	750	20	20	20	20	20	20	20	20	20
<b>Total</b>	<b>2100</b>	<b>60</b>	<b>60</b>	<b>60</b>	<b>60</b>	<b>60</b>	<b>60</b>	<b>60</b>	<b>60</b>	<b>60</b>
IG1	600	20	20	20	20	20	20	20	20	20
IG2	750	20	20	20	20	20	20	20	20	20
IG3	750	20	20	20	20	20	20	20	20	20
<b>Total</b>	<b>2100</b>	<b>60</b>	<b>60</b>	<b>60</b>	<b>60</b>	<b>60</b>	<b>60</b>	<b>60</b>	<b>60</b>	<b>60</b>
<b>Grand Total</b>	<b>9300</b>	<b>360</b>	<b>360</b>	<b>360</b>	<b>360</b>	<b>360</b>	<b>360</b>	<b>360</b>	<b>360</b>	<b>360</b>





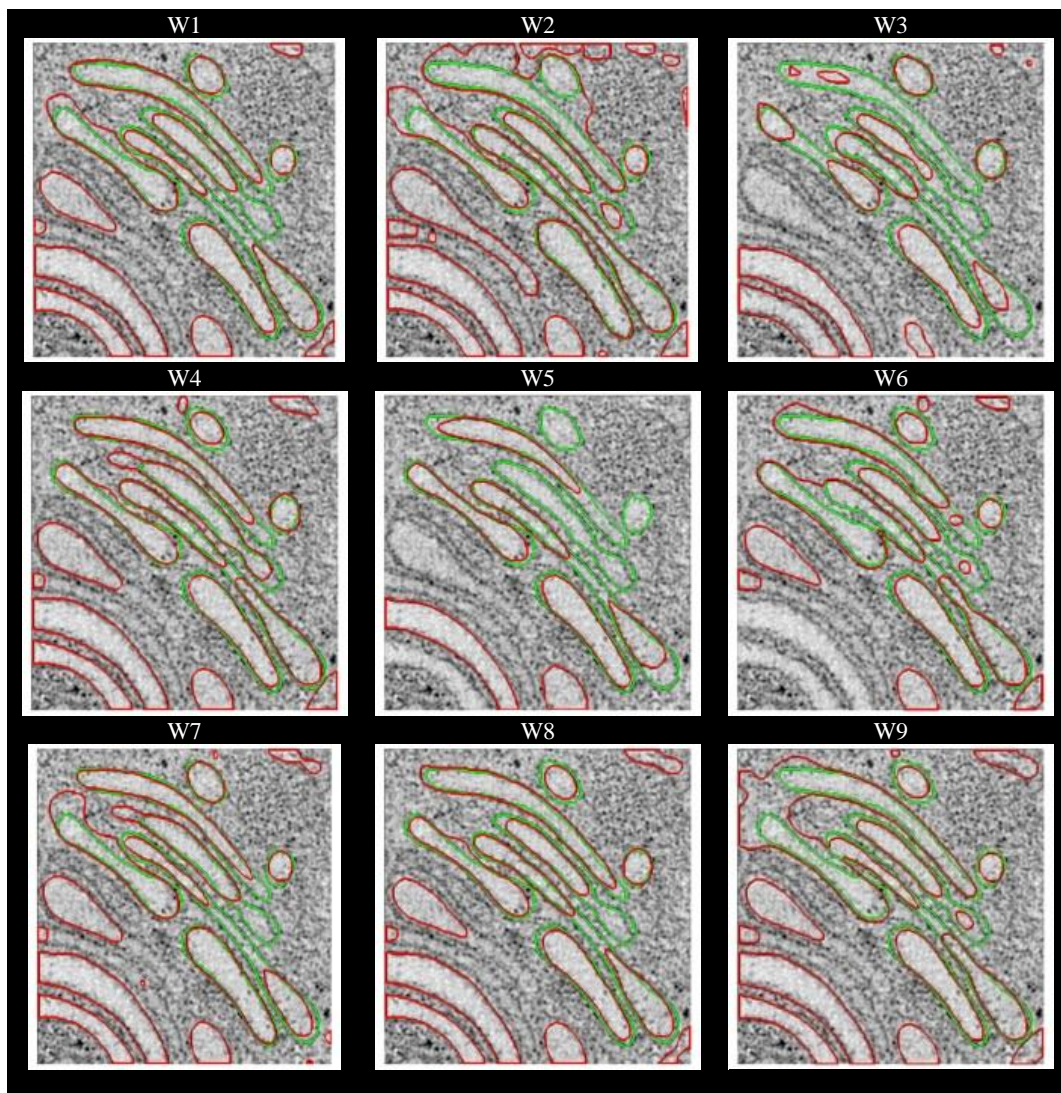
**Figure 3.12** The applications of *snakes* on the optimised filtered images (insulin granule).

(A-D) *Snakes* contours tend to converge to 'meaningless' edges when there are broken edges bounding an object. In this example, the problem begins at slice 14 (B) and becomes progressively worse (slices 32) (D). The images were filtered using optimised 2D Median and segmented using *snakes* from *ImageJ*. (*Snakes* segmentation: Gradient threshold=5, number of iterations=150). PT: 20 minutes (1200 s), SA:  $\sim 6 \times 10^4$  nm<sup>2</sup>.



**Figure 3.13** The applications of *watershed* on the optimised filtered images (insulin granule).

(A-D) Watershed algorithm applied on optimised filtered image. (A) A *labelmap* image with rough spatial shape (the result of watershed algorithm) has been transformed to a smoother shape (B). Every single object in (B1) is traced (C). For accurate membrane contouring, the organelle of interest is highlighted in light blue (D) where the light blue contour is disconnected to neighbouring contours (green). PT:  $\sim 20$  s, SA:  $\sim 8 \times 10^4$  nm<sup>2</sup>. The ground truth dataset of this example; PT: 600 s, SA:  $\sim 5 \times 10^4$  nm<sup>2</sup>.



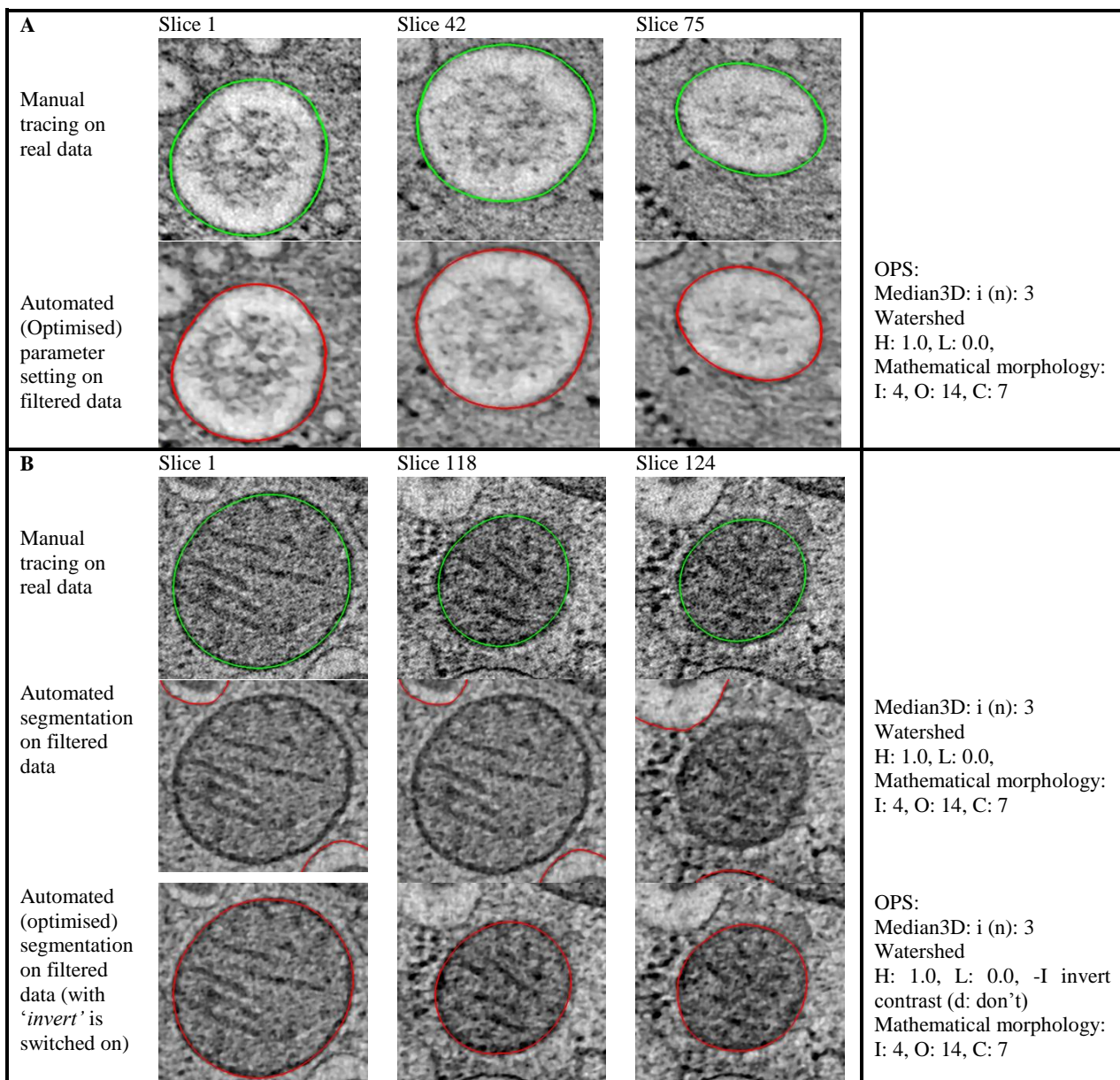
**Figure 3.14** Visual comparison between manual tracing (green contours) and automated segmentation (red contours) for the Golgi apparatus.

Majority of the tracing results show main Golgi structures (i.e. the cisternae) are traced, with a slight over- and under-segmentation. Images represent the traced contours laid over real dataset of the GA images. **W1**: Optimised Gaussian filter followed by *watershed*. **W2**: Optimised Minimum filter followed by *watershed*. **W3**: Optimised Maximum filter followed by *watershed*. **W4**: Optimised 2D Median filter followed by *watershed*. **W5**: Optimised 3D Median filter followed by *watershed*. **W6**: Optimised Kuwahara filter followed by *watershed*. **W7**: Optimised Meanshift filter followed by *watershed*. **W8**: Optimised NAD filter followed by *watershed*. **W9**: Optimised Bilateral filter followed by *watershed*.

The simplicity of the IG appearance particularly the immature granules (i.e. a single layer membrane, smaller in volume than neighbouring objects/organelles attached or close to organelle membrane) have made the automated segmentation easy and straightforward (**Figure 3.15 A**). While the most complex organelle amongst three key organelles, i.e. the Golgi apparatus, also showed promising results (**Figure 3.16**). Although there are problems such as over- and/or under-segmentation, the contours of cisternae membranes of various morphologies were successfully traced by the optimised automated settings.

Mitochondria on the other hand, could not be segmented with the initial settings (**Figure 3.15 B**). Closer analysis showed that the double-layered organelle is denser than other organelles and neighbouring objects and this appeared to directly influence the segmentation process and optimal settings required. In particular the use of the ‘*invert*’ function improved segmentation quality.

To conclude the time required by *snakes* method to manually draw the initial contour on every image slice prior to active contouring meant that total processing times were much longer than those required using the *watershed* approach (**Table 3.5**). The *watershed* approach not only had faster processing times but also exhibited a higher degree of accuracy. Thus, the *watershed* segmentation approach was selected for the development of the processing pipeline for computational segmentation and was further tested in combination with the nine denoising filters. Even though *watershed* obtained accurate tracing results, unwanted objects remain the main drawback for automated tracing. These required subsequent removal. As the project’s prime objective is to produce a rapid and accurate segmentation approach, computational approaches were sought to remove unwanted contours. Prior to this, edge or contour refinement is essential to improve the traced contours and visualisation.



**Figure 3.15 Difference image properties influenced segmented contour result.**

Two different organelle, insulin granule (A) and mitochondria (B) were manually traced. Both examples were also segmented using the recommended parameter setting of Method 5 (M5). This setting successfully traced the insulin granule membrane (A). However, it failed to draw the contour of mitochondrion membrane (instead it traced the contour of other objects). 'Invert' (parameter in watershed segmentation) is turned on in the second trial and mitochondrion membrane is finally traced. M5 - i (n): number of iteration, watershed - H: high-contour cut-off, L: low-contour cut-off, I: inversion contrast, mathematical morphology - I: initial opening, O: opening, C: closing.

### 3.3.2.3 Contour line refinement: Mathematical morphologies algorithm

Contour refinement allows ‘apparent separation’ between the contour of interest (**Figure 3.16**) and unwanted contours. Practically this can be done using a mathematical morphology algorithm. There are two operations in mathematical morphology commonly used for contour refinement. These are *opening* (i.e. erosion followed by dilation operation) and *closing* (i.e. a dilation followed by erosion operation) (Dougherty and Latufo, 2003). The *maplmorph* function in *CoAn* (Volkman et al., 2000) was used for this study. It detects edges and disconnects objects using optimised settings of *opening* and *closing* (**Figure 3.17**). This will allow the object of interest to be selected computationally.

### 3.3.2.4 Meshing: Contour volume value and mesh surface area scoring

Based on a 3D mesh contour of an object, its volume (CV – contour volume) and surface area (MSA – Mesh surface area) can be calculated and used for quantitative comparison with the manual reference set. Meshing was performed automatically by using the *imodmesh* function in *IMOD*. The process was performed on the segmented stacks of image slices of each organelle.

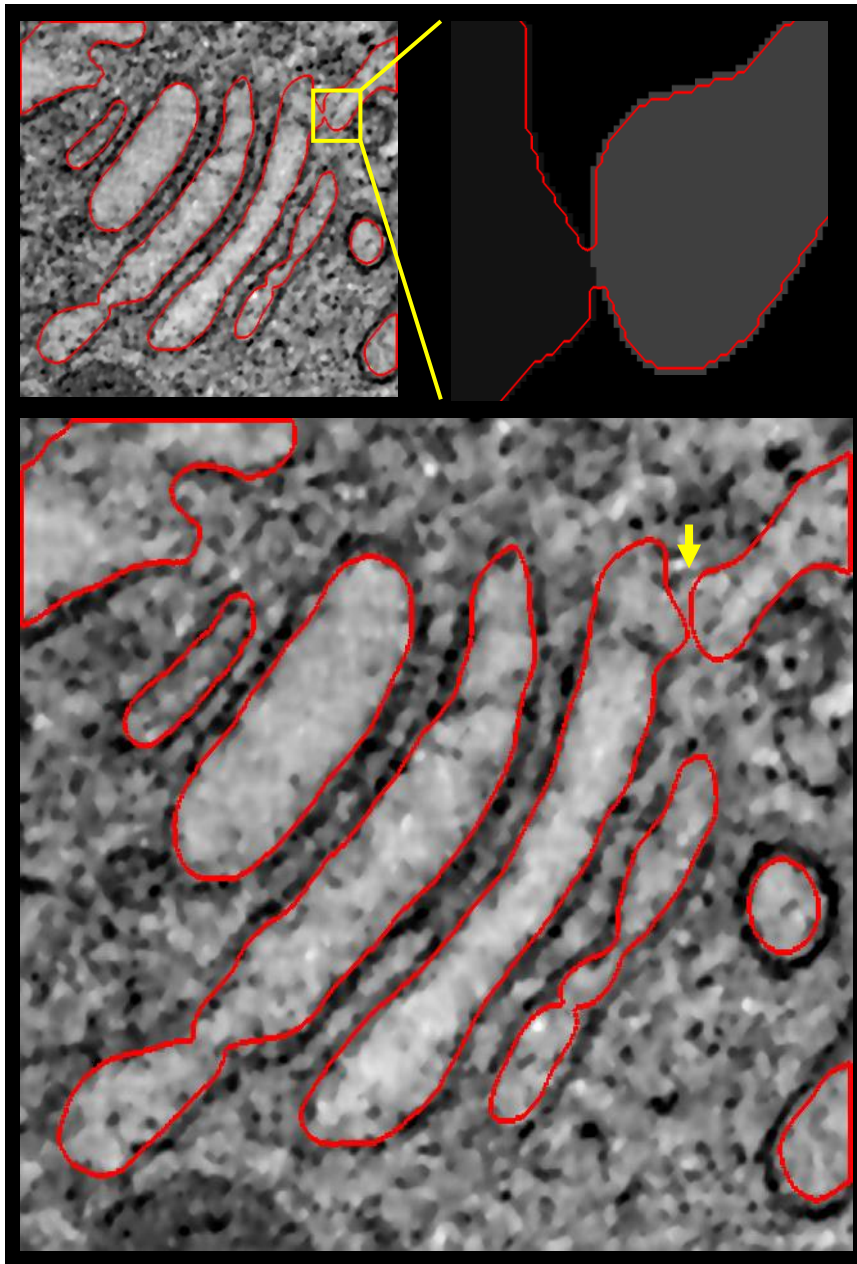
#### **Contour volume (CV):**

The contour volume (CV) is a sum of the area of contours (of each of Z slice of an object) times the distance to the connected contours in Z; The CV value is chosen for two reasons;

1. It handles the problem of skipped sections (Kremer et al., 1996)
2. It gives a slightly more accurate volume measurement for the capped regions because it integrates with a trapezoidal approximation (Kremer et al., 1996)

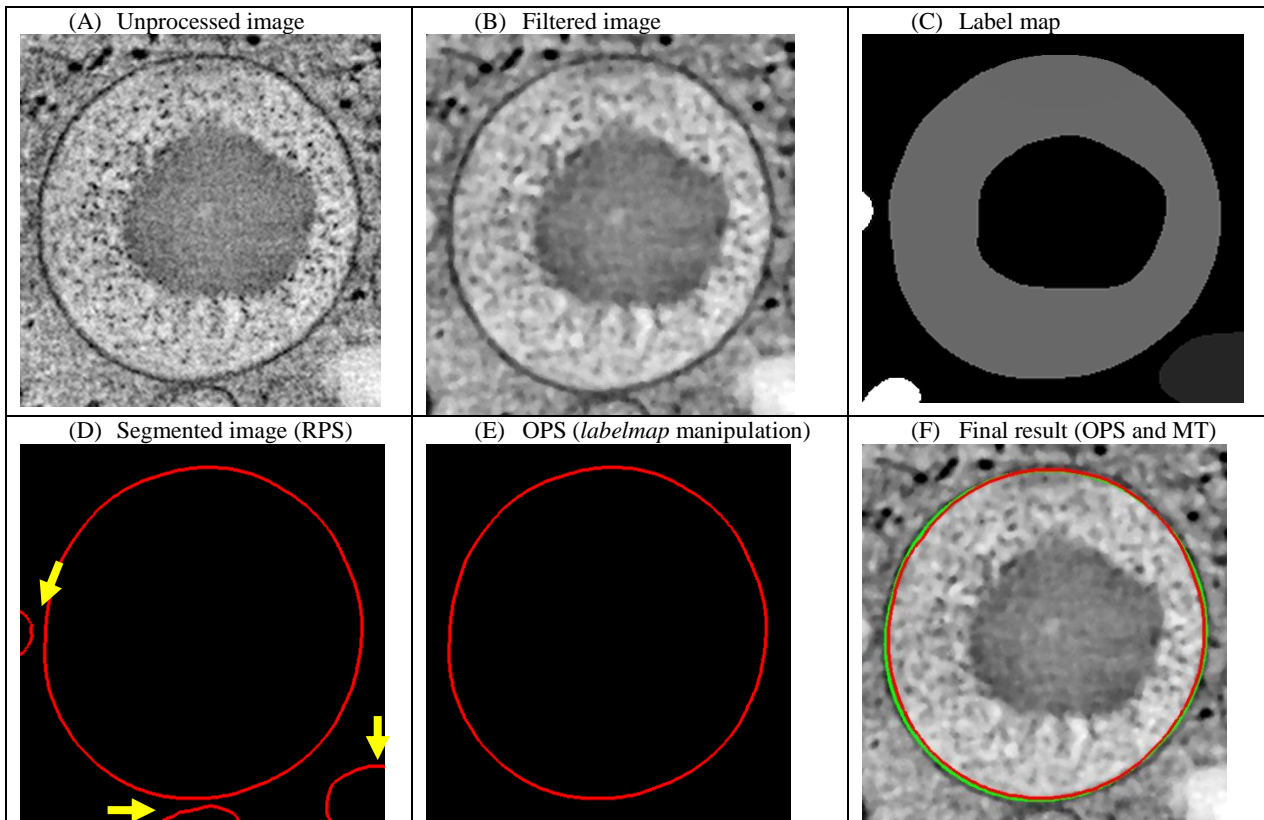
#### **Mesh surface area (MSA):**

The mesh surface area is the total surface area of a mesh volume, computed by adding the areas of all the triangles in the mesh.



**Figure 3.16** Application of *opening* and *closing* (mathematical morphologies operations) in membrane disconnection. (Upper part) A part of the Golgi cisternum membrane ‘connected (yellow box) with other contour (shown in *labelmap* image). (Below) This connected part is disconnected (yellow arrow) after mathematical morphologies algorithm applied on *labelmap*.

In theory an object accurately segmented by two independent methods should have identical contour volumes. To test the effectiveness of contour volume (CV) as a metric to quantitatively compare contour sets of automated segmentation, they were assessed in comparison to a manual reference. By doing this, unwanted contour sets could be deleted in an automated manner when the CV value of automated segmentation did not closely match the CV of manually traced referenced contour sets. Furthermore this approach proved useful when more than one contoured volume was traced in a given tomographic sub-volume as the *mappick* function (*CoAn*) can be used to detect and delete unmatched volume(s). MSA, provide an exact measure of the area of the mesh, and was used as the second assessment of the segmentation results and for identification of the best combination of method settings.



**Figure 3.17 Removing unwanted contours computationally from optimised segmentation result.**

By referring to the CV information of manual tracing contour set, unwanted object membranes were prevented from being traced to produce only the correct contour. (A) Original data of insulin granule. (B) Optimised Non-linear anisotropic diffusion (NAD) filter used to filter the image volume of (A). (C) Filtered image of (B) was converted into a 'label' map. (D) Yellow arrows show the unwanted contours. (E) Label map data in which the 'unwanted regions' identified in (D) have been deleted. (F) The final segmented contour using optimised parameter settings (OPS) (red contour) on the background of the filtered image. It compares closely to the manually traced contour (green contour).



### 3.3.2.5 Proposed method flow for automated and accurate cellular compartment segmentation

The proposed workflow is based on four main stages;

- 1) **Data preparation** (e.g. sub-volume extraction, image file conversion, denoising)
- 2) **Segmentation**
- 3) **Statistical evaluation**
- 4) **Contour selection**

In terms of data preparation there are two categories of image filter; 2-dimensional (2D) and 3-dimensional (3D). For 2D filters, the datasets (.mrc) must first be converted into a .tiff file, for input into the software package (i.e. *ImageJ*). The conversion process was conducted with *mrc2tif* function in *IMOD*. The .tiff image stacks were then filtered using 2D filters. These filtered stacks were then converted back to the .mrc file format using the *tif2mrc* function in *IMOD* for further downstream segmentation.

Unlike 2D filter methods, the 3D filters will process the original datasets (.mrc) directly. All filtered stacks of images were then segmented using the watershed function (i.e. *mapcarv*), provided by *CoAn* (Volkman et al., 2000) to produce a label map. The *CoAn* system automatically checks these label maps for unwanted contours which usually appear ‘smaller’ than the object of interest – by turning on ‘deleting blobs’ function in *CoAn*. Function *mappick* (*CoAn*) was used to delete all these unwanted densities.

Next mathematical morphology algorithm (i.e. *maplmorph*) was applied. Lastly a set of contours for every stack was produced. The process of optimising parameter settings particularly for image filtrations and watershed transform was started using the recommended settings of the respective software developers

The ‘ground truth’ datasets were generated from manual tracing of the datasets. From these contour sets, cylinder volumes (CV) were calculated by taking the area of each contour times the thickness of the sections (defined by pixel size and Z-scale) (Kremer et al., 1996), summed over all of the contours (*imodinfo*). Stacks of contours of each sub-volume were meshed, and meshed surface area (MSA) of each was calculated and saved.

The CV information of respective ground truth datasets is important to identify optimal settings of the CTS method's parameter(s). The MSA information was used to validate the best (optimised) method flow(s) amongst the nine method flows for particular cases of organelle segmentations (i.e. both calculations; CV and MSA are important and are used to stop the parameter adjustment process).

A written pseudocode – the sequence of steps taken to interpret the whole pipeline was developed (**Figure 3.18**) prior to designing a comprehensive workflow (**Figure 3.19**). The workflow is divided into three major stages. Overall, nine methods flows were suggested (M1-M9) where; **M1**: Gaussian filter followed by *watershed* and mathematical morphologies; **M2**: Minimum filter followed by *watershed* and mathematical morphologies; **M3**: Maximum filter followed by *watershed* and mathematical morphologies; **M4**: 2D Median filter followed by *watershed* and mathematical morphologies; **M5**: 3D Median filter followed by *watershed* and mathematical morphologies; **M6**: Kuwahara filter followed by *watershed* and mathematical morphologies; **M7**: Meanshift filter followed by *watershed* and mathematical morphologies; **M8**: Non-linear anisotropic diffusion (NAD) filter followed by *watershed* and mathematical morphologies; and **M9**: Bilateral filter followed by *watershed* and mathematical morphologies.

Prepare nine similar sets of the area of interest.

Convert six volumes of original data into stacks of *.tif* files (e.g. *extract001\_slice0001.tif*) by using *mrc2tif* (*IMOD*) to number the files in sequence during conversion for 2D noise reduction.

Convert another three volumes into normalised 32-bit floating point format by using *maptool* (*CoAn*), save as a *.map* volume (e.g. *extract001.map*) for 3D noise reduction.

Filtering process: image sequence *.tif* files are filtered by each 2D filter and saved as *extract001\_slice0001\_filtered.tif*, whilst the 3 *.map* volumes are filtered by each 3D algorithm and saved as *extract001\_filtered.map*.

Convert filtered 2D *.tif* stacks into *.mrc* volumes by using *tif2mrc* function (*IMOD*), then convert to normalized 32-bit floating point *.map* files as in step 3. Restore volume origin and voxel size based on original extracts.

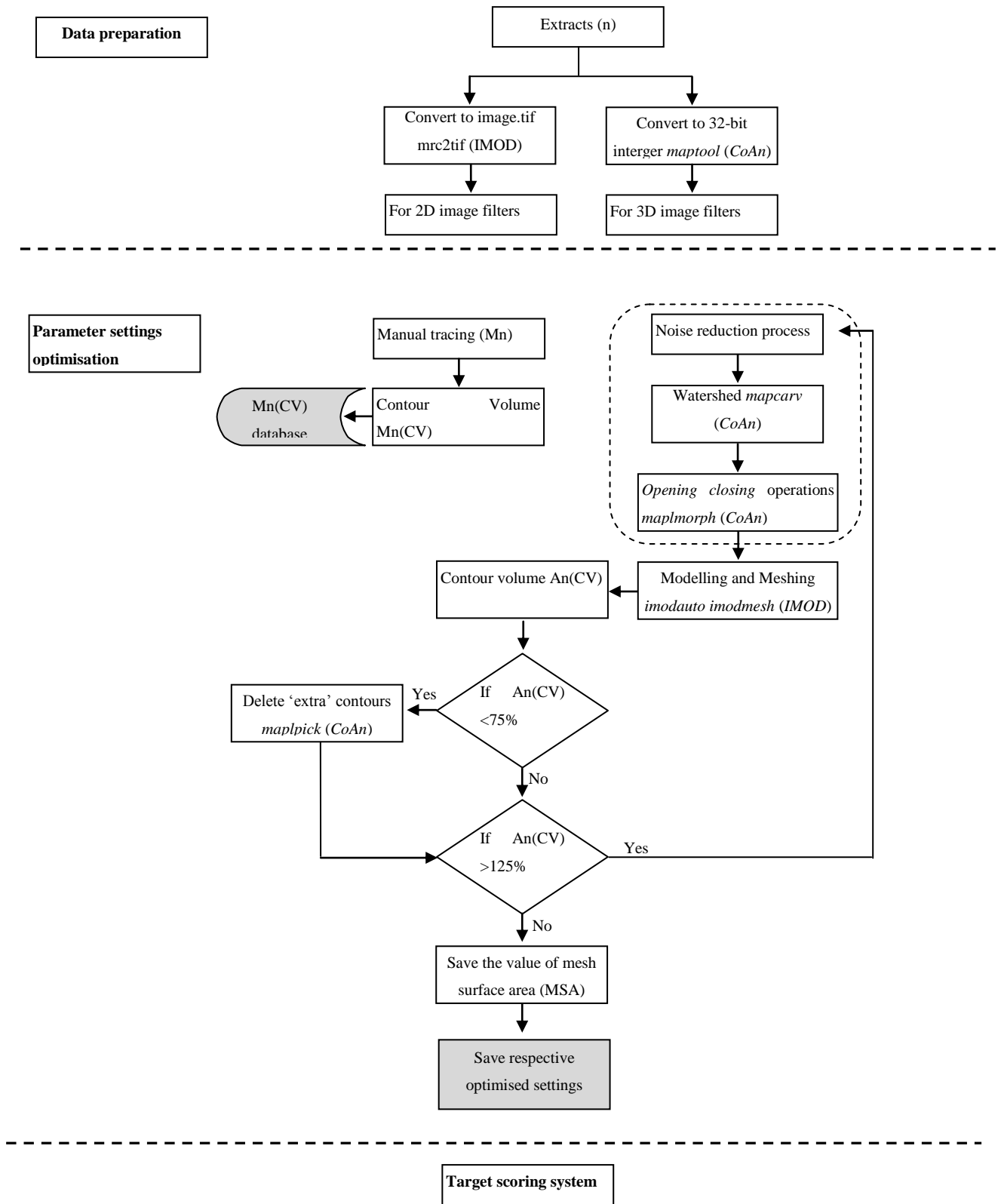
Segmentation process: All filtered volumes are then subjected to 3D watershed segmentation (*mapcarv* from *CoAn*), producing “*labelmaps*” of objects.

Remove small objects and noise from label maps using *mappick* (*CoAn*).

Apply *closing-opening* operations for some morphological correction and/or smoothing on *labelmaps* images by using *maplmorph* (*CoAn*).

Make model file by using *imodauto* (*IMOD*) and save image result as model (*.mod*) file.

**Figure 3.18 Pseudocode for the proposed pipeline of cellular compartments segmentation.**

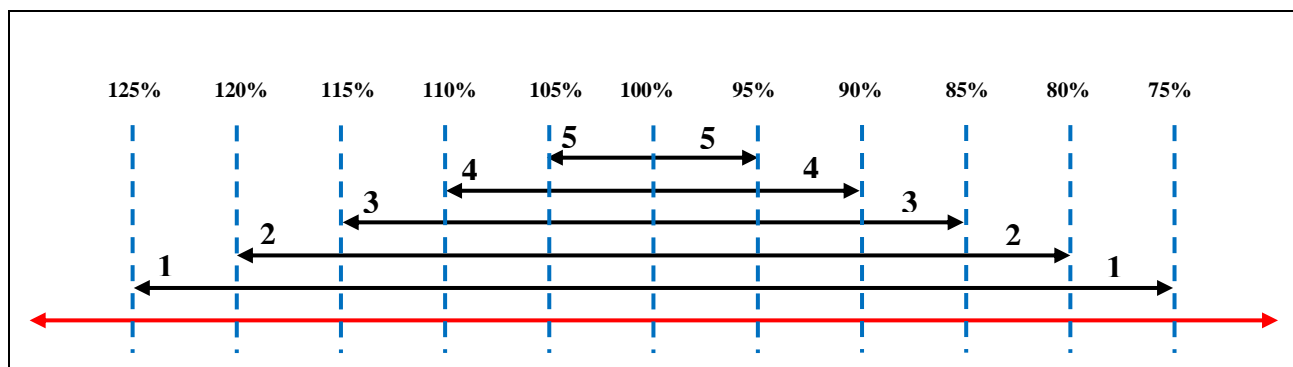


**Figure 3.19** Workflow diagram of the proposed systematic approach for accurate segmentation. Two main stages (as highlighted) proposed to comprehend the pipeline of complete segmentation procedure.

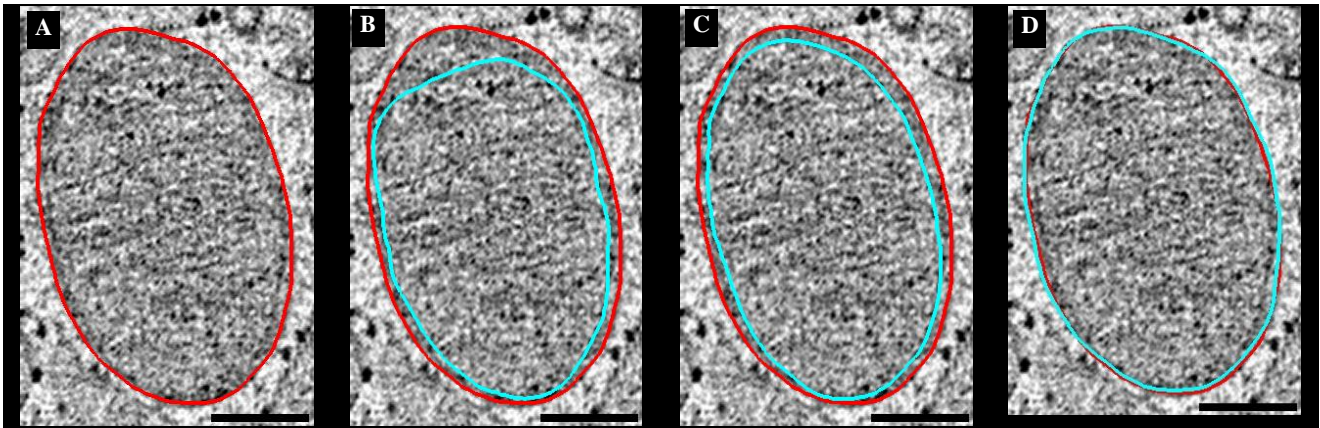
The ‘best’ setting of the method was determined when the segmentation result met these three requirements;

- 1) The membrane contour(s) of the targeted organelle was/were segmented.
- 2) No additional unwanted contours of neighbouring objects or organelles were segmented.
- 3) Once requirement (1) and (2) were achieved, the mesh surface area (MSA) of the traced contour(s) was calculated to establish whether it was within  $\pm 25\%$  (**Figure 3.20**) of the MSA calculated for the manually segmented sub-volume.

The most critical and time consuming procedure is the second one (i.e. parameter settings optimisation) as it employs a ‘trial and error’ routine. Consequently a ‘target scoring system’ was proposed to help identify the ‘best’ combination of parameter settings of the different method flows (**Figure 3.21**).



**Figure 3.20 Target scoring system. ‘100%’ is referred as a ‘target point’ of ground truth datasets.** All mesh volumes of manual tracing is ‘labelled’ as 100%. Any results of computational methods scored  $\pm 100\%$  (of respective MSA) will determine a score of 5, and so on. Target scoring for each sub-group will differ according to its ground truth (gold standard) datasets. 5 scores of MSA range were proposed where ‘5’ is the best while ‘1’ is the worst.



**Figure 3.21 Differences between segmentation results (i.e. ‘best’ settings of different method flows) for mitochondria.**

(A) Manual segmentation (red contour) of the raw data. The cyan contours in B to D are the results of ‘best’ settings of 3 different method flows that are superimposed on raw data. (B) M1 (optimised Gaussian filter followed by optimised *watershed* and mathematical morphologies) where the MSA was ~80% of the MSA manual segmentation (i.e. the MSA of M1 was less ~20% from the MSA of manual segmentation). This result score 2. (C) M9 (optimised bilateral filter followed by optimised *watershed* and mathematical morphologies), the MSA was recorded as 91% (i.e. less ~10%) compared to manual segmentation. This result score 4. (D) M8 (optimised non-linear anisotropic diffusion filter followed by optimised *watershed* and mathematical morphologies), the MSA was 101% and this was the most accurate result of the method flows tested for this mitochondrion segmentation. This result score 5. Scale bars: 100 nm.

### 3.3.3 Refining parameter settings of segmentation method flows

To refine methods capable of more automated approaches to segmentation, 10 sub-volumes of each of the three key organelles (i.e. a total of 30 sub-volumes) were systematically chosen such that a variety of sub-volumes sizes were represented for each organelle. The recommended parameter settings (RPS) of all nine method flows were employed prior to optimising the methods settings. Contour sets were meshed. These meshed volumes were then used to compute the contour volume (CV) and meshed surface area (MSA). By using the CV, unwanted contours or contour volumes (i.e. which are not similar to the CV of the ground truth) were deleted computationally. Optimisation of settings was continued until the MSA of the computational method approached the values of the manual MSA of the ground truth set (a score of 5 being best and 1 the worst).

Insulin granules and particularly immature granules with a ‘simple appearance of structure’ (i.e. empty lumen and smooth boundary membrane) were successfully contoured (score 5) with optimised image filters and optimised *watershed* of every method flow (M1 – M9). The CV and MSA value of M1-M9 for the example dataset (**Figure 3.22**) consistently achieved a score of 5 according to the ‘target scoring system’.

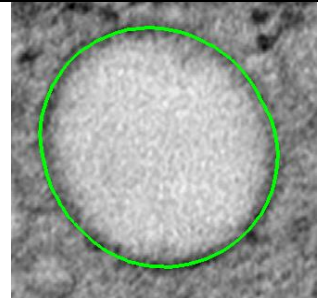

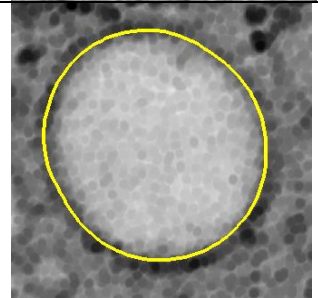
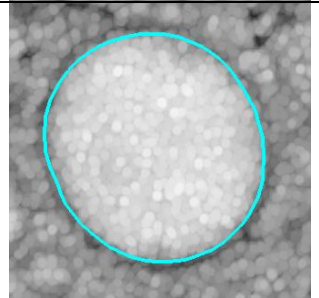
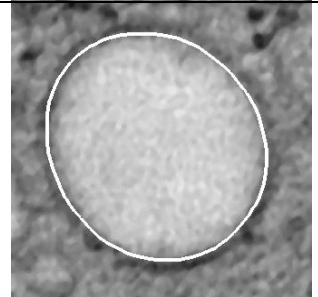
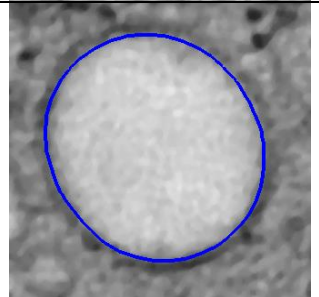
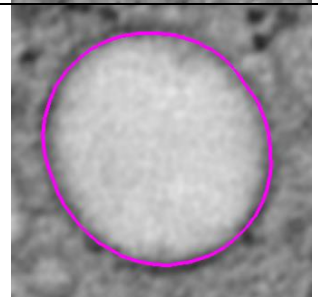
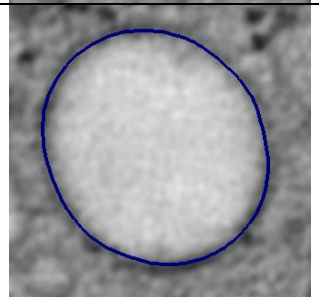
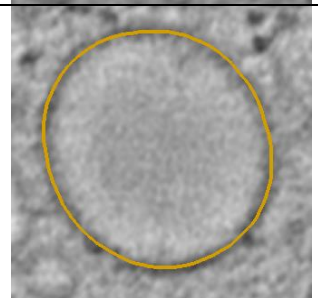

Almost all sub-volumes of the Golgi apparatus faced similar problems when segmented, exhibiting both over- and/or under-segmentation – as discussed in **Chapter 1** (see also **Figure 3.23 A**). Setting optimisation was commenced with image filtration followed by the watershed (**Figure 3.23 B**).

***(a) Study: Mean density value of filtered images could determine settings of watershed***

Optimising parameter settings of watershed algorithm is not straightforward and very time consuming, particularly when segmenting unique objects of low signal-to-noise ratio 3D images. Thus, a simple study amongst organelles image properties of segmented organelle sub-volumes was set up. From this analysis, five ‘ranges’ of mean density values were identified and the datasets were classified into these groups. From these ranges, the settings of watershed were simply observed (**Figure 3.24**). Higher values of ‘high contour cut-off’ (i.e. parameter of *watershed* algorithm) were used to segment filtered images of organelle data with lower mean density values, and vice versa. All examples used the same value of lower contour cut-off. Knowing the mean density value of filtered images could expedite the process of optimising parameters of *watershed* (Volkman, 2002) for accurate tracing of one organelle sub-volume. It also encourages the adjustment of other parameter of *watershed* for more reliable optimised settings. This not only significantly alleviates in parameter optimisation for watershed algorithm but also reduces the processing time of parameter adjustment (i.e. the trial and error approach). Mean density of the filtered image was identified as possibly being important to facilitate the process of segmentation using the watershed approach.

***(b) Organelle type determine the ‘contrast inversion’ setting***

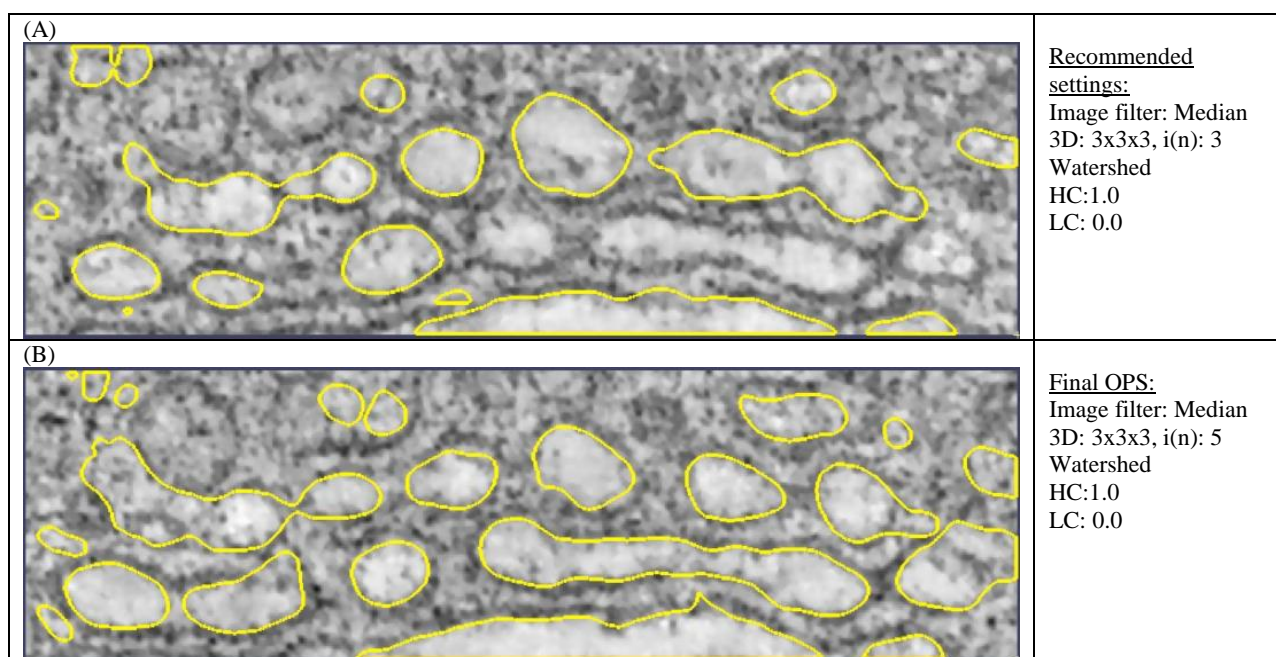
As mitochondria are radically ‘darker’ (high contrast image organelle) than the insulin granules and the Golgi apparatus the settings of watershed were run using ‘*invert*’. As image contrast was found to be important for accurate automated segmentation, classification of similar objects into separate classes could expedite their contouring.

	<p><b>MANUAL TRACING</b></p> <p>Number of contour per slice: 1                      Total number of contours: 139                      Contour volume (CV): 1746869                      Mesh surface area (MSA): 5612</p>		<p><b>M1</b></p> <p>Number of contour per slice: 1                      Total number of contours: 139                      Contour volume (CV): 1746888                      Mesh surface area (MSA): 5620                      Score: 5</p>
	<p><b>M2</b></p> <p>Number of contour per slice: 1                      Total number of contours: 139                      Contour volume (CV): 1746845                      Mesh surface area (MSA): 5615                      Score: 5</p>		<p><b>M3</b></p> <p>Number of contour per slice: 1                      Total number of contours: 139                      Contour volume (CV): 1746559                      Mesh surface area (MSA): 5612                      Score: 5</p>
	<p><b>M4</b></p> <p>Number of contour per slice: 1                      Total number of contours: 139                      Contour volume (CV): 1746190                      Mesh surface area (MSA): 5661                      Score: 5</p>		<p><b>M5</b></p> <p>Number of contour per slice: 1                      Total number of contours: 139                      Contour volume (CV): 1746285                      Mesh surface area (MSA): 5629                      Score: 5</p>
	<p><b>M6</b></p> <p>Number of contour per slice: 1                      Total number of contours: 139                      Contour volume (CV): 1746385                      Mesh surface area (MSA): 5642                      Score: 5</p>		<p><b>M7</b></p> <p>Number of contour per slice: 1                      Total number of contours: 139                      Contour volume (CV): 1746912                      Mesh surface area (MSA): 5622                      Score: 5</p>
	<p><b>M8</b></p> <p>Number of contour per slice: 1                      Total number of contours: 139                      Contour volume (CV): 1746716                      Mesh surface area (MSA): 5612                      Score: 5</p>		<p><b>M9</b></p> <p>Number of contour per slice: 1                      Total number of contours: 139                      Contour volume (CV): 1746860                      Mesh surface area (MSA): 5617                      Score: 5</p>

**Figure 3.22 Comparison of segmentation results between method 1 – method 9 with manual tracing.**

Middle Z slice of insulin granule sub-volume image stack. Visually, segmented contour in M1-M9, i.e. method 1-9, show similar contoured membrane (i.e. the object, the shape and the size) compared to manual set. All results of M1-M9 have scored 5 (the highest score according to the target scoring system) – similar results of CV (voxels) and MSA (pixels) were also recorded. Besides that the same result of mean number of contour per image slice (i.e. 1 contour) and the total number of contours, as compared to the manual tracing were recorded.





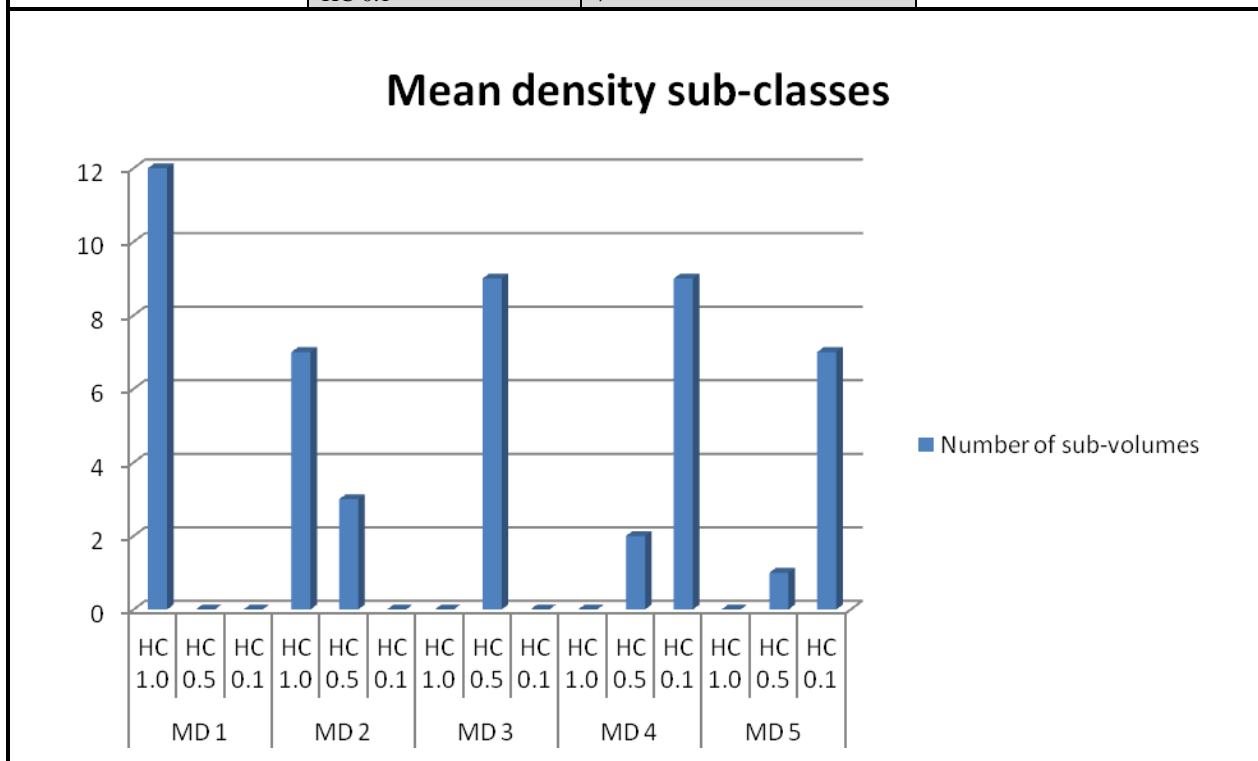
**Figure 3.23 Comparison between result retrieved from recommended settings and optimised settings of method 2 (M2).**

(A) Segmentation result of the proposed settings shows smooth segmented contours, however it is lacking in number of segmented cisternae. (B) The OPS of [M2] shows a better segmentation result where more contours of the cisternae was segmented, without adjusting the setting of watershed. Median 3D i(n): Number of iteration, Watershed HC: high contour cut-off, LC: low contour cut-off.

### 3.3.3.1 Quantitative and qualitative analyses

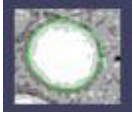
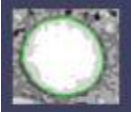
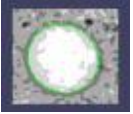

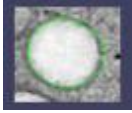
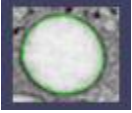

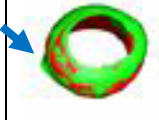
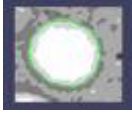
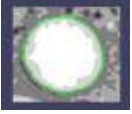
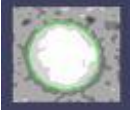

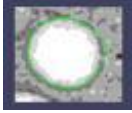



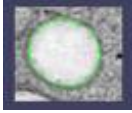

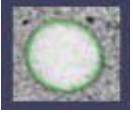





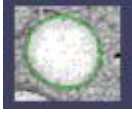







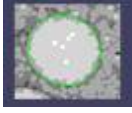



For the best analysis process of segmented result and to choose the best parameter settings of particular organelle sub-groups, quantitative and qualitative analyses were established accordingly. Number of contours (NOC) was first manually examined (**Figure 3.25** column 2). The closest NOC value of automated tracing to respective NOC obtained manually will be chosen. Then these contour sets were visually assessed and analysed (**Figure 3.25**, column 3 to 5). Visual comparison was made (**Figure 3.25** column 6) to allow experts to determine the best segmentation result(s). In the example of **Figure 3.25**, 5 results were selected (i.e. acceptable) where the comparison showed surfaces ‘free’ from ‘roughness’ (as shown by blue arrows). The next assessment is to choose the best three (amongst 5 acceptable results) using scoring system (**Figure 3.26**). Respective optimised settings of the best segmentation result (or the best three) were recorded. These settings were used to segment other organelle sub-volumes of the same organelle type. Parameter adjustment was performed for accurate tracing results of respective organelle sub-volumes.

Mean density range (density units)	HC levels	Number of sub-volumes	Percentage to organelle classification according to mean density value for parameter optimisation
MD1 ( $\geq 0-100\leq$ )	HC 1.0	12	100%
	HC 0.5	0	
	HC 0.1	0	
MD2 ( $\geq 100-150\leq$ )	HC 1.0	7	70%
	HC 0.5	3	
	HC 0.1	0	
MD3 ( $\geq 150-200\leq$ )	HC 1.0	0	100%
	HC 0.5	9	
	HC 0.1	0	
MD4 ( $\geq 200-250\leq$ )	HC 1.0	0	82%
	HC 0.5	2	
	HC 0.1	9	
MD5 ( $\geq 250-300\leq$ )	HC 1.0	0	88%
	HC 0.5	1	
	HC 0.1	7	




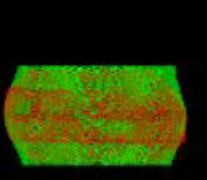

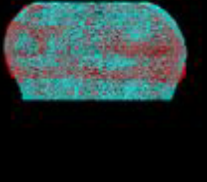

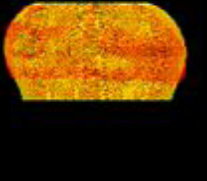

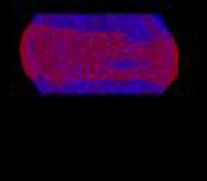

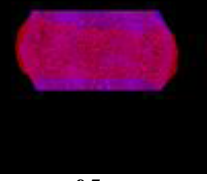
**Figure 3.24 Five ranges of mean density of filtered images identified.**

These five ranges of mean density values show significance role in dictating the parameter settings for watershed algorithm (i.e. the parameter high-contour cut-off or HC). Mean density sub-class 1 to sub-class 5 are labelled as MD 1 - MD 5. MD 1 and MD2 recorded to have setting of HC: 1.0. MD 3 recorded to have setting of HC: 0.5. MD 4 and MD 5 recorded to have setting of HC: 0.1.

granule1	# contour	Slice 10	Slice 25	Slice 40	Comparison (3D visualisation)	Comments
Optimised M1	49					Less acceptable
Optimised M2	49					Less acceptable
Optimised M3	49					Acceptable
Optimised M4	49					Less acceptable
Optimised M5	49					Acceptable
Optimised M6	49					Less acceptable
Optimised M7	49					Acceptable
Optimised M8	49					Acceptable
Optimised M9	49					Acceptable

**Figure 3.25** Nine segmentation results representing nine different method flows (M1 – M9).

**M1:** Gaussian filter and *watershed*; **M2:** Minimum filter and *watershed*; **M3:** Maximum filter and *watershed*; **M4:** 2D Median filter and *watershed*; **M5:** 3D Median filter and *watershed*; **M6:** Kuwahara filter and *watershed*; **M7:** Meanshift filter and *watershed*; **M8:** NAD filter and *watershed*; **M9:** Bilateral filter and *watershed*. The analysis starts with looking at the total number of contour produced from automated segmentation methods. In this case the sub-volume example (i.e. insulin granule) has an original stack of 49 contours. 3 image slices were randomly chosen to assess the contour of interest were traced. In the comparison column, both manual (red) and automated methods (green) were merged together for 3D visual assessment to see the 'roughness surfaces' as shown by blue arrows. Five results; **M3**, **M5**, **M7**, **M8** and **M9** were selected for this segmentation case as 'acceptable' based on comparison with manual tracing and the scoring system.

File ID	90° in X axis: before mesh (left) and after mesh (right)		Comments	Mesh surface area (MSA) / 1000 000 and the score
Manual				0.04125
M3			Acceptable Basic shape of the granule is produced. Contours of manual tracing (red) appear to be 'larger' than M3 (green) at the middle slices.	MSA/1000k: <b>0.05090</b>  Score: <b>5</b>
M5			Acceptable Basic shape of the granule is produced. Contours of manual tracing (red) appear to be 'larger' than M5 (light blue) at most of the slices.	MSA/1000k: <b>0.05086</b>  Score: <b>5</b>
M7			Acceptable Basic shape of the granule is produced. Contours of manual tracing (red) appear to be 'larger' than M6 (yellow) at most of the slices.	MSA/1000k: <b>0.05080</b>  Score: <b>5</b>
M8			Acceptable Basic shape of the granule is produced. Contours from manual segmentation (red) appear to be 'larger' than M7 (dark blue) at parts of middle slices.	MSA/1000k: <b>0.04838</b>  Score: <b>5</b>
M9			Acceptable Basic shape of the granule is produced. Contours from manual segmentation (red) appear to be 'larger' than M9 (purple) at parts of middle slices.	MSA/1000k: <b>0.04901</b>  Score: <b>5</b>

**Figure 3.26 The best five results have a score of 5.**

Using the system detailed in Section 3.3.4, the score of each segmentation result of automated techniques is given. Another comparison between manual (red) and automated methods (green, light blue, yellow, dark blue and purple) shown in the second column. The example shown in this figure represents the simplest case of image complexities. All 5 acceptable results (from previous assessment, **Figure 3.25**) have a score of 5.

### **3.4 Conclusion**

Any cellular segmentation process has to deal with image complexity and background image noise. There are many demonstrated pre-filtering methods capable of improving the signal-to-noise ratio of an image and enhancing edges such as the compartment edges and suppress the noise to facilitate the tracing process (Narasimha et al., 2008, van der Heide et al., 2007). However, most of them obtain their best capacity if the ‘noise’ is known (Rudin et al., 1992, Zhou and Zhang, 1999). To date, no single settings of mathematical segmentation method has shown its effectiveness on whole tomograms, i.e. so that every single cellular compartment is accurately traced without any ‘extra segmented regions/contours’.

Pre-processing is an essential step for accurate segmentation. Pre-processing is necessary to suppress image noise as well as enhance the organelle edges. To establish the final segmentation results for better visualisation and to benefit the analyses of results, an effective pipeline of automated segmentation for accurate segmentation result was developed (**Section 3.3.5**). The pipeline involves three main stages; 1) data preparation including sub-volume extraction and image file conversion, 2) optimised parameter settings which involve 3 main steps in automated segmentation including image filtration, watershed algorithm and mathematical morphologies operations, 3) statistical evaluation using target-scoring system that is used to identify the ‘best’ combination segmentation method amongst nine different method flows and 4) contour selection (applied when the deletion of unwanted contours are needed). Despite specific abilities in suppressing background noise, or improving edges of targeted membrane organelle, the settings of parameters for particular method flow were defined as the best (optimised) based on three primary analyses including visual observation and mathematical computation. Even though this chapter has reported a proposed segmentation pipeline that has given promising computational results and increase automated segmentation efficiency, the identification of optimal setting for 400 sub-volumes is still time consuming. It will be harder for 4000 or even 40,000 sub-volumes. It was hypothesised that additional image properties for each key organelle could expedite the identification of optimal image processing settings within the method flow, and thus further ‘simplify’ the process, with the potential to identify standard optimised settings for organelle segmentation according to its image properties. This hypothesis forms the basis of **Chapter 4** of this thesis.



**Chapter 4 3-DIMENSIONAL CHARACTERISTICS AND IMAGE  
FEATURES TO DICTATE PARAMETER OF CHOICE TOWARDS  
AUTOMATED CELLULAR TOMOGRAPHY SEGMENTATION**

---





## **4.1 Introduction**

To define the accuracy of segmentation requires comparison to a reference ‘ground truth’ data set which is provided in the form of mesh models. The production of 3D segmented mesh models by manual segmentation was described in (Noske et al., 2008) and **Chapter 3** of this PhD thesis. However, to segment more than 400 organelle sub-volumes and to have more than 1200 optimised settings is impractical. The aim of this chapter is to test the hypothesis, that it is possible to sub-classify subsets of key organelles (e.g. subsets of mitochondria classes) and to use these subsets as ‘standard’ reference sets for the determination of optimal parameter settings. The rationale for taking this approach is that the identification of optimal parameter settings for a given sub-class of objects could increase the rate and accuracy of semi-automated segmentation using the segmentation pipeline developed in **Chapter 3**.

In this chapter, ranges of image characteristics were defined for the Golgi apparatus, mitochondria and insulin granules. Image characteristics of selected organelle types include the general appearance of the organelle in the cross-sectional (i.e. 2D) images, its shape, size and volume, and internal features. Based on these features sub-classification was iteratively conducted until stable and optimal parameters settings could be identified for all of the organelles in the specified sub-class. This approach therefore allowed the identification of a combination of filter, segmentation algorithm and mathematical morphology operations that yielded accurate segmentation results in a reproducible manner.

## 4.2 Results

### 4.2.1 Classification of organelles of interest sub-types

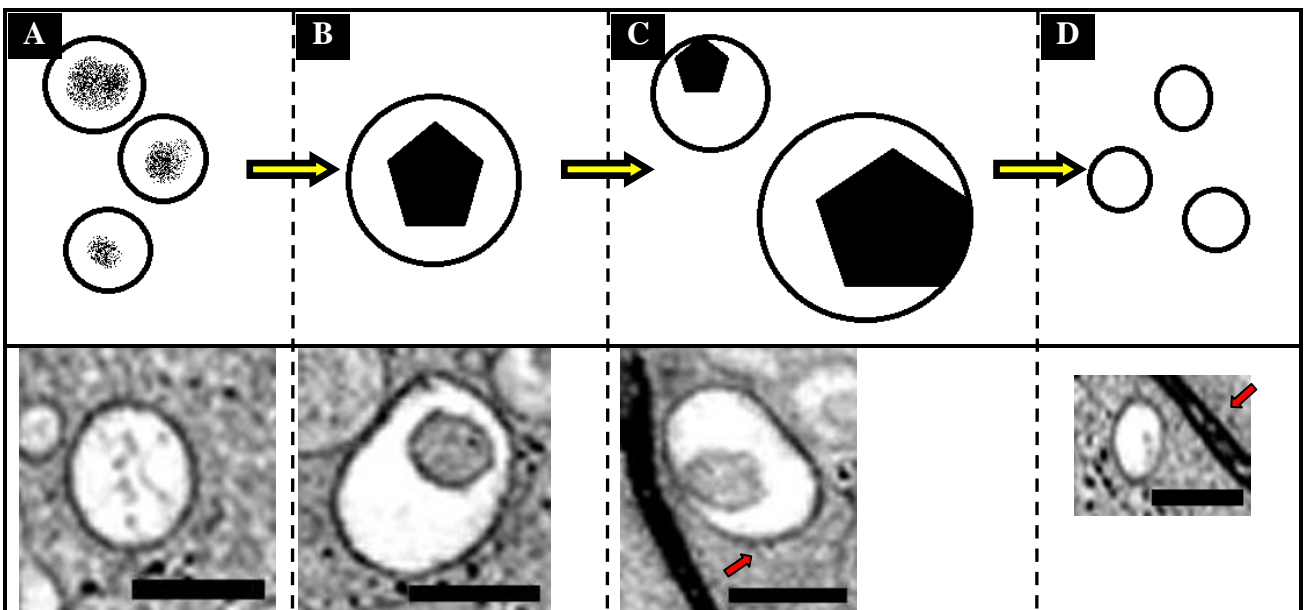
The aim of the first experiment of this chapter was to subdivide the ~400 images of insulin granules (157), mitochondria (191) and the Golgi apparatus (75) into a more finely differentiated set of structurally distinct sub-classes and to characterise their structural differences. The sub-typing of these organelles is important for three reasons. First it provides the basis for a deeper understanding of the biology of insulin secretion. Second it facilitates the development of a structural key based on 3D data to assist experts with the careful typing of subclasses of these organelles. Third the extracted organelles in each sub-class provide the data sets required to define the key parameters describing them. These parameters ultimately underlie the rules that must be defined and integrated into algorithms to facilitate automated segmentation.

Prior to the sub-classification process, 423 sub-volumes of three types of key organelles were manually contoured (Section 3.3.1) and computationally meshed. Both processes used *IMOD* tools (Kremer et al., 1996, Mastronarde, 2006). Besides the raw structural data (refer to Section 3.3.1) such as organelle dimensions (nm), minimum, mean and maximum density, mesh model related data such as the number of contours per image stack, contour volume, mesh surface area, mean area (i.e. mean contour area) were analysed and saved simultaneously. All of this information was listed and can be retrieved by using the *imodinfo* function in *IMOD*.

Next the structural features of the organelle sub-types were analysed and illustrated. A list of the XYZ dimension values ranges (nm) of organelle sub-volumes classified in a given sub-type were listed as minX, maxX, minY maxY, minZ maxZ (refer to Table 4.1, column 3, 4 and 5 from left). Here these dimensions refer to the length of the edges of a box volume just containing a given organelle; min and max refer to minimum and maximum image box dimensions of a set of such boxed organelles.

#### 4.2.1.1 Insulin granules

Based on the analysis of 157 insulin granules of non-stimulated cells, the following schematic illustrating insulin granule maturation was developed. This shows the transition of immature granules (**Figure 4.1 A**) to mature granules (**Figure 4.1 B**). When the insulin granules are ready to release the insulin (i.e. to form new vesicles/ immature granules) the crystalline core is proximal to organelle membrane (**Figure 4.1 C**) prior to forming new vesicles (**Figure 4.1 D**). This figure is consistent with previous reports (Noske and Marsh, 2011) and provides a structural key for insulin granule development.

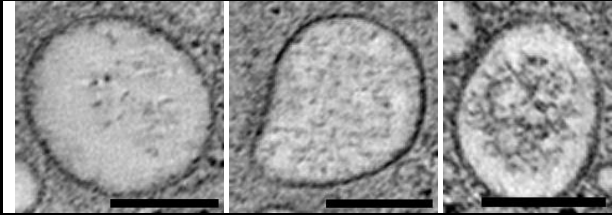
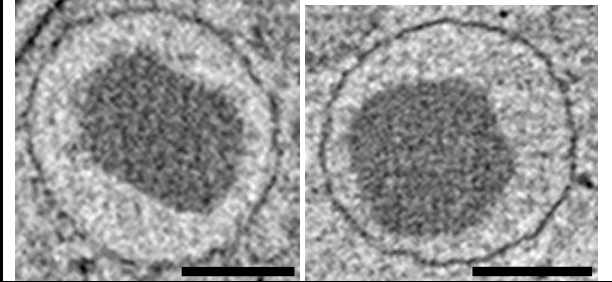
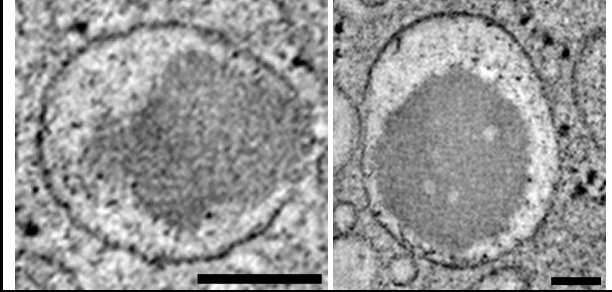


**Figure 4.1** Schematic diagram showing the transition of insulin granule appearance (upper row) and respective examples of raw data (bottom row).

(A) Immature granules with incomplete insulin core. (B) Mature granules with complete insulin core located at central of the organelle. (C) The crystal is closer to organelle membrane prior to release of insulin. This type of insulin granules usually appears close or proximal to cell membrane (red arrow). (D) Newly formed vesicles usually appear smaller than immature granules and are usually close to the cell membrane (red arrow). The order of the event is summarised and simplified from Fig. 4. (Schuit et al., 2002) and Fig. 3 (Guinamard et al., 2010). Scale bars: 100 nm.

Insulin granules were divided into two distinctive ‘types’; the ‘immature granules’ and the ‘mature granules’ based on their morphology (**Figure 4.2**). The immature insulin granules were observed to have either an empty luminal space, or ‘undeveloped’ insulin cores that presented as dispersed dots within the luminal space. These dots measured between ~4-11 nm. Both were assigned to Insulin Granule Class 1 (IG\_C1). The ‘mature granules’ appeared to have a more complete or crystal-like insulin core which presented as a ‘dense’ core within the lumen space. When the insulin core was seen to be spatially separate from the organelle membrane and located towards the centre of the luminal space, this type of insulin granule was assigned to Insulin Granule Class 2 (IG\_C2). In some cases the insulin cores were in contact with the organelle membrane and/or sometimes the

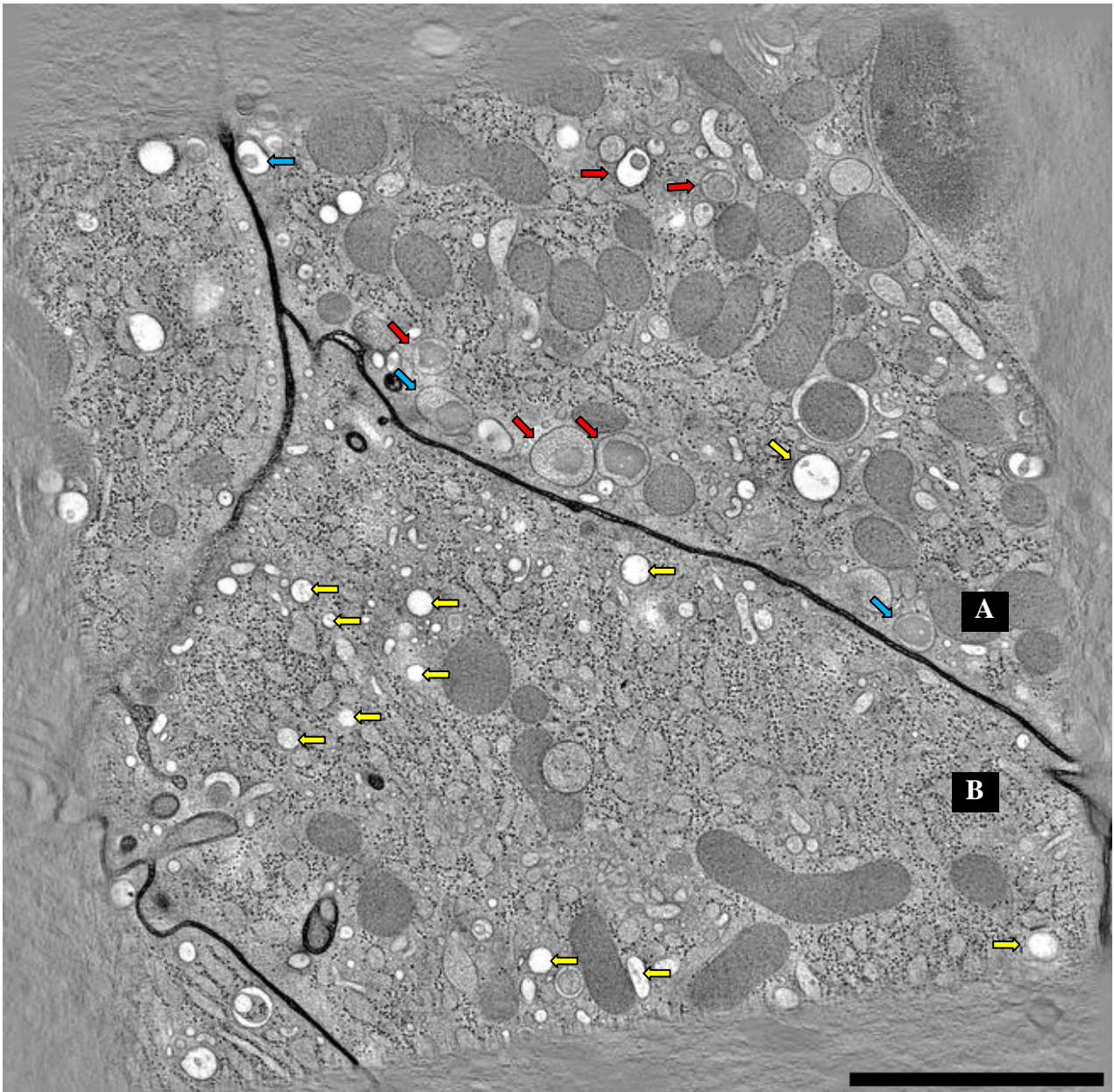
luminal spaces appeared darker or denser (not shown in the figure), they were assigned to Insulin Granule Class 3 (IG\_C3).

	<p>IG_C1</p> <p>Immature, unbound insulin</p>
	<p>IG_C2</p> <p>Mature, crystalline insulin granule</p>
	<p>IG_C3</p> <p>Mature, attached insulin crystalline granule and/or</p>

**Figure 4.2 Image classes for insulin granules.**

Class 1 of Insulin granules are defined as ‘Immature’ and the core insulin is incompletely developed. In Mature Granules’ the core insulin is more completely developed. Class 2 contained ‘crystal-like’ insulin cores within the IG membrane. Class 3 contained crystalline insulin granules that were seen to be attached to the granule membrane. Scale bars: 100 nm.

Insulin release from non-stimulated cells is a sustained, slow release process of newly formed vesicles triggered independently of sugar (D'Ambra et al., 1990, Efrat et al., 1993). However images of completely ruptured insulin granules releasing insulin were not detected in the large tomogram. The whole cell tomogram (**Figure 4.3**) shows insulin granules of each class (i.e. IG\_C1, IG\_C2 and IG\_C3) located at different distance from the cell membrane (of two cytoplasm environments, **A** and **B**).

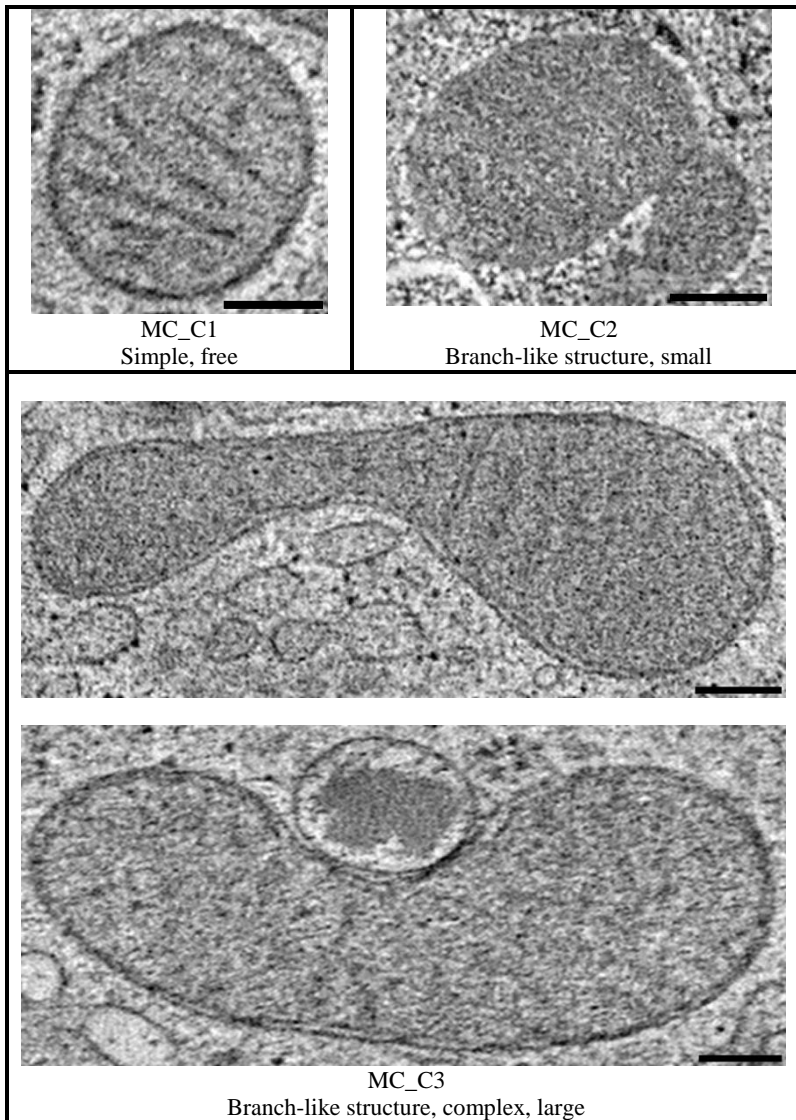


**Figure 4.3 Identification of insulin granule locations within a subcellular environment.**

In comparison with cell A where mature granules Class 2 (red arrows) and Class 3 (blue arrows) are seen, cell B has appears to have more immature granules (yellow arrow). Most of the mature granules (Class 2 and 3) are proximal to the cell membrane between cells A and B). This is because mature granules are ready to release insulin through cell membrane. Immature granules (yellow arrows) are distributed within cytoplasmic environment (shown in cell B). Higher numbers of mitochondria are seen in cytoplasm A (where mature granules are located) compared to cytoplasm B. Scale bar: 800 nm.

#### 4.2.1.2 Mitochondria

Mitochondria are also involved in insulin secretion in that they generate signals – by providing energy in the form of ATP – to initiate and support insulin secretion (Jitrapakdee et al., 2010). As shown in the tomogram (**Figure 4.3**, cell A), mitochondria are actively recruited to sub-cellular sites and this is consistent with the observations of others (Maechler et al., 1997, Chan, 2006, Chen and Chan, 2009) and also reviewed in (Wiederkehr and Wollheim, 2006). They are electron dense, double-layered organelles that, with their characteristic cristae, are relatively easy to identify. ‘Smaller’ mitochondria mostly appear to be spherical in shape and are simple in terms of their characteristic structure. Here, ‘smaller’ mitochondria were considered as having a diameter of ~270-300 nm with similar sub-volume box size (i.e. XYZ 3-Dimension) ~300 x 300 x 300 nm. Such mitochondria have been categorised as Mitochondria Class 1 (MC\_C1, **Figure 4.4**). Mitochondria can however undergo fusion and fission events (Wiederkehr and Wollheim, 2006) resulting in what appears to be a range of dynamic shapes that are referred to as ‘branch-like structures’. Mitochondria resulting from fusion and fission events appear to have a similar range of sub-volumes box sizes, (~ 600 nm x 600 nm x 600 nm) and were assigned to Mitochondria Class 2 (MC\_C2, Figure 4.4). Other mitochondria were considerably larger and varied in their diameter (from 900 nm to 2000 nm) compared to MC\_C2 (~520-850 nm). They were assigned to Mitochondria Class 3 (MC\_C3, Figure 4.4).



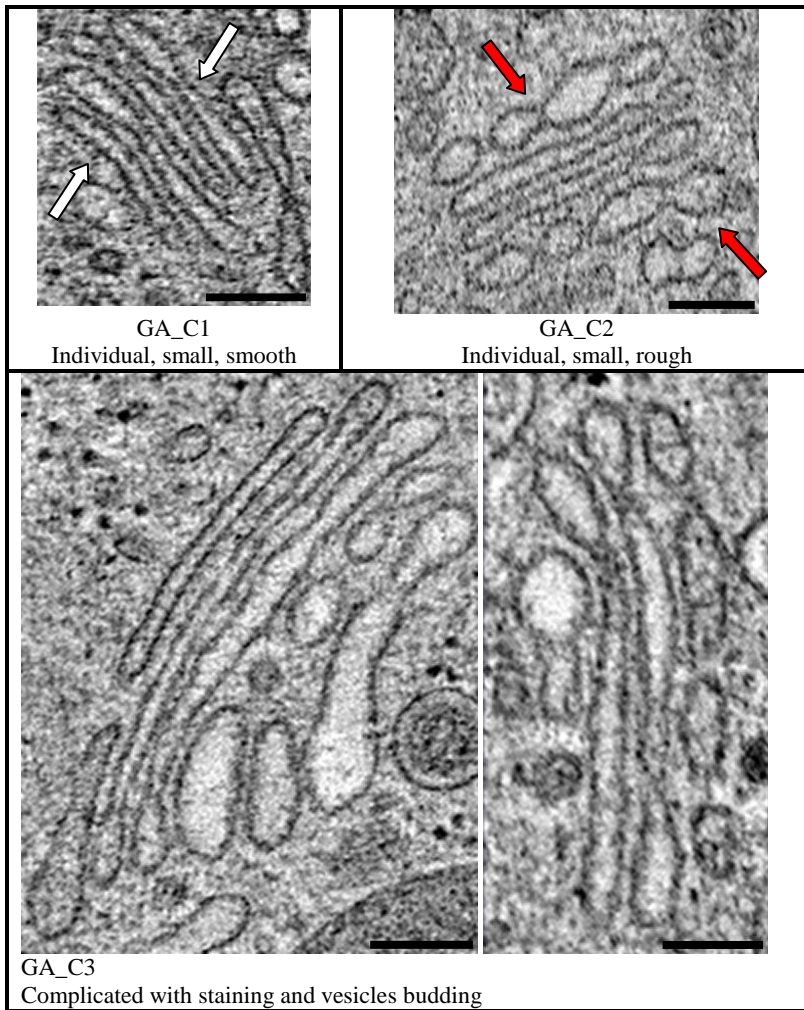
**Figure 4.4 Image classes for mitochondria.** Mitochondria show three groups of significantly different appearances. Class 1 contains 'Simple' spherical mitochondria. Class 2 contained 'Branch-like structure' mitochondria that are similar in size to class 1. Class 3 contained elongated mitochondria. Scale bars: 100 nm.

### 4.2.1.3 The Golgi apparatus

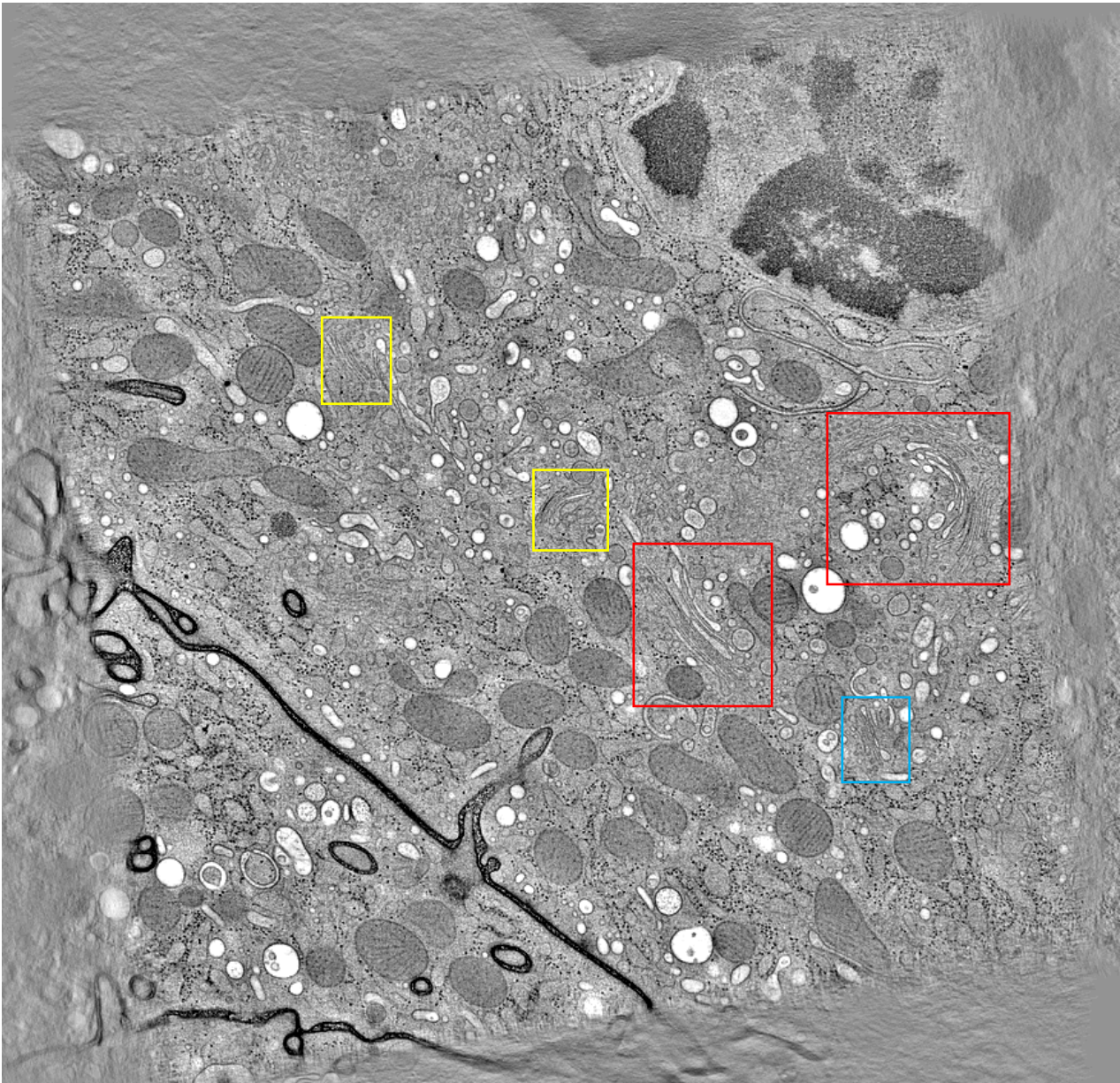
In terms of diabetes, the Golgi apparatus stacks are involved in transporting insulin after the protein is synthesised on the rough endoplasmic reticulum (Marsh et al., 2001a, van Meel and Klumperman, 2008). The Golgi apparatus (or Golgi complex) consists of a stack of cisternae. Typically each Golgi apparatus consists of about 5 to 7 cisternae. Golgi apparatus structures that were relatively small in terms of sub-volume XYZ 3-Dimension sizes (X: 428-1075 nm, Y: 428-1075 nm and Z: 535-749 nm) were classified as Golgi Apparatus Class 1 (GA\_C1) and Golgi Apparatus Class 2 (GA\_C2). Classes 1 and 2 differ in that the cisternae of Class 1 are ‘smoother’ than those of Class 2 (**Figure 4.5**). ‘Smoother’ refers to cisternae membranes being almost linear in their long axis while ‘rougher’ refers to more ‘irregular shapes’ of cisternae membrane (refer to images of raw data in **Figure 4.5**, marked with white arrows and red arrows respectively). Larger Golgi complexes were also observed. Their cisternae are not only rougher than in Class 1 and Class 2 but they also have more complex structures which appear to exhibit vesicle budding. These larger Golgi complexes were assigned to Golgi Apparatus Class 3 (GA\_C3). The cisternae were typically wider (up to 70 nm), and/or longer (between 1700 nm to 2500 nm), compared to those of smaller Golgi stacks (10 nm to 30 nm width and 400 nm to 1000 nm length). As the cisternae stacks of GA\_C3 were often ‘broken’ into a number of cisternae membranes in the cross-sectional/2D image slices, this increased the number of cisternae membranes in the stack to be segmented (i.e. ~ 7 cisternae membranes to 20 membranes per image slice).

The trans-Golgi Network (TGN) is of particular importance as this is the site where the insulin is thought to be sorted into vesicles. The TGN also contains processing enzymes and after budding from the Golgi apparatus will mature into vesicles in which pro-insulin is processed into insulin and stored in preparation for regulated secretion (van Meel and Klumperman, 2008, Emr et al., 2009). This is thought to influence the Golgi appearance. For example GA\_C3 has more budding vesicles and neighbouring vesicles (**Figure 4.6**, marked with red box) as compared to smaller Golgi stacks (i.e. Golgi apparatus Class 1 and 2). As seen in the same figure, the difference between Class 1 (yellow box) and Class 2 (blue box) is where the cisternae in Class 2 are rougher than Class 1. Class 2 also shown vesicle buds but in smaller amounts compared to Class 3.





**Figure 4.5** Image classes for the Golgi apparatus.  
Scale bar: 100 nm.



**Figure 4.6** Examples of three image classes of the GA.

Three types of the Golgi apparatus; GA\_C1 (yellow), GA\_C2 (blue) and GA\_C3 (red). GA\_C1 (yellow box) and GA\_C2 (blue box) are 'smaller' than GA\_C3 (red box) where both Golgi types have no or less neighbouring and budding vesicles.

**Table 4.1** lists key organelles sub-classes according to their image features and the numbers of sub-volumes of each class are provided. Insulin granules recorded 3 sub-classes named as IG\_C1 (96 sub-volumes), IG\_C2 (43 sub-volumes) and IG\_C3 (18 sub-volumes). Mitochondria also listed 3 sub-classes, MC\_C1 (25 sub-volumes), MC\_C2 (10 sub-volumes) and MC\_C3 (156 sub-volumes). The Golgi apparatus also recorded 3 sub-classes according to their image features, they are GA\_C1 (10 sub-volumes), GA\_C2 (9 sub-volumes) and GA\_C3 (56 sub-volumes). Classification in this manner has resulted in sub-classified particle data sets which are structurally much more homogeneous. This in turn provides cleaner datasets for the optimisation of segmentation

parameters and to yield insights into the process of insulin granule formation and structural changes of mitochondria and Golgi apparatus.

**Table 4.1 Three sub-classes were assigned to each of key organelle; insulin granules, mitochondria and the Golgi apparatus.** (A) 3 sub-classes of insulin granules; IG\_C1 (represents immature insulin granules), IG\_C2 and IG\_C3 (represent different features of mature insulin granules). (B) MC\_R1, MC\_R2 and MC\_R3, are 3 sub-classes for mitochondria. MC\_C3 has recorded highest numbers of sub-volumes compared to other sub-classes. (C) Golgi apparatus, with complex cisternae stack and diverse cisternae membrane morphologies and sizes were classified into three significant image features classes, i.e. GA\_C1, GA\_C2 and GA\_C3.

(A) Insulin granules				
Image Class	# Sub-volumes	minX, maxX	minY, maxY	minZ, maxZ
IG_C1	96	minX: 120 nm maxX: 250 nm	minY: 142 nm maxY: 250 nm	minZ: 110 nm maxZ: 250 nm
IG_C2	43	minX: 181 nm maxX: 600 nm	minY: 168 nm maxY: 600 nm	minZ: 120 nm maxZ: 570 nm
IG_C3	18	minX: 181 nm maxX: 588 nm	minY: 168 nm maxY: 600 nm	minZ: 120 nm maxZ: 570 nm
(B) Mitochondria				
Image Class	# Sub-volumes	minX, maxX	minY, maxY	minZ, maxZ
MC_C1	25	minX: 120 nm maxX: 400 nm	minY: 195 nm maxY: 400 nm	minZ: 185 nm maxZ: 400 nm
MC_C2	10	minX: 220 nm maxX: 600 nm	minY: 195 nm maxY: 600 nm	minZ: 185 nm maxZ: 600 nm
MC_C3	156	minX: 589 nm maxX: 1500 nm	minY: 570 nm maxY: 1500 nm	minZ: 550 nm maxZ: 1500 nm
(C) The Golgi apparatus				
Image Class	# Sub-volumes	minX, maxX	minY, maxY	minZ, maxZ
GA_C1	10	minX: 170 nm maxX: 450 nm	minY: 188 nm maxY: 500 nm	minZ: 185 nm maxZ: 480 nm
GA_C2	9	minX: 170 nm maxX: 500 nm	minY: 250 nm maxY: 500 nm	minZ: 297 nm maxZ: 480 nm
GA_C3	56	minX: 681 nm maxX: 1200 nm	minY: 449 nm maxY: 1200 nm	minZ: 429 nm maxZ: 1100 nm

In conclusion, this work has resulted in ~400 image stacks of the Golgi apparatus (75), mitochondria (191) and insulin granules (157) being subdivided into 3 sub-classes of insulin granule, 3 sub-classes of mitochondria and 3 sub-classes of the Golgi apparatus. **Figures 4.2, 4.4 and 4.5** present proposed sets of models of the structural transitions between these sub-classes respectively. Each sub-class type is now more structurally homogeneous providing test sets to evaluate parameter settings of the best processing pipeline strategies identified in Chapter 3.

#### 4.2.2 Parameter optimisation on each sub-class

The aim of the next experiment is to identify the top three optimal segmentation protocols for the 9 sub-classes shown in **Table 4.1 (Section 4.2.1)** which represent insulin granules (3 sub-classes), mitochondria (3 sub-classes) and the Golgi apparatus (3 sub-classes), without sacrificing the accuracy of contouring each of the sub-volumes within each class. Four sub-volumes were

randomly selected from each class. The mesh model of every sub-volume produced by manual segmentation had different contour volume (CV) and mesh surface area (MSA) values (Note: The importance of the CV and MSA values was discussed in Chapter 3, Section 3.3.4). For this experiment, CV and MSA values of every sub-class were averaged in order to calculate the mean value of CV and MSA of each respective sub-class. Then, the optimisation of parameter settings for all nine method flows was conducted.

The MSA scoring system uses the value of mesh surface area that was calculated from the mesh model of both segmentations, i.e. manual (test model) and computational. A more detailed description of the MSA scoring method is described in (Chapter 3, Section 3.3.4). For sub-volumes for which more than 3 of the ‘best’ settings met the above requirements, the difference between MSA values of automated and manual segmentation was compared manually and the best 3 selected. The process of refining these ‘best’ method settings continued until the rest of the sub-class was accurately segmented using the same optimised settings of these 3 methods. The aim of this was to identify ‘standard’ method optimised settings that accurately segment all 4 sub-volumes of a given sub-class. This process was repeated for each sub-class. Ultimately, the ‘best’ settings of the top 3 methods have been identified in every sub-class.

#### 4.2.2.1 *Insulin granules*

For sub-class 1 of insulin granules (IG\_C1) all 9 method flows of every sub-volume achieved scores of 5 (refer to the example shown in **Figure 3.14**) indicating that the MSA were within 95% to 105% compared to their respective manual test models. The image features described for IG\_C1 are not complex and so the relatively straightforward identification of optimised settings was not unexpected. Of these, the best methods identified were **M5** (3D Median filter followed by *watershed* and mathematical morphology algorithm), **M8** (NAD filter followed by *watershed* and mathematical morphology algorithm) and **M9** (Bilateral filter followed by *watershed* and mathematical morphology algorithm) (**Figure 4.7A**). Besides the fact that the organelle diameter of immature granules is smaller than that of mature granules, and generally they have similar diameter/size which is easy and fast for organelle extraction, the simple structure of the immature insulin core – normally shown as dispersed dots in luminal space simplified parameter optimisation. M5, M8 and M9 were also identified as the 3 ‘best’ methods for all 4 representative sub-volumes of IG\_C2 and IG\_C3 (i.e. image classes for mature granules). With more complex characteristics (compared to IG\_C1 or immature insulin granules) finding the ‘best’ segmentation

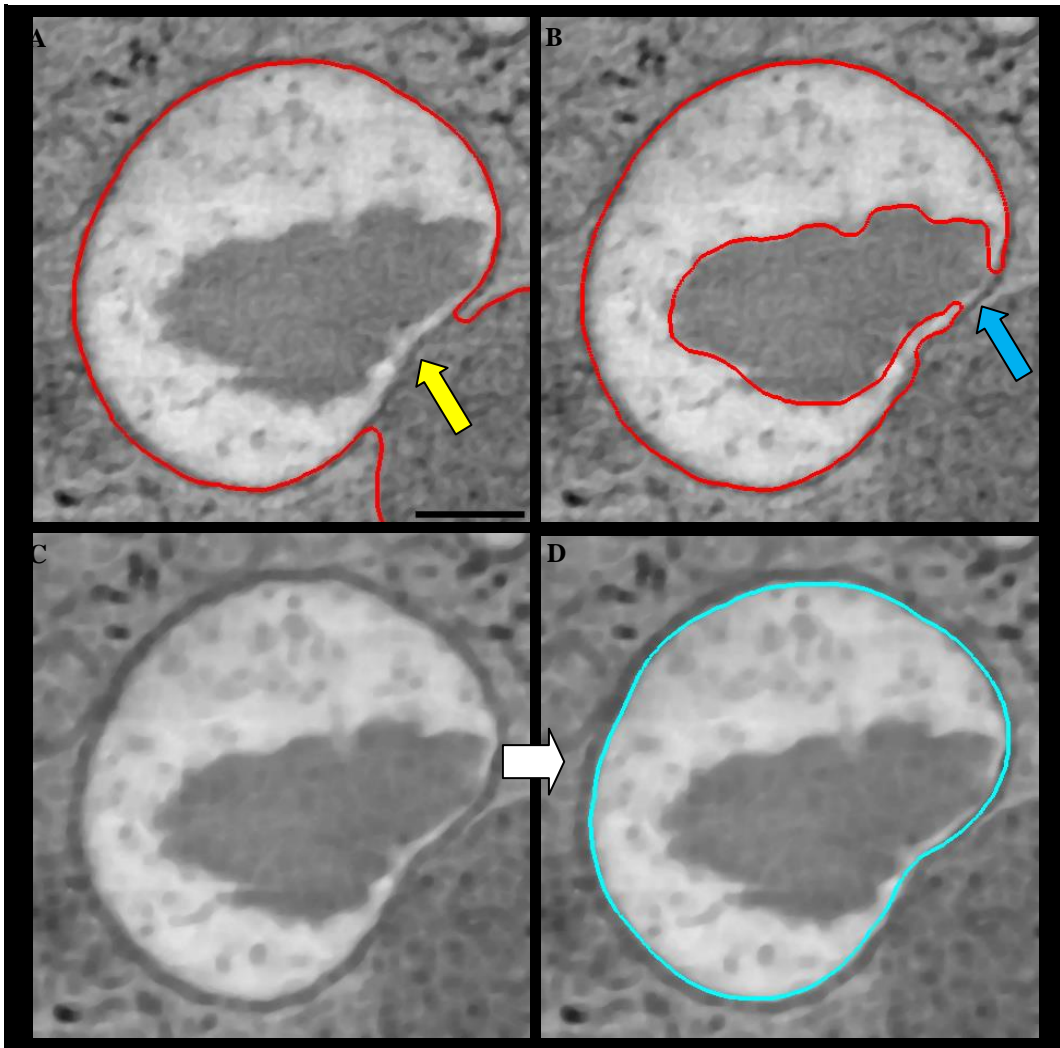
result with optimised settings for all 4 representative sub-volumes were more difficult and tricky (**Figure 4.7B**).

**Table 4.2 Analysis for the top 3 methods for insulin granule segmentation.**

M5 (3D median filter followed by watershed), M8 (non-linear anisotropic diffusion filter followed by watershed) and M9 (bilateral filter followed by watershed) were identified as the top 3 method flows for all insulin granules sub-classes.

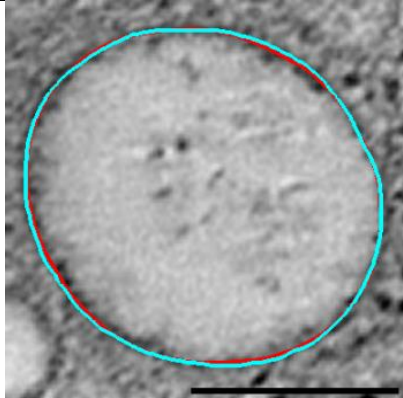
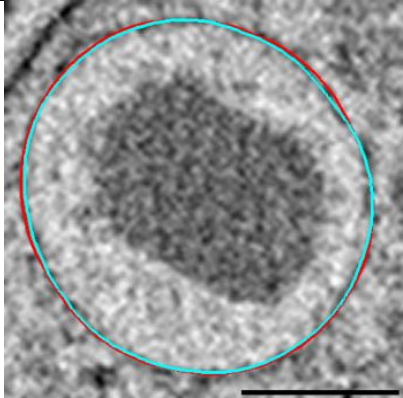
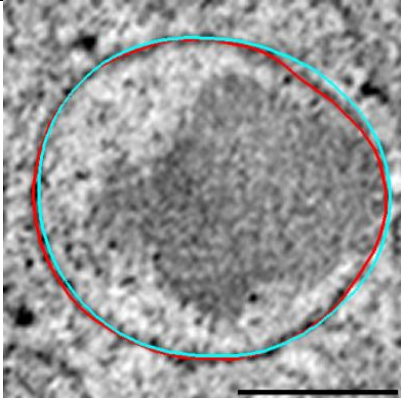
Identification of optimised settings of each method flow and MSA Scoring											
Sub-class	Sub-Volume	M1	M2	M3	M4	M5	M6	M7	M8	M9	The best 3
IG_C1	IG_C1A	5	5	5	5	5	5	5	5	5	M5, M8, M9
	IG_C1B	5	5	5	5	5	5	5	5	5	M5, M8, M9
	IG_C1C	5	5	5	5	5	5	5	5	5	M5, M8, M9
	IG_C1D	5	5	5	5	5	5	5	5	5	M5, M8, M9
IG_C2	IG_C2A	4	4	4	4	4	4	4	4	4	M5, M8, M9
	IG_C2B	3	3	2	4	5	4	4	5	4	M5, M8, M9
	IG_C2C	4	4	4	4	4	4	4	4	4	M5, M8, M9
	IG_C2D	3	3	3	4	5	4	5	5	5	M5, M8, M9
IG_C3	IG_C3A	2	2	4	4	4	3	4	4	4	M5, M8, M9
	IG_C3B	3	3	3	3	5	3	3	5	4	M5, M8, M9
	IG_C3C	3	4	4	4	4	3	4	4	5	M5, M8, M9
	IG_C3D	3	4	4	4	4	3	4	5	5	M5, M8, M9

Since image features of IG\_C2 and IG\_C3 are different in some points (refer to **Section 4.2.1**, see **Figure 4.2**), different settings of the top 3 methods (i.e. M5, M8 and M9) were determined. 3 identical method flows were identified as 3 best methods for all 3 sub-classes, IG\_C1 (**Figure 4.8 panel A**), IG\_C2 (**Figure 4.8 panel B**) and IG\_C3 (**Figure 4.8 panel C**) where M8 is the best, M5 is the second best and M9 is the third best based on the conditions tested. Different image features described for these classes appear to affect the segmentation results. In particular the watershed algorithm and mathematical operations settings are different for Insulin Granules Class 1, 2 and 3, while settings of image filtration methods (NAD filter, 3D Median filter, and Bilateral filter) remained the same for all insulin granules classes.



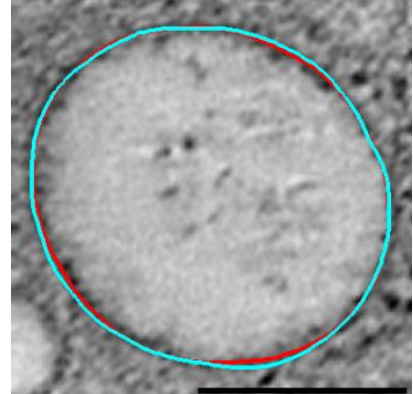
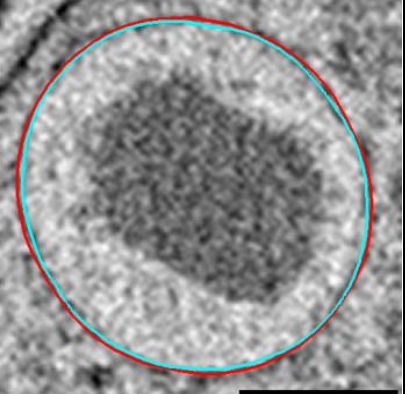
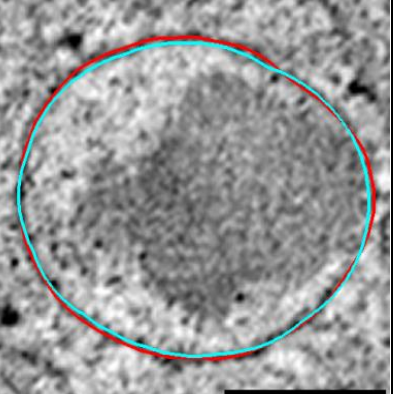
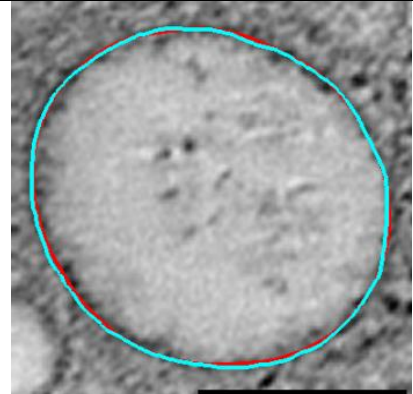
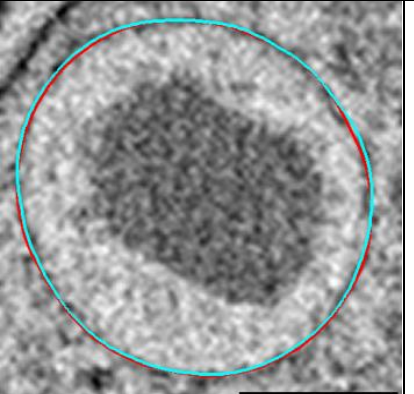
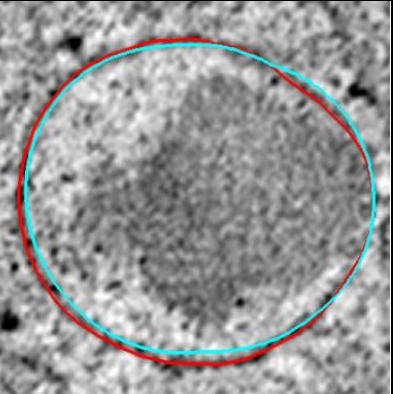
**Figure 4.7 Best methods with optimised settings for insulin granules.**

(A-D) Example of segmentation result of IG\_C3A. **A** and **B** show 2 segmentation results given a score of 2. **A** is the result of Method 1 (**M1**) using Gaussian filter followed by watershed segmentation. The yellow arrow shows the area of organelle membrane proximal to neighbouring compartment and corresponding trace deviation. **B** is the result of Method 2 (**M2**) using minimum filter followed by watershed segmentation. The blue arrow shows an example of 'broken contours'. **C-D** is the examples of segmentation result scored 5 using Method 8 (**M8**) (non-linear anisotropic diffusion filter followed by watershed). Contour (cyan) nicely traced on organelle membrane after applying watershed and mathematical morphologies function on the image. Scale bar: 100 nm.

(A) IG_C1	(B) IG_C2	(C) IG_C3
IG_C1A_M8	IG_C2A_M8	IG_C3A_M8
M8 Settings NAD filter K value: 5.6 Iteration: 20 Watershed H: 1.0 L: 0.0 S: 0.3 Mathematical operation Initial <i>Opening</i> : 4 <i>Opening</i> : 14 Final <i>Closing</i> : 7 Score: 5	M8 Settings NAD filter K value: 5.6 Iteration: 20 Watershed H: 1.5 L: 0.0 S: 0.3 Mathematical operation Initial <i>Opening</i> : 4 <i>Opening</i> : 10 Final <i>Closing</i> : 7 Score: 5	M8 Settings NAD filter K value: 5.6 Iteration: 20 Watershed H: 3.0 L: 0.5 S: 0.3 Mathematical operation Initial <i>Opening</i> : 4 <i>Opening</i> : 10 Final <i>Closing</i> : 4 Score: 5
		

**Figure 4.8 (a)** Comparison between manual tracing (red contours) and ‘best’ automated methods (cyan contours) on raw dataset (i.e. unfiltered).

The optimal settings for the best filter identified for each sub-class are provided. Best methods assigned for insulin granules sub-classes (IG\_C1, IG\_C2 and IG\_C3) are identical; i.e. M8 (the best), M5 (second best) and M9 (third best). Each segmentation result scored 5, the highest score in MSA scoring system. Scale bars: 100 nm

(A) IG_C1	(B) IG_C2	(C) IG_C3
IG_C1A_M5	IG_C2A_M5	IG_C3A_M5
M5 Settings 3D Median filter Iteration: 3 Watershed H: 1.0 L: 0.0 S: 0.3 Mathematical operation Initial Opening: 4 Opening: 14 Final Closing: 7 Score: 5	M5 Settings 3D Median filter Iteration: 3 Watershed H: 1.5 L: 0.0 S: 0.3 Mathematical operation Initial Opening: 4 Opening: 10 Final Closing: 7 Score: 5	M5 Settings 3D Median filter Iteration: 3 Watershed H: 3.0 L: 0.5 S: 0.3 Mathematical operation Initial Opening: 4 Opening: 10 Final Closing: 4 Score: 5
		
IG_C1A_M9	IG_C2A_M9	IG_C3A_M9
M9 Settings Bilateral filter SpaceSigma: 1.5 RangeSigma: 23.8 Watershed H: 1.0 L: 0.0 S: 0.3 Mathematical operation Initial Opening: 4 Opening: 14 Final Closing: 7 Score: 5	M9 Settings Bilateral filter SpaceSigma: 1.5 RangeSigma: 23.8 Watershed H: 1.5 L: 0.0 S: 0.3 Mathematical operation Initial Opening: 4 Opening: 10 Final Closing: 7 Score: 5	M9 Settings Bilateral filter SpaceSigma: 1.5 RangeSigma: 23.8 Watershed H: 3.0 L: 0.5 S: 0.3 Mathematical operation Initial Opening: 4 Opening: 10 Final Closing: 4 Score: 5
		

**Figure 4.9 (b) Comparison between manual tracing (red contours) and ‘best’ automated methods (cyan contours) on raw dataset (i.e. unfiltered).**

The optimal settings for the best filter identified for each sub-class are provided. Best methods assigned for insulin granules sub-classes (IG\_C1, IG\_C2 and IG\_C3) are identical; i.e. M8 (the best), M5 (second best) and M9 (third best). Each segmentation result scored 5, the highest score in MSA scoring system. Scale bars: 100 nm



#### 4.2.2.2 Mitochondria

Mitochondrial sub classes MC\_C1, MC\_C2 and MC\_C3 differ in terms of image features, as described in **Section 4.2.1**. The diversity of mitochondrial shapes and conditions influenced the settings of automated segmentation methods in tracing such mitochondria ‘branch-like’ or ‘elongated’ structure (**Figure 4.9**). Method flows M8 (the best), followed by M5 and M9 were identified as the top 3 method flows for class MC\_C1 (**panel A** of **Figure 4.10 a, b and c**). They were selected based on mesh surface area (MSA) scoring system.

For Mitochondria Class 2 (MC\_C2) and Class 3 (MC\_C3), the mitochondria shape is influenced by the opposing processes of mitochondrial fusion and fission (Huang et al., 2011). The sizes of 3-Dimension (3D) sub-volumes (i.e. X x Y x Z) of mitochondria MC\_C2 ranged from ~200 nm x 200 nm x 200 nm to ~600 nm x 600 nm x 600 nm. For MC\_C2, Method 8 (M8) (the best), followed by Method 5 (M5) and Method 9 (M9) with respective optimal settings have been identified to accurately segment these double-layered organelles (**panel B** of **Figure 4.10 a, b and c**).

In contrast when either fusion or fission dominates, mitochondrial elongation or fragmentation is thought to occur (Huang et al., 2011) and these mitochondria were classified in the third mitochondria sub-class, i.e. MC\_C3. The dynamic mitochondria ultrastructures may be involved in allowing mitochondria to interact with each other or other organelles through molecular interaction (Huang et al., 2011). The diameter of the longest axis for mitochondria MC\_C3 was determined to be ~600 nm - 1500 nm. More discussion about key components of mitochondria that play important roles in mitochondrial functions and development could be found in (Youle and van der Bliek, 2012). Only 2 method flows, Method 8 (M8) (the best) and Method 5 (M5) with respective optimal settings were found to be best computational methods for sub-group MC\_C3 (**panel C** of **Figure 4.10 a, b and c**).

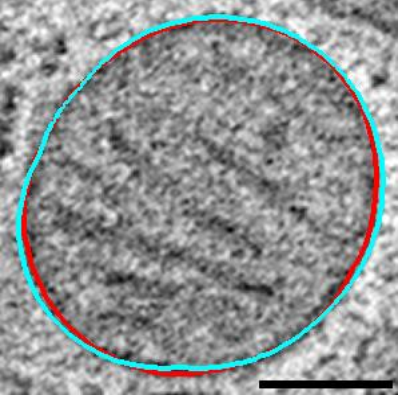
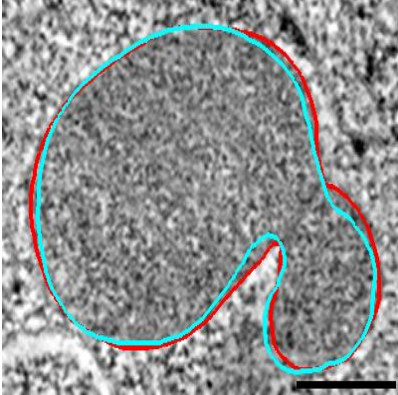
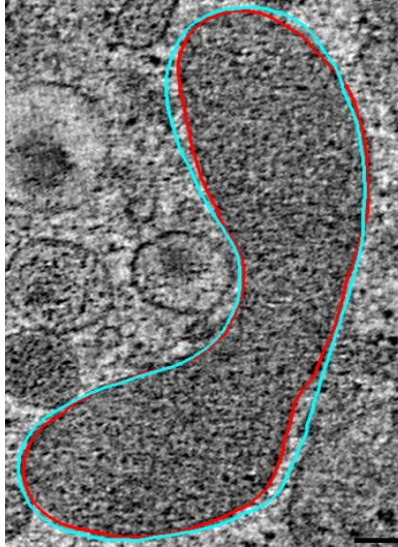
The optimised settings of M5 and M8 for MC\_C3 are different to the settings identified for MC\_C2 and MC\_C1. For M5, the homogeneity filter in *maprank* function (*CoAn* Software) is ‘turned on’. While the K value of non-linear anisotropic diffusion (NAD) – image filter used in M8 for MC\_C3 – is higher. Both methods; Method 8 and Method 5, scored 5 in MSA scoring and were recorded as ‘best methods’ for MC\_C1 (**panel A**), MC\_C2 (**panel B**) and MC\_C3 (**panel C**) of **Figure 4.10 a, b and c**.

(A) Identification of optimised settings of each method flow and MSA Scoring											
Sub-class	Sub-Volume	M1	M2	M3	M4	M5	M6	M7	M8	M9	The best 3
MC_C1	MC_C1A	4	3	3	3	5	3	4	4	5	M5, M8, M9
	MC_C1B	4	4	4	3	5	3	4	5	5	M5, M8, M9
	MC_C1C	4	4	4	3	4	3	4	5	4	M5, M8, M9
	MC_C1D	3	3	3	3	5	3	4	5	5	M5, M8, M9
MC_C2	MC_C2A	4	5	5	5	5	4	5	5	5	M5, M8, M9
	MC_C2B	5	4	5	4	5	4	4	5	4	M5, M8, M9
	MC_C2C	4	4	5	4	5	5	4	5	4	M5, M8, M9
	MC_C2D	5	4	4	5	5	5	4	5	5	M5, M8, M9
MC_C3	MC_C3A	5	4	3	4	5	3	4	5	3	M5, M8
	MC_C3B	4	4	4	4	5	4	4	5	3	M5, M8
	MC_C3C	4	4	3	4	5	4	4	5	4	M5, M8
	MC_C3D	5	4	4	3	5	3	3	5	3	M5, M8

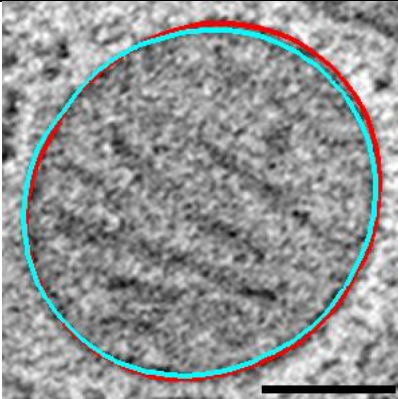
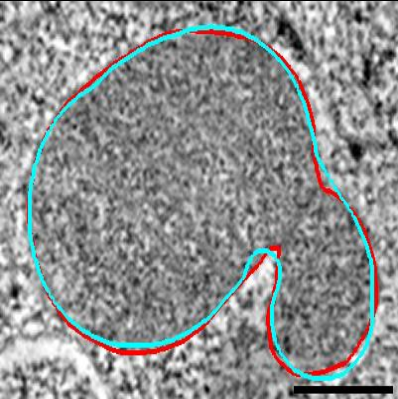
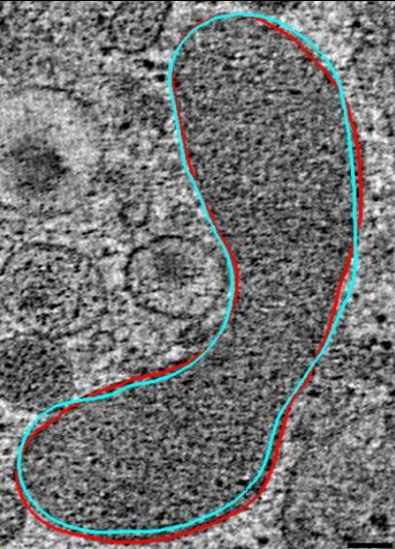
**Figure 4.10 Best methods with optimised settings for mitochondria.**

(A) The list of best method flows for 3 sub-class of mitochondria. (B-E) Segmentation result of mitochondrion example, MC\_C3A (with complete branching due to either fusion or fission). Red contours represent manual segmentation. Cyan contours represent computational segmentation (i.e. Method 5: 3D Median filter and watershed segmentation). From this example, the elongated shape changed from **B** to **C**. Yellow arrow in **D** shows the area where the density value is different with mitochondrion marked **1** and **2**. This information (i.e. mean density) affects the computational segmentation to determine the region of interest (i.e. region **1** and **2** in **D** and **E**) to be segmented. Scale bar: 200 nm.

(A) MC_C1	(B) MC_C2	(C) MC_C3
MC_C1A_M8	MC_C2A_M8	MC_C3A_M8
M8 Settings NAD filter K value: 5.6 Iteration: 20 Watershed H: 1.0 L: 0.0 S: 0.3 I: ON Mathematical operation Initial <i>Opening</i> : 4 <i>Opening</i> : 14 Final <i>Closing</i> : 7 Score: 5	M8 Settings NAD filter K value: 5.6 Iteration: 20 Watershed H: 1.5 L: 0.0 S: 0.3 I: ON Mathematical operation Initial <i>Opening</i> : 4 <i>Opening</i> : 10 Final <i>Closing</i> : 7 Score: 5	M8 Settings NAD filter K value: 5.6 Iteration: 20 Watershed H: 1.5 L: 0.0 S: 0.3 I: ON Mathematical operation Initial <i>Opening</i> : 4 <i>Opening</i> : 10 Final <i>Closing</i> : 4 Score: 5
		

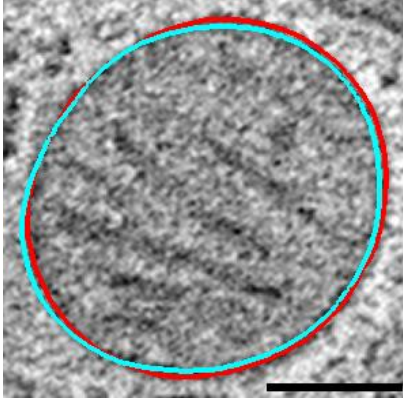
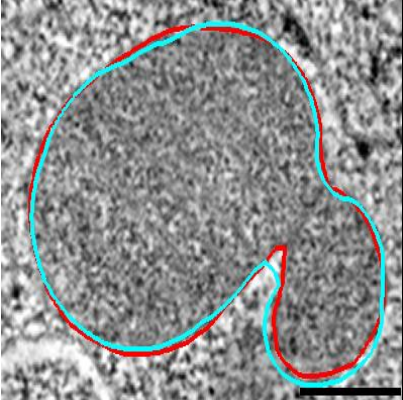
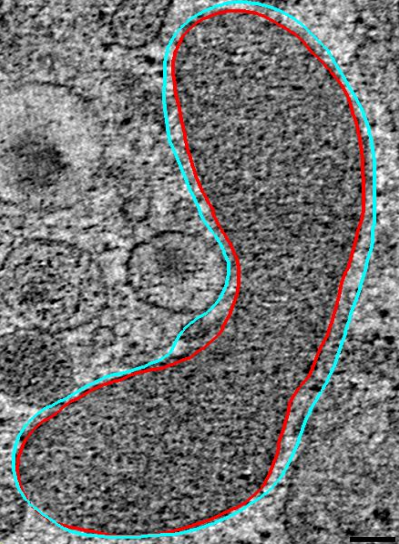
**Figure 4.11 (a) Optimised settings for different mitochondria classes.**

Noted that the ‘I’ function in watershed algorithm is turned on in order to segment an electron dense organelle, mitochondria. MC\_C1, MC\_C2 and MC\_C3 have identical best method flows; M8 (the best), M5 (the second) and M9 (the third). Every example has shown scored 5, the highest score of MSA scoring system, except M9 for MC\_C3 (score 3). Red contours represent manual tracing and cyan represent automated segmentation methods. Scale bars: 100 nm

MC_C1A_M5	MC_C2A_M5	MC_C3A_M5
M5 Settings 3D Median filter Iteration: 3 Watershed H: 1.0 L: 0.0 S: 0.3 I: ON Mathematical operation Initial <i>Opening</i> : 4 <i>Opening</i> : 14 Final <i>Closing</i> : 7 Score: 5	M5 Settings 3D Median filter Iteration: 3 Watershed H: 1.5 L: 0.0 S: 0.3 I: ON Mathematical operation Initial <i>Opening</i> : 4 <i>Opening</i> : 10 Final <i>Closing</i> : 7 Score: 5	M5 Settings 3D Median filter Iteration: 3 Watershed H: 1.5 L: 0.0 S: 0.3 I: ON Mathematical operation Initial <i>Opening</i> : 4 <i>Opening</i> : 10 Final <i>Closing</i> : 7 Score: 5
		

**Figure 4.12 (b) Optimised settings for different mitochondria classes.**

Noted that the 'I' function in watershed algorithm is turned on in order to segment an electron dense organelle, mitochondria. MC\_C1, MC\_C2 and MC\_C3 have identical best method flows; M8 (the best), M5 (the second) and M9 (the third). Every example has shown scored 5, the highest score of MSA scoring system, except M9 for MC\_C3 (score 3). Red contours represent manual tracing and cyan represent automated segmentation methods. Scale bars: 100 nm

MC_C1A_M9	MC_C2A_M9	MC_C3A_M9
M9 Settings Bilateral filter SpaceSigma: 1.5 RangeSigma: 23.8 Watershed H: 1.0 L: 0.0 S: 0.3 I: ON Mathematical operation Initial <i>Opening</i> : 4 <i>Opening</i> : 14 Final <i>Closing</i> : 7 Score: 5	M9 Settings Bilateral filter SpaceSigma: 1.5 RangeSigma: 23.8 Watershed H: 1.5 L: 0.0 S: 0.3 I: ON Mathematical operation Initial <i>Opening</i> : 4 <i>Opening</i> : 10 Final <i>Closing</i> : 7 Score: 5	M9 Settings Bilateral filter SpaceSigma: 1.5 RangeSigma: 23.8 Watershed H: 1.5 L: 0.0 S: 0.3 I: ON Mathematical operation Initial <i>Opening</i> : 4 <i>Opening</i> : 10 Final <i>Closing</i> : 7 Score: 3
		

**Figure 4.13 (c) Optimised settings for different mitochondria classes.**

Noted that the 'I' function in watershed algorithm is turned on in order to segment an electron dense organelle, mitochondria. MC\_C1, MC\_C2 and MC\_C3 have identical best method flows; M8 (the best), M5 (the second) and M9 (the third). Every example has shown scored 5, the highest score of MSA scoring system, except M9 for MC\_C3 (score 3). Red contours represent manual tracing and cyan represent automated segmentation methods. Scale bars: 100 nm

### 4.2.2.3 The Golgi apparatus

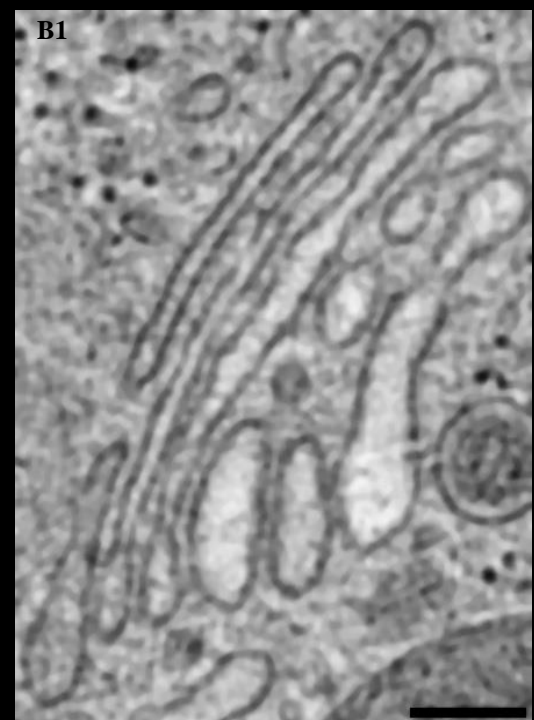
The Golgi apparatus (GA) or Golgi complex consists of stack of cisternae. Each slice of the GA sub-volumes not only includes a number of cisternae membranes (4-13 cisternae per GA) but also ‘free’ vesicles (i.e. general vesicles and/or transport vesicles). When observed, the distance between each cisternum is from 5 nm to 10 nm. Thus the minimum distance between each cisternum is set to 10 nm which then prevent those being segmented. While those ‘unwanted’ vesicles could be automatically deleted (due to optimising settings for accurate segmentation).

Golgi apparatus structures with smooth cisternae membranes (GA\_C1) exhibited consistent distances (6 – 10 nm) membranes. Their GA sub-volumes were accurately segmented with 3 best method flows; Method 8 (M8), Method 5 (M5) and Method 9 (M9) (**Figure 4.11** and **panel A of Figure 4.12 a and b**). Each of them scored 5 in MSA scoring. Rougher cisternae membranes with similar cisternae length and width describe the Golgi apparatus structures in class GA\_C2 for which similar best method flows were identified; M8 (the best) M5 (second best) and M9 (third best) (**Figure 4.11** and **panel B of Figure 4.12 a and b**). M8 and M5 scored 5 while M9 score 4. Visually, M9 is not acceptable for GA\_C2 as it failed to segment accurate cisternae membranes. Thus only 2 best method flows presented for GA\_C2. GA\_C3 have similar image features to GA\_C2 in terms of cisternae roughness but the length and the width amongst its cisternae were varied. Also the appearance of vesicles budding in some cisternae stacks made the Golgi stack more complex. Given the complexity of image features in this sub-class, identifying an optimal method for this sub-class was the most challenging. Like GA\_C2, GA\_C3 has also recorded 2 best methods; M8 and M5 where each scored 5 in MSA scoring (**Figure 4.11** and **panel C of Figure 4.12 a and b**).

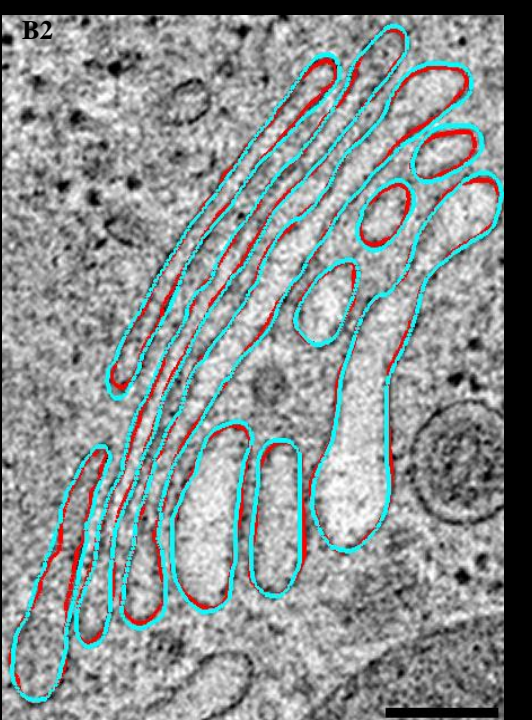
When observed, the GA\_C1 has recorded same settings of watershed algorithm and mathematical operations (**panel A of Figure 4.12 a and b**) for all 3 method flows. It shows that the Golgi apparatus of the sub-class ‘simple’ and less complex than the other 2 classes to be segmented. High-complexity of image features of the other 2 sub-classes (Class 2 and Class 3) decreased the signal to noise ratio of the Golgi apparatus which influenced the accuracy of segmentation results of other methods. Therefore 2 best methods with optimal settings for each class are acceptable. The rest of the method flows (i.e. Method 1, Method 2, Method 3, Method 4, Method 6, Method 7 and Method 9) however have scored 3 and below (according to MSA scoring) for all 4 representative sub-volumes and therefore were excluded from the ‘best’ method set.

(A) Identification of optimised settings of each method flow and MSA Scoring											
Sub-class	Sub-Volume	M1	M2	M3	M4	M5	M6	M7	M8	M9	The best 3
GA_C1	GA_C1A	3	3	3	3	5	4	4	5	3	M5, M8
	GA_C1B	3	3	3	3	5	3	3	5	3	M5, M8
	GA_C1C	4	4	3	2	5	3	3	5	4	M5, M8
	GA_C1D	3	3	3	3	5	3	3	5	3	M5, M8
GA_C2	GA_C2A	4	3	3	3	5	4	3	4	4	M5, M8
	GA_C2B	3	3	3	3	4	4	2	5	3	M5, M8
	GA_C2C	3	4	3	2	5	3	3	5	4	M5, M8
	GA_C2D	3	3	3	3	4	3	3	5	4	M5, M8
GA_C3	GA_C3A	3	3	3	2	3	3	3	5	4	M8
	GA_C3B	4	3	2	2	4	3	3	4	3	M8
	GA_C3C	3	3	3	2	4	3	3	4	3	M8
	GA_C3D	3	3	2	2	3	3	3	4	3	M8

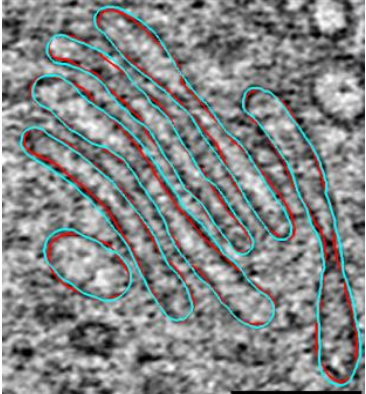
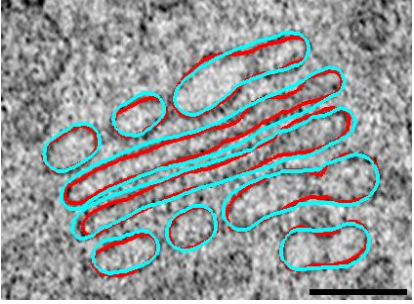
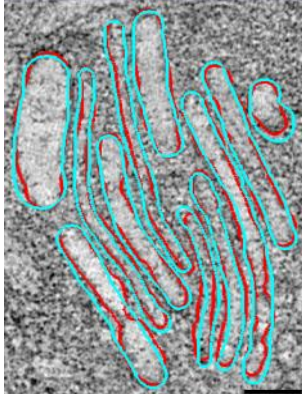
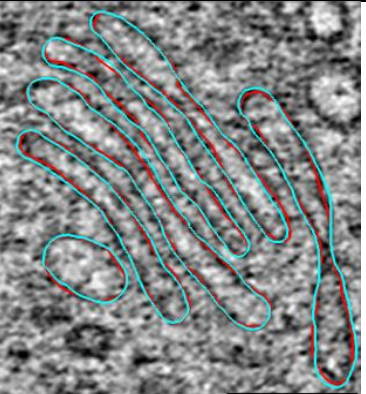
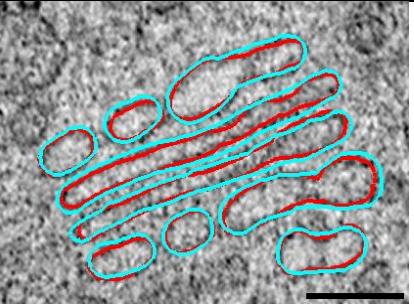
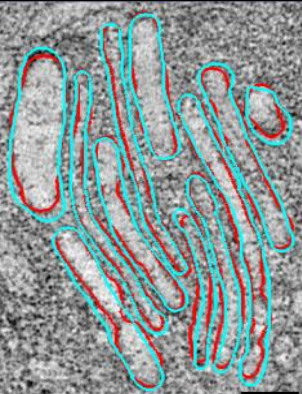


B1



B2

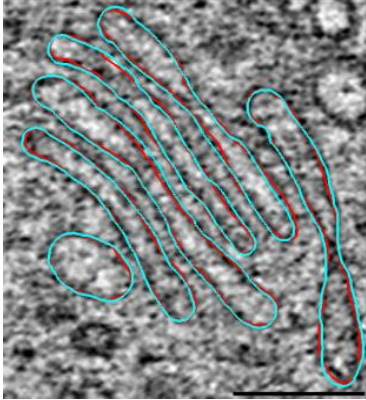
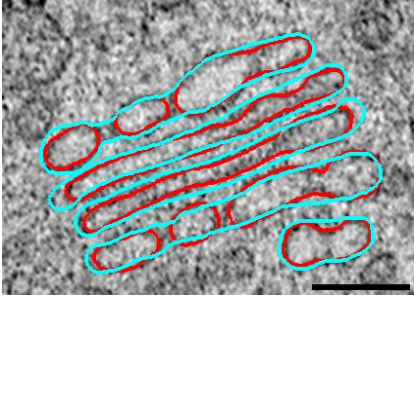
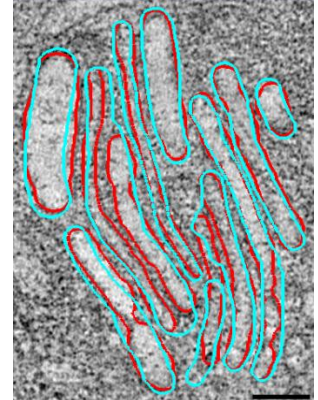
**Figure 4.14 Best methods identified for all 3 sub-classes of the Golgi apparatus.**  
 (A) List of best methods for the Golgi apparatus Class 1, 2 and 3. (B) An example of GA\_C3. (B1) GA\_C3A was filtered using non-linear anisotropic diffusion prior to segmentation with watershed algorithm. (B2) Red contours represent manual tracing, cyan represent Method 8 (M8) which scored 5 according to MSA scoring.

(A) GA_C1	(B) GA_C2	(C) GA_C3
GA_C1A_M8	GA_C2A_M8	GA_C3A_M8
M8 Settings NAD filter K value: 5.6, Iteration: 20 Watershed H: 2 L: 0.5S: 0.3 Mathematical operation Initial <i>Opening</i> : 4 <i>Opening</i> : 10 Final <i>Closing</i> : 7 Score: 5	M8 Settings NAD filter K value: 5.6, Iteration: 20 Watershed H: 2 L: 0.5S: 0.3 Mathematical operation Initial <i>Opening</i> : 4 <i>Opening</i> : 10 Final <i>Closing</i> : 7 Score: 5	M8 Settings NAD filter K value: 5.6, Iteration: 20 Watershed H: 2 L: 0.5S: 0.3 Mathematical operation Initial <i>Opening</i> : 4 <i>Opening</i> : 10 Final <i>Closing</i> : 7 Score: 5
		
GA_C1A_M5	GA_C2A_M5	GA_C3A_M5
M5 Settings 3D Median filter Iteration: 3 Watershed H: 1.0 L: 0.0 S: 0.3 Mathematical operation Initial <i>Opening</i> : 4 <i>Opening</i> : 14 Final <i>Closing</i> : 7 Score: 5	M5 Settings 3D Median filter Iteration: 3 Watershed H: 1.0 L: 0.0 S: 0.3 Mathematical operation Initial <i>Opening</i> : 4 <i>Opening</i> : 14 Final <i>Closing</i> : 7 Score: 5	M5 Settings 3D Median filter Iteration: 3 Watershed H: 1.0 L: 0.0 S: 0.3 Mathematical operation Initial <i>Opening</i> : 4 <i>Opening</i> : 14 Final <i>Closing</i> : 7 Score: 5
		

**Figure 4.15 (a) Optimised setting for different classes of the Golgi apparatus.**

Red contours represent manual tracing and cyan represent automated segmentation methods. All 3 method flows assigned as the best 3 methods for GA\_C1 has recorded the same settings of watershed and mathematical operations. Different optimal settings of watershed and mathematical operations were identified for each best method assigned for GA\_C2 and GA\_C3. Scale bars: 100 nm.



(A) GA_C1	(B) GA_C2	(C) GA_C3
GA_C1A_M9	GA_C2A_M9	GA_C3A_M9
M9 Settings Bilateral filter SpaceSigma: 1.5 RangeSigma: 23.8 Watershed H: 3.0 L: 0.5 S: 0.3 Mathematical operation Initial <i>Opening</i> : 4 <i>Opening</i> : 10 Final <i>Closing</i> : 4 Score: 5	M9 Settings Bilateral filter SpaceSigma: 1.5 RangeSigma: 23.8 Watershed H: 3.0 L: 0.5 S: 0.3 Mathematical operation Initial <i>Opening</i> : 4 <i>Opening</i> : 10 Final <i>Closing</i> : 4 Score: 4	M9 Settings Bilateral filter SpaceSigma: 1.5 RangeSigma: 23.8 Watershed H: 3.0 L: 0.5 S: 0.3 Mathematical operation Initial <i>Opening</i> : 4 <i>Opening</i> : 10 Final <i>Closing</i> : 4 Score: 4
		

**Figure 4.16 (b) Optimised setting for different classes of the Golgi apparatus.**

Red contours represent manual tracing and cyan represent automated segmentation methods. All 3 method flows assigned as the best 3 methods for GA\_C1 has recorded the same settings of watershed and mathematical operations. Different optimal settings of watershed and mathematical operations were identified for each best method assigned for GA\_C2 and GA\_C3. Scale bars: 100 nm.

### 4.2.3 Segmenting the rest of the sub-volumes of each organelle sub-class with respective optimised method settings

**Section 4.2.2** defined the ‘best’ method flows for every key organelle sub-class, using a small evaluation set of four test volumes for each of the nine identified sub-classes. The ‘best’ method flows for each sub-class and their individual optimal parameter settings are outlined in **Figures 4.8, 4.10 and 4.12**. To demonstrate that these best methods are feasible for segmenting other sub-volumes of the same sub-classes, the experiment was continued on the remaining organelle sub-volumes within each sub-class, using the most feasible method flow with individual optimal settings. If our hypothesis was correct – that the optimal method flow and method parameters could be determined from the image characteristics of the sub-volumes, then the remaining sub-volumes within each class should yield a high percentage of satisfactory segmentation results with no further parameter optimisation.

#### 4.2.3.1 Insulin granules

Insulin granules yielded the highest percentage of score 5 ratings. Indeed 95% of the 157 sub-volumes were ranked as 5 (**Table 4.3**). In IG\_C1, all 96 sub-volumes scored 5. In comparison 93% of the IG\_C2 scored 5 and 87% of the IG\_C3 scored 5.

#### 4.2.3.2 Mitochondria

About 90% of mitochondria in 2 sub-classes (MC\_C1 and MC\_C2) produced an acceptable segmentation results. In comparison, 125 of 156 MC\_C3 sub-volumes yielded scores of 5. In total, 82% of the 191 mitochondria sub-volumes were ranked as 5.

#### 4.2.3.3 The Golgi apparatus

The Golgi apparatus presented the lowest percentage of score 5 ratings with the segmentation results for 84% of the 75 sub-volumes identified as acceptable. 80% of the 10 sub-volumes of GA\_C1 scored 5, 89% of the 9 sub-volumes of GA\_C2 scored 5, while only 79% of the 56 sub-volumes of GA\_C3 scored 5.

**Table 4.3 Percentage of acceptable results (i.e. score 5) using the best method flow; i.e. Method 8 (M8) of each key organelle sub-class.**

‘Acceptable results’ is also termed as ‘high-quality results’. IG recorded 95% of the results categorised as ‘high-quality’ as the mesh models of the sub-volumes scored 5 in MSA scoring. MC and GA have similar percentage of acceptable results (i.e. ~80%). These percentages show that M8 is practically feasible to segment various image features of cellular compartments.

(A) Sub-groups	(B) Total sub-volumes	(C) Sub-volumes (acceptable)	(D) Sub-volumes (unacceptable)	(E) % acceptable results	(F) Best method
IG_C1	96	96	0	100%	<b>Optimised M8</b>
IG_C2	43	40	3	93%	<b>Optimised M8</b>
IG_C3	18	13	5	87%	<b>Optimised M8</b>
Total	157	149	8	% high-quality results for IG: 95%	
MC_C1	25	23	2	92%	<b>Optimised M8</b>
MC_C2	10	9	1	90%	<b>Optimised M8</b>
MC_C3	156	130	26	83%	<b>Optimised M8</b>
Total	191	162	29	% high-quality results for IG: 85%	
GA_C1	10	8	2	80%	<b>Optimised M8</b>
GA_C2	9	8	1	89%	<b>Optimised M8</b>
GA_C3	56	44	12	79%	<b>Optimised M8</b>
Total	75	60	15	% high-quality results for IG: 80%	

Sub-classification of insulin granules, mitochondria and the Golgi apparatus has allowed sub-volumes of sufficient uniformity of image properties to be obtained, such that these can be segmented in an automated manner using a single method flow. The importance of this is that this work provides a basis for more rapid semi-automated segmentation at least for the organelles

imaged under these conditions. These curated sub-class datasets also provide the bases for more detailed morphological characterisation and typing, which is both important from a biological perspective and for the mathematical segmentation. It also provides structural information for the typing of organelle sub-classes and the basis for more detailed morphological characterization to facilitate automatic segmentation and annotation. To conclude, it has been shown that by subclassifying according to organelle, organelle complexity and other image characteristics, accurate segmentation could be done at high proportion of the organelles automatically.

#### 4.2.4 Discussion

With ongoing development of computational segmentation and visualisation methods, e.g. image denoising algorithms, boundary- and region-based segmentation procedures, 3-dimensional image modelling methods etc., a high-fidelity cellular tomography segmentation pipeline – without any sacrifice of 3-dimensional surface model accuracy and employing only one single parameter setting (i.e. parameter free) is very close to achievable/ accomplishable. Heavy noise and the unique characteristics of different organelles remain the persisting problems that influence segmentation accuracy with standard optimised settings.

A study on different segmentation methods including a number of image filtration and segmentation algorithms, different combination of those automated and semi-automated tracing processes and test of the efficiency of mathematical morphologies on 3D mesh surface models has yielded a new pipeline developed for the automated segmentation (**Chapter 3**). Together with the newly developed mesh surface area (MSA) scoring system, this pipeline has facilitated the study conducted here: to investigate the parameter optimisation of nine combination method flows that employed nine different image denoising algorithms, and the effectiveness of these in tracing different types of organelles. To further assess the parameter optimisation of these methods flows; image characteristics of these key organelles or cellular compartments were investigated. Overall, novel algorithms presented in Chapter 4 could have emerged that somehow would have outperformed the sum of previously existing algorithms. These tools could have led to novel biological findings.

The dataset collected here represents one of the most detailed analyses of GA, MC and IG in 3D. It therefore provides a useful reference set for classification of the organelles. The dynamic conversion between the various organelle morphologies is shown in Figures 4.2, 4.4 and 4.5. Based

on my experiments, there are significant findings established where more than 90% of 423 sub-volume datasets, that were sorted into sub-groups based on their respective image characteristic, were reported to have high-quality segmentation results (i.e. according to the MSA scoring they have scored between 5 to 3, i.e. a segmentation accuracy within +/- 15% of the manually traced/ground truth dataset). This demonstrates that the assigned standard sets of optimal parameter settings could be applied on various organelles with respective/similar image characteristics. Another significant finding was that Method 8 (M8) consistently featured amongst the best of the nine method flows evaluated here. M8 is the combination of optimised NAD filter followed by optimised *watershed* and mathematical morphology algorithm. The reason this combination of processes worked best particularly at establishing object's membranes for accurate segmentation with minimal broken contours and/or over segmented contours. This has demonstrated high quality of traced contours compared to the gold standard or reference contour set and improved the contour selection process for selecting the correct contour(s) and removed the unwanted contour(s) mathematically.

#### **4.2.5 Future plan**

##### ***4.2.5.1 Improving the Golgi apparatus scoring for improved segmentation results***

As reported in **Section 4.2.2** – most of the GA sub-groups only achieved two standard sets of optimal settings. As these standard settings showed promising segmentation results, I believed that other method flows are also able to do the same; i.e. improve the scoring on every optimal setting of method flows. This could be achieved when the amendment is made within the sub-grouping datasets such as adding other characteristic values for sub-classifying this complex organelle to improve parameter settings optimisation. By doing this, other segmentation method flows would effectively identify the true cisternae membranes and correctly trace them. Thus this would produce more 'standard' sets of optimised settings and also increase the 'score' amongst different method flows.



**Chapter 5 APPLICATION OF EDGE-DETECTION FILTER IN  
SEGMENTING COMPLEX CELLULAR ORGANELLES AT HIGH  
RESOLUTION**

---

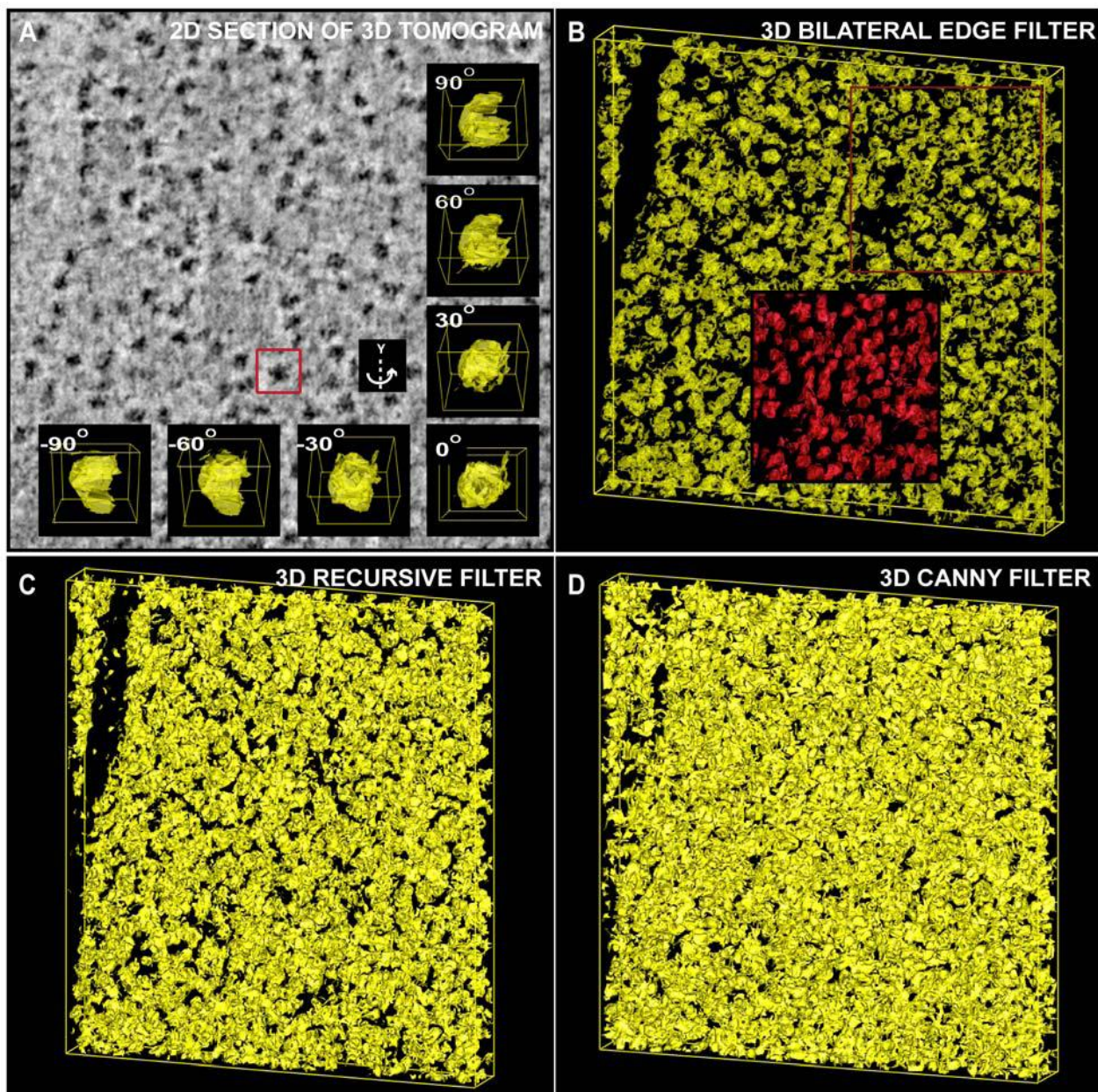


## **5.1 Introduction**

Chapters 3 and 4 have introduced and discussed the development of a workflow designed to expedite the segmentation of tomographic data, and demonstrated the implementation of this using real, high-resolution tomographic datasets. While these experiments were ongoing, Ali et al. (Ali et al., 2012) reported the implementation of a new 3-dimensional (3D) bilateral edge detection (BLE) filter, based on an earlier 2D implementation (Pantelic et al., 2006, Pantelic et al., 2007). The 3D BLE (Ali et al., 2012), potentially offers a parameter free edge-detection approach that also has the potential to semi-automate tomography.

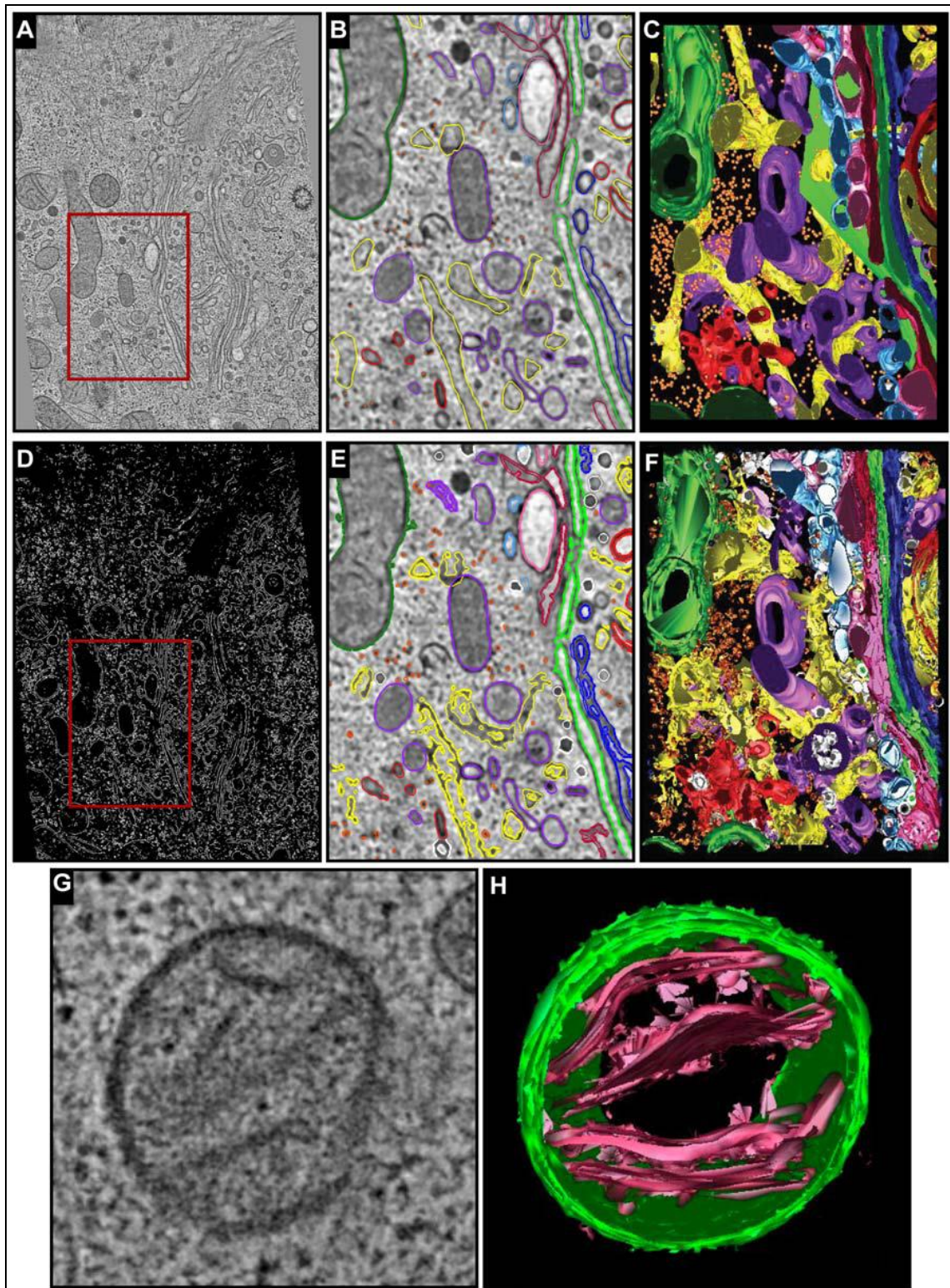
This potentially powerful tool was reported to be comparable in performance to current leading 3D filters, the Canny edge detector (Canny and John, 1986, Sonka et al., 1999, Jin, 2006) and the pseudo 3D recursive filter (Monga et al., 1991, Deriche et al., 1988). Ali et al. demonstrated that it was able to detect edges as little as 2 pixels wide both for organellar and macromolecular segmentation and so may prove to be a valuable tool for accurate sub-cellular segmentation (Ali et al., 2012). Even though 3D BLE proved be useful for individual macromolecule detection within 3D volumes, discontinuities amongst contours of subsequent slices can lead to inaccurate 3D model contours. In Ali et al. (Ali et al., 2012) these 3D discontinuities were improved by Bspline interpolation (**Figure 5.1**). The method's efficiency has demonstrated possibilities for further downstream processing such as annotation of 3D structural complexity at the sub-cellular level and sub-tomogram averaging. Due to the reported performance of the 3D BLE filter (**Figure 5.2**) its performance is here tested on the same tomographic data sets used in Chapters 3 and 4.





**Figure 5.1 Segmentation and extraction of molecular contours from electron tomography.**

Comparing segmentation results of 3D BLE, 3D recursive and 3D Canny filters. (A) 2D section of unprocessed tomogram. Dark objects are macromolecular assemblies. Isosurface rendering of randomly chosen single particle highlighted in selected number of orientations around y-axis in the inset (A). (B) 3D surface rendering of results obtained from application of the 3D BLE filter. After applying Bspline, discontinuities of particles contours are significantly improved where the surface rendering of 3D BLE shows individual macromolecules are detected and sufficiently extracted as compared (C) 3D recursive-filtered sub-volume and (D) 3D Canny-filtered sub-volume. Both (C) and (D) show respective surface rendering models.



**Figure 5.2 Segmentation of cellular tomographic reconstruction** (*previous page*).

(A) A tomographic slice of a cellular reconstruction extracted from a tomogram used and reported in Marsh et al., 2001 (Marsh et al., 2001a). (B) Region that has been demarcated from (A) was manually segmented using IMOD. Different colours were used to draw organelles contours representing different organelle types and is very useful for analysis purposes of surface-rendered 3D model shown in (C). (D) 3D BE filtered tomogram of the same tomogram in (A). (E) Manual colour coding was applied on the contours automatically detected by 3D BLE. The same colour coding as shown in (B) was used. (F) Surface-rendered 3D model of 3D BLE of the same region shown in (B) and (E). (G) An example of one of the complex organelles, mitochondrion. (H) Surface-rendered 3D

model of mitochondrion architecture of (G) shows the inner (purple) and outer (green) membranes detected by 3D BLE algorithm. Source: (Ali et al., 2012).

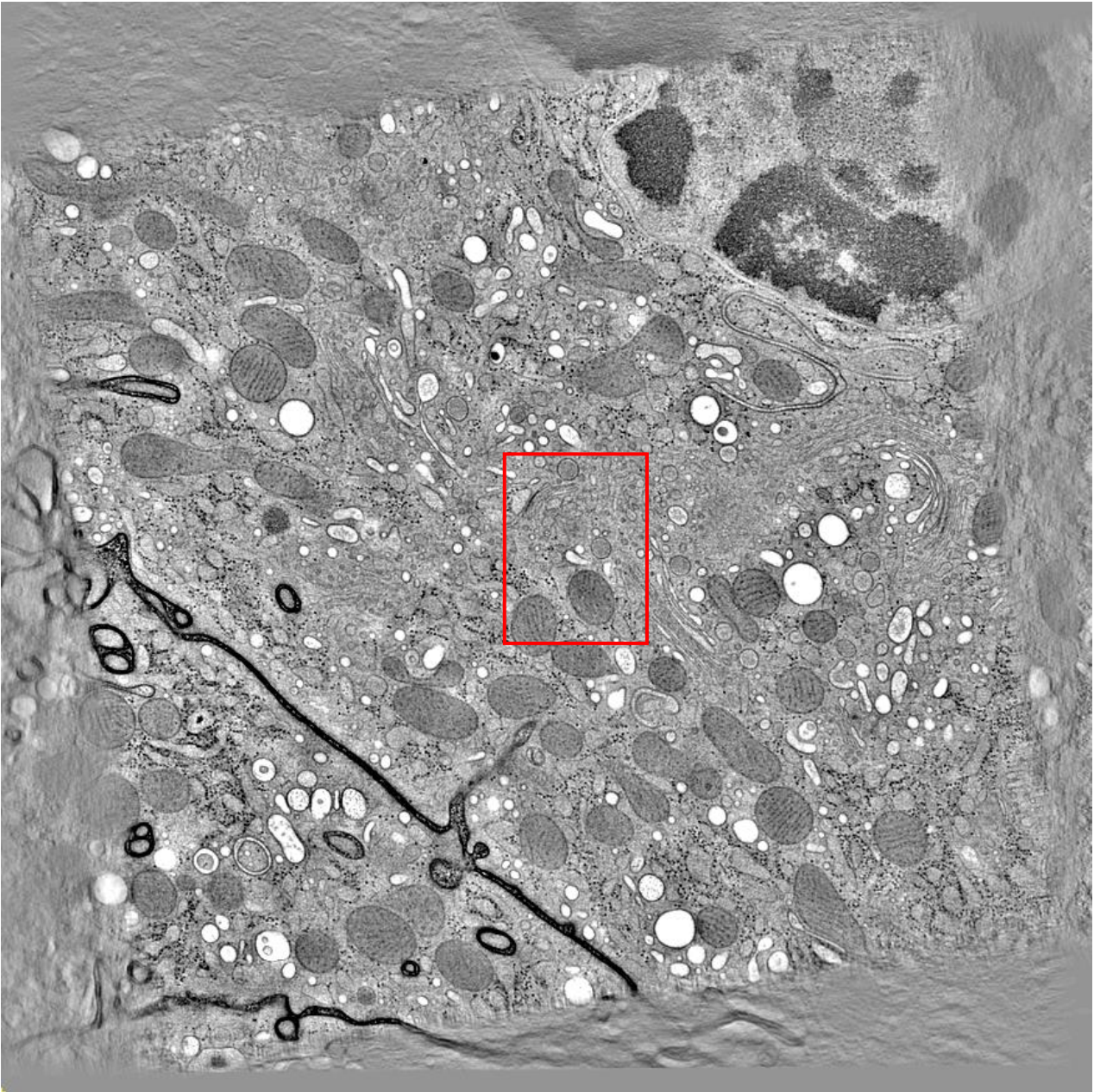
## 5.2 Results

### 5.2.1 Automated segmentation of organelles within a whole sub-cellular tomogram

To evaluate the performance of 3DBLE, one of the sub-regions of a large cellular tomogram (**Figure 5.3**) from Chapter 3 was randomly selected. There are three parameters used for 3D BLE, sigma 1, sigma 2 and threshold value. Sigma 1 ( $\sigma_1$ ; i.e. significant weights), is used to determine the size of neighbourhood for the calculation of the normalised photometric score. These significant weights are fixed standard deviation of 2 pixels (for 2D implementation of BLE) (Pantelic et al., 2007) and 2 voxels (for 3D implementation of BLE) (Ali et al., 2012). To trace edges and identify significant discontinuities of edges the photometric score is calculated and then normalised. The photometric parameter, defined as sigma 2 ( $\sigma_2$ ), controls photometric disqualification. It was used to demonstrate the filter's ability in suppressing noise during edge detection (Pantelic et al., 2007). Threshold value ( $t/h$ ) is able to selectively extract specific features to enhance edge detection. Images were pre-filtered with optimised (one pass) Gaussian filtration and (three passes) iterative median filtration (Ali et al., 2012) prior to edge detection and segmentation using 3D BLE.

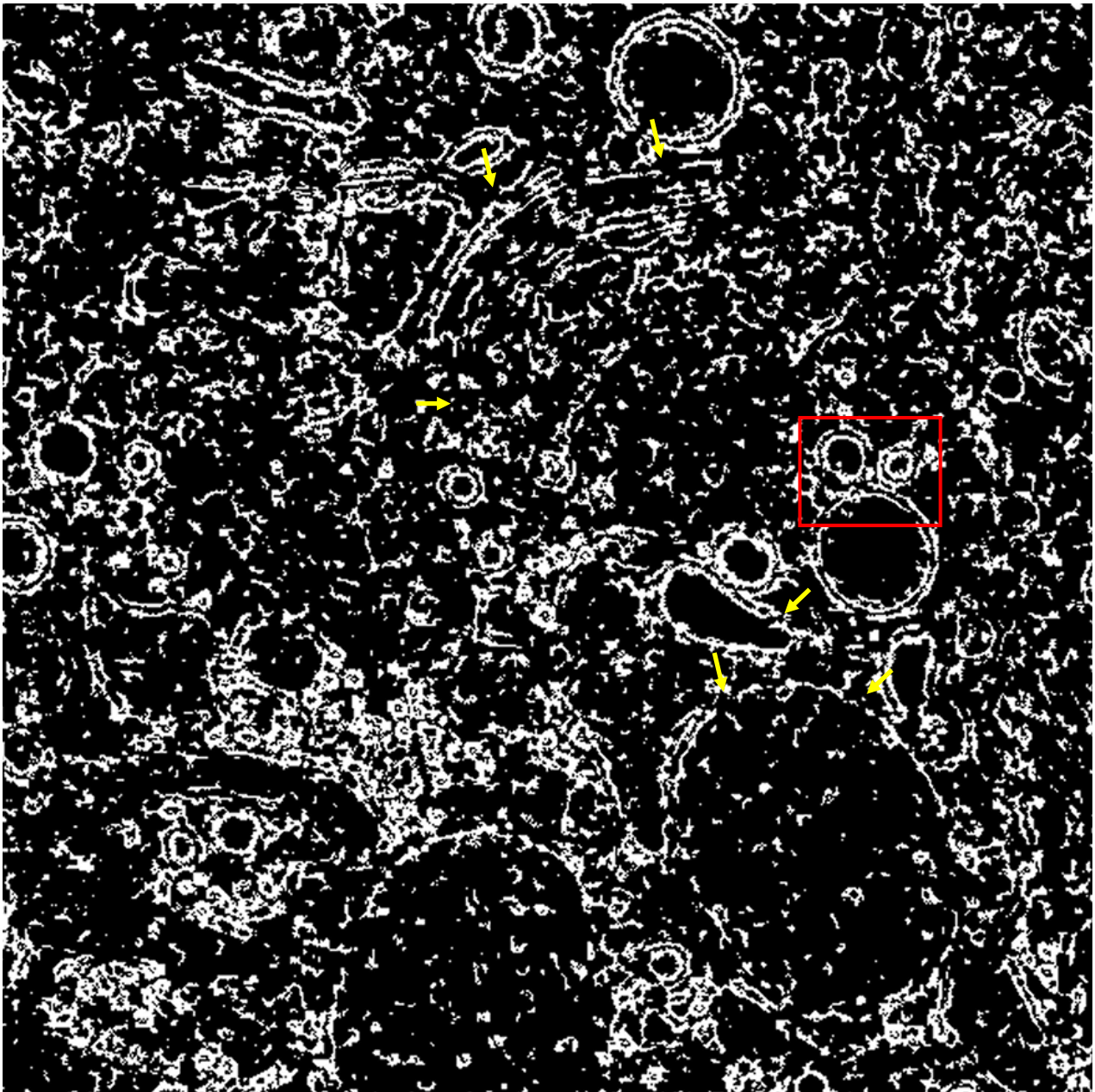
It was suggested by the developer that rather than using the 3D BLE in a fully automated fashion, instead three different sets of settings were suggested for the three tuneable parameters (sigma 1:  $\sigma_1$ ; sigma 2:  $\sigma_2$ ; threshold:  $t/h$ ) within the 3DBLE interface (Ali et al., 2012). The application of the 3D BLE will produce three sets of suggested optimised segmentation results. The idea to have different tracing results is to allow users to manually or mathematically select the 'best' result amongst the three for particular dataset(s) – depending on the user's datasets.

The tomographic volume of this project was automatically segmented with these settings. The best one was judged qualitatively and analysed (**Figure 5.4**). Contours were converted into a meshed model file for 3D evaluation as well as for MSA scoring purposes. As a result, green contours (**Figure 5.5**) directly derived from the white edges in **Figure 5.4** were produced. Sets of green contours are overlaid on the real dataset to highlight the accuracy of the traced contours. Yellow arrows marked in **Figures 5.4** and **Figure 5.5** show several examples of broken edges.



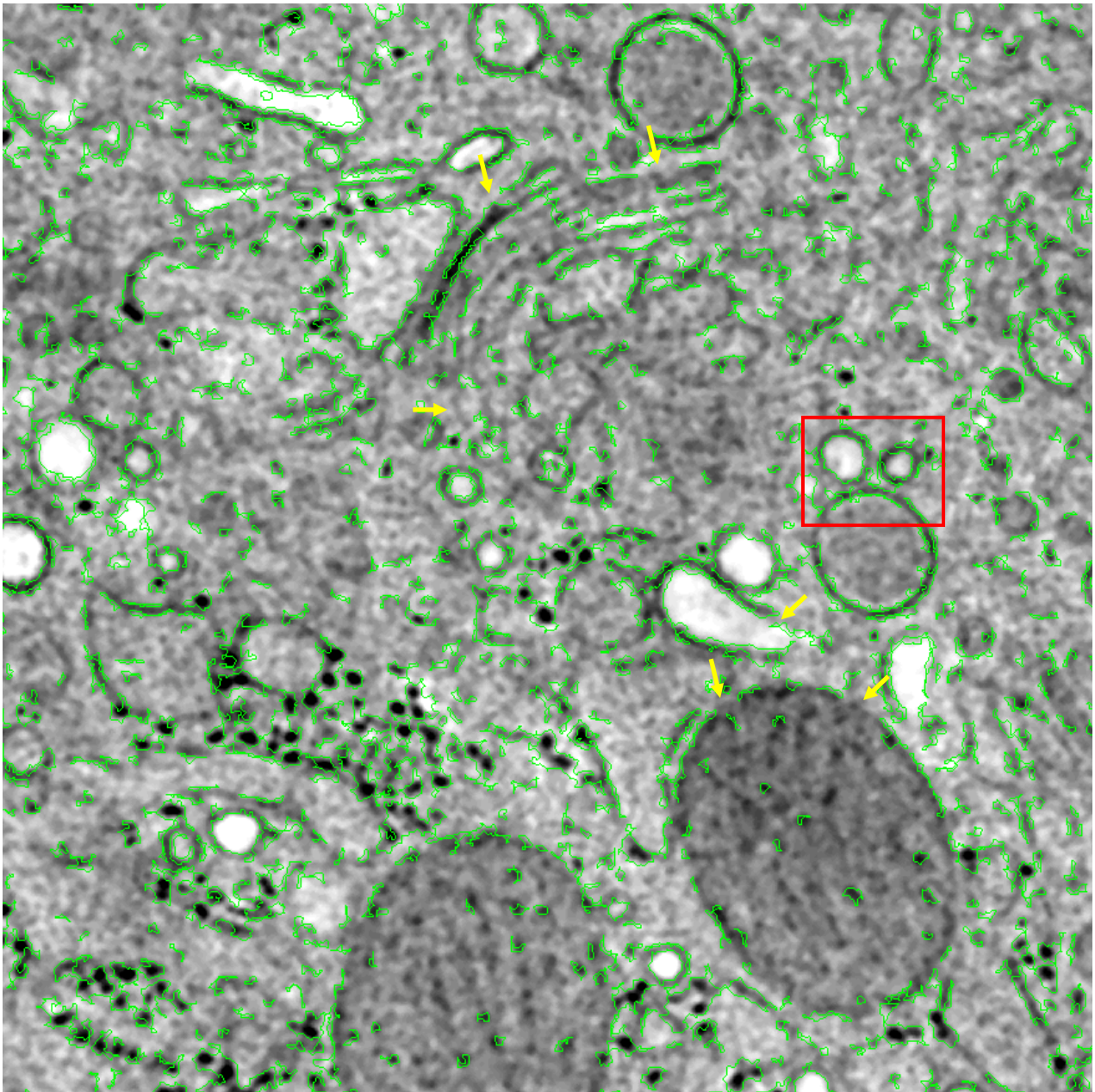
**Figure 5.3 Cellular tomogram used for this study, showing an area of complex cellular environment.**

The tomogram was filtered using one pass of a Gaussian with sigma 2 and three passes of Median filtering - as suggested in Ali et al. (Ali et al., 2012). For the purpose of this experiment only a part of this tomogram is used – i.e. region is demarcated by red box. The extracted region was chosen to include test organelles consistent with other sections of this thesis - the Golgi apparatus, mitochondria, mature insulin granules, immature insulin granules, and also contains examples of other sub-cellular compartments.



**Figure 5.4** Result of applying the 3DBLE (default settings) to the sub-tomogram extracted from Figure 5.3.

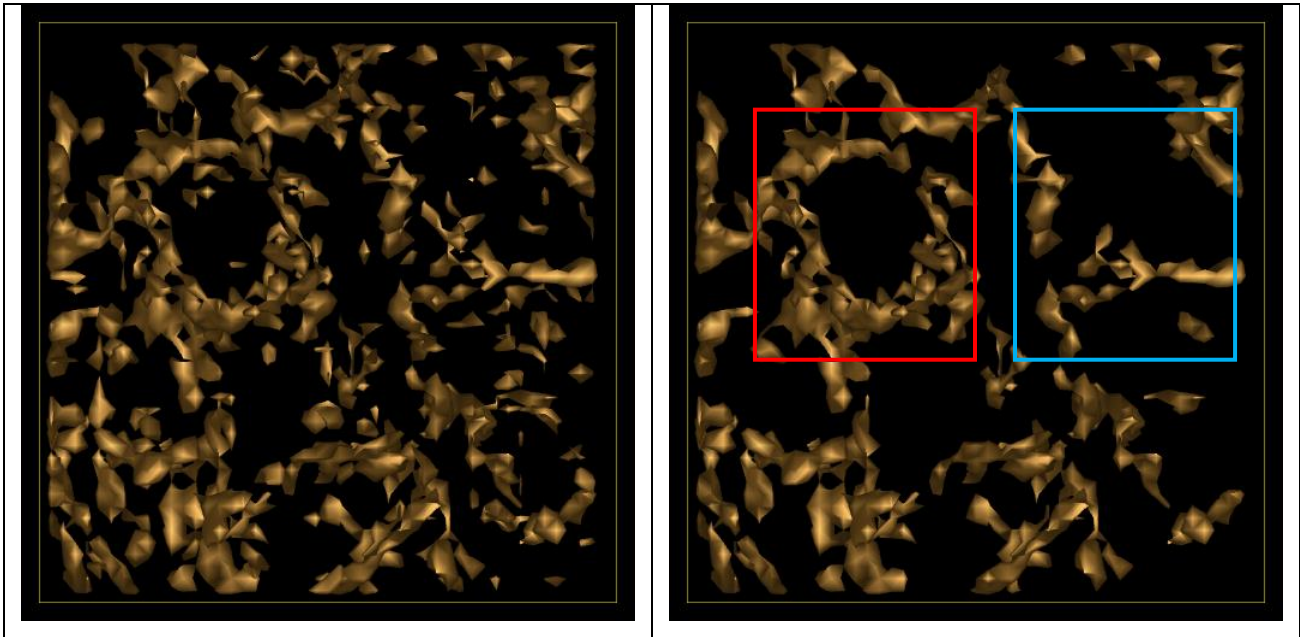
High-frequency of white contours represents every contour in the volume detected by the 3D BLE algorithm. As can be seen from this result, 'manual' identification of contours which represent 'the organelle of interest' is necessary. Yellow arrows show examples of 'broken contours' identified on the contours of organelle of interest. The volume shown here corresponds to the region bounded by the red box in Figure 5.3.



**Figure 5.5** A representation of contours after *imodauto* function presenting white contours in Figure 5.4. Yellow arrows show the ‘broken contours’ (same area shown by the yellow arrows in Figure 5.4).

‘Broken contours’ can lead to inaccurate meshed models (Meyers et al., 1992) and so B-spline interpolation was used – as proposed in Ali et al. 2012 – to complete the edges detected by 3D BLE. The red bounding box in **Figure 5.4** (the same region boxed in **Figure 5.5**) highlights two ‘objects’ (two insulin granules) of different intensity values. Even though the B-spline function has been applied to reduce discontinuity problems, it can be seen here that the performance of the B-spline function is dependent on the object (**Figure 5.6**) – i.e. one insulin granule (demarcated by the red

box) was improved but the connectivity of contours for the other insulin granule (demarcated by the blue box) remained poor.



**Figure 5.6** Surface-rendered 3D model of sub-region demarcated in red box in Figure 5.5.

(Left) 3D surface of sub-region after applying 3D BLE followed by Bspline interpolation (Ali et al., 2012). (Right) Small particles have been removed by turning on the ‘delete small pieces’ function in IMOD. Eliminating these ‘extra pieces’ improves volume visualisation, but not the accuracy of contour segmentation. The volumes shown here correspond to the regions bounded by the red boxes in Figures 5.4 and 5.5.

## 5.2.2 Automated segmentation of organelles extracted as small sub-volumes using 3DBLE

The objective of this experiment was to test whether, by using a similar approach to that outlined in the **Chapters 3 and 4**, the segmentation results obtained using the automated 3D BLE could be improved such that they were comparable to the ground truth data sets and/or comparable/superior to the performance of the previous segmentation method flow by processing individually extracted organelle sub-volumes. To achieve this, a subset of the dataset utilised in the preceding chapters, comprising 50 organelles of interest that were representative of the three key organelles (the Golgi apparatus, mitochondria and insulin granules) and each of the three organelle complexity levels, were segmented using the 3D BLE and the results compared to the those obtained by manual tracing.

The automated process of 3D BLE filtering followed by Bspline interpolation produced hundreds to thousands of contours for each sub-volume as compared to the number of ‘manual’ contours which ranged from  $1 \times 10^2$  to  $1 \times 10^7$ , depending on image characteristics. This over-segmentation is likely

due to two key problems; the existence of unwanted contours and the disconnectivity of edges defining true organelle contours. First, the ‘unwanted’ contours (i.e. the contours of neighbouring organelles and/or unidentified objects) were manually deleted. Only contours of interest – representing the organelle membranes) – were retained and meshed. The new mesh models of 3D BLE (i.e. that represented only the target organelle membrane) were compared to the respective mesh models obtained previously by manual segmentation prior to scoring (**Table 5.1**). For the sake of comparison, scores were also given to mesh models of 3D BLE prior to post-processing (i.e. manual deletion of unwanted contours). ‘Result 1’ represents the score for the 3D BLE result before post-processing or removing unwanted contours (i.e. original result of default settings of 3D BLE) and ‘Result 2’ represents the score of 3D BLE result after post-processing. For scoring purposes, meshed model of every sub-volume were created using, *imodauto* – a function in *IMOD*.

The observation is that the results were unacceptable and that across the board. The MSA values were higher for the 3D BLE processed data than the ground truth sets. This is most likely due to high levels of noise which led to false edge detection, increasing the number of contours where this in turn have resulted in a higher mesh surface area (MSA). Post-processing removed the majority of these unwanted contours and the score (Result 2) of some sub-volumes increased (as compared to respective Result 1). Unfortunately however, Result 2 remained largely unsatisfactory. The highest score achieved by a single insulin granule sub-volume was score 4. The rest scored 3 and below. A score of 0 indicates an MSA value of 3D BLE that is more or less than 125% or 75%, respectively, of the MSA value recorded for the ground truth dataset. Middle slices of representative sub-volumes are shown in **Figures 5.7-5.9**. The green contours represent those detected by the 3D BLE and red contours represent the manual tracing results.



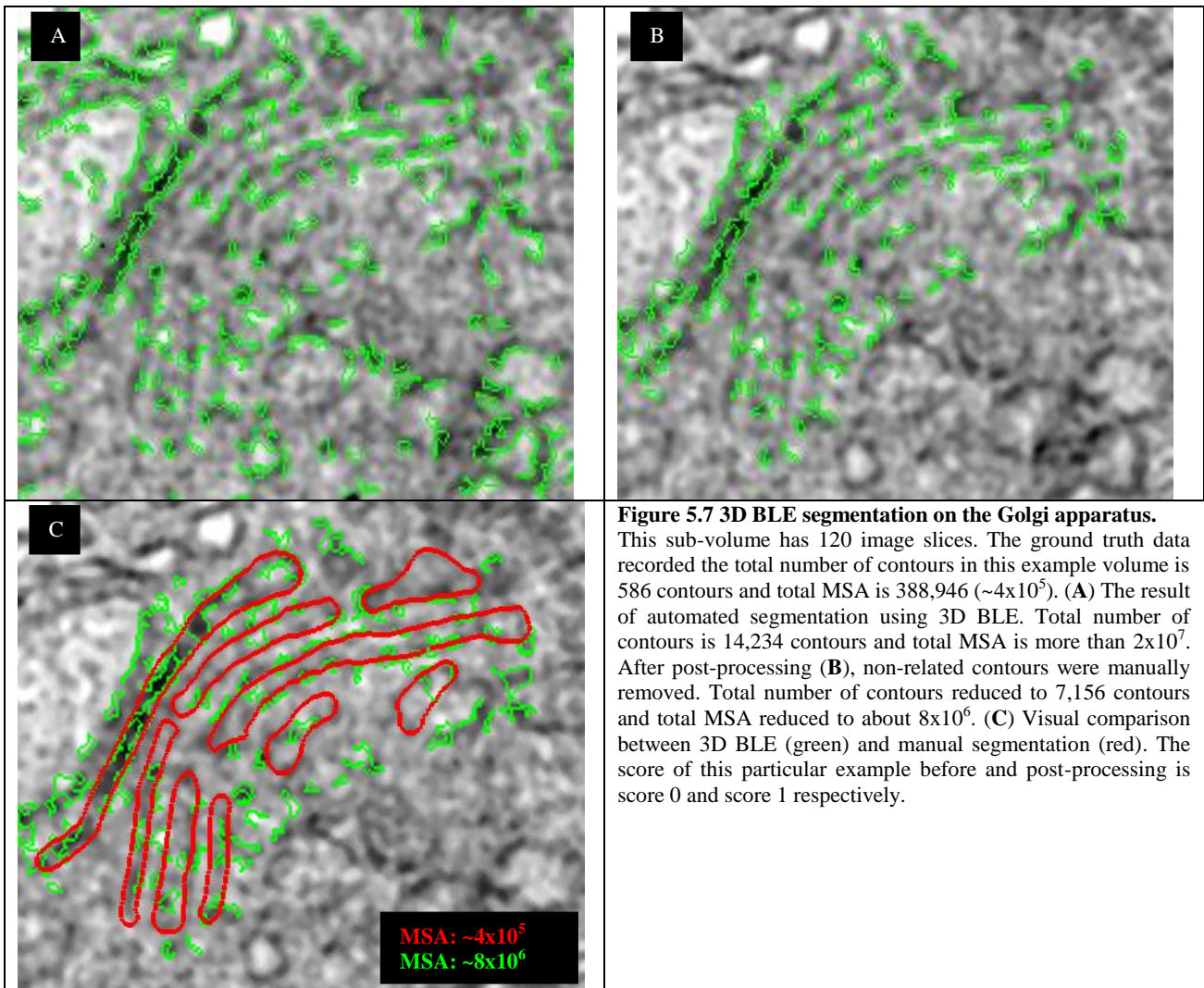
**Table 5.1 Scores for individual filtering of boxed out organelles of interest GA (Golgi apparatus), MC (mitochondria) and IG (insulin granules).**

Result 1 is the score of segmentation result before any post-processing (i.e. manual removing unwanted contours) and Result 2 is the score of segmentation result after removing unwanted contours. The identification number of respective sub-volume was written on each organelle type. This is used for experiment purpose only.

GA	Result 1	Result 2	MC	Result 1	Result 2	IG	Result 1	Result 2
GA1	0	0	MC1	0	2	IG1	2	4
GA2	0	0	MC2	0	1	IG2	0	2
GA3	0	0	MC3	0	1	IG3	0	2
GA4	0	0	MC4	0	1	IG4	0	1
GA5	0	0	MC5	0	0	IG5	0	3
GA6	0	0	MC6	0	0	IG6	0	2
GA7	0	0	MC7	0	0	IG7	0	2
GA8	0	0	MC8	0	0	IG8	0	1
GA9	0	0	MC9	0	0	IG9	0	1
GA10	0	0	MC10	0	0	IG10	0	1
GA11	0	0	MC11	0	1	IG11	0	1
GA12	0	1	MC12	0	1	IG12	0	1
			MC13	0	1	IG13	0	1
			MC14	0	2	IG14	0	0
			MC15	0	2	IG15	0	0
			MC16	0	1	IG16	0	1
			MC17	0	0	IG17	0	2
			MC18	0	1	IG18	0	0
								IG19
					IG20	0	1	
Acceptable: 0			Acceptable: 0			Acceptable: 0		
Unacceptable: 12			Unacceptable: 18			Unacceptable: 20		

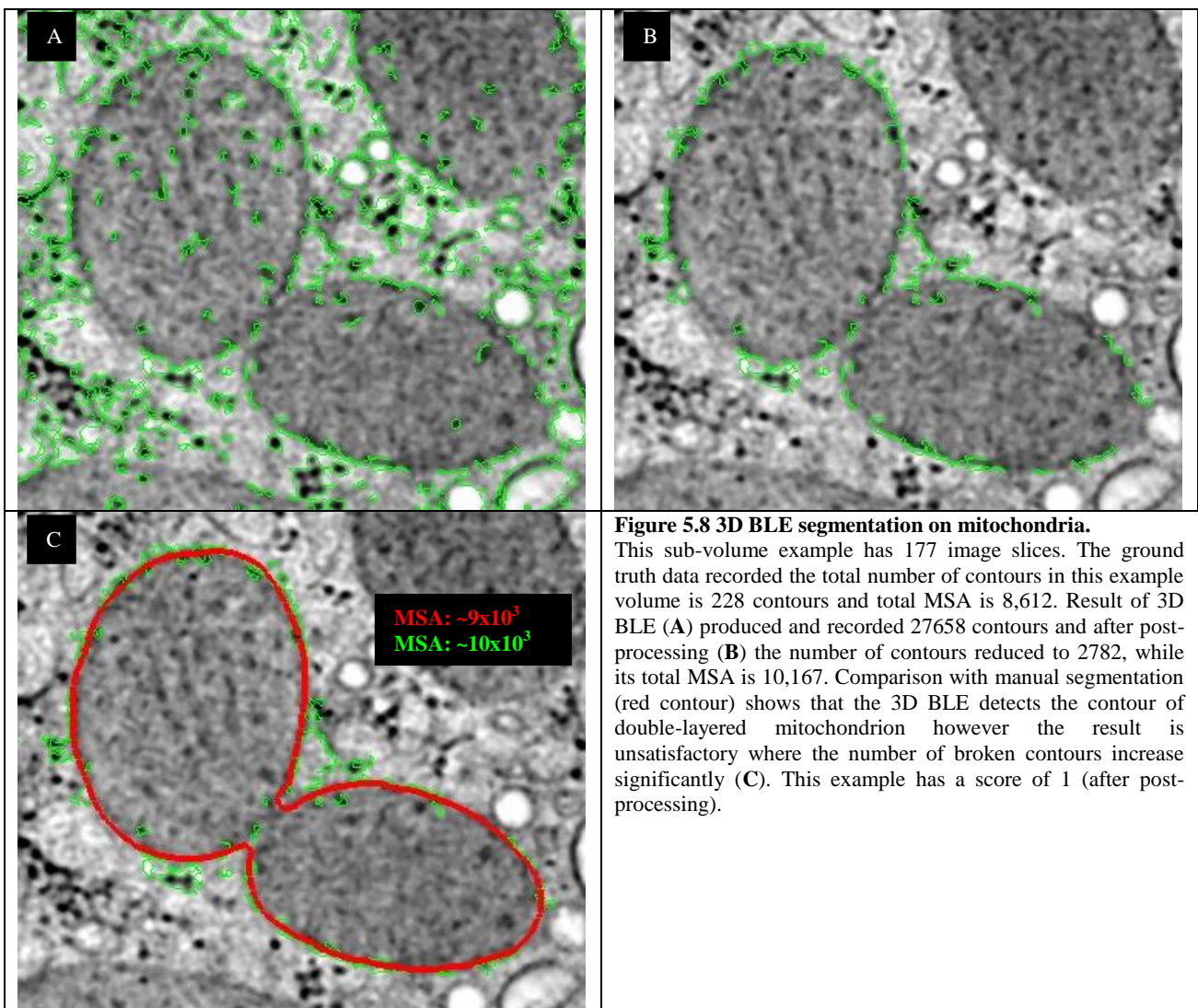
### 5.2.2.1 The Golgi apparatus (GA)

Visual inspection of (Figure 5.7 B) shows that the contours suffer from ‘broken’ cisternae membranes yielding an increased number of contours compared to the truth data. This example has an MSA score of 0 following post-processing (score 1).



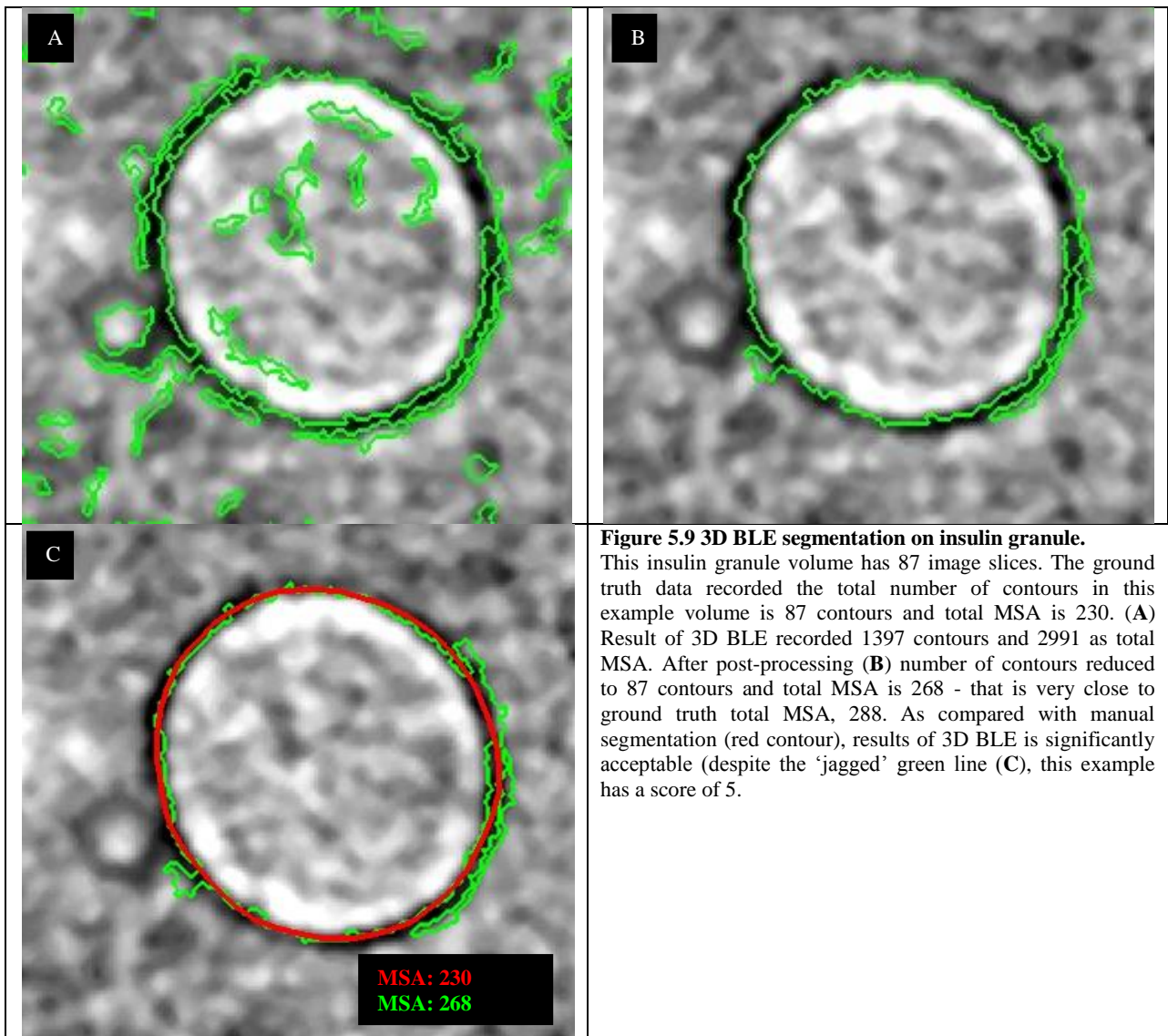
### 5.2.2.2 Mitochondria

Results of the 3D BLE analysis for mitochondria gave a range of scores from 2 to 1. Scores in this range are considered not acceptable (according to our MSA scoring system). This claim is supported by the visual examples presented in **Figure 5.8**. High-resolution tomograms have proven able to represent a high quality of cellular compartments particularly for 3D structure studies (Marsh et al., 2005). However 3D BLE was computationally designed to be very sensitive to density differences of organelles membrane. It appears that variation in density levels throughout the mitochondria causes over-segmentation and that 3D BLE interprets the contours as ‘small particles’ distributed along the true contour – these can be considered as ‘broken contours’. Like the GA, the higher numbers of contours significantly influences the total contour volume (CV) and in turn influences the value of the mesh surface area (MSA).



### 5.2.2.3 Insulin granules

In contrast to the Golgi apparatus and mitochondria, insulin granules yielded better scores (i.e. between score of 5 to 2). The example in **Figure 5.9** shows contours detected for a mature granule belonging to image class 2, i.e. the crystal is free in the membrane lumen. The organelle boundary was nicely traced by 3D BLE and has an MSA score of 5; visually demonstrate proximity with manually traced contours (red lines).



Overall, the 3D BLE segmentation results suffered from over-segmentation, as the filter operating in automated mode appeared to be too sensitive to edges within the sub-volume. Presumably, this may be as the automated settings of 3D BLE are suggested particularly for segmenting macromolecular structures (Ali et al., 2012, Pantelic et al., 2007). As the organelles of high resolution dataset (example shown in **Figure 5.3**) seems to be complex and congested, and in order to more equitably compare the 3D BLE to the processes developed in **Chapters 3 and 4**, sub-volumes were extracted in order to examine the outcomes when the 3D BLE was applied to extracted organelle sub-volumes in isolation. With the same settings (i.e. automatic 3D BLE settings), sub-volumes suffered significantly from broken contours, particularly the Golgi apparatus and mitochondria. As a consequence, a large number of false contours were generated, leading to an increasing in total surface area of the contours. To improve such discontinuities problems, optimising 3D BLE parameters was implemented.

### 5.2.3 Optimising settings of 3D BLE for segmentation of different cellular compartments

In an effort to overcome the problem of broken contours and to further examine the effectiveness of the 3D BLE algorithm in segmenting membranes of complex cellular compartments, settings of 3D BLE were optimised for each object of interest (i.e. cellular organelle). There are three parameters in 3D BLE implementation;  $\sigma_1$ ,  $\sigma_2$  and  $t/h$ . The description on these parameters is detailed in **Section 5.2.1**. As  $\sigma_1$  is fixed value (Ali et al., 2012) thus no optimisation of this parameter in this experiment. Optimising parameter setting was focused on  $\sigma_2$  and  $t/h$  values. As  $\sigma_2$  controls photometric disqualification, it was optimised to demonstrate the filter's ability in suppressing noise during edge detection (Pantelic et al., 2007). Another parameter in 3D BLE; threshold value ( $t/h$ ) able to selectively extract specific features to enhance edge detection was also manually optimised.

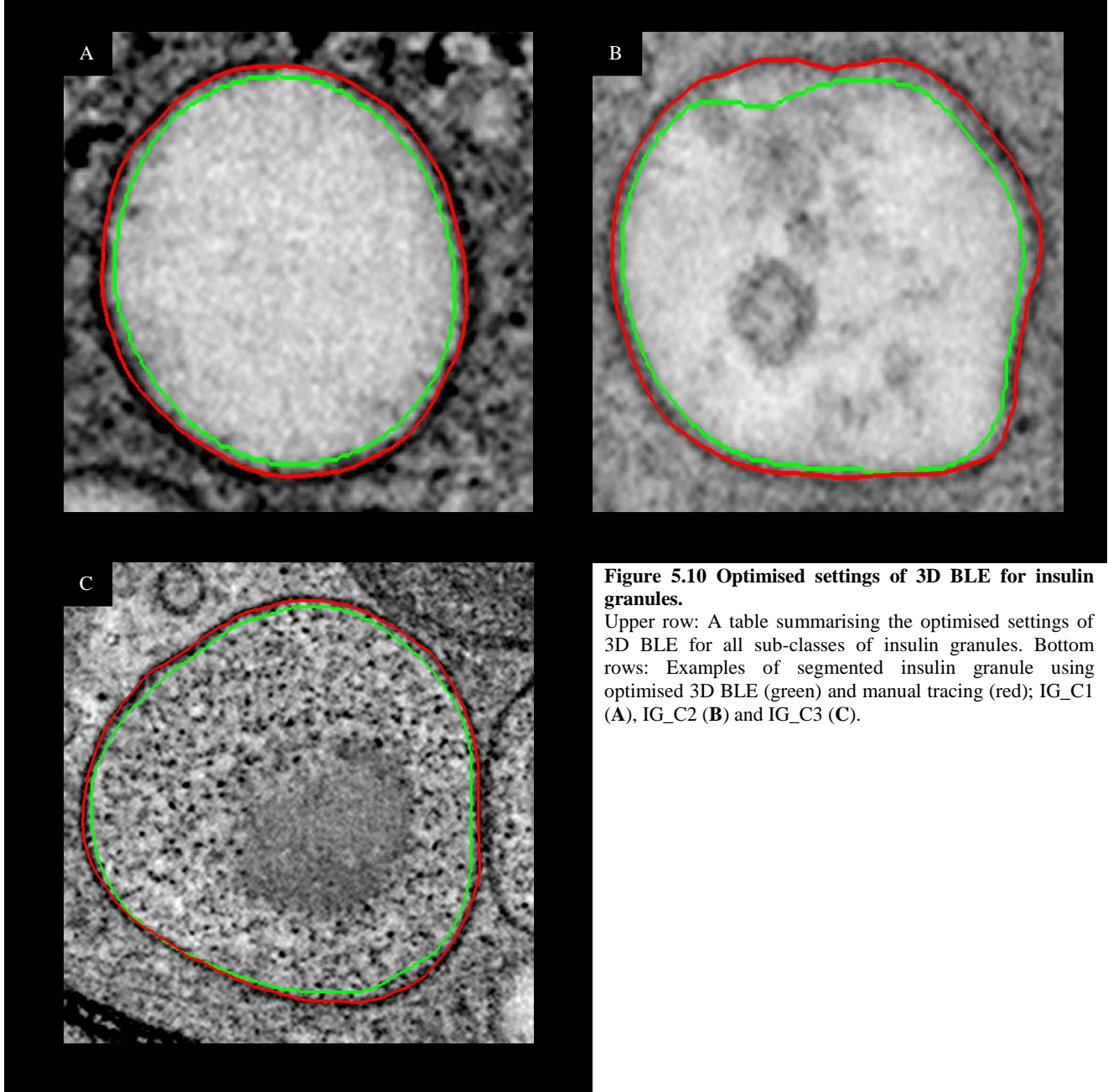
3D BLE procedure is very straightforward. However, it is difficult to predict the optimal parameters. The approach used for parameter adjustment was while the  $\sigma_2$  value is increased; the  $t/h$  value was kept constant and vice versa until the best combinations of settings was identified. On average, five to ten tuning operations were carried out for each sub-volume prior to selecting the best results (i.e. optimised 3D BLE setting). More tuning operations were needed on complex cases such as the Golgi apparatus. For initial comparison prior to selecting optimised segmentation results, visual comparison with respective manual tracing was performed on a slice by slice basis.

Following post-processing, the edges detected by 3DBLE were computationally modelled as contours using *imodauto* in *IMOD* (Kremer et al., 1996). The contours corresponding to unwanted objects were manually removed using the ‘eraser’ function in drawing tools of *IMOD*. When there only target contours remained in the volume, they were meshed with *imodmesh* in *IMOD* (Kremer et al., 1996). The value of total MSA for each contour set (i.e. each organelle sub-volume) was compared to the total MSA value of the ground truth data (i.e. manual segmentation) for each respective sub-volume. The difference between total MSA of 3D BLE and manual segmentation of each sub-volume was used for this numerical comparison and an MSA score (the implementation of the score procedure is detailed in Chapter 3) was calculated for each segmentation result. Optimising two main parameters of 3D BLE (i.e.  $\sigma_2$  and threshold value) significantly increased the quality of contour segmentation of complex cellular organelles. It also produced greater segmentation accuracy of each test data (i.e. 50 sub-volumes). More than 70% of the results are satisfactory that (i.e. ‘acceptable’ according to MSA scoring system). Overall, the contours corresponding to the organelle membranes were more accurately traced following parameter optimisation.

### 5.2.3.1 *Insulin granules*

**Figure 5.10** demonstrates the processing insulin granules with the optimised BLE. The upper row of the figure shows all 20 sub-volumes used the same setting of sigma 1 ( $\sigma_1$ ) – that is used to determine the size of neighbourhood for the following edges tracing – as suggested; i.e. 2 voxels (Ali et al., 2012). Different combinations of sigma 2 ( $\sigma_2$ ) and threshold (t/h) value – used to trace edges, identify significant discontinuities of edges and to suppress noise – indicated that there is no specific mode to establish the optimised combination settings. Red contours demonstrate manual tracing and green contours represent the optimised 3D BLE segmentation results.

IG	Opt.	$\sigma_1$	$\sigma_2$	t/h		Opt.	$\sigma_1$	$\sigma_2$	t/h		Opt.	$\sigma_1$	$\sigma_2$	t/h
IG_C1					IG_C2					IG_C3				
IG1	5	2	3.83	0.95	IG5	5	2	3.91	0.95	IG9	5	2	3.75	0.96
IG2	5	2	3.84	0.95	IG6	5	2	3.91	0.95	IG10	5	2	3.79	0.96
IG3	5	2	3.87	0.95	IG7	5	2	3.68	0.95	IG14	5	2	3.73	0.94
IG4	5	2	3.90	0.95	IG8	5	2	3.75	0.95	IG15	5	2	3.76	0.94
					IG11	5	2	3.79	0.96	IG16	5	2	3.78	0.95
					IG12	5	2	3.73	0.96	IG17	5	2	3.79	0.97
					IG13	5	2	3.74	0.96	IG18	5	2	3.70	0.99
					IG19	5	2	3.70	0.91					
					IG20	5	2	3.73	0.90					



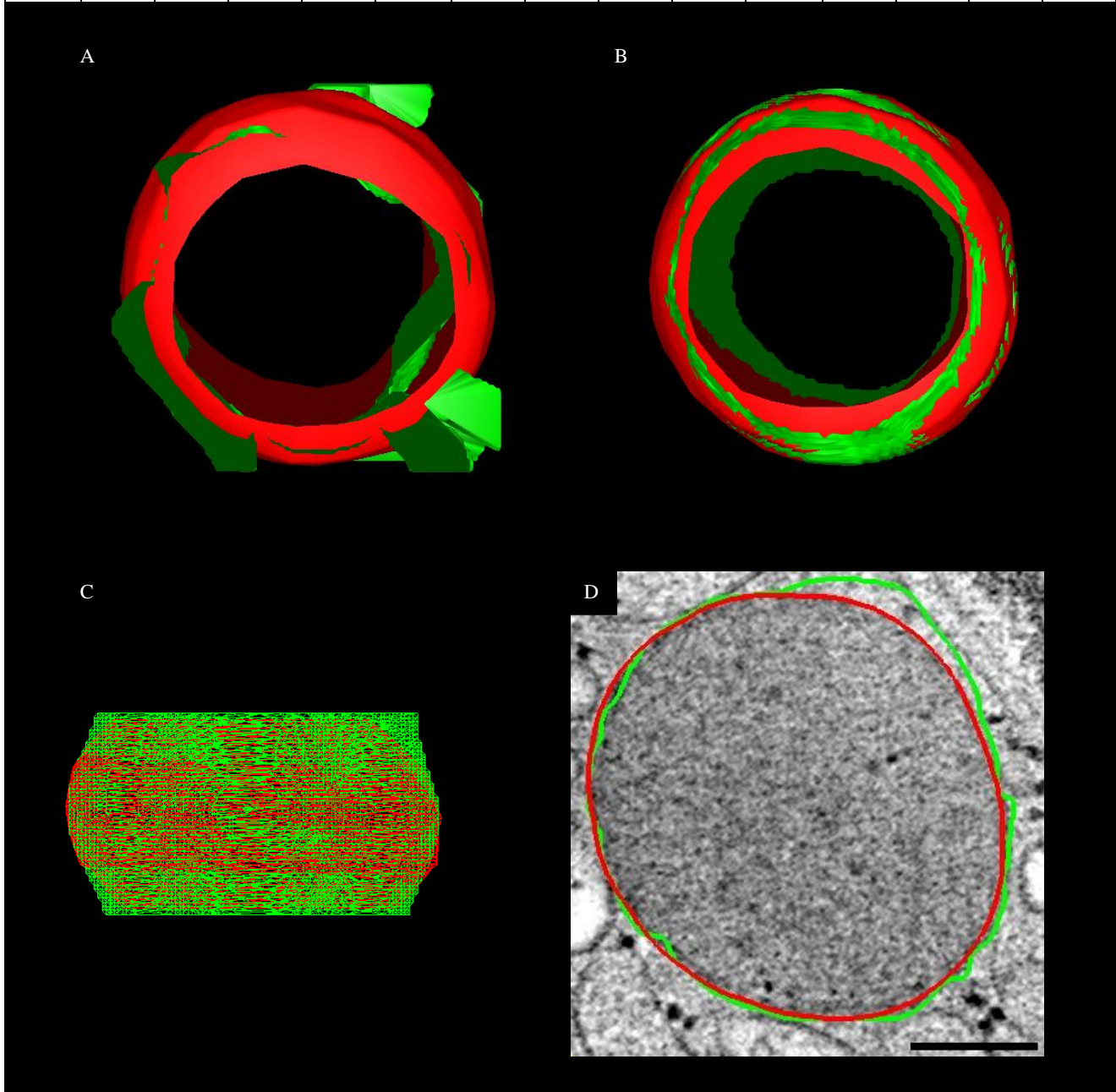
**Figure 5.10 Optimised settings of 3D BLE for insulin granules.**  
 Upper row: A table summarising the optimised settings of 3D BLE for all sub-classes of insulin granules. Bottom rows: Examples of segmented insulin granule using optimised 3D BLE (green) and manual tracing (red); IG\_C1 (A), IG\_C2 (B) and IG\_C3 (C).

### 5.2.3.2 Mitochondria

Similar to insulin granules, only  $\sigma_2$  and  $t/h$  values were adjusted, and  $\sigma_1$  was not changed (**Figure 5.11**). There is also no specific mode to determine the combination between these two parameters (i.e.  $\sigma_2$  and  $t/h$ ). As score 4 and 5 are acceptable according to the scoring system proposed in **Chapter 3** and to save time, the optimisation process was stop when it reach score 4 for a number of mitochondria sub-volumes (**Figure 5.11** upper row). The example in **Figure 5.11** (bottom rows) has recorded a score of 5. There is a significant difference between the meshed models of automated 3D BLE and optimised 3D BLE. The blue arrows (**Figure 5.11 A**) are pointing at the areas that suffered from either broken contours or wider extended areas which produced unacceptable final result (i.e. score 2). After numbers of trials, optimised settings of 3D BLE successfully specified for this example mitochondria where it significantly increased the accuracy of tracing contours (**Figure 5.11 B**). Visual comparison between manual tracing (red contour) and computational method; 3D BLE (green contour) show that most part of the mitochondria membrane has been nicely traced using optimised 3D BLE settings. The part that is slightly distanced from red contour or the original membrane boundary (yellow arrow) is however not obvious and acceptable to be accurate tracing result (**Figure 5.11 C, Figure 5.11 D**).



MC	Opt.	$\sigma_1$	$\sigma_2$	t/h		Opt.	$\sigma_1$	$\sigma_2$	t/h		Opt.	$\sigma_1$	$\sigma_2$	t/h
MC_C1					MC_C2					MC_C3				
MC1	5	2	3.45	0.92	MC4	4	2	3.74	0.95	MC12	4	2	3.76	0.99
MC2	5	2	3.66	0.95	MC5	4	2	3.77	0.95	MC13	4	2	3.91	0.99
MC3	5	2	2.98	0.95	MC7	5	2	3.72	0.95	MC14	5	2	2.70	0.92
MC6	5	2	2.98	0.95	MC8	5	2	3.60	0.95	MC17	5	2	3.74	0.97
MC9	4	2	3.55	0.95	MC11	4	2	3.40	0.97	MC18	5	2	3.74	0.95
MC10	4	2	3.74	0.97	MC15	5	2	3.14	0.96					
					MC16	5	2	3.74	0.89					



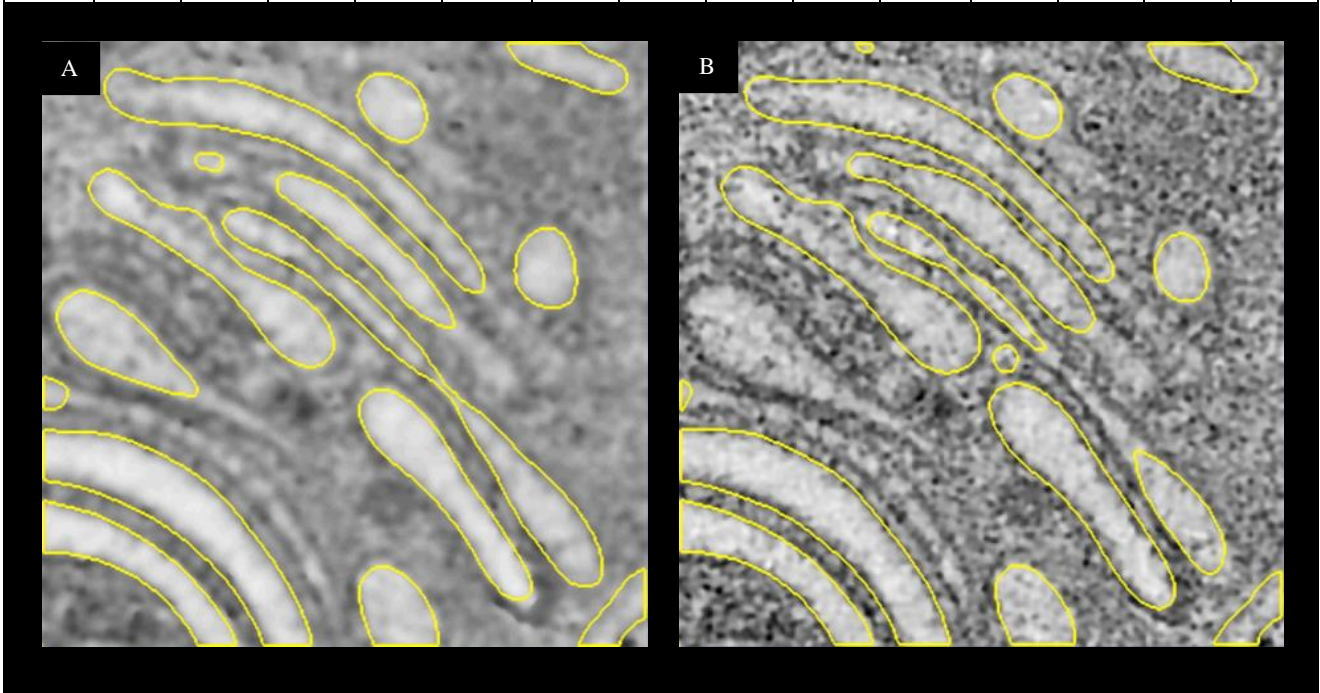
**Figure 5.11 Comparison between meshed model of 3D BLE (green) and manual tracing (red).**

(A) Meshed model of an example of unacceptable 3D BLE segmentation result (score 3) – using automated 3D BLE (pre-filtered by the Gaussian and iterative median (Ali et al., 2012)). Blue arrows show the example of areas (green) that caused the result unsatisfactory (i.e. score 3) when compared to manual segmentation (red). (B) Result of optimised 3D BLE, this meshed model of 3D BLE (green) is corresponding to the ground truth set (red). This example of mitochondrion segmentation has a score of 5. (C) A side view of image from (B). Yellow arrow show a small 'extended' area produced by 3D BLE. (D) Comparison with manual tracing (red contour) shows optimised 3D BLE is comparable to the ground truth dataset in correspondence to the image in (C). Scale bar: 100 nm.

**5.2.3.3 The Golgi apparatus**

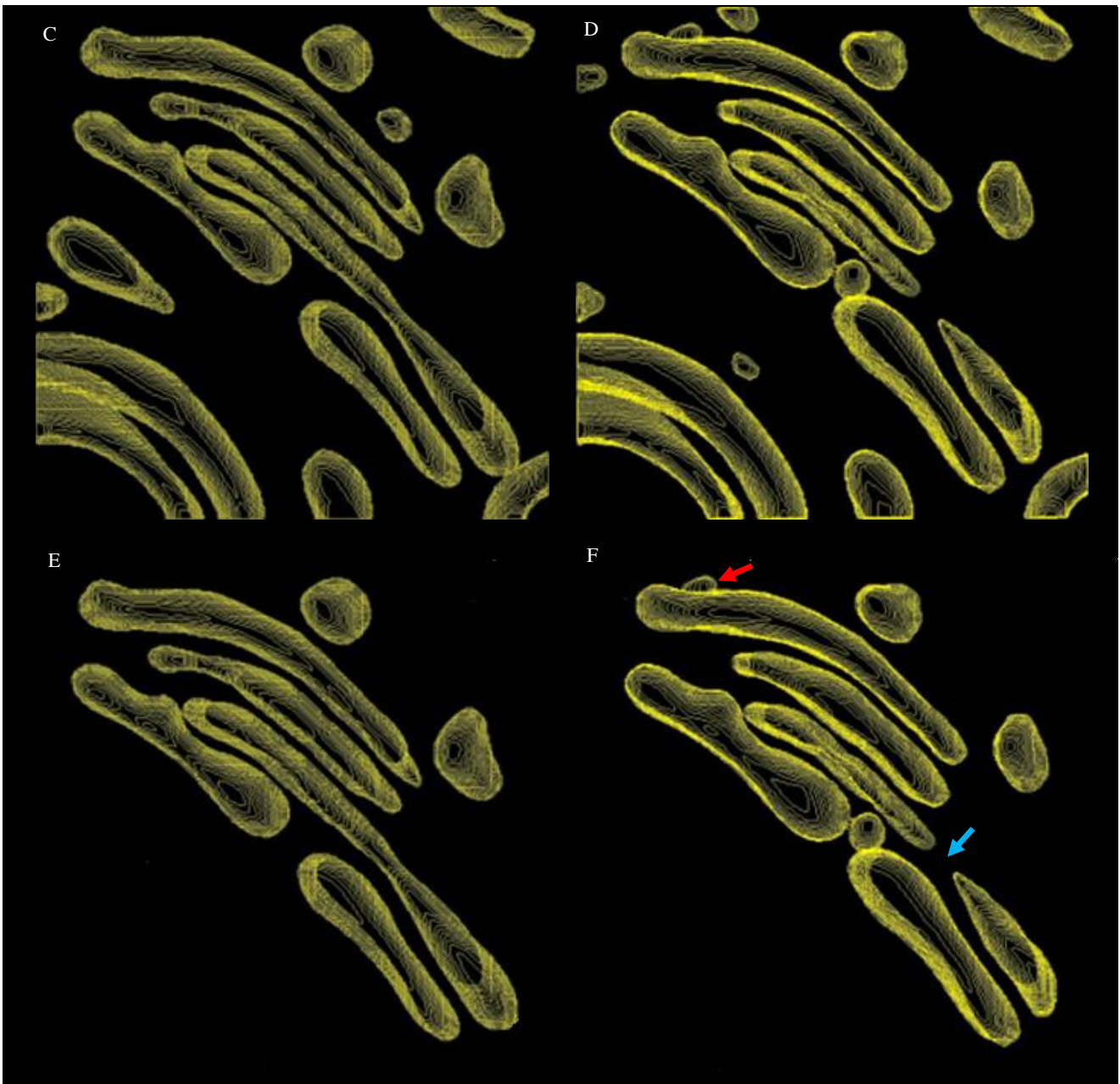
According to the scoring system, score of 3 is considered as acceptable for the Golgi apparatus (GA). Similarly, only sigma 2 ( $\sigma_2$ ) and threshold (t/h) values were adjusted, while sigma 1 ( $\sigma_1$ ) was maintained (**Figure 5.12 a and b**). As the most complex organelle, there is more than one contour (i.e. cisternum membrane) of each image slice of the GA needed to be traced. Finding the correct combination of these two parameters for optimised segmentation were time consuming. To save time, the parameter adjustment was stopped when it reached the score 3, particularly for image class 3 (i.e. GA\_C3) (**Figure 5.12 a upper row**).

GA	Opt.	$\sigma_1$	$\sigma_2$	t/h		Opt.	$\sigma_1$	$\sigma_2$	t/h		Opt.	$\sigma_1$	$\sigma_2$	t/h
GA_C1					GA_C2					GA_C3				
GA4	5	2	3.98	0.91	GA5	5	2	3.74	0.88	GA1	4	2	2.98	0.92
GA10	5	2	3.80	0.93	GA6	5	2	3.77	0.88	GA2	3	2	3.50	0.93
GA11	5	2	3.91	0.93	GA9	4	2	3.78	0.97	GA3	3	2	3.52	0.93
										GA7	4	2	2.98	0.79
										GA8	4	2	3.77	0.99
										GA12	3	2	3.90	0.89



**Figure 5.12 (a) Optimised settings of 3D BLE for the Golgi apparatus and visual comparison of image section and the GA 3D models between two methods; Method 8 (left) and 3D BLE (right).**

Upper row: Table of optimised settings of 3D BLE for the Golgi apparatus. Bottom rows: 2D image of segmentation result of our proposed workflow, M8 (i.e. cellular tomography segmentation or CTS) (A) and 3D BLE (B).



**Figure 5.13 (b) Optimised settings of 3D BLE for the Golgi apparatus and visual comparison of image section and the GA 3D models between two methods; Method 8 (left) and 3D BLE (right).**

(C) and (D) 3D models of CTS and 3D BLE respectively, before removing unwanted contours. (E) CTS 3D model after automated deletion of unwanted contours. (F) 3D BLE 3D model after manual deletion of unwanted contours. Processing time for both experiments; CTS: 3 min, 3D BLE: 19 min. 3D BLE has less accuracy of 3D visualisation where there are 'extra region' traced on one of the Golgi cisternae (red arrow) and 'broken 3D contours' (light blue arrow).

Overall, different, optimal values of  $\sigma^2$  were identified for the majority of the dataset - in particular mitochondria and the Golgi apparatus which were poorly segmented using the automated approach. As mentioned in the 3D BLE implementation paper, the sigma value represents a photometric parameter. It defines the minimum difference in intensity to be regarded as an edge. By optimising this value, the connectivity between contours was substantially improved and the number of broken contours was significantly reduced. Optimisation of this parameter has thus enabled the edge detector to segment complex organelle membranes more precisely. A range of  $\sigma^2$  and threshold values (3D BLE main parameters) were observed for different organelle type, morphologies and complexities and the requirement for Bspline interpolation varied (**Tables 5.3**). When the sub-volumes were grouped according to organelle complexity (the approach proposed in **Chapter 4**) no obvious pattern was observed in the optimised settings meaning that a trial and error approach would remain as the only feasible method to identify optimal settings for 3D BLE at this stage.

An important additional consideration is the issue of processing time. Due to the required manual 'clean up' of the unwanted contours, application of Bspline interpolation and the need to execute multiple iterations of 3D BLE to identify optimal parameters, the 3D BLE performed poorly when compared to the method workflow proposed in **Chapter 3** (i.e. CTS) and in many cases was slower than manual segmentation (**Table 5.4**). In particular, the application of the 3D BLE to the Golgi apparatus sub-volumes, the most complex morphology amongst the key organelles studied here, not only yielded inferior MSA scores with the optimised settings (i.e. between 4 and 3) but also required a longer processing time than manual segmentation (**Figure 5.11**). Thus the 3D BLE is particularly unsuited to the Golgi apparatus as compared to our proposed method workflow.

**Table 5.2 Processing time of three different segmentation methods; manual, CTS and 3D BLE.**

Those segmentation methods are manual segmentation (man), cellular tomography segmentation (CTS) – an automated method established in Chapters 3 and 4 - and semi-automated 3D BLE. The sub-volumes were sub-classified into image classes of particular organelle type. Values listed in the table are time in min.

GA	Man	CTS	3DBLE	MC	Man	CTS	3DBLE	IG	Man	CTS	3DBLE
GA_C1				MC_C1				IG_C1			
GA4	10	2	18	MC1	6	3	8	IG1	4	3	5
GA10	12	3	17	MC2	5	2	15	IG2	5	3	5
GA11	12	2	9	MC3	6	2	16	IG3	4	3	5
GA_C2				MC6	7	3	15	IG4	4	3	5
GA5	13	3	8	MC9	6	3	15	IG_C2			
GA6	10	3	8	MC10	6	3	14	IG5	5	3	5
GA9	12	2	16	MC_C2				IG6	6	3	5
GA_C3				MC4	5	3	17	IG7	4	3	5
GA1	25	3	12	MC5	6	5	16	IG8	4	3	5
GA2	13	3	9	MC7	8	4	18	IG11	4	3	5
GA3	17	3	17	MC8	6	4	19	IG12	5	3	5
GA7	22	3	20	MC11	7	3	20	IG13	4	3	5
GA8	20	2	20	MC15	6	4	16	IG19	5	3	5
GA12	36	4	19	MC16	9	4	10	IG20	5	3	5
				MC_C3				IG_C3			
				MC12	7	4	21	IG9	6	3	5
				MC13	10	4	20	IG10	7	3	8
				MC14	8	3	19	IG14	6	3	5
				MC17	9	4	20	IG15	8	3	6
				MC18	9	4	24	IG16	7	3	7
								IG17	6	3	7
								IG18	6	3	5

### 5.3 Discussion

The recently developed 3D BLE has previously proven useful for detecting edges in 3D volumes (Ali et al., 2012). Here, 3D BLE was applied to a tomographic sub-volume of an insulin secreting beta cell. Earlier in this chapter, using the fully automatic settings, the whole sub-tomogram was analysed using the method principally as outlined in the original publication describing it (Ali et al., 2012) and the results were apparently poor or not satisfactory (i.e. the accuracy of each contour, the accuracy of 3D mesh and the effectiveness of the segmentation process).

Even following deconstruction of the tomogram dataset into extracted organelle sub-volumes, it was still necessary to manually identify the contour(s) of organelles or objects of interest from thousands of contours in order to provide a visually informative result. In the test performed here, the most optimal results required manual adjustment of two tuneable parameters within the 3D BLE interface. For simpler image such as immature granules less adjustment was required than for more complex organelles and the Golgi apparatus proved particularly challenging for this method. This demonstrates that to achieve optimal performance, the 3D BLE is not truly automated. The required

parameter adjustment was time consuming and required optimisation on a case by case basis with no obvious pattern that related to the sub-volume characteristics identified as a basis for sub-classification in **Chapter 4**. Further analysis of the observed optimal parameter combinations for 3D BLE may be conducted in the future, particularly to explore whether other characteristics of the sub-volumes of interest dictate the optimal 3D BLE settings. At this stage however, the 3D BLE approach remains inferior to the CTS workflow developed in **Chapters 3 and 4** and the results presented here offer support for this as our proposed image processing approach for these types of studies.



## **Chapter 6    GENERAL DISCUSSION**

---





## 6.1 Overview

The work presented in this thesis can be broadly separated into two components: the development of novel computational semi-automated and rapid segmentation techniques and the introduction of sub-classified organelles of interest according to image properties. These are required to achieve rapid and accurate segmentation of cellular compartments, and enable the downstream biological analysis of cellular organelles. In this chapter, both the biological and technical aspects of this project are tied together and discussed in a wider context which includes a summary of biological insights and suggestions for the future directions of whole cell tomography.

The complexity and uniqueness of different organelle structures and morphologies, which range in size, and density, have made the development of widely effective and/or high throughput processes complicated. The background noise however decreases the signal to noise ratio which also affects the membrane segmentation. This is demonstrated by the poor tracing results obtained in numerous case studies that implement a variety of 2D and 3D computational tracing approaches with recommended settings (Volkman, 2002, Nguyen et al., 2003, van der Heide et al., 2007), including one of the most recent developments in this field, the 3D bilateral edge detector (3D BLE) (Ali et al., 2012). Labour intensive parameter optimisation significantly improves the segmentation accuracy, but at significant cost, both in terms of human and computational processing time (Jiang et al., 2003) – depending on the properties of the image data (van der Heide et al., 2007). In 3D cellular segmentation, necessary post-processing approaches increase the processing time required to achieve accurate extraction of the targeted membranes of organelles (van der Heide et al., 2007). Consequently more efficient methods are needed to achieve acceptable processing times while retaining a desirable level of accuracy in the final 3D reconstructions/visualisation.

A number of significant contributions and findings are detailed in this PhD work. At the outset, this project was aimed at developing a semi-automated workflow and then defining the optimal settings from it for cellular tomography segmentation. A final revised protocol, formulated in Figure 2.4, for reaching the optimum segmentation workflow as identified by this work presented a number of improvements. Firstly, the organelle of interest is extracted and each of them will have nine copies. Secondly, these organelles sub-volumes are classified according to its image sub-class. Thirdly, the optimisation of the nine workflows is done on each copy of these sub-volumes. Fourthly, using a

special scoring system proposed in this thesis, the best parameter settings for particular image sub-classes are identified.

Degenerate optimal settings identification was conducted based on the sub-classification of organelles according to specific image features of each of these three organelles (i.e. the organelle's morphologies and sizes). The image features of these organelles summarised that there are similarities in which could be used to facilitate in finding the right semi-automated method settings. This expedited the segmentation process by defining standard settings that could be applied to sub-classified groups of organelles. The study was carried out on three key organelles pertaining to the insulin secretion process; i.e. the Golgi apparatus, mitochondria and insulin granules, chosen for these studies due to their biological importance to diabetes as well as differences in their morphology. This chapter summarises the key contributions and findings from each experimental chapter as well as future directions.

## **6.2 Segmentation challenges**

### **6.2.1 Relationship between sub-cellular structures and the event of insulin secretion**

From a morphological point of view, the event of biochemical stimulus – particularly at insulin secretion process – is deterministic of sub-cellular structures. These organelles present a range of complexity levels in terms of computational segmentation. In this study, a number of object attributes were identified that has enabled classification of morphologically distinct organelles into sub-groups that can be treated with degenerate sets of image processing algorithms. Beneficially these morphologically distinct structures are linked to functional differences. For example class one insulin granules (i.e. IG\_C1) are defined structurally as simple with an empty luminal space. Functionally, this sub-class represents 'immature insulin granules'. Insulin granules in image class two have a small crystal (sometimes indistinct) and the crystal is 'free' within the luminal space. In contrast the crystals of insulin granules belonging to image class three are 'complete' in shape, bigger, and the crystal's edges usually touch the granule's membrane (i.e. luminal space boundary). When the insulin grows into a crystalline structure it is called 'mature insulin granules'. The growth process of this 'crystal' is concluded into two stages and described as image classes two and three (i.e. IG\_C2 and IG\_C3). Both image classes are functionally named as 'mature insulin granule' but are structurally different. Similarly, the Golgi apparatus was divided into three image classes;

named GA\_C1, GA\_C2 and GA\_C3. The differences used here to sub-classify the Golgi apparatus (GA) possibly represent different stages of GA function in vesicular transport. For example, the GA tends to be larger (different in size) and more numerous in cells depending on the types of proteins it synthesised (Marsh et al., 2004, Emr et al., 2009, Ladinsky et al., 2002).

### 6.2.2 The role of image classification in insulin release

Computationally, the prime objective of classifying these key organelles was to enable efficient computational segmentation for high throughput analysis. Biologically however, this image classification may allow biologists to characterise and analyse the current cell's state for future studies. These tomograms (with many of its mitochondria classified in MC\_C2 and MC\_C3) can be classified as undergoing fusion and/or fission process which relates to the cell's energy production (Chen and Chan, 2009, Wiederkehr and Wollheim, 2006, Jitrapakdee et al., 2010, Chan, 2006, Karbowski et al., 2004, Collins et al., 2002). Rapid quantitative observations such as these may enable a better understanding of the current state of a cell and the relationship to other cells (or sub-cells).

## 6.3 More accurate modelling of cells

### 6.3.1 Faster and more accurate segmentation using a semi-automated method workflow

In **Chapter 3** a semi-automated workflow for fast and accurate cellular tomography segmentation was introduced. A series of tests were conducted for the development of the workflow. The first test was to evaluate the surface-rendered models of filtered images compared to manual segmentation. Nine image filters (optimised settings) from different backgrounds were applied for the purpose of comparison. They were: Gaussian filter, Minimum filter, Maximum filter, 2D Median filter, 3D Median filter, Meanshift filter, Kuwahara filter, Non-linear Anisotropic Diffusion filter and Bilateral filter. Surface-rendered models of filtered images were initially compared to contours derived from manually segmented tomograms (**Chapter 3, Section 3.3.2.1, Figure 3.2, Figure 3.3, Figure 3.4** and **Table 3.4**). Subsequently, two segmentation algorithms were evaluated – the *snake* algorithm (semi-automated approach) and *watershed* algorithm (automated approach). Stacks of 2D images of example datasets were pre-processed (filtered) using nine noise reduction filters (at recommended settings). Example 2D image stacks pre-filtered using one of the nine noise reduction filters were

segmented by either the *snakes* or *watershed* algorithms. Contours obtained following application of both *snakes* (with parameter adjustment) and *watershed* (with parameter adjustment) were comparable to manual tracing, however, *snakes* required longer processing time (particularly influenced by the need to manually draw initial contours and parameter adjustment) compared to *watershed* algorithm and manual tracing. Thus, *watershed* was selected as a basis for workflow development.

The shortcoming of just using noise reduction together with watershed algorithm is the unwanted contours. These contours needed to be removed. In order to address this computationally, mathematical morphology modelling algorithm was added as a post-processing step, which improved the results obtained from the workflow.

Nine method flows (M1 – M9) were thus developed; each of 9 different filters, followed in turn by watershed and mathematical morphologies. The 9 different filters were **M1**: Gaussian filter; **M2**: Minimum filter; **M3**: Maximum filter; **M4**: 2D Median filter; **M5**: 3D Median filter; **M6**: Kuwahara filter; **M7**: Meanshift filter; **M8**: Non-linear anisotropic diffusion (NAD) filter; and **M9**: Bilateral filter.

Having defined these method flows, optimised settings were identified for every organelle sub-volume. The segmentation results were able to be improved further by tuning the default settings used by each of the noise reduction filters, the watershed and mathematical morphology algorithms. To quantify the results obtained from these methods flows, as compared to the manually segmented ground truth datasets, a novel scoring system was introduced that enabled identification of settings that achieved optimal tracing results. This scoring system is based on comparison of the mesh surface area (MSA) value obtained using manual and computational methods segmentation. These MSA values were calculated from the 3-D models of the organelles. Based on these comprehensive trials, the best method flow was consistently identified as non-linear anisotropic diffusion (NAD) filtering followed by *watershed* and mathematical morphologies (i.e. the flow annotated as Method 8 throughout this thesis) and is described in **Figure 4.7**, **Figure 4.8**, **Figure 4.9** and **Figure 5.11**. 3D median filtering followed by watershed (designated Method 5) and bilateral filtering followed by watershed (designated Method 9) also performed reasonably well, depending on the morphology of the target structure

### **6.3.2 The importance of identifying and sub-classifying cellular compartments according to image properties**

The identification of a single standard approach to segment all cellular tomography images has still not been achieved (van der Heide et al., 2007, Volkman, 2002). The unique nature of each organelle requires appropriate pre-filtering algorithms and parameter optimisation for accurate segmentation. For example, even though workflow M8 proved consistently optimal in the studies summarised above, within this workflow different parameter settings were required in order to optimise the segmentation results for different organelles. However, this study has demonstrated that classification of these organelle sub-volumes according to their image properties provides a feasible basis for the identification of standard optimised settings for each image sub-class, opening up the possibility for faster semi-automated segmentation and making the identification of optimal settings for image processing easier.

In Chapter 4, the study of image properties from more than 400 sub-volumes of key organelles was conducted. Three image sub-classes were defined for each key organelle (i.e. in total there were nine image classes). When organelle sub-volumes were grouped into the same class (i.e. that have similarities in properties such as morphology, structure size, organelle type) the process of automated contour tracing could be significantly expedited. Optimised settings for segmentation obtained using 10 example sub-volumes from each image class could be applied without modification to the rest of the organelle sub-volumes within the same image class. Thus, standard optimised settings for Method M8 (the best method flow) could be identified for the nine different sub-classes (**Section 4.2.3** and **Section 4.2.4, Table 4.2**) enabling rapid, subsequent contour determination for the entire 400 sub-volume dataset. This substantial finding represents the first discovery of a degenerate set of standard settings that enable the semi-automated segmentation at a satisfactory accuracy level for organelles corresponding to a defined cellular image sub-class.

### **6.3.3 Improving model accuracy of 3D BLE by optimising the settings of sigma 2 and threshold values**

In parallel with the work described here, ongoing studies conducted within the Hankamer Group from the Institute for Molecular Bioscience, UQ, were focussed on the development of a true parameter-free 3D edge detector algorithm. In 2012 (Ali et al., 2012), this was reportedly achieved through the implementation in 3D of the previously described 2D bilateral edge detection filter (Pantelic et al., 2006, Pantelic et al., 2007). The automated 3D BLE (i.e. with no parameter

optimisation) demonstrated accurate segmentation of macromolecular complexes and provides a valuable tool for accurate 3D structural complexity annotation at the sub-cellular level. The efficiency of 3D BLE was further tested in **Chapter 5**. A sub-region, extracted from a cellular tomogram used to generate the data analysed in **Chapter 3** and **Chapter 4**, was used in initial tests of the 3D BLE. As the implementation was particularly focused on detecting objects edges (sigma 2) – while reducing image noise (threshold value) – even following the application of B-spline interpolation, unfortunately default parameters of 3D BLE produced a segmented map with numerous broken contours.

Improved segmentation results could be obtained using the 3D BLE when the organelles of interest were extracted into sub-volumes and processed individually with two of the three modifiable parameters in the 3D BLE GUI – the sigma 2 and threshold values – were iteratively optimised. These optimal 3D BLE segmentation results were quantitatively compared to the results obtained from the workflow based on Method M8, outlined in **Chapter 4**. The results obtained using the workflow approach were consistently better in terms of processing time and segmentation accuracy, compared to the results of optimised 3D BLE, despite the fact that parameters were optimised for each individual sub-volume. Post-processing of the 3D BLE with the mathematical morphology operations employed in the M8 workflow improved the contour connectivity for more accurate 3D surface meshes – i.e. close to the ground truth dataset. But this post-processing further increased the time required to apply the 3D BLE.

Ultimately, both the automated 3D BLE and workflow M8 proved faster than manual tracing. However, as compared to 3D BLE, optimal settings of M8 (**Chapter 4**) score significantly better in terms of MSA than the final, optimised 3DBLE results (**Section 5.2.3**, example in **Figure 5.12**) while maintaining a significant time advantage, performing approximately 50% faster than 3D BLE (**Table 5.4**).

## **6.4 Future directions**

### **6.4.1 Towards automated annotation of cellular compartments using machine learning approaches**

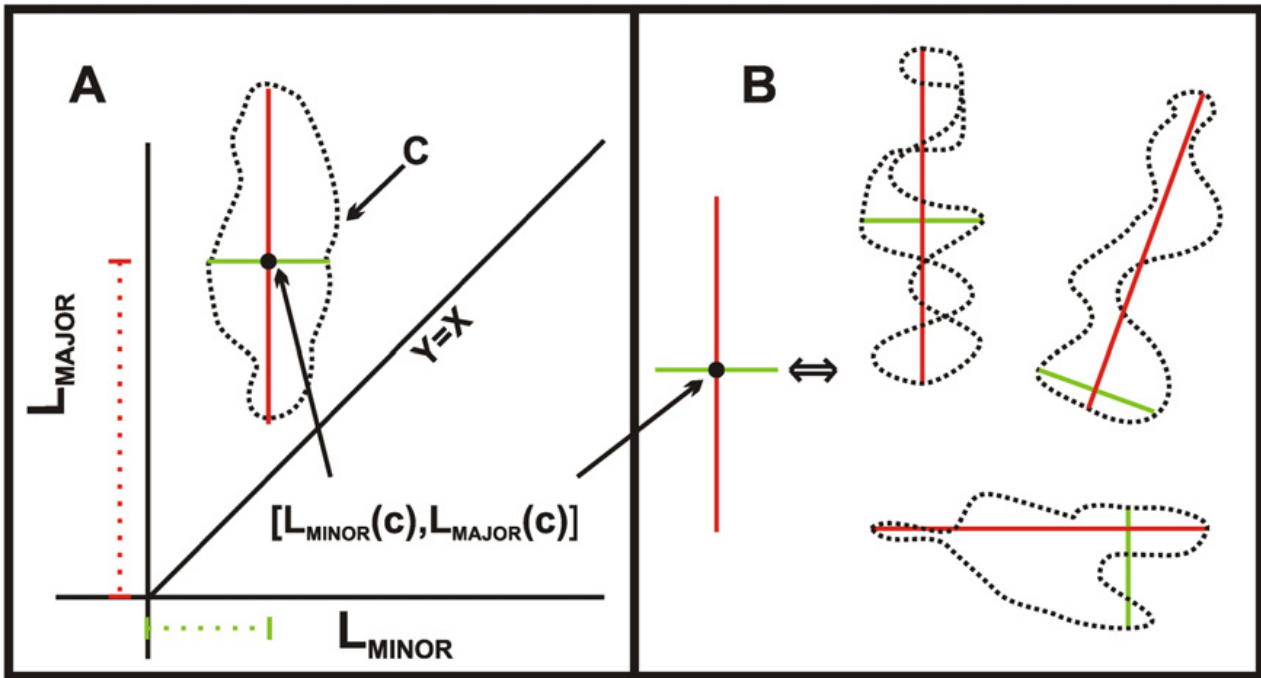
The major outcome of this thesis has been the development of a semi-automated approach for cellular tomography segmentation (semi-automated CTS) that enables relatively accurate

segmentation of complex cellular compartments at a faster rate than what has previously been possible. It produces complete stacks of contours throughout the entire object volume.

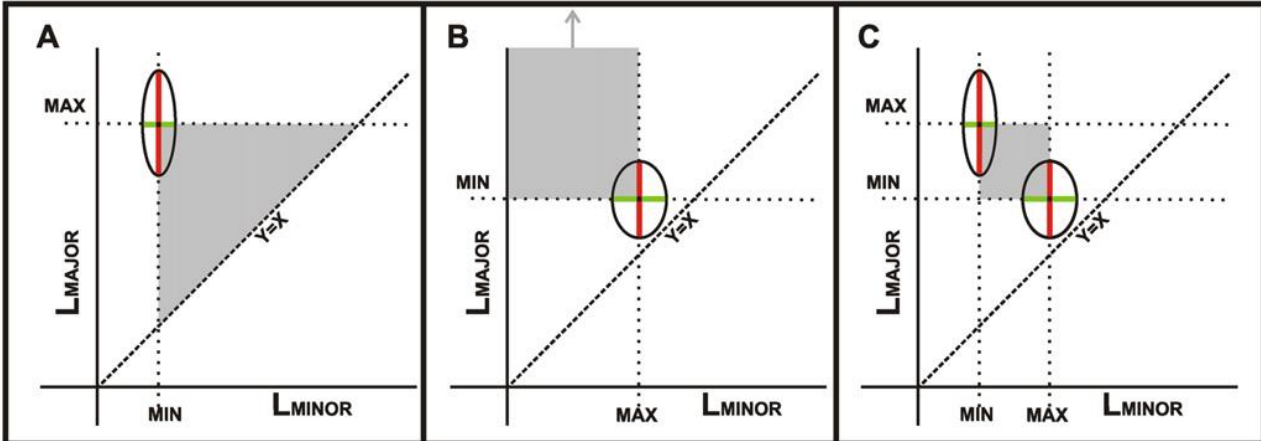
With the recent advance of single particle tomography (i.e. a subset of sub-tomogram averaging techniques), 3D sub-volumes of macromolecular assemblies are extracted from larger tomographic volumes and oriented/averaged together to generate 3D structures. Similar principles applied to those described in the Woolford paper (Woolford et al., 2007) – an algorithm which combined information about particle diameter with other parameters such as the ones described in this thesis to discriminate between true particles and false particles – may be applicable to automated particle picking in 3D. This could be used as a basis for a particle picking algorithm. The relevance to this work is that properties like particle diameter, perimeter and contour area, which in 3D equate to MSA and volume might be able to be incorporated into an automatic organelle classification system using e.g. machine learning approaches. For example, are there a set of readily identifiable features in the raw data that user could draw on to classify insulin granules as IG\_C1, C2 or C3 respectively, rather than the user having to manually assign these to an image group.

The concept of contour space and number of examples of contour spaces are illustrated in **Figure 6.1** and **Figure 6.2** respectively – adapted from (Woolford et al., 2007) – which could be combined with other image features (e.g. inverted contrast of insulin granules, number of membrane boundaries might dictate a Golgi). The paper also describes methods for counting the number of pixels inside a contour (i.e. area of a contour), and the number of pixels that make up the contour (i.e. perimeter) (in 3D this would be the volume and the total mesh surface area, which we already have).





**Figure 6.1** Concept of contour space (A) and three examples of different contours (B). (A) Example of a contour valid for  $L_{MAJOR}(c) > L_{MINOR}(c)$ , i.e. above the line  $y = x$ . The vertical axis represents the length of the contour's major axis and the horizontal axis represents the length of its minor axis. The contour (denoted  $c$ ) is described as the point  $[L_{MINOR}(c), L_{MAJOR}(c)]$  in contour space which describes the length of its major and minor axes. (B) The figure demonstrates the topology of these three contours is arbitrary even they are characterised by the same point in contour space depicted in (A). A point in contour space summarizes the lengths of a contour's major and minor axes.



**Figure 6.2** Three contour selection spaces to generate  $MAX_{MAJOR}$  and  $MIN_{MINOR}$  from the (black) contour shown in all three panels. (A) The region of contour space (shaded grey) satisfies  $L_{MAJOR}(c) \leq MAX_{MAJOR}$ ,  $MIN_{MINOR} \leq L_{MINOR}(c)$  and  $L_{MAJOR}(c) > L_{MINOR}(c)$ . (B) Grey region satisfy  $MIN_{MAJOR} \leq L_{MAJOR}(c)$  and  $L_{MINOR}(c) \leq MAX_{MINOR}$  - useful for selecting long, thin contours. (C) The approach selects contours from the intersection of the grey regions depicted in (A and B). Note that for this approach (i.e. bounded interval approach) to proceed; more than one contour must be selected interactively by the user. Upon execution of the automatic selection algorithm, all contours that coincide with the grey area in contour space will be selected automatically.

The knowledge of the differences in the image structures within image classes (as described in this study) could be extended to a wider scope by cellular biologists and even microbiologists. Prime examples are; a study of the relationship between structure and function within organelles sub-

classes such as the chemical factors which contribute to their structural differences, and a study on how the image classes of these organelles pertained to its quantity in a sample data. These studies have higher potential to be achieved when using cells with different conditions (e.g. stimulated and non-stimulated cells). Besides that, these studies could improve the efficiency of mathematical segmentation to the next level such as one standard settings of the best method (i.e. Method 8) could be applied to segment organelles from different image classes.

## **6.5 Conclusion**

As a starting point for this PhD it was shown (Marsh et al., 2001a) that the manual 3D segmentation of ~1% of an insulin-secreting HIT-T15 cell required ~ 3600 person-hours. This PhD project has demonstrated an effective semi-automated segmentation workflow based on optimised settings of image filtration, watershed algorithm and mathematical morphologies operations (for selected segmentation cases). The most efficient workflow involves pre-filtering with the non-linear anisotropic diffusion algorithm. Degenerate sets of algorithm parameters have been identified that enable the rapid and accurate segmentation of organelles belonging to one of nine image sub-classes for three key organelles. The key organelles chosen for this study, namely insulin granules, the Golgi apparatus and mitochondria, are morphologically diverse and have thus provided a robust platform for the development of this technology.

Sorting organelles of interest into morphologically distinct sub-classes has not only improved the processing time of the individual organelle sub-volume (i.e. approximately 90% to 200% faster than manual segmentation approach) but has also been critical to achieving the project aim – to identifying a range of optimal algorithms and settings that are suitable for the rapid segmentation of isolated organelle structures at sufficient accuracy to enable high throughput, quantitative comparison of cellular tomography data. The workflow developed here was able to segment >80% of organelles within an accuracy of +/- 5% of the true contour, as defined by manual segmentation; where successful detailed 3D segmentation of human cell was represented in the Marsh Group (Marsh et al., 2001a). Currently there exists no single parameter or parameter-free automated segmentation methods that can reliably tracing complex organelles within high resolution tomograms at a speed and accuracy comparable to this method. This method has shown improvement in semi-automated segmentation and thus represents an important development for future automated analysis of cellular tomograms.



## References

- AL-AMOUDI, A., NORLEN, L. P. & DUBOCHET, J. 2004. Cryo-electron microscopy of vitreous sections of native biological cells and tissues. *Journal of Structural Biology*, 148, 131-135.
- ALBERTI, K. G. M. M. & ZIMMET, P. 1998. Definition, diagnosis and classification of diabetes mellitus and its complications. Part 1: diagnosis and classification of diabetes mellitus. Provisional report of a WHO consultation. *Diabetic Medicine*, 15, 539-553.
- ALI, R. A., LANDSBERG, M. J., KNAUTH, E., MORGAN, G. P., MARSH, B. J. & HANKAMER, B. 2012. A 3D image filter for parameter-free segmentation of macromolecular structures from electron tomograms. *PLoS One*, 7, e33697.
- ANDREY, P. & BOUDIER, T. Adaptive active contours (snakes) for the segmentation of complex structures in biological images. First ImageJ User and Developer Conference, 18-19 May 2006 Luxemburg, Germany.
- APPLETON, B. & TALBOT, H. 2005. Globally optimal geodesic active contours. *Journal of Mathematical Imaging and Vision*, 23, 67-86.
- ARIAS-CASTRO, E. & DONOHO, D. L. 2009. Does median filtering truly preserve edges better than linear filtering? *The Annals of Statistics*, 37, 1172-1206.
- ASPINWALL, C. A., JONATHAN, R. T., LAKEY AND KENNEDY R. T. 1999. Insulin-stimulated Insulin Secretion in Single Pancreatic Beta Cells. *Journal of Biomedical Chemistry*, 274, 6360-6365.
- AURICH, V. & WEULE, J. 1995. Non-linear gaussian filters performing edge preserving diffusion. *Mustererkennung*. Berlin, Germany: Springer Berlin Heidelberg.
- BABU, S., PAO-CHUAN, L., SHIN, M. C. & TSAP, L. V. Towards Recovery of 3D Chromosome Structure. Computer Vision and Pattern Recognition Workshop, 27 July 2004 2004 Washington, D.C., USA., 1-1.
- BAETENS, D., MALAISSE-LAGAE, F., PERRELET, A. & ORCI, L. 1979. Endocrine pancreas: three-dimensional reconstruction shows two types of islets of langerhans. *Science*, 206, 1323-1325.
- BAJAJ, C., YU, Z. & AUER, M. 2003. Volumetric feature extraction and visualization of tomographic molecular imaging. *Journal of Structural Biology*, 144, 132-143.
- BAKKER, P., VAN VLIET, L. J. & VERBEEK, P. W. Edge preserving orientation adaptive filtering. IEEE Computer Society Conference: Computer Vision and Pattern Recognition, 23-25 June 1999 Fort Collins, United States.
- BARTESAGHI, A., SAPIRO, G. & SUBRAMANIAM, S. 2005. An energy-based three-dimensional segmentation approach for the quantitative interpretation of electron tomograms. *IEEE Transactions on Image Processing*, 14, 1314-1323.
- BAUMEISTER, W. 2002. Electron tomography: towards visualizing the molecular organization of the cytoplasm. *Current Opinion in Structural Biology*, 12, 679-684.
- BAUMEISTER, W. 2005. A voyage to the inner space of cells. *Protein Science*, 14, 257-269.
- BAUMEISTER, W., GRIMM, R. & WALZ, J. 1999. Electron tomography of molecules and cells. *Trends in Cell Biology*, 9, 81-85.
- BEUCHER, S. & MEYER, F. 1993. The morphological approach to segmentation: the watershed transformation. In: DOUGHERTY, E. (ed.) *Mathematical Morphology in Image Processing*. New York: Marcel Dekker.
- BILBAO-CASTRO, J. R., SORZANO, C. O., GARCIA, I. & FERNANDEZ, J. J. 2010. XMSF: Structure-preserving noise reduction and pre-segmentation in microscope tomography. *Bioinformatics*, 26, 2786-2787.

- BURGETH, B., DIDAS, S. & WEICKERT, J. 2009. A general structure tensor concept and coherence-enhancing diffusion filtering for matrix fields. *In: LAIDLAW, D. & WEICKERT, J. (eds.) Visualization and Processing of Tensor Fields*. Springer Berlin Heidelberg, Germany.
- CANNY & JOHN 1986. A computational approach to edge detection. *IEEE Transactions on Pattern Analysis and Machine Intelligence*, 8, 679-698.
- CARTAILLER, J.-P. 2004. *Insulin - from secretion to action* [Online]. Nashville, Tennessee: Beta Cell Biology Consortium. Available: [http://www.betacell.org/content/articleview/article\\_id/1/2011](http://www.betacell.org/content/articleview/article_id/1/2011)].
- CHAN, D. C. 2006. Mitochondrial fusion and fission in mammals. *Annual Review of Cell and Developmental Biology*, 22, 79-99.
- CHEN, H. & CHAN, D. C. 2009. Mitochondrial dynamics--fusion, fission, movement, and mitophagy--in neurodegenerative diseases. *Human Molecular Genetics*, 18, 169-176.
- CHEN, H. C. & CHAN, D. C. 2005. Emerging functions of mammalian mitochondrial fusion and fission. *Human Molecular Genetics*, 14, 283-289.
- COLLINS, T. J., BERRIDGE, M. J., LIPP, P. & BOOTMAN, M. D. 2002. Mitochondria are morphologically and functionally heterogeneous within cells. *EMBO Journal*, 21, 1616-1627.
- COMANICIU, D. & MEER, P. Mean shift analysis and applications. The Proceedings of the Seventh IEEE International of Computer Vision, 20-27 Sept 1999 Kerkyra. 1197-1203.
- CRAIG, E. L., GREIDER, M. H. & FRAJOLA, W. J. 1962. An Embedding Technique for Electron Microscopy Using Epon 812. *Journal of Cell Biology*, 12, 190.
- D'AMBRA, R., SURANA, M., EFRAT, S., STARR, R. G. & FLEISCHER, N. 1990. Regulation of insulin secretion from beta-cell lines derived from transgenic mice insulinomas resembles that of normal beta-cells. *Endocrinology*, 126, 2815-2822.
- DERGAN, J., MIRONOV, A. A. & SVETINA, S. 2006. Physical factors that affect the number and size of Golgi cisternae. *Traffic*, 7, 85-96.
- DERICHE, R., COCQUEREZ, J. P. & ALMOUZNY, G. An efficient method to build early image description. 9th International Conference on Pattern Recognition, 14-17 Nov 1988 Rome. IEEE, 588-590.
- DOUGHERTY, E. R. & LATUFO, R. A. 2003. *Hands-on Morphological Image Processing*, Bellingham, Washington, SPIE Press.
- EFRAT, S., LEISER, M., SURANA, M., TAL, M., FUSCO-DEMANE, D. & FLEISCHER, N. 1993. Murine Insulinoma Cell Line With Normal Glucose-Regulated Insulin Secretion. *Diabetes*, 42, 901-907.
- ELAYAT, A. A., ELNAGGAR, M. M. & TAHIR, M. 1995. An immunocytochemical and morphometric study of the rat pancreatic-islets. *Journal of Anatomy*, 186, 629-637.
- EMR, S., GLICK, B. S., LINSTEDT, A. D., LIPPINCOTT-SCHWARTZ, J., LUINI, A., MALHOTRA, V., MARSH, B. J., NAKANO, A., PFEFFER, S. R., RABOUILLE, C., ROTHMAN, J. E., WARREN, G. & WIELAND, F. T. 2009. Journeys through the Golgi--taking stock in a new era. *Journal of Cell Biology*, 187, 449-453.
- FARQUHAR, M. G. & PALADE, G. E. 1998. The Golgi apparatus: 100 years of progress and controversy. *Trends in Cell Biology*, 8, 2-10.
- FERNÁNDEZ, J.-J. & LI, S. 2003. An improved algorithm for anisotropic nonlinear diffusion for denoising cryo-tomograms. *Journal of Structural Biology*, 144, 152-161.
- FERNANDEZ, J. J. 2009. TOMOBFLOW: feature-preserving noise filtering for electron tomography. *BMC Bioinformatics*, 10, 178.
- FRANGAKIS, A. & HEGERL, R. 1999. Nonlinear Anisotropic Diffusion in Three-Dimensional Electron Microscopy. *In: NIELSEN, M., JOHANSEN, P., OLSEN, O. & WEICKERT, J.*

- (eds.) *Scale-Space Theories in Computer Vision*. Berlin Heidelberg, Germany: Springer Berlin Heidelberg.
- FRANGAKIS, A. S. & FORSTER, F. 2004. Computational exploration of structural information from cryo-electron tomograms. *Current Opinion in Structural Biology*, 14, 325-331.
- FRANGAKIS, A. S. & HEGERL, R. 2001. Noise reduction in electron tomographic reconstructions using nonlinear anisotropic diffusion. *Journal of Structural Biology*, 135, 239-250.
- FRANK, J. 1992. *Electron tomography: three-dimensional imaging with the transmission electron microscope*, New York, Plenum Press.
- FRAZIER, A. E., KIU, C., STOJANOVSKI, D., HOOGENRAAD, N. J. & RYAN, M. T. 2006. Mitochondrial morphology and distribution in mammalian cells. *Journal of Biological Chemistry*, 387, 1551-1558.
- FREY, T. G., PERKINS, G. A. & ELLISMAN, M. H. 2006. Electron tomography of membrane-bound cellular organelles. *Annual Review of Biophysics and Biomolecular Structure*, 35, 199-224.
- GEPTS, W. & LECOMPTE, P. M. 1981. The pancreatic-islets in diabetes. *American Journal of Medicine*, 70, 105-115.
- GOLGI, C. 1898. Sur la structure des cellules nerveuses des ganglions spinaux. *Archives Italiennes de Biologie*, 30, 60-71.
- GONZALEZ, R. C. 2002. *Digital Image Processing*, Upper Saddle River, NJ, Prentice Hall.
- GOTOH, M., MAKI, T., KIYOIZUMI, T., SATOMI, S. & MONACO, A. P. 1985. An improved method for isolation of mouse pancreatic-islets. *Transplantation*, 40, 437-438.
- GRIFFITHS, G., FULLER, S. D., BACK, R., HOLLINSHEAD, M., PFEIFFER, S. & SIMONS, K. 1989. The dynamic nature of the Golgi complex. *Journal of Cell Biology*, 108, 277-297.
- GRÜNEWALD, K., MEDALIA, O., GROSS, A., STEVEN, A. C. & BAUMEISTER, W. 2003. Prospects of electron cryotomography to visualize macromolecular complexes inside cellular compartments: implications of crowding. *Biophysical Chemistry*, 100, 577-591.
- GUINAMARD, R., DEMION, M. & LAUNAY, P. 2010. Physiological roles of the TRPM4 channel extracted from background currents. *Physiology (Bethesda)*, 25, 155-164.
- HAGYARD, D., RAZAZ, M. & ATKIN, P. Analysis of watershed algorithms for greyscale images. IEEE International Conference Proceedings on Image Processing, 16-19 Sep 1996 Lausanne. 41-44.
- HALES, K. G. 2010. Mitochondrial Fusion and Division. *Nature Education*, 3(9), 604-605.
- HEIJMANS, H. J. A. M. 1999. Connected Morphological Operators for Binary Images. *Computer Vision and Image Understanding*, 73, 99-120.
- HEYMANN, B. 1999-2014. *BSoft* [Online]. Bethesda. Available: <http://lsbr.niams.nih.gov/bsoft/>.
- HEYMANN, J. B. 2001. Bsoft: image and molecular processing in electron microscopy. *Journal of Structural Biology*, 133, 156-169.
- HEYMANN, J. B. & BELNAP, D. M. 2006. Bsoft: image processing and molecular modeling for electron microscopy. *Journal of Structural Biology*, 157, 3-18.
- HOWELL, S. L. 1974. The molecular organization of the beta granule of the islets of Langerhans. *Advances in Cytopharmacology*, 2, 319-327.
- HUANG, P., GALLOWAY, C. A. & YOON, Y. 2011. Control of Mitochondrial Morphology Through Differential Interactions of Mitochondrial Fusion and Fission Proteins. *PLoS One*, 6, e20655.
- HUTTON, J. C. 1989. The insulin secretory granule. *Diabetologia*, 32, 271-281.
- JACOB, M., BLU, T. & UNSER, M. 3-D reconstruction of DNA filaments from stereo cryo-electron micrographs. IEEE International Symposium on Biomedical Imaging, 7-10 July 2002 Washington D.C., USA. 597-600.

- JIANG, M., JI, Q. & MCEWEN, B. F. 2006a. Automated extraction of fine features of kinetochore microtubules and plus-ends from electron tomography volume. *IEEE Image Processing* 15, 2035-2048.
- JIANG, M., JI, Q. & MCEWEN, B. F. 2006b. Model-based automated extraction of microtubules from electron tomography volume. *IEEE Transaction on Information Technology in Biomedicine*, 10, 608-617.
- JIANG, W., BAKER, M. L., WU, Q., BAJAJ, C. & CHIU, W. 2003. Applications of a bilateral denoising filter in biological electron microscopy. *Journal of Structural Biology*, 144, 114-122.
- JIN, Y. 2006. *Multi-objective machine learning*, New York, USA, Springer.
- JITRAPAKDEE, S., WUTTHISATHAPORNCHAI, A., WALLACE, J. C. & MACDONALD, M. J. 2010. Regulation of insulin secretion: role of mitochondrial signalling. *Diabetologia*, 53, 1019-1032.
- KARBOWSKI, M., ARNOULT, D., CHEN, H., CHAN, D. C., SMITH, C. L. & YOULE, R. J. 2004. Quantitation of mitochondrial dynamics by photolabeling of individual organelles shows that mitochondrial fusion is blocked during the Bax activation phase of apoptosis. *Journal of Cell Biology*, 164, 493-499.
- KARBOWSKI, M. & YOULE, R. J. 2003. Dynamics of mitochondrial morphology in healthy cells and during apoptosis. *Cell Death Differentiation*, 10, 870-880.
- KARGUL, J. & LAURENT, G. J. 2009. Mitochondria matter: new concepts of dynamics and roles in pathophysiology. *International Journal of Biochemistry and Cell Biology*, 41, 1747.
- KASS, M., WITKIN, A. & TERZOPOULOS, D. 1988. Snakes: Active contour models. *International Journal of Computer Vision*, 1, 321-331.
- KREMER, J. R., MASTRONARDE, D. N. & MCINTOSH, J. R. 1996. Computer visualization of three-dimensional image data using IMOD. *Journal of Structural Biology*, 116, 71-76.
- KREMER, J. R., O'TOOLE, E. T., WRAY, G. P., MASTRONARDE, D. N., MITCHELL, S. J. & MCINTOSH, J. R. Characterization of beam-induced thinning and shrinkage of semi-thick sections in the HVEM. Proceedings XII International Congress on Electron Microscopy, 1990. 752-753.
- KUWAHARA, M., HACHIMURA, K., EIHO, S. & KINOSHITA, M. 1976. *Digital Processing of Biomedical Images*, New York, USA, Plenum Press.
- LADINSKY, M. S., MASTRONARDE, D. N., MCINTOSH, J. R., HOWELL, K. E. & STAEHELIN, L. A. 1999. Golgi structure in three dimensions: functional insights from the normal rat kidney cell. *Journal of Cell Biology*, 144, 1135-1149.
- LADINSKY, M. S., WU, C. C., MCINTOSH, S., MCINTOSH, J. R. & HOWELL, K. E. 2002. Structure of the Golgi and distribution of reporter molecules at 20 degrees C reveals the complexity of the exit compartments. *Molecular Biology of the Cell*, 13, 2810-2825.
- LEBBINK, M. N., GEERTS, W. J., VAN DER KRIFT, T. P., BOUWHUIS, M., HERTZBERGER, L. O., VERKLEIJ, A. J. & KOSTER, A. J. 2007. Template matching as a tool for annotation of tomograms of stained biological structures. *Journal of Structural Biology*, 158, 327-335.
- LUTHER, P. 2005. Sample shrinkage and radiation damage of plastic sections. In: FRANK, J. (ed.) *Electron Tomography: Methods for Three-Dimensional Visualization of Structure in the Cell*. New York, USA: Springer.
- LUTHER, P. K. 1992. Sample shrinkage and radiation damage. In: FRANK, J. (ed.) *Electron Tomography : Three-Dimensional Imaging with the Transmission Electron Microscope*. New York, USA: Plenum Press.
- LUTHER, P. K., LAWRENCE, M. C. & CROWTHER, R. A. 1988. A method for monitoring the collapse of plastic sections as a function of electron dose. *Ultramicroscopy*, 24, 7-18.

- MAECHLER, P., KENNEDY, E. D., POZZAN, T. & WOLLHEIM, C. B. 1997. Mitochondrial activation directly triggers the exocytosis of insulin in permeabilized pancreatic beta-cells. *EMBO Journal*, 16, 3833-3841.
- MARSH, B. J. 2005. Lessons from tomographic studies of the mammalian Golgi. *Biochemical and Biophysics Acta*, 1744, 273-292.
- MARSH, B. J. 2007. Reconstructing Mammalian Membrane Architecture by Large Area Cellular Tomography. 79, 193-220.
- MARSH, B. J., COSTIN, A. J., MORGAN, G. P. & HEIDE, P. V. D. 2005. 3D Structure Studies of the Pancreatic Beta Cell by High Resolution Electron Microscope (EM) Tomography. *Microscopy and Microanalysis*, 11.
- MARSH, B. J. & HOWELL, K. E. 2002. The mammalian Golgi - complex debates. *Nature Review of Molecular Cell Biology*, 3, 789-795.
- MARSH, B. J., MASTRONARDE, D. N., BUTTLE, K. F., HOWELL, K. E. & MCINTOSH, J. R. 2001a. Organellar relationships in the Golgi region of the pancreatic beta cell line, HIT-T15, visualized by high resolution electron tomography. *Proceedings of the National Academy of Science U S A*, 98, 2399-406.
- MARSH, B. J., MASTRONARDE, D. N., MCINTOSH, J. R. & HOWELL, K. E. 2001b. Structural evidence for multiple transport mechanisms through the Golgi in the pancreatic beta-cell line, HIT-T15. *Biochemical Society Transactions*, 29, 461-467.
- MARSH, B. J., VOLKMANN, N., MCINTOSH, J. R. & HOWELL, K. E. 2004. Direct continuities between cisternae at different levels of the Golgi complex in glucose-stimulated mouse islet beta cells. *Proceedings of the National Academy of Science USA*, 101, 5565-5570.
- MASTRONARDE, D. N. 1997. Dual-axis tomography: an approach with alignment methods that preserve resolution. *Journal of Structural Biology*, 120, 343-352.
- MASTRONARDE, D. N. 2003. SerialEM: a program for automated tilt series acquisition on tecnai microscopes using prediction of specimen position. *Microscopy and Microanalysis*, 9, 1182-1183.
- MASTRONARDE, D. N. 2005. Automated electron microscope tomography using robust prediction of specimen movements. *Journal of Structural Biology*, 152, 36-51.
- MASTRONARDE, D. N. 2006. Tomographic Reconstruction with the IMOD Software Package. *Microscopy and Microanalysis*, 12, 178.
- MCDONALD, K. & MORPHEW, M. K. 1993. Improved preservation of ultrastructure in difficult-to-fix organisms by high-pressure freezing and freeze substitution: 1. drosophila-melanogaster and strongylocentrotus-purpuratus embryos. *Microscopy Research and Technique*, 24, 465-473.
- MCEWEN, B. F., JIANG, M., ZHANG, W., VANDENBELDT, K. & JI, Q. 2005. Model-Based Approach to Automated Segmentation of Electron Tomographic Reconstructions. *Microscopy and Microanalysis*, 11, 328-329.
- MCEWEN, B. F. & MARKO, M. 2001. The Emergence of Electron Tomography as an Important Tool for Investigating Cellular Ultrastructure. *Journal of Histochemistry & Cytochemistry*, 49, 553-563.
- MCINTOSH, R., NICASTRO, D. & MASTRONARDE, D. 2005. New views of cells in 3D: an introduction to electron tomography. *Trends in Cell Biology*, 15, 43-51.
- MEIJSTER, A. & WILKINSON, M. H. F. 2002. A comparison of algorithms for connected set openings and closings. *IEEE Transactions on Pattern Analysis and Machine Intelligence*, 24, 484-494.
- MESSAOUDII, C., BOUDIER, T., SANCHEZ SORZANO, C. O. & MARCO, S. 2007. TomoJ: tomography software for three-dimensional reconstruction in transmission electron microscopy. *BMC Bioinformatics*, 8, 288-296.



- MEYERS, D., SKINNER, S. & SLOAN, K. 1992. Surfaces from contours. *ACM Transactions on Graphics*, 11, 228-258.
- MONGA, O., DERICHE, R., MALANDAIN, G. & COCQUEREZ, J. P. 1991. Recursive filtering and edge tracking: two primary tools for 3D edge detection. *Image Vision Computing*, 203-214.
- NARASIMHA, R., AGANJ, I., BENNETT, A. E., BORGNIA, M. J., ZABRANSKY, D., SAPIRO, G., MCLAUGHLIN, S. W., MILNE, J. L. & SUBRAMANIAM, S. 2008. Evaluation of denoising algorithms for biological electron tomography. *Journal of Structural Biology*, 164, 7-17.
- NGUYEN, H. & JI, Q. 2008. Shape-driven three-dimensional watersnake segmentation of biological membranes in electron tomography. *IEEE Transactions on Medical Imaging*, 27, 616-628.
- NGUYEN, H. T., WORRING, M. & VAN DEN BOOMGAARD, R. 2003. Watersnakes: energy-driven watershed segmentation. *IEEE Transactions on Pattern Analysis and Machine Intelligence*, 25, 330-342.
- NICOLLS, M. R., COULOMBE, M., BEILKE, J., GELHUAS, H. C. & GILL, R. G. 2002. CD4-dependent generation of dominant transplantation tolerance induced by simultaneous perturbation of CD154 and LFA-1 pathways. *Journal of Immunology*, 169, 4831-4839.
- NOSKE, A. B. 2010. *Multi-scale, spatio-temporal analysis of mammalian cell tomograms*. PhD Thesis, The University of Queensland.
- NOSKE, A. B., COSTIN, A. J., MORGAN, G. P. & MARSH, B. J. 2008. Expedited approaches to whole cell electron tomography and organelle mark-up in situ in high-pressure frozen pancreatic islets. *Journal of Structural Biology*, 161, 298-313.
- NOSKE, A. B. & MARSH, B. J. 2011. Mapping the  $\beta$ -Cell in 3D at the Nanoscale Using Novel Cellular Electron Tomography and Computational Approaches. In: AL., B. E. (ed.) *Beta Sys: Systems Biology of Regulated Exocytosis in Pancreatic B-Cells*. New York, USA: Springer New York.
- O'TOOLE, E. T., WINEY, M. & MCINTOSH, J. R. 1999. High-voltage electron tomography of spindle pole bodies and early mitotic spindles in the yeast *Saccharomyces cerevisiae*. *Molecular Biology of the Cell*, 10, 2017-2031.
- OKAMOTO, K. & SHAW, J. M. 2005. Mitochondrial morphology and dynamics in yeast and multicellular eukaryotes. *Annual Review of Genetics*, 39, 503-536.
- OLOFSSON, C. S., GOPEL, S. O., BARG, S., GALVANOVSKIS, J., MA, X. S., SALEHI, A., RORSMAN, P. & ELIASSON, L. 2002. Fast insulin secretion reflects exocytosis of docked granules in mouse pancreatic B-cells. *Pflugers Archive - European Journal of Physiology*, 444, 43-51.
- OLOFSSON, C. S., SALEHI, A., HOLM, C. & RORSMAN, P. 2004. Palmitate increases L-type  $Ca^{2+}$  currents and the size of the readily releasable granule pool in mouse pancreatic beta-cells. *Journal of Physiology*, 557, 935-948.
- ORCI, L. & UNGER, R. H. 1975. Functional subdivision of islets of Langerhans and possible role of D cells. *Lancet*, 2, 1243-1244.
- PAL, N. R. & PAL, S. K. 1993. A review on image segmentation techniques. *Pattern Recognition*, 26, 1277-1294.
- PANTELIC, R. S., ERICKSSON, G., HAMILTON, N. & HANKAMER, B. 2007. Bilateral edge filter: photometrically weighted, discontinuity based edge detection. *Journal of Structural Biology*, 160, 93-102.
- PANTELIC, R. S., ROTHNAGEL, R., HUANG, C. Y., MULLER, D., WOOLFORD, D., LANDSBERG, M. J., MCDOWALL, A., PAILTHORPE, B., YOUNG, P. R., BANKS, J., HANKAMER, B. & ERICKSSON, G. 2006. The discriminative bilateral filter: an enhanced denoising filter for electron microscopy data. *Journal of Structural Biology*

- 395-408.
- PAPARI, G., PETKOV, N. & CAMPISI, P. 2007. Artistic edge and corner enhancing smoothing. *IEEE Transactions on Image Processing*, 16, 2449-2462.
- PELHAM, H. R. B. 1998. Getting through the Golgi complex. *Trends in Cell Biology*, 8, 45-49.
- PENCZEK, P., MARKO, M., BUTTLE, K. & FRANK, J. 1995. Double-tilt electron tomography. *Ultramicroscopy*, 60, 393-410.
- PERKINS, G. A. & FREY, T. G. 2000. Recent structural insight into mitochondria gained by microscopy. *Micron*, 31, 97-111.
- PERKINS, G. A., RENKEN, C. W., SONG, J. Y., FREY, T. G., YOUNG, S. J., LAMONT, S., MARTONE, M. E., LINDSEY, S. & ELLISMAN, M. H. 1997. Electron tomography of large, multicomponent biological structures. *Journal of Structural Biology*, 120, 219-227.
- PERONA, P. & MALIK, J. 1990. Scale-space and edge detection using anisotropic diffusion. *IEEE Transactions on Pattern Analysis and Machine Intelligence*, 12, 629-639.
- PRADO, C. L., PUGH-BERNARD, A. E., ELGHAZI, L., SOSA-PINEDA, B. & SUSSEL, L. 2004. Ghrelin cells replace insulin-producing beta cells in two mouse models of pancreas development. *Proceedings Natl Acad Science U S A*, 101, 2924-2929.
- PRATT, W. K. 1978. *Digital Image Processing*, New York, USA, Wiley-Interscience.
- RADON, J. 1917. Über die Bestimmung von Funktionen durch ihre Integralwerte längs gewisser Mannigfaltigkeiten. *Berichte über die Verhandlungen der Königlich Sächsischen Gesellschaft der Wissenschaften zu Leipzig*. Leipzig.
- RASBAND, W. S. 1997-2014. *ImageJ* [Online]. U. S. National Institutes of Health, Bethesda, Maryland, USA. Available: <http://imagej.nih.gov/ij/index.html> 2009].
- RORSMAN, P., ELIASSON, L., RENSTROM, E., GROMADA, J., BARG, S. & GOPEL, S. 2000. The cell physiology of biphasic insulin secretion. *News in Physiological Science*, 15, 72-77.
- RORSMAN, P. & RENSTROM, E. 2003. Insulin granule dynamics in pancreatic beta cells. *Diabetologia*, 46, 1029-1045.
- RUDIN, L. I., OSHER, S. & FATEMI, E. 1992. Nonlinear total variation based noise removal algorithms. *Physica D: Nonlinear Phenomena*, 60, 259-268.
- RUSS, J. C. 2002. *The image processing handbook*, Boca Raton, USA, CRC Press.
- RUSS, J. C. & DEHOFF, R. T. 2000. *Practical Stereology*, New York, Kluwer Academic/Plenum.
- RYAN, M. T. & HOOGENRAAD, N. J. 2007. Mitochondrial-nuclear communications. *Annual Review of Biochemistry*, 76, 701-722.
- SANDBERG, K. 2007. Methods for image segmentation in cellular tomography. *Methods in Cell Biology*, 79, 769-798.
- SCHUIT, F., FLAMEZ, D., DE VOS, A. & PIPELEERS, D. 2002. Glucose-Regulated Gene Expression Maintaining the Glucose-Responsive State of Cells. *Diabetes*, 51, 326-332.
- SETHIAN, J. A. 1999. *Level set methods and fast marching methods: Evolving interfaces in computational geometry, fluid mechanics, computer vision, and materials science*, Cambridge, USA, Cambridge University Press.
- SHOOP, R. D., ESQUENAZI, E., YAMADA, N., ELLISMAN, M. H. & BERG, D. K. 2002. Ultrastructure of a somatic spine mat for nicotinic signaling in neurons. *Journal of Neuroscience*, 22, 748-756.
- SONKA, M., HLAVAC, V. & BOYLE, R. 1999. *Image Processing, Analysis, and Machine Vision*, Pacific Grove, CA: PWS Publishing.
- SOSINSKY, G. E., DEERINCK, T. J., GRECO, R., BUITENHUYS, C. H., BARTOL, T. M. & ELLISMAN, M. H. 2005. Development of a model for microphysiological simulations: small nodes of ranvier from peripheral nerves of mice reconstructed by electron tomography. *Neuroinformatics*, 3, 133-162.
- SRIVASTAVA, S. & GOREN, H. J. 2003. Insulin constitutively secreted by beta-cells is necessary for glucose-stimulated insulin secretion. *Diabetes*, 52, 2049-2056.

- SUBRAMANIAM, S. 2005. Bridging the imaging gap: visualizing subcellular architecture with electron tomography. *Current Opinion in Microbiology*, 8, 316-322.
- TANG, G., PENG, L., BALDWIN, P. R., MANN, D. S., JIANG, W., REES, I. & LUDTKE, S. J. 2007. EMAN2: an extensible image processing suite for electron microscopy. *Journal of Structural Biology*, 157, 38-46.
- TOMASI, C. & MANDUCHI, R. Bilateral filtering for gray and color images. Sixth International Conference on Computer Vision, 4-7 Jan 1998 1998. 839-846.
- VAN DER HEIDE, P., XU, X. P., MARSH, B. J., HANEIN, D. & VOLKMANN, N. 2007. Efficient automatic noise reduction of electron tomographic reconstructions based on iterative median filtering. *Journal of Structural Biology*, 158, 196-204.
- VAN MEEL, E. & KLUMPERMAN, J. 2008. Imaging and imagination: understanding the endo-lysosomal system. *Histochemistry and Cell Biology*, 129, 253-266.
- VINCENT, L. & SOILLE, P. 1991. Watersheds in digital spaces: An efficient algorithm based on immersion simulations. *IEEE Transactions on Pattern Analysis and Machine Intelligence*, 13, 583-598.
- VOLKMANN, N. 2002. A novel three-dimensional variant of the watershed transform for segmentation of electron density maps. *Journal of Structural Biology*, 138, 123-129.
- VOLKMANN, N., BRIAN SHEEHAN, XIAO-PING XU, CHRIS PAGE & LESPERANCE, T. 2000. CoAn [Online]. Available: <http://coan.burnham.org/pycoan>.
- WEICKERT, J. 1994. *Scale-Space Properties of Nonlinear Diffusion Filtering with a Diffusion Tensor*, Technische Universität Kaiserslautern.
- WEICKERT, J. 1998. *Anisotropic Diffusion in Image Processing*, Stuttgart, Germany, B.G. Teubner Stuttgart.
- WEICKERT, J. 1999. Coherence-Enhancing Diffusion Filtering. *International Journal of Computer Vision*, 31, 111-127.
- WIEDERKEHR, A. & WOLLHEIM, C. B. 2006. Minireview: implication of mitochondria in insulin secretion and action. *Endocrinology*, 147, 2643-2649.
- WINKLER, G. 2002. Smoothers for Discontinuous Signals. *Journal of Nonparametric Statistics*, 14, 203-222.
- WINKLER, H. 2007. 3D reconstruction and processing of volumetric data in cryo-electron tomography. *Journal of Structural Biology*, 157, 126-137.
- WINSLOW, T. 2001. *Stem cells: scientific progress and future research directions*. Madison, Wisconsin.
- WOOLFORD, D., HANKAMER, B. & ERICKSSON, G. 2007. The Laplacian of Gaussian and arbitrary z-crossings approach applied to automated single particle reconstruction. *Journal of Structural Biology*, 159, 122-134.
- YOULE, R. J. & VAN DER BLIEK, A. M. 2012. Mitochondrial Fission, Fusion, and Stress. *Science*, 337, 1062-1065.
- ZHOU, W. & ZHANG, D. 1999. Progressive switching median filter for the removal of impulse noise from highly corrupted images. *IEEE Transactions on Circuits and Systems II: Analog and Digital Signal Processing*, 46, 78-80.